Mathematical Modeling of Transient Transport Phenomena in PEM Fuel Cells

by

Hao Wu

A thesis
presented to the University of Waterloo
in fulfillment of the
thesis requirement for the degree of
Doctor of Philosophy
in
Mechanical Engineering

Waterloo, Ontario, Canada, 2009

I hereby declare that I am the sole author of this thesis. This is a true copy of the thesis, including any required final revisions, as accepted by my examiners.

I understand that my thesis may be made electronically available to the public.

Hao Wu

Abstract

The dynamic performance of polymer electrolyte membrane fuel cells (PEMFCs) is of great interest for mobile applications such as in automobiles. However, the length scale of a PEM fuel cell's main components are ranging from the micro over the meso to the macro level, and the time scales of various transport processes range from milliseconds up to a few hours. This combination of various spatial and temporal scales makes it extremely challenging to conduct in-situ measurements or other observations through experimental means. Thus, numerical simulation becomes a very important tool to help understand the underlying electrochemical dynamics and transient transport phenomena within PEM fuel cells.

In this thesis research, a comprehensive 3D model is developed which accounts for the following transient transport mechanisms: the non-equilibrium phase transfer between the liquid water and water vapor, the non-equilibrium membrane water sorption/desorption, liquid water transport in the porous backing layer, membrane hydration/dehydration, gas diffusion in the porous backing layer, the convective gas flow in the gas channel, and heat transfer. Furthermore, some of the conventionally used modeling assumptions and approaches have been incorporated into the current model. Depending on the modeling purposes, the resulting model can be readily switched between steady and unsteady, isothermal and non-isothermal, single- and multi- phases, equilibrium and non-equilibrium membrane sorption/desorption, and three water production assumptions.

The governing equations which mathematically describe these transport processes, are discretized and solved using a finite-volume based commercial software, Fluent, with its user coding ability. To handle the significant non-linearity stemming from the multi-water phase transport, a set of numerical under-relaxation techniques is developed using the programming language C.

The model is validated with experimental results and good agreements are achieved. Subsequently, using this validated model numerical studies have been carried out to probe various transient transport phenomena within PEM fuel cells and the cell dynamic responses with respect to different operating condition changes. Furthermore, the impact of flow-field design on the cell performance is also investigated with the three most common flow channel designs.

Acknowledgements

I would like to express my deepest gratitude to my supervisor, Dr. Xianguo Li and Dr. Peter Berg, for their invaluable guidance, steady encouragement, inspiration and support throughout my PhD work. I would also like to thank Saher Shakhshir and Dr. Yongxin Wang for their kind help on developing and testing a PEM fuel cell prototype for model validation.

Financial support by Natural Sciences and Engineering Research Council of Canada (NSERC) through Discovery Grants and a Strategic Project Grant is gratefully acknowledged.

Contents

List of Tables **ix**

List of Figures **xiv**

List of Symbols **xv**

1 Introduction **1**

1.1 Background 1

1.2 Operating Principal of PEM Fuel Cells 2

1.3 Fuel Cell Components 3

1.3.1 Polymer Electrolyte Membrane 3

1.3.2 Catalyst Layer 4

1.3.3 Gas Diffusion Layer 4

1.3.4 Bipolar Plate 5

1.4 PEM Fuel Cell Performance 5

1.5 Objectives and Scope of the Thesis 7

2 Literature Review **9**

2.1 Performance Models 9

2.2 CFD Models 11

2.2.1 Steady State Models 11

2.2.2 Transient Models 18

2.3 Summary 20

3 Model Formulation **22**

3.1 Assumptions 22

3.2 Transport of Gas Species 23

3.2.1 Conservation of Mass and Momentum 23

3.2.2 Reaction Kinetics 25

3.3 Transport of Multi-Water Phases 28

3.3.1 Water Formation Mechanism 28

3.3.2 Transport of Water Vapor 30

3.3.3 Transport of Dissolved Water 30

3.3.4 Transport of Liquid Water 38

3.4 Transport of Electric Charge 44

3.4.1 Conservation of Electronic Charge 45

3.4.2 Conservation of Protonic Charge 45

3.5 Transport of Energy 46

3.6 Boundary and Initial Conditions 49

3.6.1 Boundary Conditions 49

3.6.2 Initial Conditions 52

3.7 Model Input Parameters 52

3.8 Summary 53

4 Numerical Implementation **57**

4.1 Numerical Procedure 57

4.1.1 Outer Loop 58

4.1.2 Inner Loop 58

4.1.3 Under-relaxation Schemes 61

4.2 Convergence Criteria 62

4.3 Grid-Independent Solution 63

4.4 Time Step Independent Solution 67

4.5 Summary 69

5 Results and Discussion – Part I: Single-Channel Model 70

5.1 Computational Domain 70

5.2 Model Validation 72

5.3 Analysis of Several Traditional Modeling Approaches 74

5.3.1 Boundary Conditions for Solid Potential 75

5.3.2 Equilibrium vs. Non-equilibrium Water Sorption and Desorption Processes 78

5.3.3 Comparison of Water Production Mechanisms 80

5.3.4 Empirical Expressions for Capillary Pressure 85

5.3.5 Empirical Expressions for Relative Permeability 87

5.4 Dynamic Responses of PEM Fuel Cells with Respect to Operating Condition Changes 90

5.4.1 Hysteresis Effects During Voltage Sweep Test 90

5.4.2 Dynamic Response Corresponding to Nonlinear Impedance Load Change 92

5.4.3 Effect of Step Change in Relative Humidity 97

5.4.4 Effect of Step Change in Cell Voltage 97

5.4.5 Effect of Step Change in Operating Pressure 99

5.4.6 Effect of Step Change in Gas Flow Stoichiometric Ratio . . . 101

5.5 Transient Transport Phenomena Within PEM Fuel Cells 101

5.5.1 Transport of Gas Species 102

5.5.2 Transport of Multi-Water Phases 105

5.5.3 Transport of Electric Charge 112

5.5.4 Transport of Energy 118

5.6 Summary 121

6 Results and Discussion – Part II: Multi-Channel Model 124

6.1 Computational Domain 124

6.2 Flow Field 126

6.3 Oxygen Distribution 131

6.4 Liquid Water Distribution 131

6.5 Current Density Distribution 136

6.6 Summary 141

7 Summary and Future Work **142**

APPENDICES **147**

A List of User Defined Functions **148**

A.1 User Subroutines 148

A.2 Fluent Standard UDFs 151

References **159**

List of Tables

1.1 Functions and transport phenomena related with each layer of PEM fuel cells. 6

3.1 Structural parameters. 53
3.2 Electrochemical kinetic parameters [23, 30] 53
3.3 Physical and thermal parameters. 54
3.4 Source terms in conservation equations. 56

4.1 Grid independent study in the y-direction with $N^x = 20$ and $N^z = 50$. 63

5.1 Operating conditions used in the base case study. 71
5.2 Range of phase change parameters used in the thesis. 72
5.3 Comparison of computational time by implementing the two different methods in the specification of boundary conditions for the electronic potential. 76

List of Figures

1.1 Schematic and operation principle of PEM fuel cell. 3

1.2 Sample polarization curve showing the three overpotential regions . 7

3.1 Schematic of oxygen reduction reaction in the cathode catalyst layer (reproduced from Berg *et al.* [111]). 29

3.2 Water uptake of Nafion membrane at equilibrium with water vapor. 33

3.3 Schematic of equilibrium water sorption model (a) ill-posed; (b) well-posed. 34

3.4 Numerical implementation of the water source owing to back diffusion 36

3.5 Illustration of boundary condition specifications on a computational domain with a single pair of gas flow channels: (a) front view, (b) side view. 50

4.1 Illustration of the solution procedure of the segregated solver. . . . 59

4.2 Convergence history of a typical steady state run. 62

4.3 Demonstration of the grid scheme for the single-channel cell model: (a) x-y plane, (b) scaled x-z plane, and (c) scaled y-z plane. 64

4.4 Effect of N^y on the error of average current density. 65

4.5 Effect of N^y on the computational time. 66

4.6 Effect of N^y on the number of iterations required for convergence. . 66

4.7 Locally refined mesh around the corner of the gas flow channel (a) interdigitated channel, (b) serpentine channel. 68

5.1 Schematic of the computational domain of the single-channel model. 71

5.2 Model validation: hysteresis effect of the dynamic polarization curves during voltammetry sweep studies. 73

5.3 Model validation: cell dynamic response with respect to voltage changes ($0.6 \rightarrow 0.65 \rightarrow 0.6$ V) and under partially humidified conditions ($RH_{a,c} = 50\%$). 74

5.4 Schematic of two different methods in the specifications of boundary conditions for solid potential. 75

5.5 Phase potential distribution across the MEA (at $x = 3.75 \times 10^{-4}\ m$ and $z = 0.025\ m$) for the boundary conditions specified by: (a) Method 1; (b) Method 2. 77

5.6 Distribution of the actual and the equilibrium membrane water content on a line across the anode catalyst layer (ACL)-membrane-cathode catalyst layer (CCL) (at $x = 3.75 \times 10^{-4}$ m and $z = 0.025$ m) for the membrane water sorption and desorption rate coefficient of γ_a and γ_d: (a) $\gamma_a = \gamma_d$; (b) $\gamma_a = 0.1\gamma_d$. 79

5.7 Distribution of the actual and the equilibrium membrane water content along the middle x-z cross section of the anode catalyst layer (ACL): (a) $\gamma_{a,d} = 0.01$ 1/s; (b) $\gamma_{a,d} = 1.0$ 1/s; (c) $\gamma_{a,d} = 100$ 1/s; (d) equilibrium model. 81

5.8 Cell dynamic response corresponding to different water sorption rates and with respect to a step change in relative humidity from $RH_{a,c} = 1.0$ to $RH_{a,c} = 0.5$. 82

5.9 Variation of average current density with phase transfer rates, Sh_{ce}, corresponding to vapor and liquid water production assumptions. . 83

5.10 Variation of average current density with absorption/desorption rates, γ, corresponding to liquid and dissolved water production assumptions. 85

5.11 Contour plot of gas pressure and vector plot of gas velocity on a $x-y$ cross section of the CCL and cathode GDL close to the channel outlet: (a) water vapor production; (b) liquid water production; (c) dissolved water production. 86

5.12 Saturation distribution in cathode catalyst layer (CCL) and cathode gas diffusion layer (GDL) with respect to the empirical function of capillary pressure used: (a) standard Leverett function; (b) Kumbur's expression; (c)-1 Ye's expression, CCL; (c)-2 Ye's expression, GDL. 88

5.13 Saturation distribution in cathode catalyst layer (CCL) and cathode gas diffusion layer (GDL), with a power of 4.5 for the relative permeability in GDL with the capillary pressure given by: (a) standard Leverett function; (b) Kumbur's expression; (c)-1 Ye's expression, CCL; (c)-2 Ye's expression, GDL. 89

5.14 Polarization curve under partially humidified conditions ($RH_{a,c} = 0.5$) and with the voltage sweep rate of: (a) 10 mV/s; (b) 25 mV/s; (c) 50 mV/s. 91

5.15 Hysteresis response of the average membrane water content at the middle $x - z$ cross section of the anode catalyst layer (ACL) and membrane (Plane 1&2, refer to Figure 5.1), with a voltage sweep rate of: (a) 10 mV/s; (b) 25 mV/s; (c) 50 mV/s. 93

5.16 Hysteresis response of the liquid saturation at Point 1 (refer to Figure 5.1) during the voltage sweep cycles. 94

5.17 Dynamic responses of average current density, liquid saturation and temperature, corresponding to different impedance frequencies under fully humidified conditions. 95

5.18 Time extended dynamic responses of average current density, liquid saturation and temperature, corresponding to an impedance frequency of 1 Hz under fully humidified conditions. 96

5.19 Time extended dynamic responses of liquid saturation and water content, corresponding to an impedance frequency of 1 Hz under partially humidified conditions ($RH_{a,c} = 0.5$). 97

5.20 Current response corresponding to step changes in relative humidity. 98

5.21 Current response corresponding to step changes in cell voltage. . . . 99

5.22 Current response corresponding to step changes in cell voltage at partial humidified conditions ($RH_{a,c} = 0.5$). 100

5.23 Current response corresponding to step changes in operating pressure. 100

5.24 Current response corresponding to step changes in stoichiometric ratio. 101

5.25 Flow streamline (vector plot) and pressure (P, Pa) distribution (contour plot) at steady state: (a) plane 4, and (b) plane 5 (refer to Figure 5.1). 104

5.26 Transient variation of the hydrogen concentration, C_{h_2} (mol/m^3), within the anode side gas flow channel, GDL and catalyst layer (from top to bottom): (a) $t = 0.001$ s, (b) $t = 1.0$ s, (c) $t = 10.0$ s, and (d) $t = 50.0$ s. 106

5.27 Transient variation of the oxygen concentration, C_{o_2} (mol/m^3), within the cathode side gas flow channel, GDL and catalyst layer (from bottom to top): (a) $t = 0.001$ s, (b) $t = 1.0$ s, (c) $t = 10.0$ s, and (d) $t = 50.0$ s. 107

5.28 Transient variation of the water vapor concentration, C_{h_2o} (mol/m^3), within the anode flow channel, GDL and catalyst layer (from top to bottom): (a) $t = 0.001$ s, (b) $t = 1.0$ s, (c) $t = 10.0$ s, and (d) $t = 50.0$ s. 108

5.29 Transient variation of the water vapor concentration, C_{h_2o} (mol/m^3), within the cathode flow channel, GDL and catalyst layer (from bottom to top): (a) $t = 0.001$ s, (b) $t = 1.0$ s, (c) $t = 10.0$ s, and (d) $t = 50.0$ s. 110

5.30 Transient variation of the dissolved water (actual membrane water content, λ) within the anode catalyst layer, membrane, and cathode catalyst layer (from top to bottom): (a) $t = 0.001$ s, (b) $t = 1.0$ s, (c) $t = 10.0$ s, and (d) $t = 50.0$ s. 111

5.31 Transient variation of the liquid saturation, s, within the cathode side GDL and catalyst layer (from bottom to top): (a) $t = 0.001$ s, (b) $t = 1.0$ s, (c) $t = 10.0$ s, and (d) $t = 50.0$ s. 113

5.32 Distribution of the electronic potential loss, ϕ_s (V), at the middle $x - y$ cross section (Plane 4) of the GDL and catalyst layer: (a) anode side, (b) cathode side. 114

5.33 Distribution of the protonic potential, ϕ_m (V), at the middle $x - y$ cross section (Plane 4) of the ACL, membrane, and CCL. 115

5.34 Distribution of the transverse current density, J^y, at the middle $x-y$ cross section (Plane 4) of the cathode catalyst layer: (a) electronic current density, J_s^y, (b) protonic current density, J_m^y, and (c) total current density, $J^y = J_s^y + J_m^y$. 116

5.35 Distribution of the transverse current density, J^y (A/cm^2), at the middle $x - z$ cross section (Plane 2) of the membrane: (a) $RH_{a,c} = 1.0$, (b) $RH_{a,c} = 0.5$. 117

5.36 Current density distribution from experimental measurement [141]. 118

5.37 Distribution of the activation overpotential, η (V), within the: (a) anode catalyst layer, (b) cathode catalyst layer. 119

5.38 Distribution of the volumetric reaction rate, $\mathcal{R}_i$ (mol/m^{3}s), at: (a) anode catalyst layer, (b) cathode catalyst layer. 120

5.39 Transient variation of the cell temperature, T (K): (a) $t = 0.001$ s, (b) $t = 1.0$ s, (c) $t = 10.0$ s, and (d) $t = 50.0$ s. 122

6.1 Gas flow channel layouts: (a) straight parallel channel, (b) interdigitated channel, (c) serpentine channel. 125

6.2 Distribution of the gas pressure: (a) straight parallel channel, (b) interdigitated channel, (c) serpentine channel. 128

6.3 Velocity profiles: (a) straight parallel channel, (b) interdigitated channel, (c) serpentine channel. 130

6.4 Vortex around the sharp corner: (a) interdigitated channel, (b) serpentine channel. 130

6.5 Distribution of oxygen concentration (mol/m^3): (a) straight parallel channel, (b) interdigitated channel, (c) serpentine channel. 133

6.6 Multiple serpentine flow channels [143]. 133

6.7 Distribution of liquid saturation at the middle $x-z$ cross-section of the cathode catalyst layer: (a) straight parallel channel, (b) interdigitated channel, (c) serpentine channel. 135

6.8 Effect of cross flow between interdigitated channels on the distribution of liquid saturation: (a) slice 1 ($z/L_{ch} = 1/10$), (b) slice 3 ($z/L_{ch} = 5/10$), (c) slice 5 ($z/L_{ch} = 9/10$). 137

6.9 Effect of cross flow between serpentine channels on the distribution of liquid saturation: (a) slice 1 ($z/L_{ch} = 1/10$), (b) slice 3 ($z/L_{ch} = 5/10$), (c) slice 5 ($z/L_{ch} = 9/10$). 138

6.10 Effect of intrinsic permeability on the distribution of liquid saturation: (a) straight parallel channel, (b) interdigitated channel, (c) serpentine channel. 139

6.11 Distribution of the transverse current density, J^y, at the middle $x-z$ cross-section of the membrane layer: (a) straight parallel channel, (b) interdigitated channel, (c) serpentine channel. 140

List of Symbols

a	water activity; density of active area in the catalyst layer (m^2/m^3)
A	area (m^2)
A_v	reaction surface area density (m^2/m^3)
b	Tafel slope; general source term
B	pre-exponential factor
C	molar concentration (mol/m^3); compression pressure (atm)
C_f	friction coefficient
c_p	specific heat ($J/kg \cdot K$)
d	diameter (m)
D	mass diffusivity of species (m^2/s)
$\mathcal{D}$	mass diffusivity of species (m^2/s)
f_V	volume fraction of water in membrane
E	total energy (J)
EW	equivalent molecular weight of dry membrane (1.1 kg/mol)
f	impedance frequency (Hz)
$\mathscr{F}$	Faraday's constant 96487 (C/mol)
G	Gibbs free energy (J/mol)
h	enthalpy (J)
H_o	Henry's constant for the dissolution of oxygen in liquid water ($Pa \cdot m^3/mol$)
j_0^{ref}	reference exchange current density (A/m^3)
$\vec{J}$	current density (A/m^2)
k	thermal conductivity (W/mK); reaction rate constant
K	permeability (m^2)
L	length scale (m)
$\dot{m}$	mass flux (kg/m^2s)
M	molecular weight (kg/mol)
n	number of electrons transferred in the half cell reaction; unit normal vector
N	number of grid points; diffusion flux of species (mol/m^2s)
n_d	electro-osmotic drag coefficient (H_2O/H^+)
P	pressure (atm)
R	residual; ohmic resistance (Ω)
$\mathscr{R}$	universal gas constant 8.314 ($J/mol \cdot K$)
Re	Reynolds number
RH	relative humidity
$\mathcal{R}$	reaction rate (A/m^3)

s	liquid saturation
S	source terms; entropy (J/K)
Sh	Sherwood's number
t	time (s)
T	temperature (K)
$\vec{u}$	velocity (m/s)
V	volume (m^3)
wt %	wettability
x	x-coordinate
X	molar fraction
y	y-coordinate
Y	mass fraction
z	z-coordinate

Greek letters

α	transfer coefficient; under-relaxation factor
β	reaction order
δ	thickness (m)
ε	porosity
η	overpotential (V)
γ	sorption/desorption rate coefficient (1/s)
Γ	uptake coefficient
λ	membrane water content
μ	dynamic viscosity (kg/ms)
ν	species coefficient involved in the reaction
$\omega_i^{''}$	rate of production (mol/m^3s)
ϕ	electric potential (V)
Ψ	variables
ρ	density (kg/m^3)
σ	electric conductivity (S/m); surface tension (N/m)
τ	tortuosity
$\overline{\overline{\tau}}$	stress tensor
θ_c	contact angle (°)
Θ	variables
ξ	stoichiometric flow ratio

Subscripts

a	anode
act	activation
ad	adsorption/desorption

b	bipolar plate; backward reaction
c	cathode; capillary pressure
ce	condensation/evaporation
$cell$	cell characteristic
cl	catalyst layer
d	dissolved water phase; desorption
diff	back diffusion
$drag$	electroosmotic drag
e	equilibrium state
f	forward reaction
g	gas phase
gdl	gas diffusion layer
i	the i^{th} component
in	internal current density; inlet
irr	irreducible saturation
j	the j^{th} species
k	phase k
l	liquid water; limiting current density
m	gas mixture; membrane; mass transfer
mem	membrane
nb	neighboring cells
nw	non-wetting phase
ohm	ohmic
P	center cell
pore	pores of the porous media
$reac$	reaction
rev	reversible
rg	relative permeability of gas phase
rl	relative permeability of liquid phase
s	solid phase; species transport
v	water vapor
vd	phase transfer between vapor and dissolved water
vl	phase transfer between vapor and liquid water
w	water, wetting phase
0	standard conditions (273 K, 1 atm); inlet conditions

Superscripts

eff	effective value
n	the n^{th} iteration
new	value from the current iteration
ref	reference state
sat	saturation pressure (atm)

1D/2D/3D	one/two/three- dimensional
ACL	anode catalyst layer
AMG	algebraic multigrid
B.C.	boundary conditions
CCL	cathode catalyst layer
CFD	computational fluid dynamics
CL	catalyst layer
DOF	degree of freedom
FEM	finite element method
FVM	finite volume method
GDL	gas diffusion layer
HOR	hydrogen oxidation reaction
LBM	Lattice Boltzmann method
MEA	membrane electrode assembly
MD	molecular dynamics
MPL	micro-porous layer
ORR	oxygen reduction reaction
PEM	polymer electrolyte membrane, or proton exchange membrane
PTFE	polytetrafluoroethylene
RHS	right hand side
SUR	successive under-relaxation
TPZ	triple-phase zone
UDF	user defined function
UDS	user defined scalar
VOF	volume of fluid

Chapter 1

Introduction

1.1 Background

With the increasing concerns about sustainable energy and environmental issues, hydrogen and fuel cell technology is attracting more and more attention from academic research, industry and governments. One of the most promising fuel cells is the polymer electrolyte membrane (PEM) fuel cell, an electro-chemical energy conversion device which converts hydrogen and oxygen directly to electrical energy with by-products of pure water and heat only. Compared to the conventional energy conversion devices, a PEM fuel cell is exceptionally fuel-efficient. It converts about two to three times more energy from fuel into usable power than the automobile power system used today. Other advantages of PEM fuel cells include low operating temperature ($< 100\ ^{o}$C), quiet operation, high power density, quick startup and, of outmost importance, zero emissions, which leads directly to a reduction of air pollution and greenhouse gases. All these advantages make it the prime candidate for automotive applications, as well as portable systems such as cell phones or laptops.

As an emerging new technology, the development of PEM fuel cells is still facing many challenges that must be tackled before widespread commercialization, for example, cost reduction, durability and reliability, system integration, thermal and water management, to name a few. Cost used to be the most prohibiting factor for the widespread implementation of PEM fuel cells. However, with the progress of new materials, improved fabrication processes, and especially the reduction of platinum usage, the cost of a PEM fuel cell system for automotive applications has been reduced significantly from about \$4000/kW at year 1995, to only about \$50/kW at year 2008. It is anticipated that the cost can eventually reach about \$30/kW at 2015 [1], at which it will be comparable to the cost of the combustion engine which is about \$20-30/kW. In order to overcome above challenges and achieve the ultimate goal, various research activities have been carried out by national labs, universities, and industrial companies in the past two decades. These studies can be generally grouped into two categories: experiment and numerical simulation.

In the laboratory experiment, a fuel cell (or a stack) is assembled and measurements are made regarding its performance. Nevertheless, the length scale of PEM fuel cells' main components are ranging from the micro over the meso to the macro level, and the time scales of various transport processes range from milliseconds up to a few hours. This combination of various spatial and temporal scales makes it extremely challenging to conduct in-situ measurements or other observations through experimental means. Furthermore, physical prototyping can be very expensive and time consuming, depending on the system complexity. Thereby, numerical simulation has become a very important tool to help understand the underlying electrochemical dynamics and transport phenomena within PEM fuel cells.

Over the past decades, numerous efforts in terms of numerical modeling have been made to investigate the operation of PEM fuel cells. Most of these studies were focused on steady state phenomena and the transient transport processes have been usually overlooked. Yet, for mobile applications like vehicles or portable devices, the dynamic characteristics of the fuel cell are of paramount importance. Therefore, the current thesis research aims at the unsteady modeling of various transient transport phenomena and dynamic responses of PEM fuel cells. The details of this thesis research will be presented in later chapters (Chapters 3-6), while the remaining part of this chapter will discuss the background of PEM fuel cells and state the objectives and outline of the present thesis research.

1.2 Operating Principal of PEM Fuel Cells

Figure 1.1 illustrates the operational principle of a PEM fuel cell. Pure hydrogen or reformed hydrogen gas enters the anode channel and diffuses through the porous anode electrode towards the anode catalyst layer (ACL), where hydrogen molecules are stripped of their electrons with the help of a platinum catalyst and become positively charged hydrogen ions (protons), based on the *hydrogen oxidation reaction* (HOR):

$$H_2 \rightarrow 2H^+ + 2e^- \tag{1.1}$$

Protons migrate through the ion-selective membrane and the electrons travel through the external circuit, thereby creating electric current. On the cathode side, a humidified air stream enters the cathode channel and diffuses towards the cathode-side catalyst layer (CCL). At the platinum catalyst surface, protons recombine with electrons and oxygen molecules to produce water and heat, following the *oxygen reduction reaction* (ORR):

$$\frac{1}{2}O_2 + 2H^+ + 2e^- \rightarrow H_2O \tag{1.2}$$

Reaction (1.1) is slightly endothermic and reaction (1.2) is strongly exothermic, so that overall heat is generated. By combining the reactions (1.1) and (1.2), the

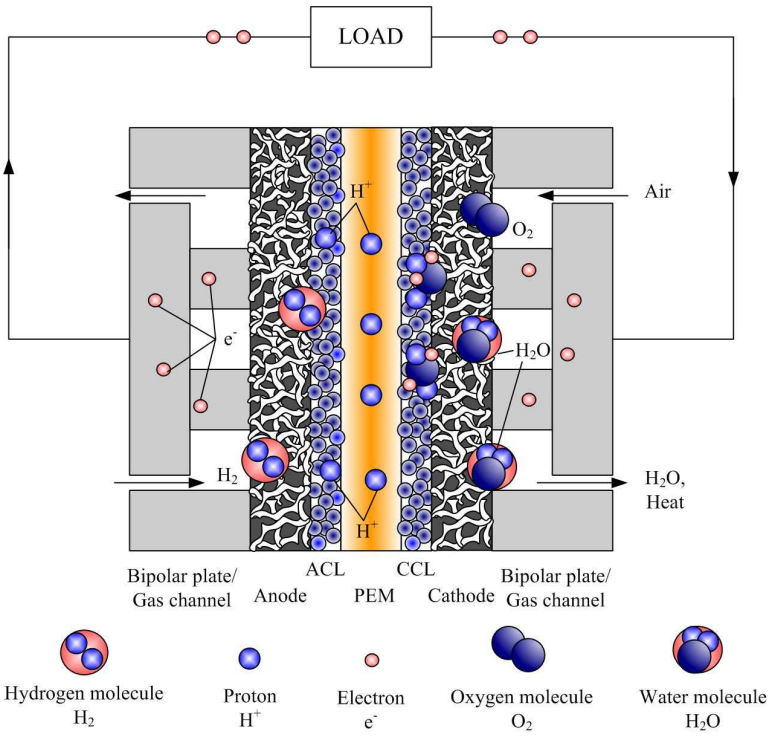

Figure 1.1: Schematic and operation principle of PEM fuel cell.

overall reaction in the PEM fuel cell can be summarized as

$$H_2 + \frac{1}{2}O_2 \rightarrow H_2O + heat + electrical\ energy \tag{1.3}$$

The voltage of a single PEM fuel cell is typically in the range of 0.4 to 0.8 V and the cell current density is usually less than 1 A/cm^2. In practice, the fuel cell shown in Figure 1.1 would be combined in series with other cells to produce a fuel cell stack. This fuel cell stack would then be part of a fuel cell system which would include fuel pumps, fuel processors, heat exchangers, humidifies, and other equipment. The power of such PEM fuel cell systems can vary from a few Watts which is suitable for portable applications, up to million Watts such as in the stationary applications in power plant.

For a more detailed discussion on the PEM fuel cell and its applications, the reader is referred to [2, 3, 4].

1.3 Fuel Cell Components

1.3.1 Polymer Electrolyte Membrane

The polymer electrolyte membrane (PEM) is a critical component of a working fuel cell. Its function is to conduct protons efficiently while repelling the electrons,

thus forcing the electrons to travel through the outer circuit to produce electric work. A desirable membrane in a PEM fuel cell should possess the characteristics of high proton conductivity, good insulation regarding electronic current, low fuel crossover properties, and it must also be robust enough to be assembled into a fuel cell stack and have high chemical and thermal stability. The most commonly used and investigated membrane material is Nafion, made by Dupont, which will be considered predominately in this study. The Nafion membrane belongs to a class of poly-perfluoro-sulfonic acids which consists of a hydrophobic tetrafluoroethylene backbone with pendant side chains of perfluoronated vinyl-ethers terminated by sulfonic acid groups. Proton conductivity in Nafion and most other polymer electrolytes increases with the water activity and that is the prime reason to humidify the incoming gas reactants. Sufficient water must be absorbed into the membrane to ionize the acid groups, whereas excess water can flood the cathode of the fuel cell, diminishing fuel cell performance and limiting the power output. Therefore, water management in the fuel cell is critical for PEM fuel cell operation, and it is one important task of this modeling study.

1.3.2 Catalyst Layer

Normally, the electrochemical reactions (1.1) and (1.2) would occur very slowly at the low operating temperature of a PEM fuel cell, especially at the cathode side. In order to speed up these two reactions, the membrane is coated with a thin catalyst layer on each electrode side. The catalyst layer usually consists of microscale carbon particles, each of which can support nanoscale platinum (Pt) catalyst particles, loosely embedded in a matrix of ionomer. The ionomer microstructure and ionomer-catalyst layer interface are important factors for the performance of a fuel cell; they determine the ion exchange across the membrane that allows the fuel cell reaction to occur. The optimum thickness of the catalyst layer is found to be around 10 μm since almost all of the reactions occur within a 10 μm thick layer. On the other hand, the electrochemical reaction is not evenly distributed over the catalyst layer; therefore, the Pt particles must be properly distributed in the catalyst layer to maximize the reaction efficiency and minimize the cost.

The platinum catalyst has strong affinity for CO. Therefore, a common problem of the fuel cell is anode catalyst CO poisoning if the hydrogen is derived from an alcohol or hydrocarbon fuel. Developers are currently exploring platinum/ruthenium catalysts that are more insensitive to CO. This problem does not exist if pure hydrogen is supplied.

1.3.3 Gas Diffusion Layer

Gas diffusion layers (GDL) consist of porous material resembling carbon cloth or carbon fiber paper, with typical thicknesses between 200 and 300 μm. They serve to provide structural support of the catalyst layer and transport the reactant gases

towards the reaction sites through its hydrophobic pore structure. In addition, they provide an interface where ionization takes place and transfer electrons through the solid matrix. A GDL also plays an important role in heat removal from the reacting site and the water management of the cell. Without a GDL, the membrane would be dried out by the channel gases.

The GDL and catalyst layer together are usually referred to as the porous backing layer. Moreover, the polymer electrolyte membrane, electrodes (anode and cathode), and catalyst together are usually called the membrane electrode assembly (MEA).

1.3.4 Bipolar Plate

The important role of the bipolar plate is to feed the reactant gases towards the GDL, and to assemble individual cells into a cell stack. Gas-flow channels are curved into bipolar plates to provide pathways for reactant gases and, in practice, straight, serpentine, or interdigitated flow fields are commonly used designs. The ratio between channel area and land area is important for any flow field. The channel area should be as large as possible to supply enough reactant gases and to reduce the cell weight and volume requirements; on the other hand, the greater the land area, the better the electrical connection between the bipolar plates and the GDL, and the lower the contact resistance and ohmic losses. A sensible compromise between the above two factors should be sought to achieve the best possible cell performance. The most commonly used material in bipolar plate fabrication is graphite; it has favorable properties such as high electrical conductivity, high thermal conductivity, low corrosion rate, and light weight. However, it is expensive to machine the flow pathways into graphite. Apart from graphite, metal alloy and carbon composites are also materials widely used for manufacturing bipolar plates.

The functions and the physical and chemical phenomena related to each component of the PEM fuel cell are summarized in Table 1.1.

1.4 PEM Fuel Cell Performance

The most general indicator of fuel cell performance is the *polarization curve*. This curve is a plot of the average current density through the fuel cell, I, along the abscissa, versus the cell voltage, ϕ_{cell}, on the ordinate (Figure 1.2). For an ideal fuel cell, this curve would be flat, thus providing a constant, reversible voltage, ϕ_{rev}, independent of the quantity of current drawn from the device. However for a real device, irreversible voltage losses, also known as overpotentials, occur for any finite value of current drawn from the cell. The sum of these overpotentials is known as the cell overpotential, η_{cell}. The relationship between the cell voltage, reversible voltage, and the cell overpotential is given by:

$$\phi_{cell} = \phi_{rev} - \eta_{cell} \tag{1.4}$$

Table 1.1: Functions and transport phenomena related with each layer of PEM fuel cells.

Layer	Functions & Transport Phenomena
Bipolar plate	• Guiding gas reactants flow • Provide structural support for stack assembling • Electron transport • Liquid water transport • Heat transfer
Electrode backing layer	• Gas reactant porous media flow • Water evaporation and condensation • Liquid water porous media flow • Electron transport • Heat transfer
Catalyst layer	• Electrochemical reactions • Gas reactant porous media flow • Water evaporation and condensation • Liquid water porous media flow • Membrane (dissolved) water transport • Membrane water sorption/desorption • Electron transport • Proton transport • Heat transfer
Membrane	• Repelling electrons • Impermeable barrier to gas reactants • Membrane (dissolved) water transport • Proton transport • Heat transfer

A sample polarization curve is shown in Figure 1.2. When examining polarization curves, it is helpful to divide the curve into three regions. A different mode of irreversible loss dominates each of these regions, although they coexist simultaneously in each region. Thus, the shape of the polarization curve can provide the viewer with some information regarding the internal dynamics of the fuel cell.

The first region is called the *activation polarization* region. It is associated with a steep slope and low current densities. This region occurs due to a sluggishness of electrocatalysis at low voltage drops across the cell. In order to provide the electrocatalysis, an activation energy is required to drive the reaction, thus providing the name for this region. In this region, cell voltages (and hence efficiencies) are high, but current density (and hence power density) is very low. Thus, this is not

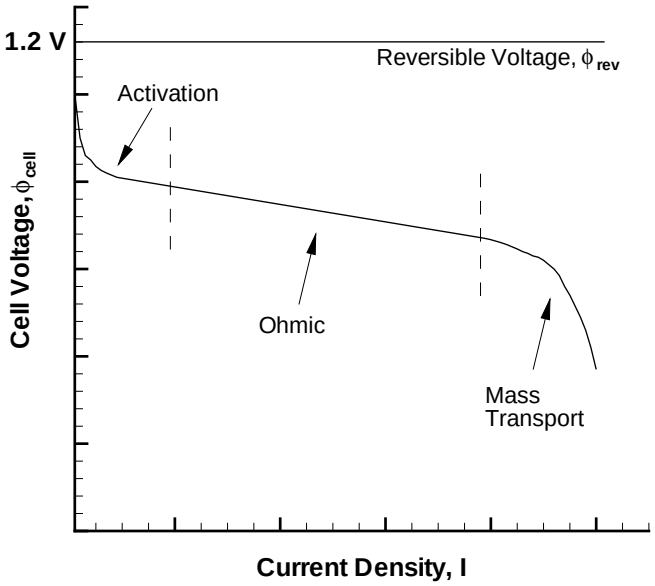

Figure 1.2: Sample polarization curve showing the three overpotential regions

a very useful region in which to operate a practical fuel cell.

The second region is called the *ohmic polarization* region. It is associated with a gradual slope that traverses most of the polarization curve. The losses associated with the activation polarization are relatively constant in this region, hence the slope is principally due to ohmic losses across the membrane and electrode layers.

The third region is called the *concentration polarization* region. It is associated with a steep slope and high current densities. In this region, the transport processes of this electro-chemical device begin to limit performance. Mass diffusion rates limit the transport of the reactants, thus preventing an increase in reaction rate. Decreasing the cell potential in this region results in a negligible increase in current density, thus simply reducing the power density. The maximum current is reached at zero cell potential.

1.5 Objectives and Scope of the Thesis

The main objectives of this thesis are to:

- identify the weakness and effectiveness of the previous modeling approaches, then develop a comprehensive multi-phase transient mathematical model for PEM fuel cells based on this analysis;
- implement the mathematical model into a commercial software Fluent, with user coded subroutines;

- provide insight into the electrochemical kinetics and transient transport phenomena within PEM fuel cells;
- investigate the dynamic performance of PEM fuel cells with respect to various operating condition changes;
- analyze liquid water removal through various flow channel designs.

To achieve these objectives, a comprehensive 3D PEM fuel cell model will be developed which accounts for seven main transient processes, namely, the non-equilibrium phase transfer between the liquid water and water vapor, the non-equilibrium membrane water sorption/desorption, liquid water transport in the porous backing layer, membrane hydration/dehydration, gas diffusion in the porous backing layer, the convective gas ow in the gas channel, and heat transfer. Subsequently, numerical simulations of various transient processes will be conducted. The resulting model will then be used to investigate the change of operation conditions, such as the output cell voltage, relative humidity of the gas reactants, operating pressure, etc., on the dynamic performance of the fuel cell. Furthermore, the model can also be used for flow-field designs. Channel flow is a truly 3-D phenomenon which has a great impact on reactants supply and liquid water removal. In fact, a main point of 3-D simulations is to figure out where the liquid water is in the GDL and channel. This is particularly important when one wants to purge the cell before shut off due to freezing concerns in wintry conditions.

This thesis is organized as follows: firstly, the steady state and transient models that currently exist in the published literature are reviewed in Chapter 2. Then the mathematical formulation of the current model is described in Chapter 3 and the numerical procedure of implementing this mathematical model is illustrated in Chapter 4. Next, the results from a single-channel model and several multi-channel models with different flow channel designs are presented in Chapter 5 and Chapter 6, respectively. Finally, conclusions and some suggestions for future work are summarized in Chapter 7.

Chapter 2

Literature Review

PEM fuel cells research has achieved considerable progresses in the past two decades, and it is on track to extensively replace the internal combustion engines which are currently used in automobiles. When reviewing the efforts and achievements that have been made, it is undeniable that mathematical modeling has played an indispensable role. Extensive PEM fuel cell modeling has greatly helped to better understand the functionality of the device and improve the cell performance.

A mathematical PEM fuel cell model can be as simple as an empirical function which predicts the cell performance solely based on several fitting parameters. This kind of model is usually referred to as performance model. In contrast, a mathematical model can be very complicated as well. It may be composed of a bunch of closely coupled partial differential equations that describe the transport phenomena which occur within PEM fuel cells. Advanced *Computational Fluid Dynamics* (CFD) techniques are usually required to solve such equation systems, thus providing their name – CFD model.

2.1 Performance Models

Performance models characterize the electrical performance of a cell by using a single equation, i.e. cell voltage versus current density. A general form of the performance model is [4]:

$$\phi_{cell} = \phi_{rev} - b \ln\left(\frac{J + J_{in}}{J_0}\right) - R(J + J_{in}) + m \ln\left(1 - \frac{J + J_{in}}{J_l}\right) \tag{2.1}$$

As can be seen, the above equation resembles the Equation (1.4), with the second, third and last term on the right hand side representing the activation, ohmic and concentration overpotential, respectively. Here, b is the Tafel slope related to the ORR, R is the overall ohmic resistance, m is a constant in the concentration overpotential, J_{in}, J_0 and J_l are the equivalent internal current density, exchange current density, and limiting current density, respectively.

Ticianelli *et al.* [6] and Srinivasan *et al.* [7] were one of the first to use the empirical equation (Equation 2.1) to analyze their experimental polarization results. They determined the kinetic parameters and general ohmic resistance through a nonlinear least square fit of the experimental data. The theoretical analysis of Paganin *et al.* [8] shows that in some cases the Tafel slope can be categorized into two different regions depending on the operating cell voltage or current density, and the limiting current density is affected by the structural parameters of the electrode. Kim *et al.* [9] investigated the effects of operating temperature, pressure, and oxygen compositions on the determination of the fitting parameters. Similar work was later presented by Beattie and coworkers [10]. They determined the kinetic and mass transport parameters for the oxygen reduction reaction for two different membranes (Nafion® 117 and BAM® 407) under various pressure and temperature conditions. Squadrito *et al.* [11] proposed an empirical equation similar to Equation (2.1) in which the exponential term that determines the concentration overpotential was refined. Furthermore, this new equation appears to be able to separate the ohmic contribution from the others.

More complicated performance models are also developed using a combination of numerical and empirical techniques. Amphlett *et al.* [12], Pisani *et al.* [13], Kulikovsky [14], and Ceraolo *et al.* [15] adopted a semi-empirical approach, where the analytical form of the limiting current density and concentration overpotential constant (m) are determined by solving the Stefan-Maxwell equation that governs the multi-species transport. Baschuk and Li [16] proposed a PEM fuel cell stack model in which the distributions of the pressure and mass flow rate for the fuel and oxidant streams in the stack are determined by a hydraulic network analysis. Using these distributions as operating conditions, the performance of each cell in the stack is governed by a single cell performance model. They found that the cell performance depends on the manifold size, number of gas channels and the uniformity of the reactants distribution. Furthermore, analytical solutions for the polarization performance are also reported by Standaert *et al.* [17, 18] and Gurau *et al.* [19].

In addition, the performance models have been incorporated into many system-level models concerning the whole fuel cell system. These system models are built from discrete elements, representing subcomponents (fuel cell stack, reformers, compressors, etc.) of the system. The models closely follow the physical layout of the actual system and the performance of each part is represented by empirical formulas. Francesco and Arato [20] developed a system model for an automotive PEM fuel cell system. By varying external conditions, they investigated the effect of relative humidity and temperature of the incoming air flow on the cell start-up processes. In the study of Gao *et al.* [21], a fuel cell model is coupled with nonlinear dynamic models for reactant pressures and manifold flows, and applied for the control design for a fuel cell stack system where pressurized air and hydrogen are utilized. Current control and reactant pressure control are implemented and the simulation is carried out in MATLAB/Simulink. In a separate study, Grasser and Rufer [22] elaborated a control-oriented PEM fuel cell system model in two

distinct steps. First, the fuel cell auxiliary systems (i.e. air and hydrogen supply along with thermal management) are described in a state-space approach which links user input to fuel cell operating conditions. A performance model then describes the effect of those operating conditions on the overall system performance. The model allows implementation of advanced control strategies such as multi variables control with decoupling, actuator sensitivity analysis or maximum efficiency tracking algorithms.

In general, the performance models are useful in analyzing the overall performance of the PEM fuel cell stack or system. However, they do not provide insight into the underlying transport and electrochemical phenomena that occur inside the fuel cells. Thus, CFD models for the detailed inter-cell operating conditions form the focus of the discussion in the next section.

2.2 CFD Models

It is difficult to categorize all existing PEM fuel cell CFD models, since the researchers have focused on different aspects of the cell. However, a general classification of those modeling efforts can be identified as: from one-dimensional to multi-dimensional, from isothermal to non-isothermal, from single-phase to multiphases, from single components to the cell unit, and from steady state to transient. For the purpose of this thesis, the published CFD models are generally categorized as steady state models and transient models.

2.2.1 Steady State Models

Water and heat management have been widely recognized as some of the most challenging issues to reach the commercialization of PEM fuel cells. The water transport within PEM fuel cells entails two competing effects: on one side, the membrane electrical conductivity increases with the membrane water content; hence the membrane should be as hydrated as possible to facilitate the proton transport. On the other side, excess water may accumulate in the porous pore of the GDL and catalyst layer and block the pathway for reactants transport, resulting in a significant concentration overpotential. A similar situation exists for heat management: the electrochemical reaction is enhanced at high operating temperature. This is especially true for the sluggish ORR at the cathode side. However, excessive high temperature tends to dry out the membrane, thus reducing its proton transfer capability. Therefore, a dynamic water and thermal balance is necessary for a sound operation of the fuel cell. In the following, the review of the literature will roughly follow these two threads.

Macroscopic Water Transport Modeling

Reviewing the literature, it is not hard to see that most of the modeling discrepancies originated from the intricate water transport in different cell regions. Generally, previous water transport studies can be categorized into two main groups: water transport through the polymer electrolyte membrane; and two-phase water transport in the backing layer and gas flow channel. Each of these two main groups can be further divided into several subgroups.

The breadth of membrane water transport submodels proposed to date ranges from molecular dynamics simulations and statistical mechanics models, to empirical macroscopic models. The focus in this subsection is on the development of macroscopic models required for computational simulations of complete fuel cells. Hence, only the macroscopic models are reviewed below. In general, three macroscopic modeling approaches of membrane water transport exist: convective (or hydraulic) models, diffusive models, and chemical potential models.

The convective models began with the pioneering work of Bernardi and Verbrugge. In 1991 and 1992, Bernardi and Verbrugge [23, 24] published a one-dimensional isothermal model of the gas-diffusion electrodes and a fully humidified membrane, providing valuable information about the physics of the electrochemical reactions and the transport phenomena in these regions. Fuller and Newmann, [25] and Nguyen and White [26] subsequently developed pseudo-two-dimensional models accounting for compositional changes along the flow path. In their models, the MEA is greatly simplified by assuming ultra thin gas diffusion electrodes, and the volume of the liquid phase is assumed to be negligible. Such models are useful for small cells, while their applicability to large scale fuel cells, particularly under high fuel utilization and low humidity conditions, is limited. Eikerling *et al.* [27] proposed a model in which phenomenological transport equations coupled with the capillary pressure isotherm are used, involving conductivity, permeability and electro-osmotic drag coefficients that depend on the local water content. The effects of membrane parameters on current-voltage performance are investigated. Berning *et al.* [28] developed a 3D model which unified the liquid water transport in the whole cell. The liquid water transport in the porous backing layer is governed by Darcy's law and the membrane water transport is governed by the Schlögl equation, while the back diffusion due to the water concentration difference between the anode and cathode side is totally neglected.

In the convective model, the flow of liquid water caused by a pressure gradient is included. However, experimental work [50] has shown that the application of a pressure difference between the cathode and anode did not have a large effect upon the drag coefficient, which is contrary to what is suggested by the convective model. Hence, the diffusive model is more frequently employed in the literature. Springer *et al.* [30, 31] were some of the pioneers working with the diffusive membrane hydration mechanisms. They implemented a one-dimensional isothermal model which accounts for the variation of membrane water content. Empirical correlations between the water activity and membrane water content (water sorption

isotherm) were developed based on experimental data measured at 30 ^oC. Other transport properties such as the water diffusivity and membrane electrical conductivity were considered as functions of membrane water content. Using the same diffusive model, Gurau and coworkers [32] developed a two-dimensional steady-state model of a whole fuel cell, i.e., both flow channels with MEA in between. The model considers the gas phase and the liquid phase in separate computational domains, which means that the interaction between both phases is not considered. In a separate development, Um *et al.* [33] carried out a two-dimensional simulation which coupled the electrochemical kinetics and transport processes. The three-dimensional version of the same model was demonstrated later [34]. Additional work on generalized, fully three-dimensional models was performed by Dutta *et al.* [35, 36], Zhou and Liu [37], Mazumder and Cole [38], Lee *et al.* [39] and many others. Recently, Kulikovsky [40] used a new set of correlations regarding the water sorption isotherm based on the experimental work of Hinatsu *et al.* [41] who conducted measurements at 80 ^oC, and implemented a model similar to Springer *et al*, which differentiates the water transport in the membrane from the water vapor transport in the GDL and gas channel. In the catalyst layer (CL), two phases are coupled together through an equilibrium assumption and the membrane water concentration is converted to the water vapor concentration through mathematical relations. Using a similar mathematical technique, Um and Wang [34] proposed a single-domain water transport model which converts the water concentration in the electrolyte to water vapor concentration both in the catalyst layer and the bulk membrane layer. The resulting water transport equation is casted into a general form that is valid across the whole domain. The same approach is also adopted by [43, 44, 45].

In both the convective and diffusive models, the proton concentration is assumed constant across the membrane domain and only the water concentration varies spatially in the membrane. Consequently, the electric potential within the membrane is exclusively determined through Ohm's law. A more fundamental and general approach to macroscopic modeling of water transport in membranes requires microscopic consideration of the dominant interactions between the aqueous system and the polymer and how they affect the proton transport properties. Models that consider such interactions based on the fundamentals of multi-component diffusion have recently been derived and they are generally referred to as chemical potential models. This kind of model treats the membrane as a mixture of solid matrix, hydronium ions and liquid water. Here, the transport phenomena within the polymer membrane are solved by means of a generalized Stephen-Maxwell equation. Despite different names, the dusty fluid models [46, 47], generalized Stefan-Maxwell equation models [48, 49], and concentrated solution theory models [50, 51] can be categorized into this group. Generally speaking, the chemical potential model can be considered as a superclass of diffusive/convective models; the diffusive/convective models are only valid in certain situations (constant proton concentration), while the chemical potential model is a more comprehensive approach which applies to a much larger range. Nevertheless, all above mentioned chemical potential mod-

els are invariably confined to the membrane region along with many simplifications. Further, several parameters and correlations related to this model class remain unknown, such as the diffusion coefficient of hydronium, the interaction properties of water and hydronium with the solid matrix, etc. Hence, the application of the chemical potential model in full cell modeling needs to be explored further.

The second main group of modeling efforts, two-phase water transport in the catalyst and backing layer, can also be divided into three modeling approaches, including the mixture models, two-fluid models, and the volume of fluid (VOF) models. Wang and Cheng [52] were one of the first groups to apply multi-phase mixture theory to PEM fuel cell research. The mixture model is a kind of single-fluid model. It solves a single set of conservation equations for the phase mixture assuming phase equilibrium. Subsequently, the volume fraction of the phases, as well as the relative velocity among different phases, are obtained in a post-processing manner. Pasaogullari *et al.* [53] developed a two-phase model of the PEM fuel cells with a micro-porous layer (MPL) based on the multiphase mixture model formulation of Wang and Cheng [52]. Subsequently, You *et al.* [54, 55] published similar work investigating the effects of several operating parameters on two-phase transport. Mazumder and Cole [56] also presented a numerical study based on the multi-phase mixture model. Their model appears to be valid only in the two-phase regime where there is liquid water. Under low humidity inlet conditions where the liquid saturation is zero, this model yielded zero electro-osmotic drag through the polymer membrane.

The two-fluid model, on the other hand, solves individual sets of equations for each phase while the interaction among different phases is explicitly taken into account through limited phase transfer terms. In PEM fuel cell modeling, the two-fluid model is usually simplified by combining the continuity and momentum equation with the help of Darcy's law and a capillary pressure function. Compared to the mixture model, the advantage of the two-fluid models is that only one extra equation for liquid saturation is added, while allowing for the simulation of non-equilibrium phase transfer processes. Here, however, the choice of the empirical expressions for relative permeability and capillary pressure are crucial and many different relationships have been proposed in literature. He *et al.* [57] developed a 2D, two-fluid model for the cathode side with interdigitated channels. Considerable simplifications with a constant interfacial drag coefficient and liquid diffusivity are made which is deemed reasonable only for small saturations. Later, Natarajan *et al.* [95] improved He *et al.*'s model by utilizing a linear function for relative permeability and an exponential expression for the capillary pressure. This revised model can be used to study conventional gas distributors where the liquid saturation is more significant. In the model of Zhang and Wang [59], power law relations and Leverett J-functions were used for the relative permeability and capillary pressure, respectively. Leverett J-functions are traditionally used in geological engineering to study water transport behavior in materials that have homogeneous wetting properties, like soil and rock. However, due to the lack of experimental data in the early days, it has been extensively used in PEM fuel cell modeling as

an approximation. This situation is changed with the emergence of several recent experimental studies [60, 61, 62, 63, 64, 65], which will be elucidated in more details later on. Furthermore, some studies were intended to investigate and analyze the two-phase transport in a hydrophobic GDL. Nam and Kaviany [66] described a one-dimensional two-fluid model for liquid water transport through a hydrophobic GDL. In this model, the gas-phase pressure is assumed to be uniform, thereby rendering the liquid-phase transport governed by the gradient in capillary pressure. The model was used to assess the effects of GDL fiber diameter, porosity, and capillary pressure on the liquid water distribution. Independently, Pasaogullari and Wang [67] proposed a systematic theory of liquid water transport through a hydrophobic GDL. Condensation results in a tree-like liquid water percolation network in the porous GDL. Liquid water then reaches the interface of the porous GDL with the gas channel, forming liquid droplets. Inside the GDL, liquid water is driven by capillary action. In a hydrophobic GDL, the capillary pressure is negative; hence, the liquid pressure is larger than the gas-phase pressure, whereas in hydrophilic media, the gas-phase pressure is higher than of the liquid phase.

Recently, the VOF model has attracted increasing attention from the PEM fuel cell modeling community. The biggest advantage of a VOF model is its ability to trace the trajectory of the liquid droplet movement. Quan and coworkers [68] developed a VOF model for the cathode gas channel using the commercial software FLUENT. Even when no electrochemical reactions were considered and the simulation has to start from arbitrarily specified liquid droplet locations, it provides valuable information on liquid water removal, especially the two-phase flow behavior around the channel bend region. Similar VOF simulations were later presented by the same group for various flow channel designs [69, 70]. Using an in-house VOF code, Theodorakakos *et al.* [71] investigated the dynamics of droplet detachment from a porous surface under the influence of the incoming air flow. Comparison of their simulation results to experimental CCD images shows successful prediction of the droplet detachment process. Similar studies regarding liquid droplet emergence and detachment from porous GDL are also presented by Zhu *et al.* [72], and Bazylak *et al.* [73]. In general, due to the nature of the extremely small time-steps and intensive computing related to VOF methods, its application so far has been restricted to investigating the physical properties of certain components, such as the permeability, the gas diffusivity in the backing layer, or the analysis of liquid behavior in the porous electrode [72, 73] or gas flow channels [68, 69, 70, 71].

Microscopic Water Transport Modeling

Some recent modeling studies have investigated the membrane water transport and liquid water transport in the backing layer from a microscopic point of view. For example, *Molecular Dynamics (MD)* simulations have been conducted to understand the water filled network within the polymer membrane. The MD simulation models the fluid flow by studying the trajectory of individual molecules that make up the fluid. Thus, a knowledge of the average energy of the molecules, the inter-molecular

interactions, and collision behavior, etc., are required. Based on a structural analysis of the microphase-separated morphologies of the membrane, Vishnyakov and Neimark [74] developed a MD model for a Nafion membrane. They found that as the water content increased, temporary bridges between water clusters formed and broke apart dynamically on a time scale of 100 ps instead of forming permanent water channels. It suggests that there is no percolating network of connected water pathways, but local disconnected water pools which are only transiently linked. Such findings have important implications for water uptake as well.

The number of molecules considered in classical MD models are very limited, owing to the challenging requirement of computer resources. Hence, they are not able to predict the structure-related properties of the membrane at long time ($>$ 10 ns) and length scales ($>$ 10 nm). To bridge the gap, a so-called coarse-grained approach has recently been developed to study the structure of hydrated ionomers at varying water content. The coarse grained treatment implies simplification in inter-molecular interactions, which can be systematically improved with advanced force-matching procedures, but it allows simulating systems with sufficient size and sufficient statistical sampling. Khalatur *et al.* [75] built a predictive model using a highly coarse-grained representation of the side groups along the backbone. They found that the water and polar sulfonic acid groups are segregated into a three-layer structure, and a linear dependency of microscopic swelling on water content. More examples regarding the classical and coarse-grained MD simulations can be found in [76, 77].

Utilizing the *Lattice Boltzmann Method (LBM)*, microscopic simulations of the liquid water transport in the porous backing layer, gas channel and PEM have also been explored by many research groups recently [78, 79, 80]. Compared to the MD simulation, the LBM approach assumes that the fluid is made of large amounts of fluid "particles" instead of individual molecules. A fluid particle is a large group of molecules which, although much larger than a molecule, is still considerably smaller than the smallest length scale of the simulation. Then by solving the Boltzmann equation in conjunction with a lattice gas model, the trajectory of the liquid droplet movement can be resolved and the macroscopic fluid properties (density, velocity, energy, etc.) are evaluated from the particle distribution function. Niu *et al.* [78] presented a LBM model in which a water-gas flow in the GDL is simulated and the saturation-dependent transport properties under different conditions are investigated. In the study of Koido *et al.* [79], the capillary pressure and relative permeability within a carbon-fiber paper GDL are predicted using the LBM approach.

Similar to VOF models, a common disadvantage of MD and LBM models is that only extremely small time and length scales can be simulated due to their intensive computational requirements. Therefore, their applications so far have been restricted to investigating a small region of certain components. Full geometry PEM fuel cell models that incorporate these approaches (VOF, MD, LBM) have not been tried to the best of the authors' knowledge.

Heat Transfer Modeling

A heat transfer sub-model is also necessary for a rigorous numerical analysis. Compared to water transport, heat transfer in PEM fuel cells is much easier to model and, hence, there is less discrepancy in the literature. However, almost all physical parameters and transport processes are related to temperature. To reduce the computational complexities of the system, heat transfer effects are neglected by most of the researchers. Nguyen and White [26] developed a two-dimensional PEM fuel cell model with one-dimensional heat transfer in the flow direction. The model considered phase change of water in the flow channel as the only heat source, allowing convective heat transfer between the gas and solid phases. Yi and Nguyen [60] further extended Nguyen and White's [26] model to include reversible and irreversible reaction heat. However, this model allowed for temperature variation of the solid phase in the flow direction only, assuming uniform temperature in the through-membrane direction. Wöhr *et al.* [81] developed a one-dimensional thermal model for heat and mass transfer in the through-plane direction, particularly for PEM fuel cell stacks. Accounting for reversible and irreversible reaction heat, they computed the temperature profile in the through-membrane direction and predicted the maximum temperature as a function of the number of cells contained in a stack. In the work of Rowe and Li [82], the heat transfer in the cell is considered as the combination of the following two mechanisms: conductive heat transfer in the solid matrix; and convective heat transfer in the pores, with local thermodynamic equilibrium between the two phases. The heat generation/adsorption effects during the water phase change are also taken into account in this work.

A number of three-dimensional thermal models have been published in the literature. In the 3D models developed by Maggio *et al.* [83] and Shimpalee *et al.* [84], the heat source terms were treated globally and not made location specific. While in the study of Zhou and Liu [37], the entropic reaction heat was totally ignored. Ju *et al.* [85] presented a single phase non-isothermal model which coupled the heat transfer with electrochemical reactions and mass transport. A parametric study on the GDL thermal conductivity is conducted and the heat release in each part of the cell is analyzed in detail. The authors conclude that the thermal effects become more critical at higher current density and/or lower GDL thermal conductivity. Berning *et al.* [86] later presented a similar conductive-convective heat transfer model. In their model, the temperature in solid and fluid phases are solved independently, and a rather arbitrary heat transfer coefficient is used to account for the heat exchange between the two phases.

Large-scale Modeling

Large-scale simulation resolving all three dimensions for industrial-scale fuel cells featuring tens of flow channels is now being made possible by parallel computing on PC clusters using millions of computational grid points. Meng and Wang [87] developed a model with a 5-channel serpentine flow-field using STAR-CD. The re-

sults reveal that the current distribution is determined by the oxygen concentration distribution under fully humidified conditions, while determined by the water distribution under low humidity conditions. They also show that the ohmic losses due to proton transport in the catalyst layer are comparable to that in the membrane. Wang and Wang [88] presented an ultra large-scale simulation for a 200 cm^2 cell. The model was implemented in FLUENT and solved using a 32-node computer cluster. Two cases which investigate the effect of bipolar plate cooling on membrane dry out and electrode flooding were studied and compared. Also using FLUENT, Shimpalee *et al.* [89] undertook the flow-field optimization of a practical-scale cell. Both flow-field patterns (serpentine and interdigitated) along with the variation of channel numbers were investigated in detail.

2.2.2 Transient Models

Reviewing the literature, it is found that the majority of previous studies are focused on steady state modeling, while the transient phenomena within PEM fuel cells are usually overlooked.

The main transient transport mechanisms within a PEM fuel cell includes:

- the non-equilibrium phase transfer between the liquid water and water vapor (condensation/evaporation);
- the non-equilibrium membrane water sorption/desorption;
- capillary diffusion of liquid water in the porous backing layer;
- water transport within the bulk membrane (membrane hydration/dehydration);
- gas diffusion in the porous backing layer;
- convective flow in the gas channel;
- heat transfer; and
- electrical double layer charge/discharge.

The electrical double layer charge/discharge process occurs almost instantaneously and has been generally omitted in all previous modeling studies. The transient processes of membrane hydration/dehydration, gas transport and heat transfer can be easily resolved even with single-phase models, and they were the primary focus in several early transient modeling studies. On the other hand, study of the first three dynamic processes involves intricate water transport and phase transfer modeling. A robust multi-phase model is thus needed.

Wang and Wang [90] developed a three-dimensional, single-phase, isothermal model using Star-CD, which studied the evolution of water accumulation in the

membrane and the corresponding dynamic responses of the cell performance, while the effect of mass transport of gaseous reactants is not explicitly dictated. In the studies of Shimpalee *et al.* [91, 92], a three-dimensional, single-phase, isothermal model was developed using FLUENT. The magnitude of the current density undershoot/overshoot with respect to the changing rate of cell voltage or other operating conditions are investigated in detail. In their model, the current overshoot/undershoot are mainly caused by oxygen transport. The effect of the slow water transport process on the cell dynamic performance is not shown though. Yan *et al.* [93] demonstrated a half-cell transient model which is capable of predicting gas transport dynamics with respect to different channel/landing ratios and electrode porosities. Their results show that the species transport are taking place on the order of 10 seconds, which are almost two orders higher than the experimental values. However, all above-mentioned transient models are isothermal and none of them investigated the cell as a water transport and thermally coupled system. Recently, Wu *et al.* [44, 94] presented a single-phase non-isothermal model in which both the gas transport, heat transfer and membrane hydration/dehydration transient processes are analyzed and investigated in detail. Their results showed that the membrane hydration process has the most significant effect on the cell dynamic response. The thermal effect is also non-negligible which causes output current oscillation and it further delays the cell response. The overshoot/undershoot at the initial stage is mainly caused by the sluggish oxygen transport. This situation can be alleviated under lower humidity operation conditions.

A number of research groups have developed multi-phase transient models to show the temporal liquid water transport within the porous backing layer. Natarajan and Nguyen [95] presented a two-dimensional two-phase transient model for the cathode gas diffusion layer (GDL) and catalyst layer (CL). Both multi-species flow and capillary diffusion of the liquid water are taken into account in their model. Berg *et al.* [96] presented a half-cell transient discharge model for a delicately segmented PEM fuel cell, and used it for parameter tuning and determination of liquid water in the membrane electrode assembly (MEA). Stumper *et al.* [97] used a similar approach to determine the MEA resistance and oxygen diffusion coefficient in the cathode GDL. Meng [98] developed a 2D, two-fluid model and studied the temporal variation of the liquid saturation. His results indicate that the inclusion of liquid water transport only influences the magnitude of the current overshoot/undershoot, but not the overall response time. In the work of Wang and Wang [99], a 2D mixture model is implemented by assuming that the liquid water is always in thermodynamic equilibrium with the water vapor. Both anode and cathode flooding have been investigated. It is shown that the anode water is removed faster than the water at the cathode because the water diffusivity at the anode side is several times larger than at the cathode side.

It should be noted that the finite-rate membrane sorption/desorption processes are neglected in the above mentioned models. Recent experimental studies have shown that the time scale for membrane to reach its sorption equilibrium state in humid air is on the order of 100-1000 s [100, 101] which means that membrane

sorption/desorption is one of the most important dynamic processes and, hence, is essential for transient modeling of PEM fuel cells. One of the earliest transient models which considered the non-equilibrium membrane sorption/desorption processes was developed by Vorobev *et al.* [102]. A parametric study of the sorption rate is conducted to identify the effect of the finite-time equilibration on the cell dynamics. However, the condensation/evaporation processes along with the liquid water transport in the CL and GDL are entirely neglected in this model. Another 1D transient model which incorporates the non-equilibrium sorption/desorption process, is derived by Shah *et al.* [103]. The saturation variations under various changes in operating conditions are demonstrated and the cell dynamics pertaining to temperature, pore sizes, contact angles are discussed. The author's comparison to experimental results exhibits qualitatively the right trends. In the 3D cathode-side only model of Gurau *et al.* [104], the dynamic sorption/desorption process is mathematically implemented but no related results are shown. Their main concerns were focused on the dynamic transition of the liquid saturation in the three dimensional GDL. However, there is one figure exhibiting the convergence history of their solution. It shows that the residuals are on the order of 10^{-1} to 10^{-3} for all variables, which puts their convergence criterion into doubt. Recently, Gerteisen *et al.* [105] presented a 1D two-phase transient model that incorporates both the non-equilibrium membrane sorption/desorption and condensation/evaportion processes. The anode side geometry (GDL and catalyst layer) is greatly simplified and modeled as an interface. The model is validated against their experimental results and impressive agreements are demonstrated. In the most recent study of Wu *et al.* [106, 107, 108], a rigorous 3D transient model has been developed through a comprehensive inclusion of various transient transport phenomena and phase transfer processes. It is found that the finite-rate membrane sorption/desorption process and water condensation/evaporation process are essential for transient modeling of PEM fuel cells, yet they have been generally neglected in previous studies. A sinusoidal impedance approach is employed to identify the time scales for different dynamic transport processes. The dynamic response to changes in some typical operating conditions have been investigated and the results demonstrate qualitatively good agreement with experimental results.

2.3 Summary

Overall, up to around the year 2000, most of the fuel cell models were one or two-dimensional, isothermal, single-phase, with certain simplifications and assumptions. The main concerns of these studies were focused on the MEA based on several empirical correlations. Many efforts have been expended over the last ten years upon development of three-dimensional and two-phase models, using large-scale simulations under a decreasing number of restrictive assumptions. The effects of reactant transport and liquid water removal have attracted much of the modeling interests during this period.

On the other hand, the study of transient phenomena and dynamic responses of PEM fuel cells has been largely overlooked in the literature. Most of the dynamic modeling was carried out at the system level, using a performance model where the underlying transient phenomena within the PEM fuel cell are of no concern. For these CFD transient models, the modeling domain is usually simplified by either reduced dimensions (1D, 2D) or reduced components (e.g., cathode only) due to the intensive computing requirements related with transient modeling. Furthermore, the dynamic transition among multi-water phases (dissolved, liquid and vapor) and non-isothermal effects impacting the cell dynamic performance is still rarely touched.

In summary, a rigorous three dimensional transient model that has a comprehensive inclusion of various transient transport phenomena and phase transfer processes is highly desirable. It is the main objective of this thesis.

Chapter 3

Model Formulation

Despite of its relative simplicity in structure, the physical and electrochemical mechanisms of a PEM fuel cell are rather complicated. To mathematically describe a PEM fuel cell, one needs to consider the transport of multi-component gas species, transport of the multi-water phases, phase change processes, multi-step electrochemical reaction kinetics, transport of the electric charges, and also, transport of the energy which is inherent to all aforementioned processes. Baschuk and Li [48] have proposed a general macroscopic mathematical model in which the volume-averaging procedure is applied to the conservation of momentum, species and mass, and energy for each phase, the interactions between different phases are accounted for with interfacial source terms, which differ layer-to-layer in the fuel cell. However, this model is not applicable to a practical simulation, because many parameters and source terms remain unknown due to the spareness of experimental data and insufficient understanding of the phase interactions and multi-step reaction kinetics. Therefore, a certain level of simplification of this general model is required, as Baschuk suggested in [109].

In this chapter, the mathematical model used in this thesis research is presented, including simplified phase interactions and electrochemical reaction kinetics. Firstly, the assumptions that are necessary for the simplification of the model are provided, followed by the derivation of the conservation equations that govern various transport processes. Then, the computational domain along with the boundary and initial conditions are illustrated and the input parameters of the model are tabled. Finally, a short summary of the governing equations is given.

3.1 Assumptions

Without losing the generic physical characteristics of a PEM fuel cell, some assumptions have been made for the mathematical model to make numerical simulation more tractable, including:

- gravity effects are ignored;

- the gas reactants are ideal gases;
- the gas flow in the channel is laminar flow;
- the cell is operated with pure hydrogen, thus no contamination effects are considered;
- the membrane is impermeable to gas species and, hence, no gas species crossover;
- the liquid water in the gas flow channel is in a mist state and it can be instantaneously removed by the gas flow. As such, the liquid saturation in the gas channel is negligible.

These assumptions are easily justified except the last one. In typical PEM fuel cell operation, both fuel and air streams are fully humidified so that the product water is normally removed in the form of liquid water in the flow channels. The two-phase channel flow is important in the transport and removal process of product water from the cell. However, such two-phase flow simulation (e.g., droplet adhesion to the wall surface, droplet distortion/deformation due to the shearing force of the gas phase flow, multi-droplet interaction, the possibility of thin water film on the wall surface, droplet detaching from the surface and move with the gas phase in a suspended state, etc.) is very computationally demanding. In the present thesis research the focus is on the phenomena inside the PEM fuel cell (GDLs, catalyst layers and membrane), therefore, a simplified assumption is made for the flow in the channel: liquid water is assumed in a low loading mist state and with gas phase fully saturated, so that the overall channel flow can be treated as if it is a single-phase gas flow.

Furthermore, there are a few other assumptions that pertain to certain transport phenomena. They will be illustrated in the context of specific transport processes.

3.2 Transport of Gas Species

3.2.1 Conservation of Mass and Momentum

First of all, the transport of any individual phase has to satisfy the conservation of mass and momentum. For the gas phase, that entails [110]

$$\frac{\partial}{\partial t}\left(\epsilon^{\text{eff}}\rho_g\right) + \nabla\cdot\left(\rho_g\vec{u}_g\right) = S_m \tag{3.1}$$

$$\frac{\partial}{\partial t}\left(\frac{1}{\epsilon^{\text{eff}}}\rho_g\vec{u}_g\right) + \nabla\cdot\left(\frac{1}{\left(\epsilon^{\text{eff}}\right)^2}\rho_g\vec{u}_g\vec{u}_g\right) = -\nabla P_g + \nabla\cdot\left(\overline{\overline{\tau}}\right) + S_u \tag{3.2}$$

where ϵ^{eff} is the effective porosity for gas phase transport, which is related to the bulk porosity of the material, ϵ, and liquid saturation, s, as

$$\epsilon^{\text{eff}} = \epsilon(1 - s), \tag{3.3}$$

ρ_g, $\vec{u}_g$, and P_g are the superficial values of the density, velocity, and the pressure of the gas phase, respectively; $\overline{\overline{\tau}}$ is the stress tensor; S_m and S_u are the source terms which have different values depending on the cell region.

On the other hand, the gas phase consists of several gas species. The transport of each species can be described with a general form of the convection-diffusion equation:

$$\frac{\partial}{\partial t}\left(\epsilon^{\text{eff}} C_i\right) + \nabla \cdot \left(-D_{i,m}^{\text{eff}} \nabla C_i\right) + \nabla \cdot (\vec{u}_g C_i) = S_i \tag{3.4}$$

where C_i and S_i are the concentration and gain/loss of the ith species, respectively, and $D_{i,m}^{\text{eff}}$ represents the effective mass diffusion coefficient for species i in the mixture.

One extra relation is required to close the equation set (Equation (3.1)-(3.4)) for the gas phase transport, that is, the sum of all species molar fractions should equal to 1

$$\sum_{i=1}^{N} X_i = 1, \tag{3.5}$$

where N denotes the number of species in the fuel cell, and X_i denotes the species molar fraction which is evaluated as

$$X_i = \frac{C_i}{\sum_{i=1}^{N} C_i}. \tag{3.6}$$

With the assumption that the cell is fed with pure hydrogen at the anode side and air at the cathode side, there are mainly four species to be considered in this study, namely, hydrogen, oxygen, water vapor, and nitrogen. Only the first three of the four species need to be numerically resolved, leaving the fourth one to be determined through Equation (3.5).

Furthermore, the continuity equation and the species transport equation are correlated through the following relations

$$S_m = \sum_{i=1}^{N} S_i, \tag{3.7}$$

$$\rho_g = \sum_{i=1}^{N} M_i C_i, \tag{3.8}$$

where M_i denotes the molecular weight of the ith species.

It should be noted that the thermal (Soret) and pressure diffusion effects are neglected in the diffusion flux, which is the second term on the left hand side (LHS)

of Equation (3.4), since their gradients are relatively insignificant compared to the concentration gradient in PEM fuel cells. Finally, the diffusion flux is approximated using Fick's law. It can serve as an acceptable approximation for a multi-component system as well, provided that a corrected diffusivity ($D_{i,m}^{\text{eff}}$) is used [97]

$$D_{i,m}^{\text{eff}} = \frac{1 - X_i}{\sum_{j,j\neq i} (X_j / \mathcal{D}_{ij}^{\text{eff}})}, \tag{3.9}$$

where $\mathcal{D}_{ij}^{\text{eff}}$ is the effective binary mass diffusion coefficient of component i in component j. It is determined by

$$\mathcal{D}_{ij}^{\text{eff}} = \mathcal{D}_{ij} \frac{T}{T^{\text{ref}}} \frac{P^{\text{ref}}}{P} \frac{\epsilon^{\text{eff}}}{\tau}, \tag{3.10}$$

where $\mathcal{D}_{i,j}$ is the bulk binary diffusivity at the reference temperature ($T^{\text{ref}} = 20\,^{\text{o}}\text{C}$), and pressure ($P^{\text{ref}} = 1$ atm); and τ is the tortuosity of the porous material.

3.2.2 Reaction Kinetics

The species source term (S_i) on the right hand side (RHS) of Equation (3.4) accounts for the consumption or production of species due to electrochemical reactions or phase changes. Among the three gas species of interest (hydrogen, oxygen, and water vapor), the phase change occurs only in the transport of water vapor and it will be elucidated in more detail in Section 3.3.2. The objective for this section is to establish the relation between the rate of hydrogen and oxygen consumption, and the electrochemical reaction kinetics.

For a generalized electrochemical reaction [3], it has

$$\underbrace{\sum_{i=1}^{N} \nu_i^{'} M_i}_{\text{Reactant}} \overset{k_f}{\underset{k_b}{\rightleftharpoons}} \underbrace{\sum_{i=1}^{N} \nu_i^{''} M_i}_{\text{Product}}, \tag{3.11}$$

where M_i is the chemical formula for reactant species i; $\nu_i^{'}$ and $\nu_i^{''}$ are the number of moles for species i in the reactant and product mixture, respectively; k_f and k_b are the reaction rate constant for the forward and backward reaction, respectively; and N is the total number of species in the chemically reacting system.

According to the law of mass fraction, the net rate of reaction for species i can be expressed as

$$\begin{aligned} \omega_i^{''} &= \omega_{i,f}^{''} + \omega_{i,b}^{''} \\ &= \left(\nu_i^{''} - \nu_i^{'}\right) \left[k_f \prod_{i=1}^{N} [M_i]^{\nu_i^{'}} - k_b \prod_{i=1}^{N} [M_i]^{\nu_i^{''}} \right], \end{aligned} \tag{3.12}$$

where $\omega^{''}$ represents the rate of production, and $[M_i]$ represents the molar concentration for the chemical species i which is equivalent to C_i.

Then, Faradays law relates the rate of electrochemical reaction in the reaction zone layers to the current density as

$$\begin{aligned} J = J_f - J_b &= -n\mathscr{F}\omega_i^{''}, \\ &= k_f C_R - k_b C_P \end{aligned} \tag{3.13}$$

where J_f and J_b are the current produced in association with the forward and backward reactions, respectively; n is the number of electrons transferred during the electrochemical reaction, $\mathscr{F}$ is Faraday's constant (96487 C/mol); and C_R and C_P are the concentration of reactant and product, respectively.

According to the transition state theory, the reaction rate constant may be expressed in the form

$$k_f = B_f T \exp\left(-\frac{\triangle g_f}{\mathscr{R}T}\right) \tag{3.14}$$

$$k_b = B_b T \exp\left(-\frac{\triangle g_b}{\mathscr{R}T}\right) \tag{3.15}$$

where $\mathscr{R}$ is the universal gas constant (8.314 J/mol $\cdot$ K), B are the pre-exponential factors, and $\triangle g$ are the actual molar Gibbs functions of activation for the oxidation (forward) or reduction (backward) reactions. The actual Gibbs functions of activation can be further related to their values at the equilibrium state as

$$\triangle g_f = \triangle g_{f,r} - \alpha n \mathscr{F} \eta \tag{3.16}$$

$$\triangle g_b = \triangle g_{b,r} - (1-\alpha) n \mathscr{F} \eta \tag{3.17}$$

Here, the parameter α is called the transfer coefficient (or symmetry factor), whose values lies between zero and one. Experimentally it is often found to be in the vicinity of 0.5 [3]; η is the overpotential, the difference between the electrode potential, ϕ, and its equilibrium value, ϕ_r

$$\eta = \phi - \phi_r. \tag{3.18}$$

Substituting Equation (3.14)-(3.17) into Equation (3.13) results in

$$\begin{aligned} J &= J_f - J_b \\ &= J_0 \left\{ \exp\left(\frac{\alpha n \mathscr{F} \eta}{\mathscr{R}T}\right) - \exp\left(-\frac{(1-\alpha) n \mathscr{F} \eta}{\mathscr{R}T}\right) \right\}, \end{aligned} \tag{3.19}$$

where

$$J_0 = B_f C_R T \exp\left(-\frac{\triangle g_{f,r}}{\mathscr{R}T}\right) = B_b C_P T \exp\left(-\frac{\triangle g_{b,r}}{\mathscr{R}T}\right) \tag{3.20}$$

is the exchange current density (A/cm^2). It is a measure of the amount of electron transfer activity at the equilibrium electrode potential, ϕ_r, and also represents how

easy an electrochemical reaction can take place. In a real reaction, the reaction steps involved are often a summary of several or many elementary reactions. For such a scenario, the exchange current density is revised as

$$J_0 = J_0^{\text{ref}} \left(\frac{C_R}{C_R^{\text{ref}}} \right)^{\beta}, \tag{3.21}$$

where β is the reaction order with respect to the reactant R.

Finally, the volumetric current density, $\mathcal{R}$, can be expressed as

$$\begin{aligned} \mathcal{R}_i &= A_v J \\ &= A_v J_0^{\text{ref}} \left(\frac{C_R}{C_R^{\text{ref}}} \right)^{\beta} \left\{ \exp\left(\frac{\alpha n \mathscr{F} \eta}{\mathscr{R} T} \right) - \exp\left(-\frac{(1-\alpha) n \mathscr{F} \eta}{\mathscr{R} T} \right) \right\} \end{aligned} \tag{3.22}$$

which is known as the *Butler-Volmer equation*. Here, A_v is the reactive surface area density, defined by

$$A_v = \frac{\text{Actual reactive surface area}}{\text{Volume of electrode}} \tag{3.23}$$

Therefore, the volumetric current density in the anode catalyst layer, $\mathcal{R}_a$, can be written as

$$\mathcal{R}_a = a J_{a,0}^{\text{ref}} \left(\frac{C_{h_2}}{C_{h_2,0}^{\text{ref}}} \right)^{\beta_a} \left\{ \exp\left(\frac{\alpha n \mathscr{F} \eta_a}{\mathscr{R} T} \right) - \exp\left(-\frac{(1-\alpha) n \mathscr{F} \eta_a}{\mathscr{R} T} \right) \right\}. \tag{3.24}$$

Similarly, the volumetric current density in the cathode catalyst layer, $\mathcal{R}_c$, is

$$\mathcal{R}_c = a J_{c,0}^{\text{ref}} \left(\frac{C_{o_2}}{C_{o_2,0}^{\text{ref}}} \right)^{\beta_c} \left\{ \exp\left(\frac{\alpha n \mathscr{F} \eta_c}{\mathscr{R} T} \right) - \exp\left(-\frac{(1-\alpha) n \mathscr{F} \eta_c}{\mathscr{R} T} \right) \right\}. \tag{3.25}$$

From Reactions (1.1)-(1.3), it is known that for each mole of electron draw from the electrochemical reaction, 1/2 mole of hydrogen and 1/4 mole of oxygen are consumed. Therefore, once the volumetric current flow is known, the reaction rate of hydrogen and oxygen can be easily determined as

$$S_{h_2} = -\frac{1}{2\mathscr{F}} \mathcal{R}_a, \tag{3.26}$$

$$S_{o_2} = -\frac{1}{4\mathscr{F}} \mathcal{R}_c, \tag{3.27}$$

or in a compact form

$$S_i = -\frac{\nu_i}{n\mathscr{F}} \mathcal{R}_i, \tag{3.28}$$

where n is the number of electrons participating in the half-cell reaction, hence $n = 2$, and ν_i is the stoichiometric coefficient of the species involved in the reaction, which equals 1 for hydrogen, and 1/2 for oxygen. Equation (3.28) is valid in the catalyst layer since the electrochemical reaction occurs in the catalyst layer only. In all other regions, the source/sink of the hydrogen and oxygen are simply zero.

3.3 Transport of Multi-Water Phases

Water transport behavior probably is the most active research area in the previous experimental or numerical studies of PEM fuel cells, and this trend seems to continue as long as PEM fuel cell research proceeds. The main challenges involved in the intricate multi-phase water transport are: firstly, the cell performance is significantly affected by the liquid water removal process. However, it is very difficult to quantify the liquid water flow behavior in the porous backing layer, and in the gas flow channels as well. Secondly, the mechanism of water transport in the electrolyte membrane is poorly understood. This is mainly due to the phase in which water molecules exist in the electrolyte and this is still not very clear. Some researchers simply treated it the same as liquid water, while others consider the water in a dissolved phase where several water molecules are closely bonded with a proton and appear as a clustered block. Water molecules may also exist in three phases within the electrolyte: those close to the sulfonic group are present in a dissolved phase; those far away from the solid site are in the liquid phase; those in between are in a transitional phase. In this study, the water in the membrane electrolyte is assumed to be of the dissolved phase. Consequently, there are three water phases in the fuel cell. They are the water vapor, liquid water and dissolved water, respectively. The co-existence of three water phases in the catalyst layer results in various phase transfer processes between different phases. This is an another challenging part for the water transport modeling.

To fully appreciate the multi-water phase transport characteristics of the current model, water transport within three different phases will be described in this section, keeping the above challenges in mind.

3.3.1 Water Formation Mechanism

Before any of the water transport processes are presented, it is worthwhile to clarify a misconception on how the water is produced and what the state of the produced water is during the electrochemical reaction, more specifically, the ORR. A very common assumption that has repeatedly appeared in the literature is whether the produced water is in vapor or liquid form. Is this true?

To answer this question, it is necessary to examine the reaction process from a microscopic perspective. Figure 3.1 illustrates a schematic of the ORR in the cathode catalyst layer (CCL). As indicated in Section 1.2, one condition needs to be met for the ORR to occur spontaneously in the CCL, i.e. the co-existence of platinum catalyst, oxygen molecule, proton, and electron. That means the reaction can only occur at the so-called triple-phase zone (TPZ), where the protons and dissolved oxygen molecules reach the reaction site through the electrolyte (Nafion), and electrons reach the TPZ through the solid matrix of the carbon support. Consequently, water can only be produced at the TPZ, which is obviously part of the electrolyte.

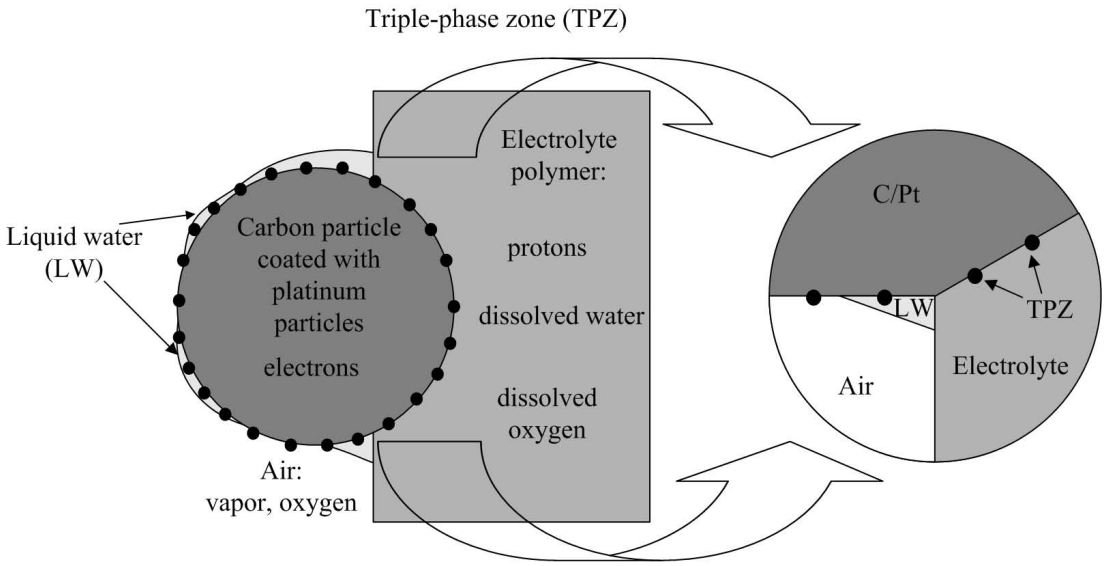

Figure 3.1: Schematic of oxygen reduction reaction in the cathode catalyst layer (reproduced from Berg *et al.* [111]).

On the other hand, unless the electrolyte is heated to a very high temperature so that the protons are no longer hydrated (at this point the ionic polymer is very likely to start degrading), the ionic group ($SO_3^-H^+$) in Nafion will retain at least one water molecule per proton. Under typical fuel cell operation, the number of water molecules per proton is rarely below 3. With at least three water molecules closely bound to a proton, these water molecules cannot be considered to be in a gaseous state since their corresponding mean free path is much less than gas. Hence, when a water molecule is generated at the solid catalyst surface, it joins a group of water molecules already present at the ionic group which are already in a condensed state. Therefore, in a PEM fuel cell water is generated at the catalyst surface in the form of dissolved water!

How these water molecules leave the electrolyte at the electrolyte/gas phase interface, whether as a gas or liquid, will depend on the gas phase. If the gas phase is not saturated and sufficient energy is available, water can evaporate and leave as vapor. If the gas phase is saturated, water will leave this interface as a liquid which is then transported away by capillary diffusion or other forced mechanisms.

When liquid water is present in the gas pore, protons could in principle migrate through liquid water [112] and the electrochemical reaction could occur in the liquid phase. Consequently, water may be produced in the liquid phase directly. However, the amount of protons diffused into the liquid water is significantly smaller than that in the electrolyte. Therefore, it can be assumed that the amount of liquid water production is insignificant compared to that of dissolved water production.

Later in this thesis research, a comparison will be made between the mechanism of water production in the electrolyte and that of water production in the vapor or liquid phase, assessing their implications for the numerical results.

3.3.2 Transport of Water Vapor

For better cell performance, the gaseous reactants are usually humidified before entering the gas flow channel. The transport of water vapor is governed by the same convection-diffusion equation as the transport of hydrogen and oxygen

$$\frac{\partial}{\partial t}\left(\epsilon^{\text{eff}} C_v\right) + \nabla \cdot (-D_v \nabla C_v) + \nabla \cdot (\vec{u}_g C_v) = S_v, \tag{3.29}$$

where C_v is the water vapor concentration, D_v is the water vapor diffusivity, and S_v is the water vapor source term, which arises from the multi-water phase change processes.

As one of the main assumptions listed in Section 3.1, liquid water is assumed in a mist state which is virtually the same as water vapor. Therefore, there is no phase change occurring in the gas flow channel.

In the porous gas diffusion layer (GDL), phase change occurs between the water vapor and liquid water in terms of condensation/evaporation processes, and the source term has the form

$$S_v = -\frac{S_{vl}}{M_w}, \tag{3.30}$$

where M_w is the molecular weight of water, and S_{vl} is the amount of vapor gain or loss during the evaporation/condensation. It will be formulated in the section of liquid water transport (Section 3.3.4).

In the catalyst layer, both water vapor, liquid water and dissolved water are present. Consequently, the vapor source consists of two parts: the phase change between water vapor and liquid water in terms of the evaporation/condensation process, and the phase change between water vapor and dissolved water in terms of the sorption/desorption process

$$S_v = -\frac{S_{vl}}{M_w} - S_{vd}. \tag{3.31}$$

For comparison purposes, the assumption that water produced during the ORR is in a vapor phase has been investigated in this study. In such a case, the source term in the cathode catalyst layer needs to be revised to

$$S_v = -\frac{S_{vl}}{M_w} - S_{vd} + \frac{\mathcal{R}_c}{2\mathscr{F}}. \tag{3.32}$$

Here, the last term represents the water production from the electrochemical reaction.

3.3.3 Transport of Dissolved Water

The pore sizes of the polymer electrolyte are of the order of only ten nanometers. Clusters of water molecules tend to be localized and less connected in such small

pores. Therefore, water is usually assumed to be in a "dissolved" phase in the electrolyte region rather than in a liquid state. At the anode catalyst layer, water vapor is absorbed into the electrolyte and the water molecules tend to move with the protons towards the cathode catalyst by means of the electro-osmotic drag. At the cathode catalyst, water is generated at the solid catalyst surface and the enhanced local water concentration tends to counteract the water movement from the anode side. If the concentration gradient is large enough, water will diffuse back to the anode side.

Followed the diffusive approach proposed by Springer *et al.* [30], the above process is described by

$$\frac{\partial}{\partial t}(\epsilon_m C_d) + \nabla \cdot (-D_d \nabla C_d) + \nabla \cdot \left(\frac{n_d}{\mathscr{F}} \vec{J}_m\right) = S_d, \tag{3.33}$$

where C_d is the dissolved membrane water concentration, ϵ_m is the volume fraction of the polymer membrane ($\epsilon_m < 1$ in the catalyst layer), D_d is the dissolved water diffusivity in the electrolyte, n_d is the electro-osmotic drag coefficient, $\vec{J}_m$ is the membrane phase current density which will be determined later in the section of electric charge transport, and S_d is the source term of the dissolved phase.

The diffusivity of dissolved water in the electrolyte is usually determined based on the curve fit of experiment data. Many independent studies have been conducted in the literature and the one proposed by Kulikovsky [40] is used in this study

$$D_d = \epsilon_m 4.1 \times 10^{-10} \left(\frac{\lambda}{25}\right)^{0.15} \left[1 + \tanh\left(\frac{\lambda - 2.5}{1.4}\right)\right]. \tag{3.34}$$

It can be seen that, D_d is a unique function of the membrane water content, λ, defined as the number of water molecules per sulfonic acid group within the polymer electrolyte. It relates to the dissolved water concentration as

$$\lambda = \frac{EW}{\rho_m} C_d, \tag{3.35}$$

where ρ_m denotes the dry membrane density, and EW is the equivalent molecular weight (e.g., 1.1 kg/mol for Nafion) of the dry membrane.

The electro-osmotic drag coefficient, n_d, is also an empirical formula that has to be experimentally determined. In this study, a linear function developed by Springer *et al.* [30] is employed

$$n_d = \frac{2.5\lambda}{22} \tag{3.36}$$

From Equations (3.34)-(3.36) it can be seen that the coefficients in the dissolved water transport equation (Equation 3.33) are functions of the dissolved water concentration itself, indicating the nonlinearity of the equation. In the literature, the numerical implementation of the Equation (3.33) has been conducted in two different approaches with potential pitfalls, and they are described below:

Approach 1: Equilibrium Membrane Water Sorption

The equilibrium water sorption approach can be traced back to the very beginning of PEM fuel cell research with the pioneering work of Springer *et al.* [30], and it is still overwhelmingly adopted by today's models. The main assumption of this approach is that membrane water uptake occurs instantaneously and the dissolved water is always in equilibrium with other water phases in the catalyst layer, i.e. vapor and liquid. As such, the dissolved water concentration (C_d) can be simply evaluated by its counterpart, the water vapor concentration (C_v) in terms of the so-called *sorption isotherm* relation

$$C_d = f'(C_v). \tag{3.37}$$

For convenience, the dissolved water concentration (C_d) is converted to the membrane water content (λ) through Equation (3.35), and the water vapor concentration (C_v) is converted to the water activity a, defined as

$$a = \frac{\mathscr{R}T}{P^{\text{sat}}} C_v, \tag{3.38}$$

where the water saturation pressure, P^{sat}, is determined through [30]

$$P^{\text{sat}} = 10^{-2.1794+0.02953(T-273)-9.1837\times10^{-5}(T-273)^2+1.445\times10^{-7}(T-273)^3}. \tag{3.39}$$

Furthermore, it can be seen that the water activity (a) is equivalent to the relative humidity. Hence, a is in the range of zero to 1.

Finally, the sorption isotherm becomes

$$\lambda = f''(a), \tag{3.40}$$

where f' in Equation (3.37) and f'' in Equation (3.40) are both algebraic functions.

Several correlations for the function f'' have been developed in the literature based on the isotherm water uptake measurement. Among them, the formula developed by Springer *et al.* [30] has been extensively used in previous modeling studies without justifying the temperature effect. In fact, the experimental data presented by Springer *et al.* was measured at 30 °C, which has non-negligible differences from the data at 80 °C measured by Hinasu *et al.* [41]. This can be easily seen in Figure 3.2.

In this thesis research, all the simulations are carried out at the optimum temperature of the PEM fuel cell (around 80 °C). Hence, an expression that was developed by Kulikovsky [40] is employed, which is based on the water uptake data at 80 °C [41]

$$\lambda = 0.3 + 6a\left[1 - \tanh\left(a - 0.5\right)\right] + 3.9\sqrt{a}\left[1 + \tanh\left(\frac{a - 0.89}{0.23}\right)\right]. \tag{3.41}$$

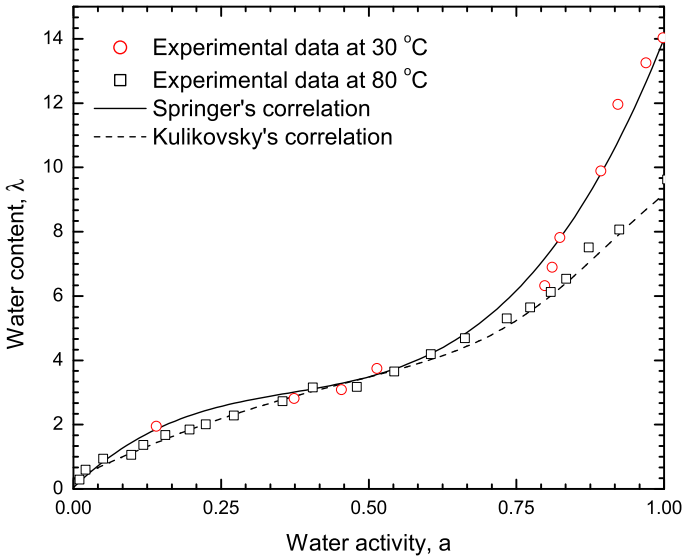

Figure 3.2: Water uptake of Nafion membrane at equilibrium with water vapor.

It should be noted that Equation (3.41) is only valid for $a < 1$ since the relative humidity can by no means exceed 1. However, it has been extrapolated to the region $1 < a < 3$ in many studies to account for the supersaturation conditions which commonly appear in single-phase models, such as in [33, 34, 40, 44, 90].

In the practical operation of a PEM fuel cell, over-saturated water vapor will condense at the solid surface and the electrolyte may be in contact with liquid water directly. Water sorption studies have shown that the polymer membrane exhibits much higher water uptake ability when it contacts with liquid water than with water vapor, a phenomenon usually referred to as Schroeder's paradox. To account for the liquid water uptake effect appearing in the multi-phase model, Equation (3.41) has been revised based on the suggestion of Weber and Newmann [51]

$$\lambda = \begin{cases} 0.3 + 6a\left[1 - \tanh\left(a - 0.5\right)\right] + 3.9\sqrt{a}\left[1 + \tanh\left(\dfrac{a - 0.89}{0.23}\right)\right], & \text{if } s \leq 0, \\ 16.8s + \lambda\big|_{(a=1)}\big(1 - s\big), & \text{if } s > 0, \end{cases} \tag{3.42}$$

where s denotes the liquid water saturation which will be the main topic of next section.

The mechanism of equilibrium water sorption is schematically illustrated in Figure 3.3(a). It shows that the water content in the dissolved phase, λ (or C_d), is always at its equilibrium value, λ_e, determined by the vapor phase (C_v and T) and described by the sorption isotherm

$$f_1(C_d) = \lambda = \lambda_e = f_2(C_v, T). \tag{3.43}$$

where the function f_1 is in the form of Equation (3.35), and f_2 is a combined function of Equations (3.38) and (3.41).

The problem arises when one needs to define the boundary conditions of the system at points 2 and 3 (refer to Figure 3.3a). For lack of better knowledge, it seems appropriate to set both the dissolved water flux, which enters the GDL (point 3), and the water vapor flux, which enters the bulk membrane (point 2), to zero, represented by zero gradients and assuming diffusion dominates. However, at constant temperature and given Equation (3.43) which implies

$$\frac{df_1}{dC_d}\frac{dC_d}{dy} = \frac{d\lambda}{dy} = \frac{df_2}{dC_v}\frac{dC_v}{dy}, \tag{3.44}$$

it is seen immediately that this would also imply zero gradients at points 1 and 4, and hence zero fluxes also. This leads to an ill-posed (steady-state) model since water is produced in the catalyst layer but it is prevented from leaving the domain.

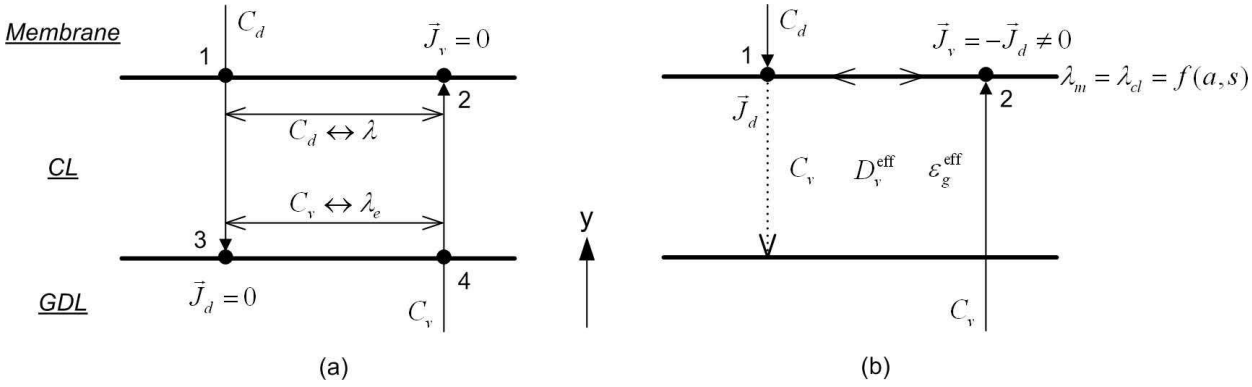

Figure 3.3: Schematic of equilibrium water sorption model (a) ill-posed; (b) well-posed.

In the model of Springer *et al.* [30] and some other earlier 1D/2D models, the catalyst layer is treated as an interface and the dissolved water transport in the catalyst layer is entirely neglected. Therefore, the ill-posed issue is simply bypassed in these models.

For subsequently developed 2D/3D models, however, the catalyst layer is usually explicitly accounted for with finite thickness and, thus, this issue becomes unavoidable. To tackle this problem, Kulikovsky [40] proposed an approach which solves the dissolved water transport only in the bulk membrane region with its boundary values being determined by the local water activities at the adjacent catalyst layer, an approach similar to Springer *et al.*'s [30]. In the catalyst layer, the dissolved water concentration is converted mathematically into water vapor concentration by use of the empirical sorption isotherm relation

$$\frac{\mathrm{d}C_d}{\mathrm{d}C_v} = \frac{\rho_m}{EW}\frac{P^{\mathrm{sat}}}{\mathscr{R}T}\frac{\mathrm{d}\lambda}{\mathrm{d}a} \tag{3.45}$$

Correspondingly, the governing equation of water vapor transport, Equation (3.29), is revised to account for the dissolved water transport in the catalyst layers and takes the shape of an effective water transport, including both dissolved water and vapor

$$\frac{\partial}{\partial t}\left(\epsilon_v^{\text{eff}} C_v\right) + \nabla \cdot \left(-D_v^{\text{eff}} \nabla C_v\right) + \nabla \cdot \left(\vec{u}_g C_v\right) = S_v, \tag{3.46}$$

where the effective porosity (ϵ_v^{eff}) and effective diffusivity (D_v^{eff}) are determined as

$$\epsilon_v^{\text{eff}} = \epsilon^{\text{eff}} + \epsilon_m \left(\frac{\mathrm{d}C_d}{\mathrm{d}C_v}\right), \tag{3.47}$$

$$D_v^{\text{eff}} = D_v + D_d \left(\frac{\mathrm{d}C_d}{\mathrm{d}C_v}\right). \tag{3.48}$$

With such a treatment, the equilibrium model now becomes well-posed and the implementation is schematically illustrated in Figure 3.3(b). Since the dissolved water transport in the catalyst layer, which is rolled into an effective total water transport, would be decoupled from that of the membrane using this formulation, an explicit coupling between these two regions is necessary. This is usually done by specifying boundary conditions at the membrane-CL interface. Two boundary conditions are required here: a Dirichlet boundary condition for the dissolved water transport equation, Equation (3.33), and a mass flux condition for the vapor transport equation, Equation (3.46), which accounts for the water gain or loss from back diffusion.

In some commercial CFD software packages, such as the package FLUENT used in this study, it is hard to implement internal flux boundary conditions. In such cases, the mass fluxes are usually converted to source/sink terms and applied only to the first layer cells adjacent to the interface. As an example, the implementation of the water source term in the ACL is illustrated in Figure 3.4. In the first layer grids of the ACL, both drag force and back diffusion are present, and the back diffusion is determined by the conditions of the first layer grids at the membrane side via

$$S_{\text{diff}} = (-D_d \nabla C_d + n_d \vec{J}_m)\frac{\triangle A}{\triangle V}. \tag{3.49}$$

The first term on the right hand side represents the water back diffusion from the membrane region, the second term represents the electro-osmotic drag force in the membrane, $\triangle A$ is the interfacial surface area of the unit cell, and $\triangle V$ is the volume of the unit cell. In the other layer grids of the ACL, the water source includes the electro-osmotic drag only, as shown in Figure 3.4.

On the other hand, the same mathematical conversion technique can be applied to the dissolved water in the bulk membrane region as well. As such, the dissolved water in all regions is converted mathematically to water vapor and the dissolved water transport equation, Equation (3.33), can be eliminated entirely [33, 44]. In such models, the back diffusion process is self-consistent. Hence, no extra boundary conditions or source terms are required.

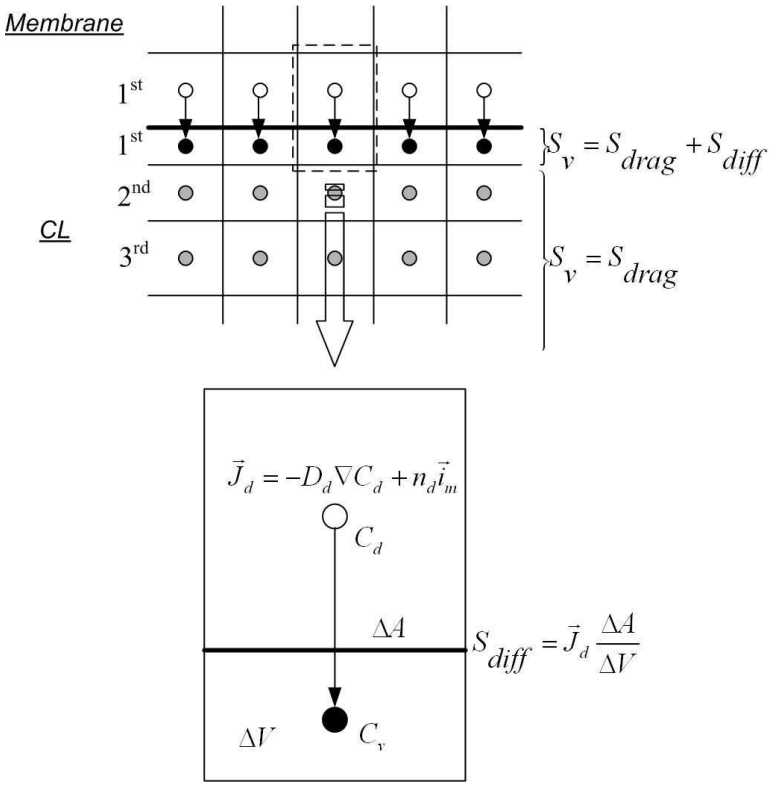

Figure 3.4: Numerical implementation of the water source owing to back diffusion

It should be noted that even though the equilibrium model is well-posed when following this mathematical treatment, each water phase is not modeled explicitly and its boundary conditions are not addressed explicitly. Therefore, the effective water flux within the catalyst layer and across the boundaries really consists of two fluxes: water in the ionomer and water vapor in the gas pores. However, since only a combination of the two is modeled, we have no explicit control over the fluxes of each phase at the membrane-CL and CL-GDL interfaces. Physically speaking, this is a big disadvantage of this combined model.

A more important drawback of the equilibrium model is that the last term $(\frac{d\lambda}{da})$ in the mathematical conversion equation, Equation (3.45), is not strictly valid for multi-phase modeling since the membrane water content, λ, now becomes a function of both water activity, a, and liquid saturation, s, as indicated in Equation (3.42). However, Equation (3.45) has so far been adopted in all the previous multi-phase equilibrium models as an approximation.

Approach 2: Non-equilibrium Membrane Water Sorption

A non-equilibrium water sorption model circumvents all drawbacks of the equilibrium model, and it is not only mathematically better posed but also physically more meaningful.

It has been shown that the time scale for membrane to reach its sorption equilibrium state in humid air is on the order of 100-1000 s [100, 101]. In the recent work of Onishi *et al.* [113] the membrane water uptake takes even longer. They reveal that the water content of a membrane (with an appropriate thermal history) which is in contact with saturated vapor, is actually the same as one in contact with liquid water as the membrane relaxes to its equilibrium state over several weeks or months. Therefore, the so-called Schroeder's paradox does not appear to exist. All these studies indicate that the equilibrium sorption assumption made in most of the previous studies is inaccurate or invalid for PEM fuel cell catalyst layers, given the timescales of key water transport and production mechanisms [47].

Rather than making an equilibrium assumption for the water content, Berg *et al.* [47] proposed an approach in which the flux of water into and out of the electrolyte is assumed to be proportional to the difference between the local ionomer water content and its equilibrium sorption value. A similar approach was later adopted in [102, 103, 114] but, in general, the study of non-equilibrium water sorption is still relatively new and many characteristics of this approach remain poorly understood.

Even though the underlying physical phenomena of non-equilibrium sorption are much more complicated than that of an equilibrium system, the numerical implementation of the non-equilibrium approach is much easier. The dissolved water transport equation, Equation (3.33), is solved in the entire computational domain with two source terms imposed in the catalyst layer

$$S_d = \begin{cases} S_{vd} = \gamma_a \dfrac{\rho_m}{EW} (\lambda_e - \lambda) & \text{(ACL)} \\ S_{d,reac} + S_{ld} = \dfrac{\mathcal{R}_c}{2\mathscr{F}} + \gamma_d \dfrac{\rho_m}{EW} (\lambda_e - \lambda) & \text{(CCL)} \end{cases} \tag{3.50}$$

where $S_{d,reac}$ is the dissolved water production from the electrochemical reaction; λ is the actual membrane water content which is evaluated by Equation (3.35); λ_e is the equilibrium membrane water content which is evaluated by Equation (3.42); γ_a and γ_d are the rate coefficients of membrane absorption and desorption, respectively, and their numerical values at the anode and cathode catalyst layers need to be established.

It is challenging to determine sorption/desorption rates (γ_a, γ_d) in an actual PEM fuel cell and somewhat arbitrary values, ranging from 0.1 to 100 1/s, have been generally used in the literature. However, the study of Ge *et al.* [115] shows that sorption/desorption rates are in fact dependent on the local membrane hydration level and they vary with time. The recent study of Satterfield and Benziger [101] also confirmed such behavior. They found that the physical mechanism of membrane absorption is different from that of desorption which is mainly limited by the interfacial mass transport. Water absorption presents a two-step behavior: uptake for the initial 35% of water absorption is described by the same interfacial transport rate coefficient as that of desorption, while for the value above 35%, water absorption is controlled by the dynamics of membrane swelling and relaxation. It is found that the absorption process is 10 times slower than that of desorption in the second stage.

In order to precisely describe the sorption/desorption dynamics, two empirical expressions of sorption/desorption rates that were developed by Ge *et al.* [115], are employed in the present study

$$\gamma_a = \frac{1.14 \times 10^{-5} f_V}{\delta_{\text{cl}}} \exp\left[2416\left(\frac{1}{303} - \frac{1}{T}\right)\right], \tag{3.51}$$

$$\gamma_c = \frac{4.59 \times 10^{-5} f_V}{\delta_{\text{cl}}} \exp\left[2416\left(\frac{1}{303} - \frac{1}{T}\right)\right]. \tag{3.52}$$

It should be noted that a slight modification has been made by incorporating the finite thickness of the catalyst layer, δ_{cl}, into the original form of Ge *et al.*'s expression. A similar treatment has been used by Berg *et al.* [111] in a mathematical model concerning the catalyst layer only. Here, f_V is the volume fraction of water in the electrolyte membrane and it is calculated as

$$f_V = \frac{\lambda V_w}{V_m + \lambda V_w}, \tag{3.53}$$

where V_w and V_m are the molar volumes of water and dry membrane, respectively.

3.3.4 Transport of Liquid Water

Derivation of The Governing Equation

In multi-phase flow, the general continuity equation for each phase is

$$\frac{\partial \rho_k}{\partial t} + \nabla \cdot (\rho_k \vec{u}_k) = S_k, \tag{3.54}$$

where the density ρ_k is the superficial phase density of phase k in the whole volume, which is variable.

After a volume averaging procedure, the above equation becomes

$$\frac{\partial \left(\epsilon_k \langle \rho_k \rangle\right)}{\partial t} + \nabla \cdot \left(\epsilon_k \langle \rho_k \rangle \langle \vec{u}_k \rangle\right) = \Gamma_{M,k}. \tag{3.55}$$

Here, $\langle\rangle$ is the volume averaged property, ϵ_k is the volume fraction of phase k within the total volume. In PEM fuel cell modeling, it is assumed

$$\epsilon_k = \epsilon s, \tag{3.56}$$

where ϵ is the porosity, defined as the volume fraction of void space within the total volume. s is the liquid saturation, which is the ratio between liquid volume and void space volume, i.e.

$$s = \frac{\text{volume of liquid}}{\text{volume of void}}. \tag{3.57}$$

There is no interfacial source term for the superficial mass conservation. Therefore, S_k in Equation (3.54) only represents the source terms due to chemical reactions or add-in sources from outside. On the other hand, the source term in Equation (3.55) accounted for the interfacial mass transfer among different phases, i.e.

$$\Gamma_{M,k} = S_k + \sum \Gamma_{s,k}, \tag{3.58}$$

where $\Gamma_{s,k}$ represents gain or loss of phase k from adjacent phase s.

Now, applying the mass conservation Equation (3.55) to the liquid phase, it gives

$$\frac{\partial \left(\epsilon s \left\langle \rho_l \right\rangle\right)}{\partial t} + \nabla \cdot \left(\epsilon s \left\langle \rho_l \right\rangle \left\langle \vec{u}_l \right\rangle\right) = S_l. \tag{3.59}$$

The volume averaged density $\langle \rho_l \rangle$ is constant ($\langle \rho_l \rangle = 970$ kg/m^3), and S_l is the source term of the liquid phase. For convenience, the bracket of the volume averaged density is omitted and the constant $\rho_l = 970$ kg/m^3 will be used exclusively hereafter.

In porous media, the liquid velocity $\langle \vec{u}_l \rangle$ can be approximated using *Darcy's Law*, as

$$\epsilon s \left\langle \vec{u}_l \right\rangle = \vec{u}_l = -\frac{K_{rl} K}{\mu_l} \nabla P_l, \tag{3.60}$$

where $\vec{u}_l$ is the superficial velocity of the liquid water, K is the intrinsic permeability of the porous media which is determined by Kozeny-Carman equation [116]

$$K(s) = \frac{\epsilon^3 (1-s)^3}{150 \left(1 - \epsilon(1-s)\right)^2} \bar{d}^2, \tag{3.61}$$

where $\bar{d}$ is the characteristic length of the porous material; K_{rl} is the relative permeability of the liquid phase, μ_l and P_l are the dynamic viscosity and pressure of the liquid phase, respectively.

Substitute Equation (3.60) into Equation (3.59), the continuity equation now becomes

$$\frac{\partial \left(\epsilon s \rho_l\right)}{\partial t} + \nabla \cdot \left(\rho_l \vec{u}_l\right) = S_l \tag{3.62}$$

On the other hand, the liquid phase pressure P_l is related to the capillary pressure by

$$P_c = P_{nw} - P_w = P_l - P_g \tag{3.63}$$

Here, P_c denotes the capillary pressure, P_{nw} and P_w denote the pressure of the non-wetting phase and wetting phase, respectively. In the scenario of PEM fuel cells where hydrophobic material is usually used to remove the water, the non-wetting phase is the liquid phase, and the wetting phase is the gas phase.

If substitute Equation (3.63) into Equation (3.60), it becomes

$$\vec{u}_l = -\frac{K_{rl} K}{\mu_l} \nabla P_g - \frac{K_{rl} K}{\mu_l} \nabla P_c. \tag{3.64}$$

Next, applying Darcy's law to the gas phase, it gives

$$\nabla P_g = -\frac{\mu_g}{K_{rg}K}\vec{u}_g, \tag{3.65}$$

where μ_g and K_{rg} are the dynamic viscosity and relative permeability of the gas phase, respectively.

Now, combining Equation (3.64), (3.65) and (3.62) gives

$$\frac{\partial\left(\epsilon s \rho_l\right)}{\partial t} + \nabla \cdot \left(-\frac{\rho_l K_{rl} K}{\mu_l}\nabla P_c + \frac{\rho_l \mu_g K_{rl}}{\mu_l K_{rg}}\vec{u}_g\right) = S_l. \tag{3.66}$$

The capillary pressure can be further expressed as a function of the liquid saturation

$$P_c = f(s) \qquad \Longrightarrow \qquad \nabla P_c = \frac{dP_c}{ds}\nabla s. \tag{3.67}$$

More details regarding the empirical capillary function will be given shortly.

Finally, the governing equation for the liquid water transport is generated in terms of the liquid saturation

$$\frac{\partial\left(\epsilon \rho_l s\right)}{\partial t} + \nabla \cdot \left[\left(-\frac{\rho_l K_{rl} K}{\mu_l}\frac{dP_c}{ds}\right)\nabla s + \frac{\rho_l \mu_g K_{rl}}{\mu_l K_{rg}}\vec{u}_g\right] = S_l. \tag{3.68}$$

Determination of The Source Term

From Equation (3.58), it is known that the source of liquid water may come from the electrochemical reactions or from other water phases. The electrochemical reaction and membrane desorption occur in the cathode side catalyst layer. Hence, the source term in CCL has the form

$$S_l = \frac{\mathcal{R}_c}{2\mathscr{F}} - M_w S_{ld} + S_{vl} \tag{3.69}$$

The first source term on the right hand side represents the water production from the electrochemical reaction assuming a liquid water production mechanism; the second term is the water source from membrane desorption and it is determined by Equation (3.50); the last term is the interfacial mass transfer between liquid and vapor phases during evaporation and condensation.

In other regions, phase change occurs between the liquid and vapor phase only, thus

$$S_l = S_{vl}. \tag{3.70}$$

From kinetic theory [117, 118], assuming an ideal gas and neglecting interactions between individual molecules, the net mass transfer of the evaporation and condensation can be estimated using the Hertz-Knudsen-Langmuir equation

$$S_{vl} = A\sqrt{\frac{M_w}{2\pi\mathscr{R}}}\left(\zeta_c\frac{P_v}{\sqrt{T_v}} - \zeta_e\frac{P_l}{\sqrt{T_l}}\right). \tag{3.71}$$

Here, A is the liquid/vapor specific interfacial area which depends on the saturation, ζ_c and ζ_e are the condensation and evaporation rate coefficient, respectively; P_v and P_l are the vapor and liquid pressure, respectively, and T_v and T_l are the vapor and liquid temperature, respectively.

A comprehensive investigation of the condensation and evaporation process is rather sophisticated and needs to be performed in the surrounding region of the liquid/vapor interface at the molecular level. For PEM fuel cell modeling, it is impractical to incorporate such processes and a revised form of the above equation is usually used [57, 95]

$$S_{vl} = A\zeta_{ce}^{'}\left(\frac{P_v}{\mathscr{R}T} - \frac{P^{\text{sat}}}{\mathscr{R}T}\right) = A\zeta_{ce}\left(\rho_w - \rho^{sat}\right), \tag{3.72}$$

where ζ_{ce} (or $\zeta_{ce}^{'}$) is the analogous condensation/evaporation rate and it reads

$$\zeta_{ce} = \Gamma_m\sqrt{\frac{\mathscr{R}T}{2\pi M_w}}. \tag{3.73}$$

Here, Γ_m is an uptake coefficient that accounts for the combined effects of heat and mass transport limitations in the vicinity of the liquid/vapor interface. From the analysis of [66], this coefficient is about 0.006.

The specific liquid/vapor interfacial area is calculated as

$$A = \Gamma_s A_{\text{pore}}, \tag{3.74}$$

where A_{pore} is the pore surface area per unit volume which varies from 13 to 30 m^2/cm^3 for different GDL materials [63] and a value of 20 m^2/cm^3 is used in the current study; Γ_s is an accommodation coefficient similar to Γ_m. The study of [119] shows that Γ_s rarely exceeds 20% for spherical particles with small water saturation. In this study, the mass transfer uptake coefficient Γ_m is varied in the range of $0.001 - 0.006$ and the interfacial area accommodation coefficient Γ_s is varied in the range of 1%-20% to roughly estimate a range for the condensation/evaporation rate.

Similar to the membrane water absorption/desorption processes, the water condensation/evaporation dynamics are limited by the mass transport in the vicinity of the liquid/vapor interface. Then Equation (3.72) can be further revised to

$$S_{vl} = A_{\text{pore}}\frac{Sh_{ce}D_w}{\bar{d}}(\rho_w - \rho^{sat}), \tag{3.75}$$

where $\bar{d}$ is the characteristic length for water diffusion, D_w is the mass diffusivity of water vapor, and Sh_{ce} is a dimensionless number accounting for mass transport capability during condensation/evaporation. This is analogous to the Sherwood number for mass transfer, and it is calculated as

$$Sh_{ce} = \Gamma_s\Gamma_m\sqrt{\frac{\mathscr{R}T}{2\pi M_w}}\frac{\bar{d}}{D_w}. \tag{3.76}$$

The values of D_w and $\bar{d}$ are not important here since they will cancel out in Equation (3.75). The diffusivity of water vapor and the pore size from a network model are used here:

$$\bar{d} = 4d_0 \tag{3.77}$$

where d_0 is the fiber diameter of the carbon material.

Furthermore, to differentiate the condensation and evaporation processes, a Langumir-type correction is incorporated and the resulting condensation/evaporation source term is related to the local liquid saturation in the form of

$$S_{vl} = \begin{cases} A_{\text{pore}} \dfrac{Sh_c D_w}{\bar{d}} (1-s)(\rho_w - \rho^{sat}) & \text{if } \rho_{\text{v}} \geq \rho_{\text{sat}}, \text{ (condensation)} \\ A_{\text{pore}} \dfrac{Sh_e D_w}{\bar{d}} s(\rho_w - \rho^{sat}) & \text{if } \rho_{\text{v}} < \rho_{\text{sat}}, \text{ (evaporation)} \end{cases} \tag{3.78}$$

where Sh_c and Sh_e are the phase transfer rate coefficients of condensation and evaporation, respectively. It should be noted that the saturated water vapor density, ρ^{sat}, depends exponentially on temperature and, hence, even a small variation of temperature can have a large impact on the saturation.

Determination of The Capillary Pressure

As indicated earlier in Equation (3.67), a functional relationship between the capillary pressure and liquid saturation is required in order to solve the liquid water transport equation (Equation (3.68)). Owing to the lack of experimental data the determination of the capillary pressure in the porous backing layer of PEM fuel cells has been traditionally performed in terms of the Leverett function [120]

$$P_c(s) = \sigma \cos(\theta_c) \sqrt{\frac{\epsilon}{K}} (1.417s - 2.120s^2 + 1.263s^3), \tag{3.79}$$

where σ is the surface tension between the liquid water and gas phase, and θ_c is the assumed uniform contact angle of the porous materials.

The Leverett approach was derived based on experimental data of homogeneous soil or a sand bed with uniform wettability. In the backing layer of the PEM fuel cell, however, the pore size ranges from nanometer to micrometer, and its wettability is strongly affected by both the hydrophilic carbon substrate and the level of the hydrophobic polytetrafluoroethylene (PTFE) coating. Therefore, the Leverett approach is incapable of precisely predicting the capillary pressure in PEM fuel cells. Many experiments [60, 61, 62, 63, 64, 65] have been carried out recently, trying to assess the real situation in PEM fuel cells. However, due to the differences in their measurement approaches, facilities, experimental conditions, and the materials being investigated, their results do not agree with each other very well. To date, there exist no correlations which can quantify the capillary pressure for all materials used in PEM fuel cells under all possible conditions. In this study, therefore, no intention has been made to propose a general capillary pressure modeling approach. Instead,

two of the newly developed capillary pressure correlations that are specific to PEM fuel cells are examined and the resulting saturation characteristics are compared with the standard Leverett function approach.

The first new correlation is proposed by Kumbur *et al.* [63, 64, 65], based on their drainage capillary pressure-saturation measurements of the SGL 24 serials composite carbon paper and E-TEK Elat 1200W carbon cloth materials. It has the following form

$$P_c = \sigma \left(\frac{293}{T}\right)^6 2^{0.4C} \sqrt{\frac{\epsilon}{K}} \kappa(s), \tag{3.80}$$

$$\kappa(s) = (\text{wt }\%)[0.0469 - 0.00152(\text{wt }\%) - 0.0406s^2 + 0.143s^3] + 0.0561 \ln(s).$$

In the above correlation, the effects of temperature, T, compression pressure, C, and mixed wettability, wt %, representing the amount of PTFE in the GDL, have been incorporated into a modified form of the standard Leverett function. Since no micro-porous layer (MPL) is considered in the current study, the $\kappa(s)$ function has been extended from its original range, $0 < s < 0.5$, to $0 < s < 1$ to eliminate the effect of the MPL, as suggested by the authors.

In the current model, the temperature is coupled through the energy equation; the compression pressure is assumed to be 1 MPa; for the mixed wettability, it is found that it is not really accounted for by the above expression. This is mainly because the derivative of the capillary pressure (dP_c/ds) is the actual form (refer to Equation (3.68)) that is being used in the model. In Kumbur's expression, it results in

$$\frac{dP_c}{ds} = \sigma \left(\frac{293}{T}\right)^6 2^{0.4C} \sqrt{\frac{\epsilon}{K}} \left[(\text{wt }\%)(-0.0812s + 0.429s^2) + \frac{0.0561}{s}\right]. \tag{3.81}$$

It is easily seen that for small saturations as in PEM fuel cells, Equation (3.81) is essentially dominated by the second term ($1/s$) while the effect of PTFE loading that is described by the first term is greatly subdued.

The second correlation used in this study was derived from a fit by Ye and Nguyen [114] based on the experimental data of Nguyen *et al.* [60]. Both drainage and imbibition processes have been investigated in this experiment. The capillary pressure within a Toray TGP-H-060 GDL with 10% PTFE loading has been measured, using a volume displacement technique, while the capillary pressure within a thickened catalyst layer (55 μm) that is composed of the same material is obtained through neutron imaging techniques. Accordingly, two separate correlations for GDL and CL are developed [114]

$$P_{c,\text{gdl}} = 2.09\left(e^{22.2(0.321-s)} - e^{44.9(0.321-s)}\right) + 35.6, \tag{3.82}$$

$$P_{c,\text{cl}} = 2431\left(e^{0.0088(0.567-s)} - e^{92.36(0.567-s)}\right) - 2395. \tag{3.83}$$

It should be noted that the experimental method used in [60] is naturally limited by break-through and break-off liquid pressures of the GDL materials. Consequently, the capillary pressure they measured lies in a relatively small range (one

to two orders smaller than that of Gostick *et al.*'s [61], Fairweather *et al.*'s [62], and Kumbur *et al.*'s [63, 64, 65]). Physically, smaller capillary pressure means higher water retention ability, thus a higher level of saturation would be expected by this expression.

Determination of the Relative Permeability

In addition to the capillary pressure, two other parameters need to be determined in the liquid saturation equation, Equation (3.68). They are the relative permeability for the liquid and gas phase, K_{rl} and K_{rg}, respectively. Similar to the capillary pressure, various forms of relative permeability correlations have been employed in previous PEM fuel cells modeling efforts due to the lack of experimental support. Predictive models for the relative permeability were developed from conceptual models of flow in capillary tubes combined with models of pore-size distribution. The common predictive models are the power law function [121], Burdine and Mualem functions [122], Van Genuchten function [123] and the Brooks-Corey function [124]. Among them, the power law function is the most widely used in fuel cell modeling. The general form of the power law function is

$$K_{rl} = (s_w^{\text{eff}})^n, \tag{3.84}$$

$$K_{rg} = (s_{nw}^{\text{eff}})^n, \tag{3.85}$$

where the subscript w denotes the wetting phase, and nw denotes the non-wetting phase. The effective saturation, s_w^{eff}, is defined as

$$s_w^{\text{eff}} = \frac{s_w - S_{w,\text{irr}}}{1 - S_{nw,\text{irr}} - S_{w,\text{irr}}}, \tag{3.86}$$

where $S_{w,\text{irr}}$ and $S_{nw,\text{irr}}$ are the irreducible saturation for the wetting and non-wetting phase, respectively. The exponent n in Equation (3.84)&(3.85) is usually determined through a curve fit of experimental data. In PEM fuel cell modeling, a factor of 3, the so-called Wyllie's cubic power law [125], is commonly adopted in the literature and it is used as the base case in this study.

On the other hand, based on the analysis of [61, 126], several recent studies [114, 126] have used an exponent of $n = 4.5$ for the GDL while keeping the exponent at 3.0 in the CL. As a comparison to the cubic power law, this approach is examined in this study to investigate the effect of relative permeability on the distribution of the liquid saturation.

3.4 Transport of Electric Charge

As illustrated in Section 1.2, hydrogen molecules are stripped of their electrons and become positively charged hydrogen ions (protons) during the HOR. Protons

migrate through the ion-selective membrane directly and reach the cathode side catalyst layer, while electrons are expelled by the membrane and have to travel through the solid part of the backing layer and external circuit to reach the cathode catalyst, where they recombine with protons to form water following the ORR.

3.4.1 Conservation of Electronic Charge

The governing equation for the electron transport can be written as

$$\nabla \cdot \left(\vec{J_s} \right) = S_\phi, \tag{3.87}$$

where S_ϕ is the source term denoting the generation or consumption of electrons, and $\vec{J_s}$ denotes the electronic current density through the solid phase. Notice that the current density is a vector quantity, and only the transverse component (normal to the GDL surface) is useful and contributes to the power output of the cell; the lateral component only decreases the cell output. Therefore, the lateral component should be minimized through appropriate designs.

The electronic current density is related to the electric potential in terms of *Ohm's law*

$$\vec{J_s} = -\sigma_s \nabla \phi_s. \tag{3.88}$$

Here, ϕ_s is the electric potential in the solid phase, and σ_s is the electric conductivity of the solid material.

Therefore, Equation (3.87) can be further extended to

$$\nabla \cdot (-\sigma_s \nabla \phi_s) = S_\phi. \tag{3.89}$$

In the ACL, electrons are generated. The source term is

$$S_\phi = \mathcal{R}_a. \tag{3.90}$$

In the CCL, electrons are consumed, thus

$$S_\phi = -\mathcal{R}_c. \tag{3.91}$$

In other regions, no electrochemical reaction occurs and hence

$$S_\phi = 0. \tag{3.92}$$

3.4.2 Conservation of Protonic Charge

In a similar manner, the governing equation for proton transport can be written as

$$\nabla \cdot \left(\vec{J_m} \right) = S_\phi, \tag{3.93}$$

where S_ϕ is the source of proton generation or depletion, and $\vec{J}_m$ is the protonic current density which lies within the electrolyte membrane only.

According to *Ohm's law*, the protonic current density is calculated as

$$\vec{J}_m = \sigma_m \nabla \phi_m. \tag{3.94}$$

Here, ϕ_m is the electric potential in the electrolyte membrane, and σ_m is the electric conductivity of the membrane which is affected by the local membrane water content through an empirical correlation [30]

$$\sigma_m = \epsilon_m (0.005139\lambda - 0.00326) \exp\left[1268\left(\frac{1}{303} - \frac{1}{T}\right)\right]. \tag{3.95}$$

Consequently, Equation (3.93) is converted to

$$\nabla \cdot (\sigma_m \nabla \phi_m) = S_\phi. \tag{3.96}$$

Corresponding to the electron transport, the amount of proton gain or loss must equal that of the electron. Therefore, in the ACL, the source term for proton transport is

$$S_\phi = \mathcal{R}_a \tag{3.97}$$

and in the CCL it is

$$S_\phi = -\mathcal{R}_c. \tag{3.98}$$

In all other regions, no electrochemical reaction occurs. Therefore, it has

$$S_\phi = 0 \tag{3.99}$$

3.5 Transport of Energy

The temperature variation is generally not very large in PEM fuel cells but can be important nevertheless due to the sensitivity of two-phase flow towards temperature. Therefore, heat transfer processes are usually simplified to some extent to reduce the model complexity. Based on the analysis of Wang [127], two main simplifications have been made in this study: (i) the heat transfer through the liquid phase is neglected since the liquid saturation is relatively small (< 0.1) and, (ii) it is assumed that the gas phase and solid phase are always in a thermal equilibrium state.

As such, the energy equation that accounts for the effect of multi-species, multiphase flow in porous media can be stated as [110]

$$\frac{\partial}{\partial t}\left(\sum_{k=g,s}(\epsilon\rho E)_k\right) + \nabla\cdot(\vec{u}_g\,(\rho_g E_g + P_g)) = \nabla\cdot\left[k^{\text{eff}}\nabla T - \left(\sum_i h_i \vec{N}_i\right) + (\overline{\overline{\tau}}\cdot\vec{u}_g)\right] + S_T, \tag{3.100}$$

where k^{eff} is the effective conductivity, and $\vec{N}_i$ is the diffusion flux of species i. The first three terms on the right-hand side of Equation (3.100) represent energy transfer due to conduction, species diffusion, and viscous dissipation, respectively. S_T includes the heat of chemical reaction, phase change, and any other volumetric heat sources.

In Equation (3.100), E denotes the total energy in the respective phase and it is calculated as

$$E = h - \frac{p}{\rho} + \frac{v^2}{2} \tag{3.101}$$

where the sensible enthalpy h is defined for ideal gases as

$$h = \sum_i Y_i h_i \tag{3.102}$$

with Y_i the mass fraction of species i

$$Y_i = X_i \left(\frac{M_i}{\sum_i X_i M_i} \right) \tag{3.103}$$

and

$$h_i = \int_{T^{\text{ref}}}^{T} c_{p,i}\, dT, \tag{3.104}$$

where T^{ref} is 298.15 K and $c_{p,i}$ is the specific heat of the i^{th} species.

Similarly, the sensible enthalpy for the solid phase is determined by

$$h = \int_{T^{\text{ref}}}^{T} c_p\, dT, \tag{3.105}$$

where c_p is the specific heat of the solid material.

The effective thermal conductivity, k^{eff}, is evaluated based on the volume fraction of each phase as

$$k^{\text{eff}} = \epsilon k_g + (1 - \epsilon) k_s. \tag{3.106}$$

The thermal conductivity of the solid phase can be specified directly, while the thermal conductivity of the gas mixture is calculated based on kinetic theory

$$k_g = \sum_i \frac{X_i k_i}{\sum_j X_j \phi_{ij}}, \tag{3.107}$$

where

$$\phi_{ij} = \frac{\left[1 + \left(\frac{\mu_i}{\mu_j} \right)^{1/2} \left(\frac{M_j}{M_i} \right)^{1/4} \right]^2}{\left[8 \left(1 + \frac{M_i}{M_j} \right) \right]^{1/2}}. \tag{3.108}$$

Moreover, the diffusion flux of species in Equation (3.100) is estimated using Fick's law as mentioned earlier in Section 3.2

$$\vec{N}_i = -D_{i,m}^{\text{eff}} \nabla C_i. \tag{3.109}$$

The last term in Equation (3.100) represents the heat source. Five kinds of heat sources were considered in the current model. They are the reversible heat release during the electrochemical reaction, irreversible (activation) heat generation, ohmic heating, latent heat during condensation/evaporation, and the latent heat during membrane water sorption/desorption, respectively. Thus,

$$S_T = S_{T,rev} + S_{T,act} + S_{T,ohm} + S_{T,con/eva} + S_{T,sor/des} \tag{3.110}$$

In the CCL, all five types of heat generation are present and the heat source has the form

$$S_T = \underbrace{\left|\frac{\mathcal{R}_c}{4\mathscr{F}}\right|(T\triangle S)}_{rev} + \underbrace{|\eta_c \mathcal{R}_c|}_{act} + \underbrace{\frac{J_s^2}{\sigma_s} + \frac{J_m^2}{\sigma_m}}_{ohm} + \underbrace{S_{vl} h_{fg}}_{con/eva} + \underbrace{M_w S_{ld}(h_{m,fg} - h_{fg})}_{des}, \tag{3.111}$$

where $\triangle S$ represents the entropy change of the ORR, h_{fg} represents the latent heat of water vapor condensation, and $h_{m,fg}$ represents the latent heat of water vapor sorption.

Similarly, the heat source in the ACL is

$$S_T = |\eta_a \mathcal{R}_a| + \frac{J_s^2}{\sigma_s} + \frac{J_m^2}{\sigma_m} + S_{vl} h_{fg} + \underbrace{M_w S_{vd} h_{m,fg}}_{sor}. \tag{3.112}$$

The reaction heat during the HOR is very small and has been neglected from the above equation. Furthermore, water sorption from water vapor to dissolved water in the ACL, and desorption from dissolved water to liquid water in the CCL, have been assumed here.

Water vapor sorption into a membrane is a process similar to a vapor condensation process and involves a release of heat (exothermic). Similarly, water molecules leaving a membrane as vapor is similar to a liquid evaporation process and requires heat (endothermic). Ostrovskii and Gostev [128] show that the differential heat of sorption decreases with the hydration level from 68 kJ/mol at a water content $\lambda \simeq 0$ to about 45 kJ/mol at $\lambda \simeq 5$ but not below the latent heat of water condensation, 40.7 kJ/mol, in any case. In this study, a constant value ($1.5 \times 40.7 \simeq 60$ kJ/mol) that is deemed to be larger than the real case is used and serves as an upper bound. It is found that the inclusion of this overestimated heat source does not affect the temperature field significantly ($\triangle T_{max} < 0.2$ K). In fact, the source of reaction heat from the ORR is on the order of 10^8 W/m^3 which is much more significant than the heat source from the membrane sorption, $10^6 \sim 10^7$ W/m^3. Furthermore, the swelling of the membrane due to water sorption is an endothermic process and

the endothermic "swelling energy" must be smaller than the exothermic solvation energy for water sorption to occur [101]. Therefore, this energy term would be negligibly small as well.

In the GDL, both ohmic heating and condensation/evaporation are present. Therefore, the heat source is

$$S_T = \frac{J_s^2}{\sigma_s} + S_{vl} h_{fg}. \tag{3.113}$$

In the membrane layer, the heat source only includes the ohmic heating caused by protonic current flow

$$S_T = \frac{J_m^2}{\sigma_m}. \tag{3.114}$$

In the gas flow channels, the heat sources are simply zero.

3.6 Boundary and Initial Conditions

3.6.1 Boundary Conditions

In order to complete the model formulation, boundary conditions at different locations of the cell domain are required. A single computational domain approach is employed in this study and, thus, boundary conditions are only needed to be specified on the outer surfaces of the domain.

It has been shown in [129] that for bipolar plate made of graphite, its effect on unit cell performance is negligible because of its high electrical and thermal conductivity. Furthermore, the effects of the cooling channel can also be minimized by appropriate specifications of temperature boundary conditions. Thus, both the bipolar plate and the cooling channel have been excluded from the current study.

The boundary conditions, for a computational domain with a single pair of gas flow channels, are illustrated in Figure 3.5. The same boundary condition scheme can be simply extended to multi-channel domains without any modification.

Basically, these boundary conditions represent the real operating conditions of a PEM fuel cell. When testing a PEM fuel cell, several operating conditions can be varied, such as:

- the flow rate of the reactants;
- the purity (concentration) of the reactants;
- the relative humidity of the reactants flow;
- the operating temperature;

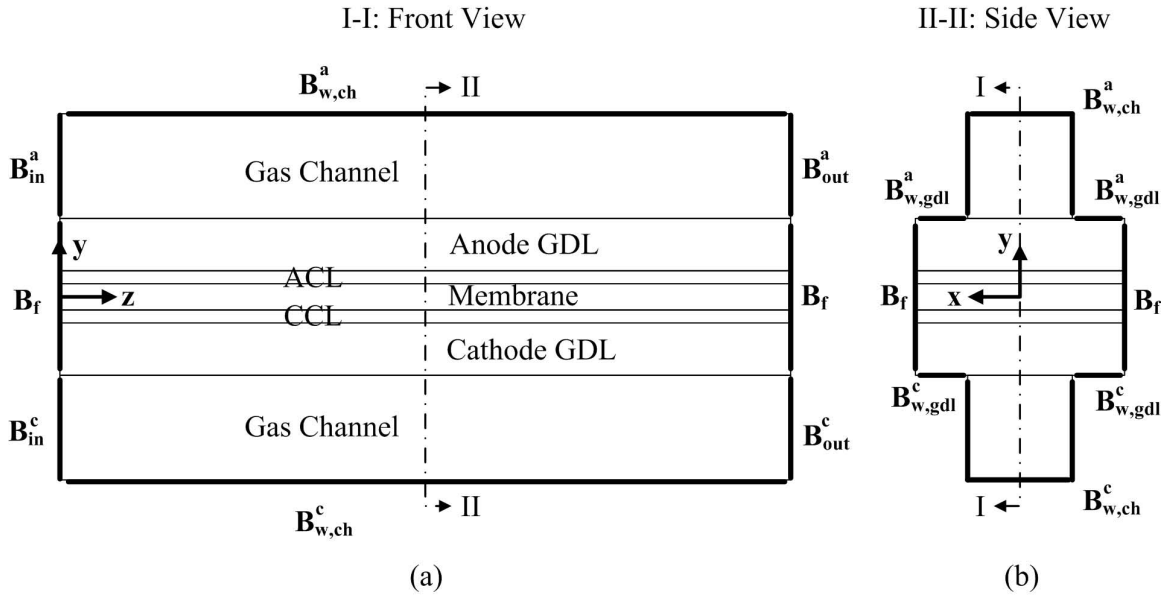

Figure 3.5: Illustration of boundary condition specifications on a computational domain with a single pair of gas flow channels: (a) front view, (b) side view.

- the operating pressure and
- the electrical load.

The boundary conditions present in Figure 3.5 can be classified into four types: the inlet, outlet, wall, and zero flux boundary conditions, and they are represented as $\mathrm{B_{in}}$, $\mathrm{B_{out}}$, $\mathrm{B_w}$, $\mathrm{B_f}$, respectively.

At the gas flow channel inlets ($\mathrm{B^a_{in}}$ and $\mathrm{B^c_{in}}$), the gas composition, mass flux, and temperature of the incoming gas flow are specified. Additionally, the fluxes of all other variables are set to zero, as indicated by the last condition in Equation (3.115). Here, Θ can be any variables not explicitly specified.

$$\left\{ \begin{array}{c} \dot{m}'' \cdot \vec{n} = \text{Specified} \\ C_i = \text{Specified} \\ T = \text{Specified} \\ \dfrac{\partial \Theta}{\partial \vec{n}} = 0 \end{array} \right\} \text{at } \mathrm{B^a_{in}}, \mathrm{B^c_{in}} \tag{3.115}$$

The mass fluxes of gas species are given by their respective stoichiometric ratios, ξ_a and ξ_c, defined at a reference current density, $J^{\mathrm{ref}} = 1$ A/cm^2, as

$$\dot{m}''_a = \frac{\rho_g \xi_a J^{\mathrm{ref}} A}{2\mathscr{F} C_{h_2}}, \tag{3.116}$$

$$\dot{m}''_c = \frac{\rho_g \xi_c J^{\mathrm{ref}} A}{4\mathscr{F} C_{o_2}}, \tag{3.117}$$

where A is the active reaction area.

The inlet concentrations of hydrogen, C_{h_2}, and oxygen, C_{o_2}, can be obtained through the following relations

$$C_{h_2} = \frac{(P_a - RH_a P^{\text{sat}})}{\mathscr{R}T_0}, \tag{3.118}$$

$$C_{o_2} = \frac{0.21(P_c - RH_c P^{\text{sat}})}{\mathscr{R}T_0}, \tag{3.119}$$

where T_0 is the inlet gas temperature, P_a and P_c are the inlet gas pressure at anode and cathode, respectively, RH_a and RH_c are the inlet relative humidities of anode and cathode, respectively. The coefficient 0.21 represents the molar fraction of O2 in air.

At the gas flow channel outlets ($\mathrm{B}^{\mathrm{a}}_{\mathrm{out}}$ and $\mathrm{B}^{\mathrm{c}}_{\mathrm{out}}$), the flow is assumed to be fully developed. Thus, the fluxes of all variables do not vary in the normal direction. Moreover, the gas pressure is specified.

$$\left\{ \begin{array}{c} P = \text{Specified} \\ \dfrac{\partial \Theta}{\partial \vec{n}} = 0 \end{array} \right\} \text{at } \mathrm{B}^{\mathrm{a}}_{\mathrm{out}}, \mathrm{B}^{\mathrm{c}}_{\mathrm{out}} \tag{3.120}$$

At the channel walls ($\mathrm{B}^{\mathrm{a}}_{\mathrm{w,ch}}$ and $\mathrm{B}^{\mathrm{c}}_{\mathrm{w,ch}}$), a constant operating temperature is prescribed. In addition, no-slip boundary conditions apply, along with zero flux conditions for other variables.

$$\left\{ \begin{array}{c} \vec{u}_g = 0 \\ T = \text{Specified} \\ \dfrac{\partial \Theta}{\partial \vec{n}} = 0 \end{array} \right\} \text{at } \mathrm{B}^{\mathrm{a}}_{\mathrm{w,ch}}, \mathrm{B}^{\mathrm{c}}_{\mathrm{w,ch}} \tag{3.121}$$

Similarly, the operating temperature and electronic potential are directly defined at the GDL surfaces that are exposed to the bipolar plate ($\mathrm{B}^{\mathrm{a}}_{\mathrm{w,gdl}}$ and $\mathrm{B}^{\mathrm{c}}_{\mathrm{w,gdl}}$).

$$\left\{ \begin{array}{c} \vec{u}_g = 0 \\ T = \text{Specified} \\ \phi_s = \text{Specified} \\ \dfrac{\partial \Theta}{\partial \vec{n}} = 0 \end{array} \right\} \text{at } \mathrm{B}^{\mathrm{a}}_{\mathrm{w,gdl}}, \mathrm{B}^{\mathrm{c}}_{\mathrm{w,gdl}} \tag{3.122}$$

For the remaining boundaries not specifically mentioned here, a *no-flux* condition or *symmetry* condition applies

$$\left\{ \frac{\partial \Theta}{\partial \vec{n}} = 0 \right\} \text{at } \mathrm{B_f} \tag{3.123}$$

3.6.2 Initial Conditions

The initial conditions required by the transient modeling are usually the flow solutions from a steady-state run. Furthermore, the transient simulation can also start from an initialized flow field to simulate cell start-up processes for which the concentration of gas species and dissolved water are specified, all other variables are set to zero.

3.7 Model Input Parameters

In addition to boundary conditions, the mathematical model is also constrained by various parameters. The input parameters of the current model can be roughly grouped into four kinds: the structural parameters, the electrochemical kinetic parameters, the physical and thermal parameters, and the operating parameters.

The structural parameters of the current model are listed in Table 3.1. The anode and cathode layers are identical; hence, the same parameters apply to the gas flow channels, GDL and catalyst layers on the anode and cathode sides. The geometric parameters of the gas channel are design parameters and, thus, they represent the real experimental conditions, while the parameters in the porous region are highly dependent on the chosen types of porous material (e.g., carbon paper, carbon cloth), the fabrication processes (loading of PTFE, Nafion, Pt, etc.), and the assembling processes (e.g, compression pressure). It is extremely hard, if not impossible, to measure the material properties in an assembled fuel cell. Therefore, these parameters are usually estimated, based on empirical expressions. The dependence of the cell performance on these estimated parameters can be evaluated through parametric studies.

The electrochemical kinetic parameters are experimentally determined at reference conditions. In this study, the values measured by Springer *et al.* [30] and Bernadi *et al.* [23] are used. They are listed in Table 3.2.

In Table 3.3, the physical and thermal properties that are encountered in the mathematical model are summarized. These parameters can be easily found in common thermodynamic books and/or come with the commercialized materials in the specification sheets.

In addition, there are some variable parameters that are relevant to the cell operating condition, such as the operating pressure, temperature, gas flow rate, and relative humidity, etc. They are pertaining to a specific case study and, hence, will be provided in Chapter 5 along with the modeling results.

Table 3.1: Structural parameters.

Parameter	Value
Gas channel width, (mm)	1.0
Gas channel height, (mm)	1.0
Gas channel length, (mm)	50.0
Land width between two adjacent channels, (mm)	1.0
Thickness of CL, δ_{cl}, (μm)	10.0
Thickness of GDL, δ_{gdl}, (μm)	200.0
Thickness of membrane (Nafion112), δ_{mem}, (μm)	50.0
Porosity of CL, ϵ_{cl}	0.3
Porosity of GDL, ϵ_{gdl}	0.6
Volume fraction of Nafion membrane in CL, ϵ_m [130]	30 %
Fiber diameter of carbon paper (AvCarb GDL), d_0, (μm) [131]	7.5
Characteristic length of the void pore, $\bar{d}$, (μm) [66]	30.0
Pore surface area per unit volume, A_{pore}, (m^2/cm^3) [63]	20.0
Contact angle of the porous materials, θ_c, (^{o}) [57]	110.0
PTFE loading in GDL [63]	5-20 wt %

Table 3.2: Electrochemical kinetic parameters [23, 30]

Parameter	Value
Reference anodic exchange current, $aj_{a,0}^{\text{ref}}$ (A/m^3)	5.0E8
Reference cathodic exchange current, $aj_{c,0}^{\text{ref}}$ (A/m^3)	1.2E2
Reference hydrogen concentration, $c_{h_2,0}^{\text{ref}}$ (mol/m^3)	56.4
Reference oxygen concentration, $c_{o_2,0}^{\text{ref}}$ (mol/m^3)	3.39
Anodic transfer coefficient, α_a	0.5
Cathodic transfer coefficient, α_c	0.5
Anodic reaction order, β_a	0.5
Cathodic reaction order, β_c	1.0

3.8 Summary

The mathematical model developed in this thesis research accounts for all typical transport phenomena occurring within a PEM fuel cell. The complete set of governing equations consists of the conservation of mass, momentum and species for the gas phase, the conservation of species for dissolved water and liquid water, the conservation of electric charge, and the conservation of energy for all phases and species.

$$\frac{\partial}{\partial t}\left(\epsilon^{\text{eff}}\rho_g\right) + \nabla\cdot\left(\rho_g\vec{u}_g\right) = S_m \tag{3.124}$$

$$\frac{\partial}{\partial t}\left(\frac{1}{\epsilon^{\text{eff}}}\rho_g\vec{u}_g\right) + \nabla\cdot\left(\frac{1}{\left(\epsilon^{\text{eff}}\right)^2}\rho_g\vec{u}_g\vec{u}_g\right) = -\nabla P_g + \nabla\cdot\left(\overline{\overline{\tau}}\right) + S_u \tag{3.125}$$

Table 3.3: Physical and thermal parameters.

Parameter	Value	
Hydrogen diffusivity in water vapor, $D_{h_2-h_2o(g)}$ (m^2/s) [28]	9.15E-5	
Oxygen diffusivity in water vapor, $D_{o_2-h_2o(g)}$ (m^2/s) [28]	2.82E-5	
Oxygen diffusivity in nitrogen, $D_{o_2-n_2}$ (m^2/s) [28]	2.2E-5	
Water vapor diffusivity in nitrogen, $D_{h_2o(g)-n_2}$ (m^2/s) [28]	2.56E-5	
Oxygen diffusivity in liquid water, $D_{o_2-h_2o(l)}$ (m^2/s) [28]	2.4E-9	
Electrode conductivity, σ_s (S/m)	7.5E2	
Density of liquid water, ρ_l (kg/m^3) [132]	9.72E2	
Liquid water dynamic viscosity, μ_l (Pa s) [132]	3.517E-4	
Surface tension, σ (N/m) [57]	6.25E-2	
Henry's constant for oxygen, H_o (Pa m^3/mol) [47]	2.0E4	
Density of electrode, $\rho_{\text{gdl,cl}}$ (kg/m^3) [133]	2.2E3	
Density of membrane (Nafion), ρ_m (kg/m^3) [133]	1.98E3	
Density of hydrogen, ρ_{h_2} (kg/m^3) [132]	6.9E-2	
Density of air, ρ_{air} (kg/m^3) [132]	0.995	
Density of water vapor, ρ_v (kg/m^3) [132]	0.632	
Specific heat of electrode, $c_{p,\text{gdl}}$ ($J/kg \cdot K$) [133]	1.05E3	
Specific heat of hydrogen, c_{p,h_2} ($J/kg \cdot K$) [132]	1.44E4	
Specific heat of air, $c_{p,air}$ ($J/kg \cdot K$) [132]	1.01E3	
Specific heat of water vapor, $c_{p,v}$ ($J/kg \cdot K$) [132]	1.96E3	
Specific heat of liquid, $c_{p,l}$ ($J/kg \cdot K$) [132]	4.197E3	
Thermal conductivity of GDL, k_{gdl} ($W/m \cdot K$) [44]	$k^{xx} = k^{zz} = 10,\ k^{yy} = 1.3$	
Thermal conductivity of CL, k_{cl} ($W/m \cdot K$) [44]	0.8725	
Thermal conductivity of membrane, k_m ($W/m \cdot K$) [44]	0.445	
Thermal conductivity of hydrogen, k_{h_2} ($W/m \cdot K$) [132]	0.204	
Thermal conductivity of air, k_{air} ($W/m \cdot K$) [132]	0.03	
Thermal conductivity of water vapor, k_v ($W/m \cdot K$) [132]	0.023	
Thermal conductivity of liquid water, k_l ($W/m \cdot K$) [132]	0.67	
Condensation/evaporation latent heat, h_{fg} (J/kg) [132]	±2.308E6	
	Liquid water	Water vapor
Standard Entropy change, $\triangle S^{\text{ref}}$ ($J/mol \cdot K$) [3]	-163.25	-44.42
Entropy change at working conditions, $\triangle S$ ($J/mol \cdot K$) [3]	-149.142	-43.207
Standard Gibbs free energy change, $\triangle G^{\text{ref}}$ (J/mol) [3]	2.37E5	2.29E5

$$\frac{\partial}{\partial t}(\epsilon^{\text{eff}} C_i) + \nabla \cdot \left(-D_{i,m}^{\text{eff}} \nabla C_i\right) + \nabla \cdot (\vec{u}_g C_i) = S_i \tag{3.126}$$

$$\frac{\partial}{\partial t}(\epsilon_m C_d) + \nabla \cdot (-D_d \nabla C_d) + \nabla \cdot \left(\frac{n_d}{\mathscr{F}} \vec{J}_m\right) = S_d \tag{3.127}$$

$$\frac{\partial}{\partial t}(\epsilon \rho_l s) + \nabla \cdot \left[\left(-\frac{\rho_l K_{rl} K}{\mu_l} \frac{dP_c}{ds}\right) \nabla s + \frac{\rho_l \mu_g K_{rl}}{\mu_l K_{rg}} \vec{u}_g\right] = S_l \tag{3.128}$$

$$\nabla \cdot (-\sigma_s \nabla \phi_s) = S_\phi \tag{3.129}$$

$$\nabla \cdot (\sigma_m \nabla \phi_m) = S_\phi \tag{3.130}$$

$$\frac{\partial}{\partial t}\left(\sum_{k=g,s} (\epsilon \rho E)_k\right) + \nabla \cdot (\vec{u}_g (\rho_g E_g + P_g)) = \nabla \cdot \left[k^{\text{eff}} \nabla T - \left(\sum_i h_i \vec{N}_i\right) + (\overline{\overline{\tau}} \cdot \vec{u}_g)\right] + S_T \tag{3.131}$$

In total, 12 variables need to be determined. These equations are closely coupled through the RHS source terms, which either stem from the electrochemical reactions or from the interfacial mass transfer among different phases. The expressions for these source terms have been summarized in Tables 3.4.

A comprehensive inclusion of various transient transport phenomena and phase transfer processes has been achieved in this model including: the non-equilibrium phase transfer between the liquid water and water vapor (condensation/evaporation); the non-equilibrium membrane water sorption/desorption; water transport within the bulk membrane (membrane hydration/dehydration); liquid water transport in the porous backing layer; heat transfer; gas diffusion towards the reaction sites; and the convective gas flow in the gas channel.

The water production mechanism is clarified and it is shown that the water production during the ORR is in the dissolved phase. Another two commonly used water production assumptions (liquid water production and water vapor production) are also integrated into the current model formulation. Later in Chapter 6, comparisons will be made between these assumptions to show the potential error they may induce.

The non-equilibrium condensation/evaporation processes and membrane water sorption/desorption processes have been generally neglected in most of the previous modeling studies, owing to a lack of experimental data and understanding of the phase transfer mechanism. However, these phase transfer processes are crucial in evaluating the dynamic performance of PEM fuel cells and, hence, have been incorporated into the current model with two newly developed submodels.

In addition, the boundary and initial conditions, along with the modeling parameters are stated.

Table 3.4: Source terms in conservation equations.

	S_m	S_u	S_i	S_l	S_d	S_ϕ	S_T
Channel	0	0	0	0	0	0	0
Electrode	S_v	$-\frac{\mu_g}{K}\vec{u}_g$	$S_v = -\frac{S_{vl}}{M_w}$	S_{vl}	0	0	$\frac{J_s^2}{\sigma_s} + S_{vl}h_{fg}$
ACL	$S_{h_2} + S_v$	$-\frac{\mu_g}{K}\vec{u}_g$	$S_{h_2} = -\frac{\mathcal{R}_a}{2\mathscr{F}}$ $S_v = -\frac{S_{vl}}{M_w} - S_{vd}$	S_{vl}	S_{vd}	$\mathcal{R}_a$	$\eta_a\mathcal{R}_a + \frac{J_s^2}{\sigma_s} + \frac{J_m^2}{\sigma_m} + S_{vl}h_{fg} + M_wS_{vd}h_{m,fg}$
CCL	$S_{o_2} + S_v$	$-\frac{\mu_g}{K}\vec{u}_g$	$S_{o_2} = -\frac{\mathcal{R}_c}{4\mathscr{F}}$ $S_v = \begin{cases} vp: & -\frac{S_{vl}}{M_w} + \frac{\mathcal{R}_c}{2\mathscr{F}} \\ lp: & -\frac{S_{vl}}{M_w} \\ dp: & -\frac{S_{vl}}{M_w} \end{cases}$	$\begin{cases} vp: & S_{vl} - M_wS_{ld} \\ lp: & S_{vl} - M_wS_{ld} + \frac{M_w\mathcal{R}_c}{2\mathscr{F}} \\ dp: & S_{vl} - M_wS_{ld} \end{cases}$	$\begin{cases} vp: & S_{ld} \\ lp: & S_{ld} \\ dp: & S_{ld} + \frac{\mathcal{R}_c}{2\mathscr{F}} \end{cases}$	$\mathcal{R}_c$	$\left(\left\lvert\frac{(T\triangle S)}{4\mathscr{F}}\right\rvert + \eta_c\right)\mathcal{R}_c + \frac{J_s^2}{\sigma_s} + \frac{J_m^2}{\sigma_m} + S_{vl}h_{fg} + M_wS_{ld}(h_{m,fg} - h_{fg})$
Membrane	0	-10^{30}	0	0	0	0	$\frac{J_m^2}{\sigma_m}$

vp: vapor production; *lp*: liquid production; *dp*: dissolved production.

Chapter 4

Numerical Implementation

As shown in the previous chapter, some coefficients of the governing equations in PEM fuel cell systems are functions of variables, and the source terms of these equations originate from electrochemical reactions and/or phase changes. The electrochemical reaction is mathematically described by a so-called *Butler-Volmer* equation which is an exponential function of the reaction overpotential, while the phase changes are depending highly on the local temperature and water transport in all three phases (vapor, liquid and dissolved). Consequently, a comprehensive PEM fuel cell model is highly nonlinear and very stiff, and effective numerical techniques are usually required to solve such a system. In this chapter, the numerical implementation and some techniques developed in this thesis research for a general PEM fuel cell model will be illustrated.

4.1 Numerical Procedure

A structured non-uniform grid scheme (more details will be given in Section 4.3) is employed in this study which is built with a pre-processing software, GAMBIT 2.3. Then, the grid is imported into a finite volume based commercial software, FLUENT 6.3, where the complete equation set (Equation (3.124)-(3.131)) is discretized and solved. However, FLUENT does not have built-in modules for the non-standard governing equations for charge, dissolved water and liquid water. Thus, four user-defined scalar (UDS) equations have been defined for the electronic potential, protonic potential, dissolved water concentration and liquid water saturation, respectively. Moreover, various source terms, model parameters, empirical correlations, material properties, and boundary conditions were coded using the programming language C in terms of the user defined functions (UDF). In addition, some controlling strategies and under-relaxation schemes were also developed with UDFs. A complete list of the UDFs used in this study have been summarized in Appendix A.

The pressure-based segregated solver of FLUENT has been tested to be the best solver choice in terms of convergency and computational speed for the current

model and, hence, has been exclusively used for all studies presented in this thesis. By using the segregated solver, the individual governing equations for the variables (e.g., u, v, w, p, C_{h_2}, C_{o_2}, C_{h_2o}, C_d, s, ϕ_s, ϕ_m, T, etc.) are solved sequentially. Each governing equation, while being solved, is "decoupled" or "segregated" from other equations. The constraint of mass conservation on the velocity field is achieved by solving a pressure correction equation. The pressure equation is derived from the continuity and the momentum equations in such a way that the velocity field, corrected by the pressure, satisfies the continuity. Specifically, the SIMPLE algorithms is used for steady state simulations and the PISO algorithm is used for transient simulations in this thesis. The PISO algorithm uses a little more CPU time per iteration than the SIMPLE/SIMPLEC algorithms since two additional corrections are performed, but it dramatically decreases the number of iterations required for convergence and the total computational time can be greatly reduced for transient problems.

Since the governing equations are nonlinear and coupled to one another, the solution loop must be carried out iteratively in order to obtain a converged numerical solution. This loop is usually referred to as the outer loop. Solution of individual equations also involves iterations and it is usually referred to as the inner loop.

4.1.1 Outer Loop

The steps of the outer loop are illustrated in Figure 4.1 and outlined below:

1. Initialize the flow field.
2. Update fluid properties (e.g, density, diffusivity, conductivity, specific heat), based on the current solution.
3. Solve the momentum equations, one after another, using the recently updated values of pressure and face mass fluxes.
4. Solve the pressure correction equation, using the recently obtained velocity field and the mass-flux.
5. Correct face mass fluxes, pressure, and the velocity field, using the pressure correction obtained from Step 4.
6. Solve the equations for additional scalars, such as energy, species, charge, dissolved water, and liquid saturation, using the current values of the solution variables.
7. Update the source terms arising from the interactions among different phases.
8. Check for the convergence of the equations.

The loop continues until the convergence criteria are met.

4.1.2 Inner Loop

In the inner loop, the individual governing equations are discretized and solved. Discretization of the governing equations can be illustrated most easily by con-

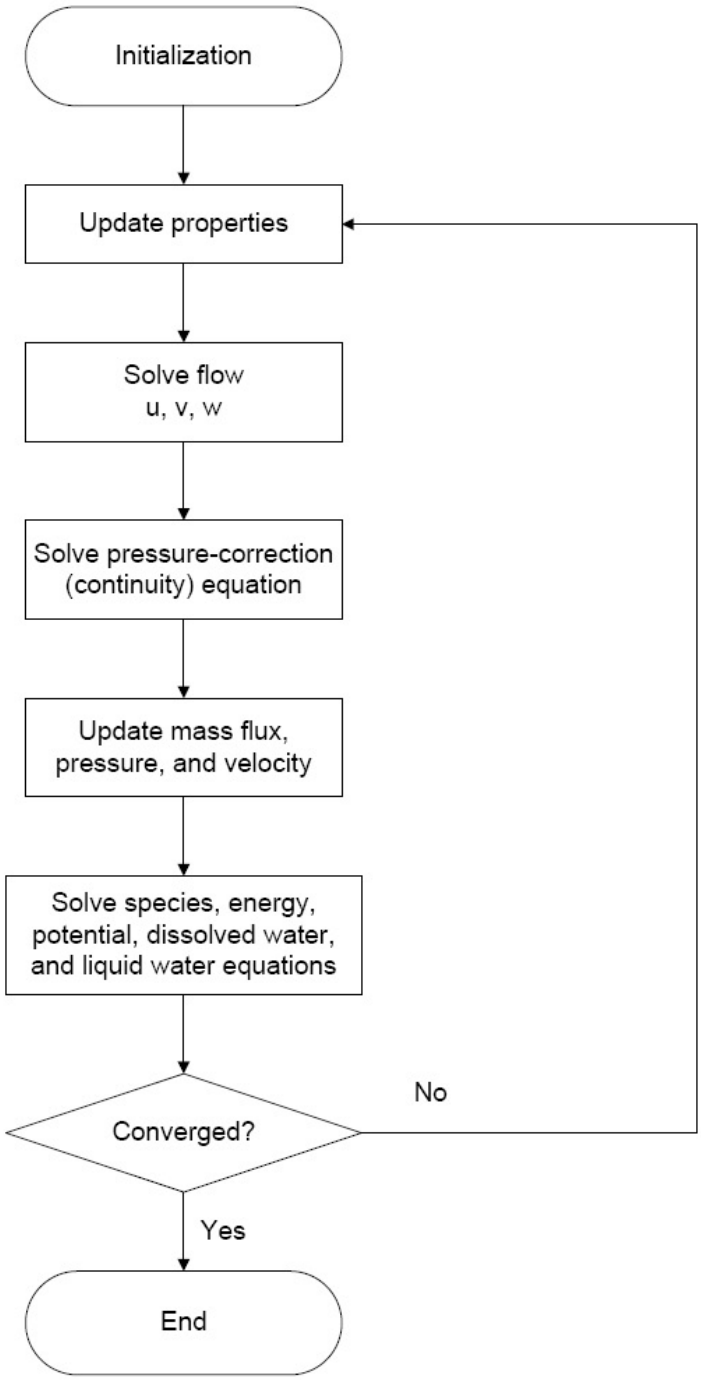

Figure 4.1: Illustration of the solution procedure of the segregated solver.

sidering the unsteady conservation equation for the transport of a scalar quantity Θ. This is demonstrated by the following equation written in integral form for an arbitrary control volume V

$$\int_V \frac{\partial \rho \Theta}{\partial t}\, dV + \oint \rho \Theta \vec{v} \cdot d\vec{A} = \oint \Gamma_\Theta \nabla \Theta \cdot d\vec{A} + \int_V S_\Theta \, dV, \tag{4.1}$$

where ρ denotes the density, $\vec{v}$ the velocity vector, $\vec{A}$ the surface area vector, Γ the diffusion coefficient, and S_Θ the source of Θ per unit volume.

Discretization of Equation (4.1) on a given cell yields

$$\frac{\partial \rho \Theta}{\partial t}\, V + \sum_f^{N_{\text{faces}}} \rho_f \vec{v}_f \cdot \vec{A}_f = \sum_f^{N_{\text{faces}}} \Gamma_\Theta \, \nabla \Theta_f \cdot \vec{A}_f + S_\Theta \, V. \tag{4.2}$$

The above discretized transport equation contains the unknown variable Θ at the cell center as well as the unknown values in surrounding neighbor cells. This equation will, in general, be non-linear with respect to these variables.

Next, an appropriate discretization scheme is chosen to convert the above equation into a linearized form

$$a_P \, \Theta = \sum_{\text{nb}} a_{\text{nb}} \Theta_{\text{nb}} + b, \tag{4.3}$$

where nb denotes the neighboring nodes, p denotes the central nodes at which variables are being evaluated, a is the linearized coefficient, and b is a general source term.

Similar equations can be written for each cell in the computational grid. Finally, the linearized algebraic equations result in a sparse coefficient matrix and it is solved using an implicit Gauss-Seidel linear equation solver in conjunction with an algebraic multigrid (AMG) method [110].

Discretization Schemes

For the continuity equation (Equation (3.124)), a second-order upwind scheme is used for the discretization of density; while for the face pressure which appears in the linearized momentum equation (Equation (3.125)), it is evaluated based on a standard linear interpolation of the adjacent node values. For other convection-diffusion alike equations (Equation (3.126)-(3.131)), the diffusion term is discretized with a central difference approach which is naturally of second-order accuracy. Since the flow in the porous backing layer is not aligned with the grids, a second-order upwind scheme is chosen for the convective terms to reduce numerically induced diffusion errors. The time derivative is discretized using a backward difference scheme which is first-order accurate. Furthermore, the whole equation is evaluated in an implicit manner at each time step. Hence, it is unconditionally stable with respect to time step size.

4.1.3 Under-relaxation Schemes

The above specifications are still not enough to handle the stiffness of the PEM fuel cell system, especially when the multi-phase water transport is taken into consideration. In fact, the diffusivity of the liquid saturation equation is a highly nonlinear function of the saturation itself (refer to Equation (3.128)). The liquid saturation is very close to zero in most of the regions, which makes the saturation equation extremely stiff. A similar issue arises for the dissolved water equation (Equation (3.127)), but it is a less severe matter compared to the saturation equation. In this thesis research, two kinds of under-relaxation techniques have been developed to tackle such stiffness difficulties.

In the first kind of under-relaxation, the source terms and intermediate variables that are evaluated by other equations are under-relaxed in an explicit manner

$$S_\Theta^n = S_\Theta^{n-1} + \alpha \left(S_\Theta^{\text{new}} - S_\Theta^{n-1} \right), \tag{4.4}$$

$$\Psi^n = \Psi^{n-1} + \alpha \left(\Psi^{\text{new}} - \Psi^{n-1} \right). \tag{4.5}$$

Here, α is the under-relaxation factor which ranges from 0 to 1, $()^{n-1}$ is the solution from the previous iteration, and $()^{\text{new}}$ is the solution from the current iteration. As such, the new solution is stabilized based on a Gauss-Seidel type successive under-relaxation (SUR). This kind of under-relaxation technique has been deployed for the inner loop which solves individual linearized algebraic equations.

The second type of under-relaxation, known as the implicit relaxation of the equation, is performed on the outer loop which couples all equations together, as follows

$$\frac{a_p \Theta^n}{\alpha} = \sum_{nb} a_{nb} \Theta_{nb}^n + b + \frac{1-\alpha}{\alpha} a_p \Theta^{n-1}. \tag{4.6}$$

This kind of under-relaxation was proposed by Patankar [134]. The main idea of this technique is to limit the change in each variable from one outer iteration to the next, because a change in one variable changes the coefficients in the other equations, which may slow or prevent convergence.

It is found that the second kind of under-relaxation is more crucial for the present model, especially for the highly nonlinear saturation equation where an extremely small under-relaxation factor ($\alpha = 0.0001$) has to be used at an early stage of iterations so as to avoid divergence. As the solution reaches a certain level of stabilization, this factor can then be increased to a more aggressive value to speed up the convergence. The same procedure is repeated many times until a converged solution is achieved. Typically, an increase in the under-relaxation factors entails a slight increase in the residuals, but these increases usually disappear as the solution progresses, as shown in Figure 4.2.

It may be worthwhile to mention that the above illustrated under-relaxation techniques can also be applied to PEM fuel cell models that have additional transport considerations or geometric domains. For example, a cold start model based

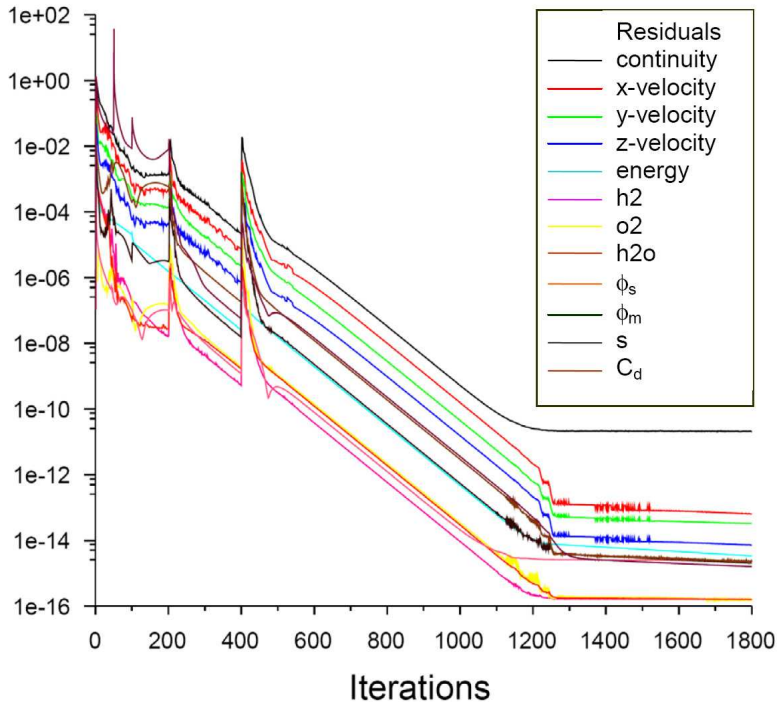

Figure 4.2: Convergence history of a typical steady state run.

on these techniques has been recently built in our group by adding extra equations regarding ice and non-frozen water; a 3D model includes CO poisoning effects is another ongoing effort. Moreover, these numerical techniques should be applicable to other finite volume based software or in-house codes as well.

4.2 Convergence Criteria

At the end of each outer iteration, the residuals for each of the conserved variables are computed and the computation stops when all residuals are below the convergence criteria. For the segregated solver of FLUENT, the residual is defined as

$$R^{\Psi} = \frac{\sum_{\text{cells}} |\sum_{\text{nb}} a_{\text{nb}} \Psi_{\text{nb}} + b - a_P \Psi_P|}{\sum_{\text{cells}} |a_P \Psi_P|} \tag{4.7}$$

It represents the summation of imbalance in Equation (4.3) scaled by a factor representative of the flow rate of Ψ through the domain.

The convergence history of a typical steady state run of the current model has been demonstrated in Figure 4.2. As can be seen, a fully converged solution is achieved after about 2300 iterations with the residuals all dropping below 1×10^{-12}. In fact, residuals of 1×10^{-8} are sufficiently accurate, including solution errors of all variables are less than 0.1%. This has been defined as the convergence criteria in this study.

4.3 Grid-Independent Solution

The dominating source of error involved in the numerical simulation resides in the discretization process during which the continuous conservation equations are casted onto discrete grid points. Theoretically, an exact solution can be achieved when the grid size is infinitely small. In practice, however, for the consideration of computational expense it is always desirable to limit the number of grid points to as few as possible. This is usually achieved through a grid independent study.

Stringent numerical tests were performed in this study to ensure that the solutions are independent of grid size. The final mesh is illustrated in Figure 4.3. To simplify the testing process, the same *number of grid points* in the y direction and the same *grid size* in the x and z directions are used for all layers of the fuel cell. Notice that the width (x-direction) of the gas channel is half that of other layers

$$N^x_{\text{mem}} = N^x_{\text{cl}} = N^x_{\text{gdl}} = 2N^x_{\text{ch}}, \tag{4.8}$$

$$N^y_{\text{mem}} = N^y_{\text{cl}} = N^y_{\text{gdl}} = N^y_{\text{ch}}, \tag{4.9}$$

$$N^z_{\text{mem}} = N^z_{\text{cl}} = N^z_{\text{gdl}} = N^z_{\text{ch}}, \tag{4.10}$$

where mem, cl, gdl, and ch denote the membrane, catalyst layer, gas diffusion layer, and gas channel, respectively; and N^x, N^y, and N^z denote the number of grid points in the x, y, and z directions, respectively. The total number of computational cells, N_{total}, is calculated as

$$N_{total} = \sum_{layers} N^x N^y N^z = 6N^x N^y N^z \tag{4.11}$$

Determination of the number of grid points in each direction (N^x, N^y, and N^z) was conducted in three steps. During each step, the number of grid points is only varied in one direction while the number along the other two directions were fixed. For the first step, the number of grid points in the x and z directions were fixed ($N^x = 20$ and $N^z = 50$), while the number of grid points in the y direction (N^y) was varied in a series as shown in Table 4.1.

Table 4.1: Grid independent study in the y-direction with $N^x = 20$ and $N^z = 50$.

Case:	1	2	3	4	**5**	6	7	8
N^y:	5	6	8	10	**15**	20	25	40 (uniform)

The solution variables change significantly in the through plane direction (y-direction) since the length scales in that direction are much smaller than the other two directions for most of the cell regions. For such scenarios, non-uniform grid schemes are usually used as far as the grid economy and efficiency are concerned. In this study, a double sided non-uniform grid scheme with an increasing factor of

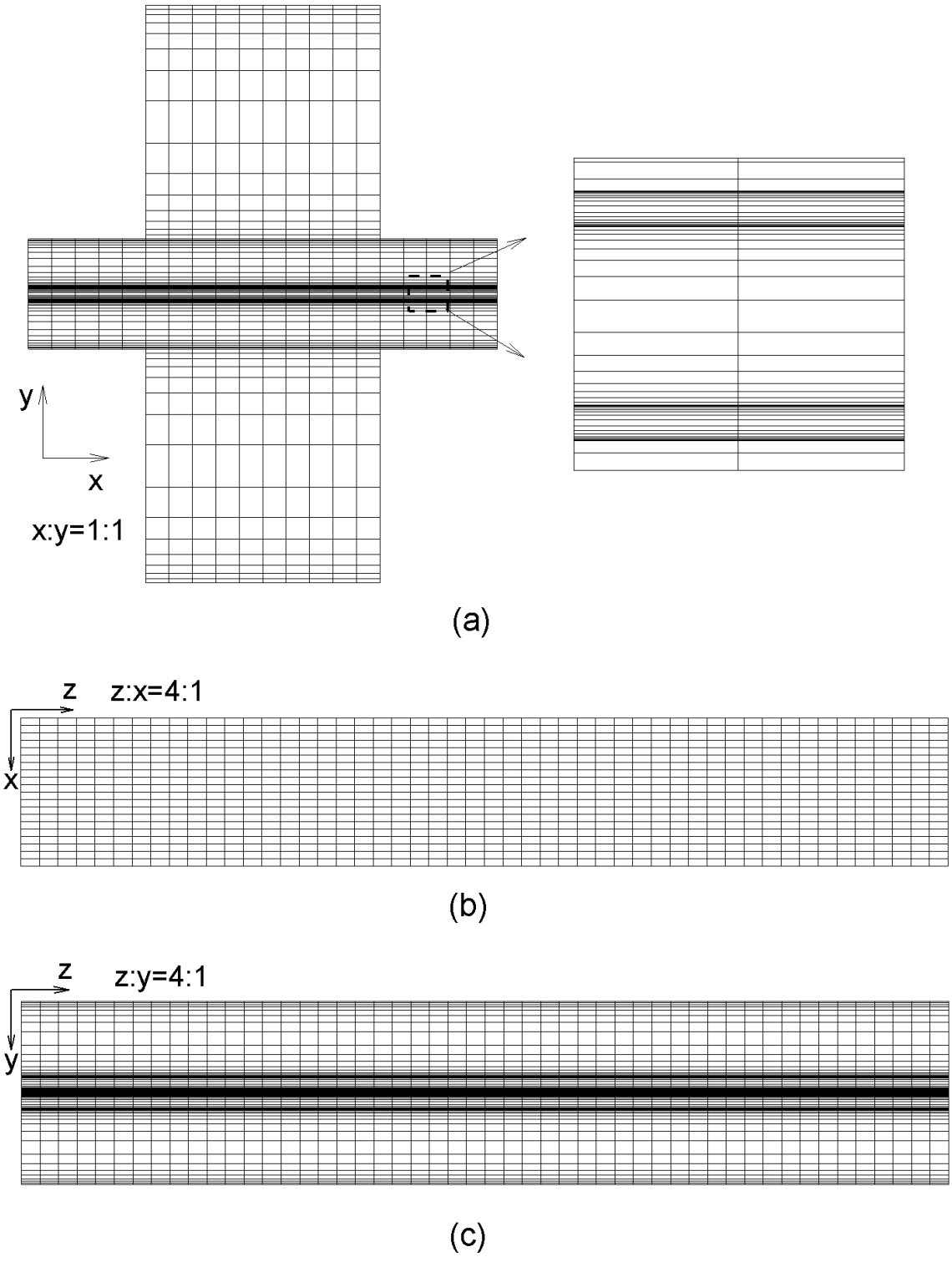

Figure 4.3: Demonstration of the grid scheme for the single-channel cell model: (a) x-y plane, (b) scaled x-z plane, and (c) scaled y-z plane.

1.4 was deployed in the y-direction (refer to Figure 4.3) for Case 1 to Case 7. In addition, a uniform grid scheme is investigated in Case 8 for comparison purposes.

It is found that the model quickly diverges when N^y is below or equal to 5 since the discretization error becomes too large and the solution is very likely oscillating and diverging. On the other hand, it also fails to achieve a converged solution when the non-uniform grid number is beyond 25. This is probably due to the increasingly high grid aspect ratio which tends to impair the stability of the system. Therefore, $N^y = 25$ has been referred to as the "exact solution" and the relative errors induced in other cases are defined accordingly as

$$\mathrm{Err}^{\mathrm{y}} = \left| \frac{\Theta_{\mathrm{N}^{25}} - \Theta_{\mathrm{N}^{\mathrm{y}}}}{\Theta_{\mathrm{N}^{25}}} \right| \times 100\%, \tag{4.12}$$

where Θ represents the variables to be compared.

In Figure 4.4, the effect of N^y on the error of average current density is demonstrated. It is seen that as long as the non-uniform grid scheme is used, the precision of the solution increases with the grid number. The error is approximately 1.88% for $N^y = 15$, which is even more accurate than the uniform grid scheme (with $N^y = 40$) which has an error of 2.57%.

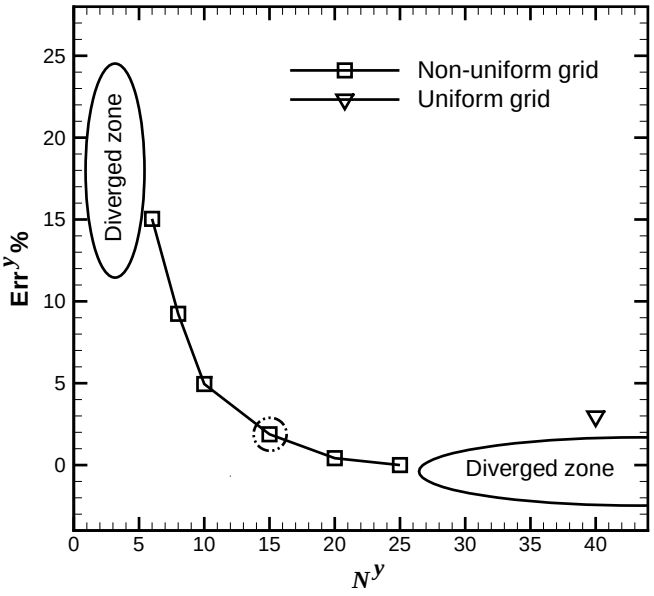

Figure 4.4: Effect of N^y on the error of average current density.

The effects of N^y on the computational expenses are also investigated and the results are shown in Figure 4.5 & 4.6. Figure 4.5 shows that the time required per 100 iterations almost linearly increases with N^y, regardless of uniform or non-uniform grid scheme; while Figure 4.6 indicates that the number of iterations required for

a converged state-state simulation is more significantly affected by N^y. This is probably also due to the increased grid aspect ratios.

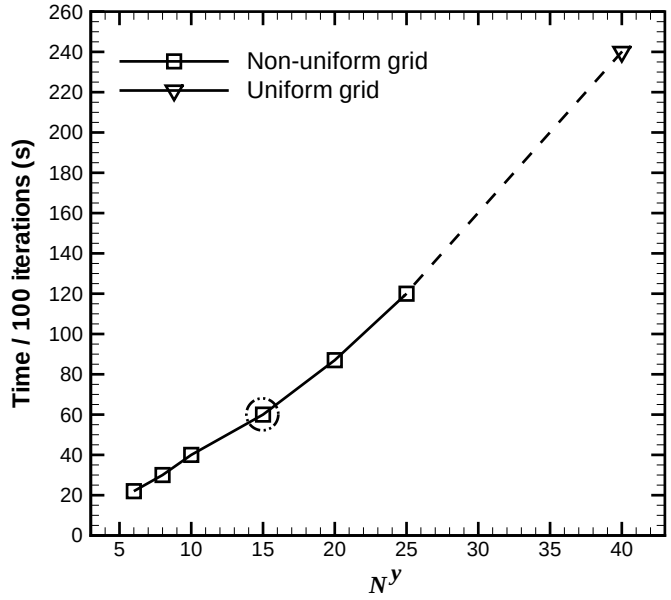

Figure 4.5: Effect of N^y on the computational time.

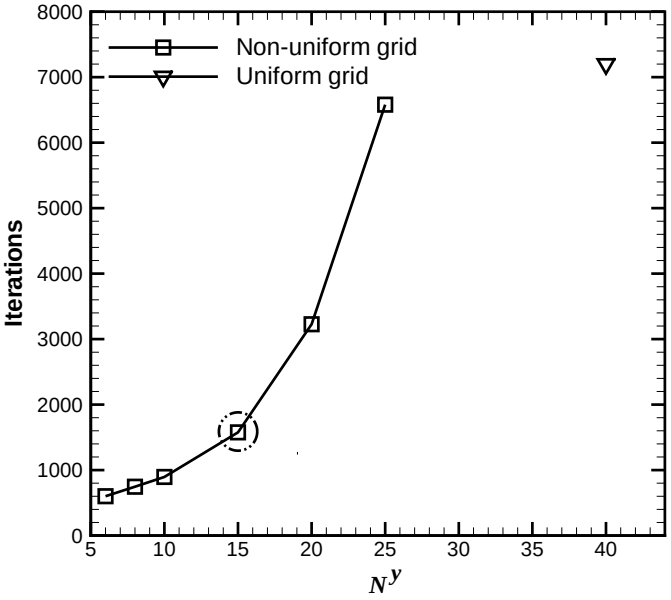

Figure 4.6: Effect of N^y on the number of iterations required for convergence.

Taking into account all three figures (Figure 4.4-4.6) regarding the grid independent study, it is seen that Case 5 ($N^y = 15$) presents the best performance in terms of system stability and computational expenses, while its solution precision (1.88%) is reasonably ensured. For example, it saves as much as 8 times computational time when compared to Case 7. This can be considered as a tremendous advantage, especially for transient simulations.

In the second and third steps, the values of N^x and N^z for a grid independent solution are determined in a similar manner as in the first step, thus the procedures are not repeated here. Generally speaking, the model is much less sensitive to the grid numbers on the x and z directions and relatively coarse uniform grid schemes with $N^x = 20$ and $N^z = 50$ are found to be sufficient in these directions. The corresponding solution errors in the x and z directions are $\mathrm{Err^x} = 0.49\%$ and $\mathrm{Err^z} = 0.009\%$, respectively. Consequently, the total error for the final mesh is roughly estimated as

$$\mathrm{Err} \leq \sqrt{|\mathrm{Err^x}|^2 + |\mathrm{Err^y}|^2 + |\mathrm{Err^z}|^2} = 1.94\%. \tag{4.13}$$

Now, the total number of control volumes for a single channel geometry can be calculated using Equation (4.3)

$$N_{total} = 6 \times 15 \times 20 \times 50 = 90,000 \tag{4.14}$$

For the multi-channel model, the meshes at the end of the gas channel and those underneath the MEA are further refined in order to resolve the complex flow behavior around the corner. Therefore, the total number of control volumes for each single channel-related geometry is actually larger than the value estimated above. Two sample meshes around the channel bend of the multi-channel model are demonstrated in Figure 4.7.

4.4 Time Step Independent Solution

Apart from the determination of the grid points, selection of the time step is also essential for transient simulations. If the time step is too small, the computational expense may be too high; if the time step is too large, the solution accuracy may not be acceptable. In this study, an adaptive time stepping algorithm is adopted, which is based on the estimation of the truncation error associated with the time integration scheme [110], and it is able to automatically determine the time step as the calculation proceeds. Consequently, solution accuracy is ensured along with the optimum computational expense.

The shortest time scale in the current model is associated with the gas species transport, which is on the order of 10^{-2} to a few seconds depending on the flooding status of the GDL [94]. Numerical tests with respect to various time step choices

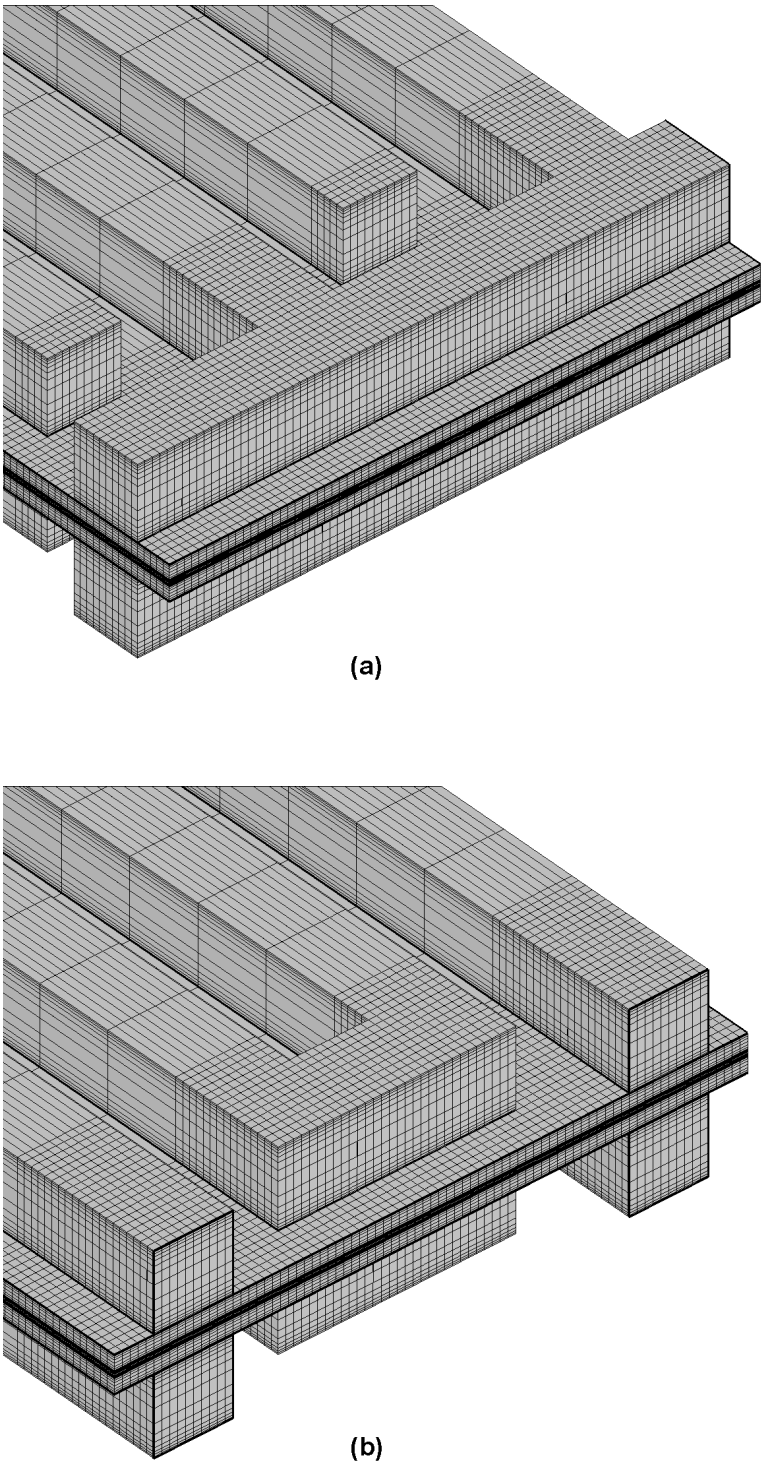

Figure 4.7: Locally refined mesh around the corner of the gas flow channel (a) interdigitated channel, (b) serpentine channel.

were performed and the results show that a minimum time step of 10^{-4} s is able to deliver sufficient resolution on all transient transport processes. Thus, 10^{-4} s has been defined as the lower limit of the adaptive time step range. Furthermore, a maximum time step size of 1 s is set as the upper limit.

4.5 Summary

In this chapter, an in-depth explanation of the numerical implementation and some techniques developed in this thesis research for a general PEM fuel cell model have been presented. This numerical scheme has demonstrated superior performance when handling the stiffness of the PEM fuel cell system.

Stringent numerical tests were performed to ensure that the solutions were independent of grid size. It is found that the number of grid points in the through plane direction (y-direction) dominates the solution precision and model stability as compared to these of the in-plane direction (x-direction) and along-channel direction (z-direction). Moreover, it is found that coarsening or refining of the mesh may both lead to divergence. The former is mainly due to the increased discretization error, while the latter is more likely due to the increased cell aspect ratio.

Chapter 5

Results and Discussion – Part I: Single-Channel Model

With the mathematic model and the computational mesh scheme presented in the previous chapters, extensive numerical simulations have been conducted to investigate the dynamic response characteristics of the PEM fuel cells and the transient transport phenomena within the cells. Two kinds of model geometries, a single-channel model and a multi-channel model, have been studied. The transient simulation is very time consuming and, hence, has been carried out only with the singe-channel model; while the multi-channel model is mainly investigated with steady-state simulations to show the effects of different flow field designs on the gas and liquid flow behavior, and on the overall cell performance.

In this chapter, the results from the single-channel model are presented. Firstly, the computation domain of the single-channel model is given. Then, several approaches that are widely used in the literature are examined and the pros and cons associated with them are addressed. With the optimized model, the dynamic responses of a PEM fuel cell with respect to some typical operating condition changes are demonstrated, and the transient transport phenomena within the PEM fuel cell are presented. The results from the multi-channel model will be presented in the next chapter.

5.1 Computational Domain

For the single-channel model, only half of the cell domain needs to be modeled since the cell is symmetric with respect to the $y-z$ plane. However, a slight modification of the boundary conditions is required for the symmetry plane, where a symmetric B.C. in place of the interior should be used. All other boundary conditions remain the same as illustrated in Section 3.6.1. The final computational domain of the single-channel model is schematically shown in Figure 5.1.

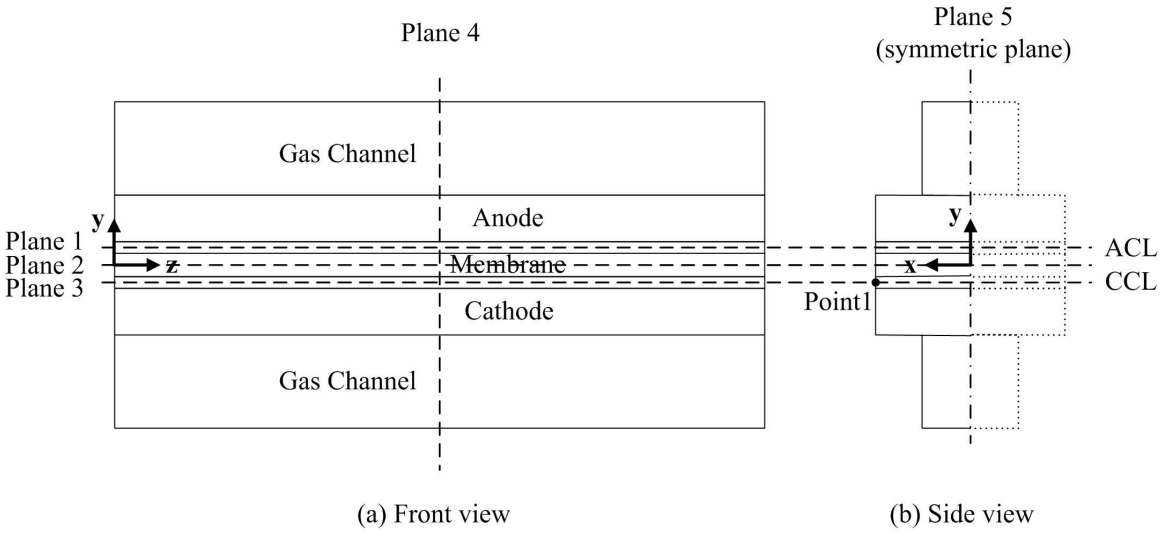

Figure 5.1: Schematic of the computational domain of the single-channel model.

In the present model, there are eight input parameters that can be varied to study different working conditions. They are the stoichiometric ratios ξ_a, ξ_c, inlet gas relative humidities RH_a, RH_c, inlet gas pressures P_a, P_c, cell temperature T_0, and cell output voltage, ϕ_{cell}. High stoichiometric flow ratios and gas pressures tend to increase the concentration gradient between the gas flow channel and the reaction site, resulting in enhanced reactants diffusion and cell performance. However, high stoichiometric ratios and pressures also lead to larger parasitic losses as one needs to pressurize the incoming gas even further. Therefore, the moderate stoichiometric ratios ($\xi_a = 1.2$, $\xi_c = 2$) and gas pressures ($P_a = P_c = 2$ atm), which are commonly used in the real experimental conditions, were used as the base case conditions in this study. In addition, many studies have shown that the optimum operating temperature for PEM fuel cells is around 80 °C (353 K). Therefore, the cell temperature is fixed at 353 K for all cases in this study. The operating conditions used in the base case study are summarized in Table 5.1.

Table 5.1: Operating conditions used in the base case study.

Parameter	Value
Cell output voltage, ϕ_{cell} (V)	0.65
Operating temperature, T_0 (K)	353.0
Gaseous pressure at the anode flow channel outlet, P_a (atm)	2.0
Gaseous pressure at the cathode flow channel outlet, P_c (atm)	2.0
Relative humidity of the anode side incoming gas flow, RH_a	100%
Relative humidity of the cathode side incoming gas flow, RH_c	100%
Stoichiometric ratio of the anode side incoming gas flow, ξ_a	1.2
Stoichiometric ratio of the cathode side incoming gas flow, ξ_c	2.0

In addition, there are two parameters being used to investigate the non-equilibrium

liquid/vapor phase transfer characteristics, namely the dimensionless condensation/evaporation rate coefficients Sh_c and Sh_e, and two parameters to study the non-equilibrium water sorption/desorption process, i.e. the sorption/desorption rate coefficients γ_a and γ_d. Using Equation (3.76) and the parameters listed in Table 3.1, the condensation/evaporation rates are evaluated to be in the range of 2.04E-3 to 2.45E-1. On the other hand, the sorption/desorption rates are dependent on the local membrane water content and temperature, as described in Equation (3.51)-(3.52). In Section 5.3, however, some commonly used constant sorption/desorption values are employed for comparison purposes. The phase transfer parameters are summarized in Table 5.2 with their values used in the base case highlighted.

Table 5.2: Range of phase change parameters used in the thesis.

Parameter	Value
Dimensionless condensation and evaporation rates, SH_{ce}	**2.04E-3** – 2.45E-1
Membrane sorption/desorption rates, γ_{ad} (1/s)	1.0/10.0/100.0
	Equation (3.51)-(3.52)

5.2 Model Validation

Firstly, the mathematical model is validated by means of the most popular criterion, the polarization curve. The polarization curves from two experimental voltammetry sweep studies along with the curve from the current model are show in Figure 5.2. In the study of Hamelin *et al.* [135], a Ballard fuel cell stack system Mark 5-E is investigated and a ramp sweep of the current output is conducted with a rate of current change of 4 A per 0.15 seconds; hydrogen is fully humidified and pressurized to 3 bar at the anode side, while the cathode side gas conditions are not explicitly mentioned. In the study of Yu *et al.* [136], the dynamic responses of a PEM fuel cell under partially dry operating conditions and a voltage sweep rate of 10 mV/s are investigated using a cell with a single meander-shaped channel and with 1 cm^2 active area. Same as Yu *et al.*, the numerical study is also carried out at partially humidified conditions with a voltage sweep rate of 10 mV/s. It can be easily seen that a hysteresis effect exists in both these experimental and numerical studies. Without any parameter fittings, the numerical model predicts the dynamic polarization curve and the hysteresis effect reasonably well as compared to the experimental data of Yu *et al.* Compared to the data of Hamelin *et al.*, a qualitatively good agreement on the hysteresis phenomena is also achieved, even two studies were operated with different conditions.

The current model is also validated against experimental data measured with an in-house developed PEM fuel cell. The material for the bipolar plate in experiments is a graphite plate grooved with a single serpentine channel with 52 branch channels. The MEA used is a three-layer combination of a PEM (Nafion-112) and catalyst

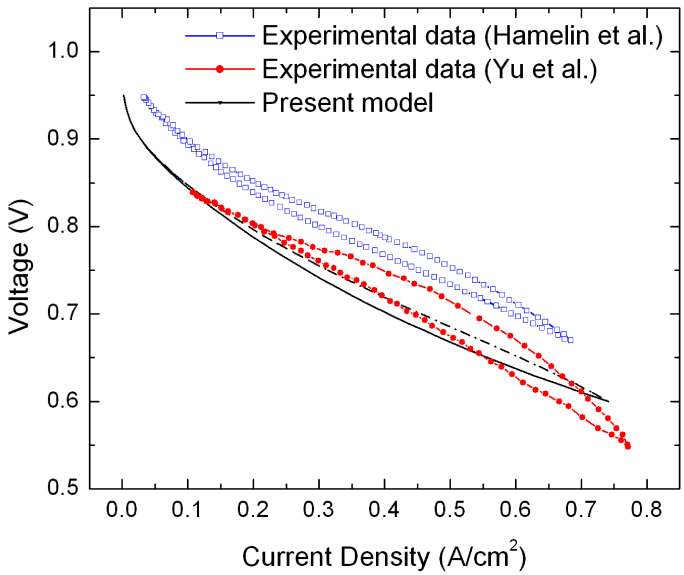

Figure 5.2: Model validation: hysteresis effect of the dynamic polarization curves during voltammetry sweep studies.

layers with a platinum content of 0.4 mg Pt/cm^2. The size of the MEA is 10×10 cm, that is, an effective reaction area of 100 cm^2. The anode side GDL is a SolviCore^{TM} GDL with a micro-porous layer, and the cathode side GDL is a SpectraCarb^{TM} 2050 GDL with customized 25% PTFE coating on the surface that facing the membrane. Both GDLs are 200 μm in thickness. In addition, a silicon seal is used between the bipolar plate and MEA to avoid of gas leakage, and a carbon paper is sandwiched between the bipolar plate and the copper collector plate to reduce the contact resistance.

The experiments were carried out under partially humidified conditions (50% relative humidity for both hydrogen and air streams), the back pressure is maintained at 2.0 atm, the stoichiometric ratios are set as 1.2 at the anode side and 2.0 at the cathode side, and the operating temperature is fixed at 80 ^oC. The cell dynamic responses with respect to two step changes on cell voltage were investigated and the results are shown in Figure 5.3. To validate the mathematical model, a specific case has been implemented with available operating and physical parameters that identical to the in-house made fuel cell prototype. However, it is found that the current density predicted by the current model is higher than that of the experimental data. A possible reason for this overestimation might because there are still some factors, such as thermal and electrical contact resistances, anisotropic structure of the real materials, compression effects, and some man-made factors, were not taken into account in the mathematical model. Therefore, in order to obtain the same current density as the experimental data, certain kind of parameter fitting is re-

quired. Follow the fitting procedure as illustrated by Baschuk [109], two parameters were fitted through a test and error shooting process. Specifically, the reference exchange current density is reduced from ($aj^{\text{ref}}_{a,0}$ = 5.0E8 A/cm^3, $aj^{\text{ref}}_{c,0}$ = 1.2E2 A/cm^3) to ($aj^{\text{ref}}_{a,0}$ = 1.0E7 A/cm^3, $aj^{\text{ref}}_{c,0}$ = 1.3E1 A/cm^3), and the electric conductivity of the carbon paper is reduced from 750 S/m to 620 S/m. With these new parameters, it is seen that the model agrees very well with the experimental results, as shown in Figure 5.3.

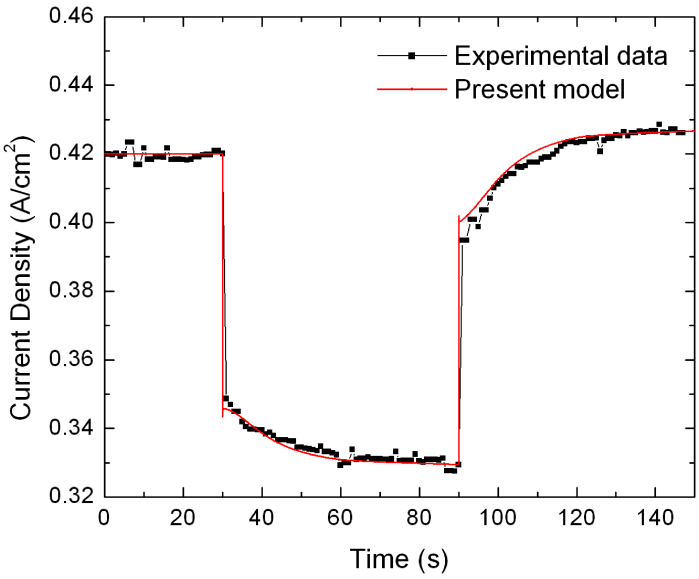

Figure 5.3: Model validation: cell dynamic response with respect to voltage changes (0.6 $\rightarrow$ 0.65 $\rightarrow$0.6 V) and under partially humidified conditions ($RH_{a,c}$ = 50%).

Figure 5.3 demonstrates that the present model is capable of predicting practical fuel cell operations with certain level of parameter fittings. In the rest of this thesis, however, no further parameter fittings were attempted. All parameters were kept the same as the data set that validated through the experimental data of Yu *et al.* [136].

5.3 Analysis of Several Traditional Modeling Approaches

The transport phenomena inside a PEM fuel cell are complex and many uncertainties related to electrochemical dynamics and transport behavior in micro-scale porous domains are still not fully understood and are undergoing active investigation. Accompanying this process, various modeling assumptions and approaches

have been proposed in the literature, some of which requires further investigation to confirm its validity, and this is the main focus of this section.

5.3.1 Boundary Conditions for Solid Potential

As indicated in Equation (3.122), boundary conditions (B.C.) for the electronic (solid phase) potential are specified at the surfaces of the anode and cathode that are exposed to the bipolar plate. In practice, there are two approaches to accomplish this and they are schematically shown in Figure 5.4.

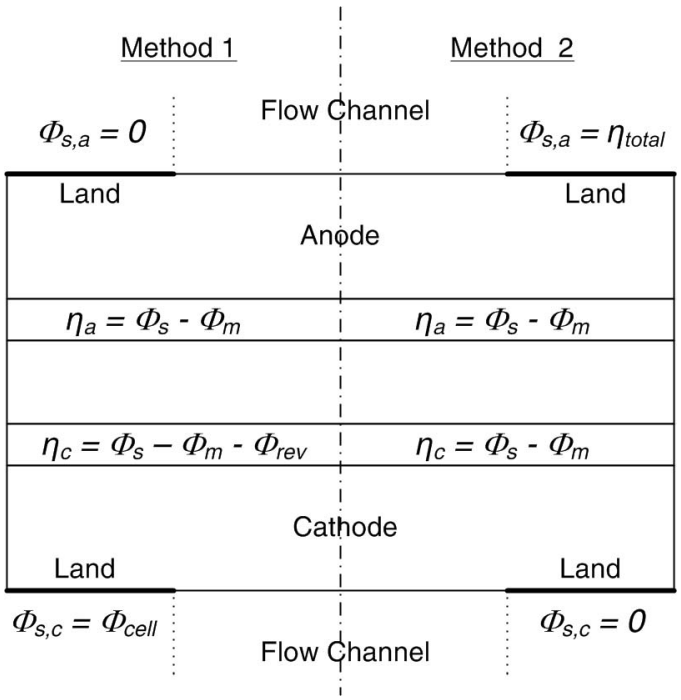

Figure 5.4: Schematic of two different methods in the specifications of boundary conditions for solid potential.

In the first approach (Method 1), the electronic potential at the upper surface of the anode is set at $\phi_{s,a} = 0$ for convenience, then the electronic potential at the cathode bottom surface equals the cell output voltage, i.e. $\phi_{s,c} = \phi_{cell}$. The over-potential in the ACL is simply the difference between the solid phase and membrane phase potentials, $\eta_a = \phi_s - \phi_m$, while the over-potential at the CCL is calculated as $\eta_c = \phi_s - \phi_m - \phi_{rev}$, where ϕ_{rev} is the theoretical reversible cell potential. It is calculated from the modified form of the Nernst equation by assuming that the overall cell reaction is at thermodynamic equilibrium [137]

$$\phi_{rev} = \frac{\triangle G^{\text{ref}}}{2\mathscr{F}} + \frac{\triangle S^{\text{ref}}}{2\mathscr{F}}\left(T - T^{\text{ref}}\right) + \frac{\mathscr{R}T}{2\mathscr{F}}\ln\left[\left(\frac{P_{h_2}}{P^{\text{ref}}}\right)\left(\frac{P_{o_2}}{P^{\text{ref}}}\right)^{1/2}\right]. \tag{5.1}$$

Here, $\triangle G^{\text{ref}}$ is the Gibbs free energy change and $\triangle S^{\text{ref}}$ the entropy change for the overall reaction at reference temperature, T^{ref}, and pressure P^{ref}. P_{h_2} and P_{o_2} are the partial pressure of hydrogen and oxygen, respectively.

In the second approach (Method 2), a zero electronic potential is set at the bottom surface of the cathode, i.e. $\phi_{s,c} = 0$, while at the top surface of the anode, the total cell potential loss η_{total} is imposed. It relates to the cell output voltage and reversible cell potential via $\eta_{total} = \phi_{rev} - \phi_{cell}$. In comparison, the second method of boundary condition specification is rarely used in the literature.

Both methods have been implemented in this study and it is found that there are no observable differences in the results between these two approaches, except for a constant off-set for the distribution of phase (solid & electrolyte) potential (ϕ_s, ϕ_m). Figure 5.5 shows the potential distribution on a line that crosses the membrane electrode assembly (MEA). Generally speaking, the potential distribution from Method 1 is more physically meaningful since it demonstrates the real potential distributions within the cell. In contrast, the potential distribution from Method 2 is more intuitive since it reveals in a straightforward manner the potential loss from each component of the cell.

Since both approaches are applicable, the issue of computational expense is of concern. Comparisons of the computational time by using two different B.C. specifications are performed for three cases and the results are summarized in Table 5.3. To ensure that the final conclusion is geometry and solver independent, the comparison is firstly made for a simplified 2D model (for more details, please see [129]) in Case-1, using a finite element based commercial software, COMSOL Multiphysics. Case-2 is simply the base case, a 3D domain with a single straight channel and it is solved in Fluent. In Case-3, parallel processing is conducted on a Beowulf cluster system with 8 CPUs, using Fluent. A full-size cell (25 cm^2) with 25 parallel channels is studied and the resulting mesh possesses about 2.2 million nodes. The results from all three cases indicate that the implementation of Method 1, the most popular B.C. specification in literature, is less efficient. For instance, assuming a typical parallel case that requires about 1000 iterations, using the Method 1 will waste about 3×8 CPU hours of computational time compared to Method 2.

Table 5.3: Comparison of computational time by implementing the two different methods in the specification of boundary conditions for the electronic potential.

	2D, Comsol (sec/case)	Base case (min/100 iter)	Parallel (min/100 iter)
Method 1	808	5.12	131.7
Method 2	733	4.48	114.3

The reason for the accelerated computation of Method 2 may lie in the initialization of the flow field. As shown in Figure 5.5, the potential varies in a relatively narrow range when using Method 2, thus the initial guess is comparatively more close to the final solution than that of Method 1. Moreover, it is found that Method

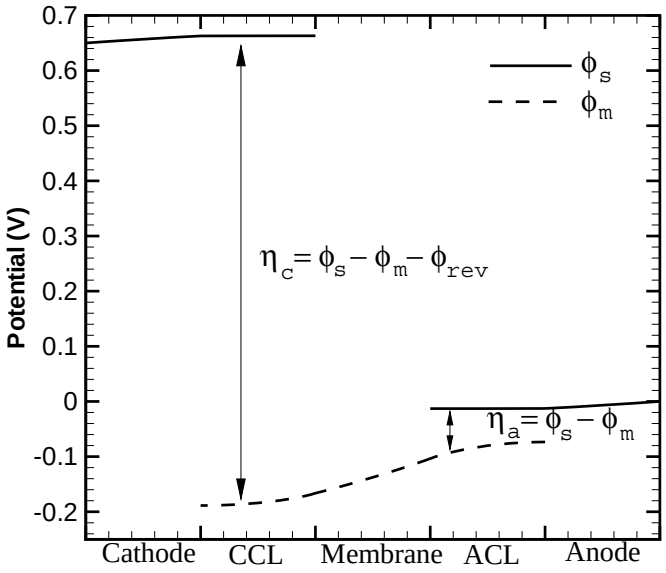

(a)

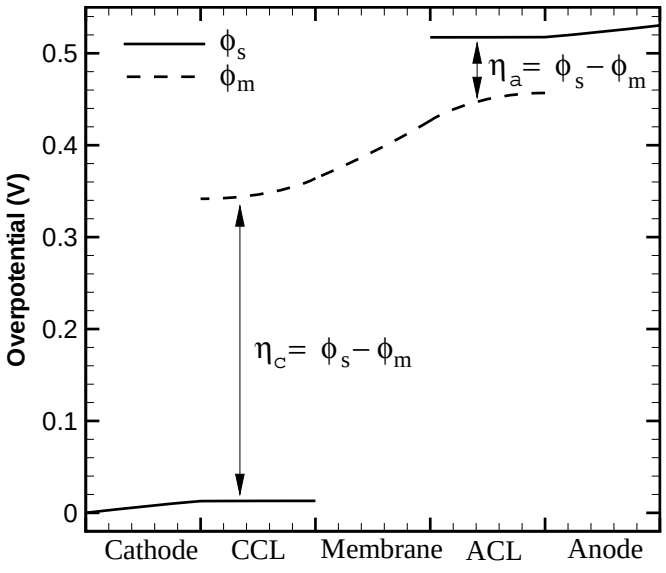

(b)

Figure 5.5: Phase potential distribution across the MEA (at $x = 3.75 \times 10^{-4}$ m and $z = 0.025$ m) for the boundary conditions specified by: (a) Method 1; (b) Method 2.

1 is more dependent on the initialization of the phase potential. It easily causes divergence if the initial guess is too far off from the final solution. In contrast, Method 2 is more tolerant towards the initialization process. Actually, no special care is required for the initialization of the solid phase potential. This may be treated as another advantage of Method 2.

5.3.2 Equilibrium vs. Non-equilibrium Water Sorption and Desorption Processes

Both equilibrium and non-equilibrium water sorption modeling has been conducted, using the approaches described in Section 3.3.3. For equilibrium sorption modeling, the flux of back diffusion is converted to source terms in both ACL and CCL as illustrated in Figure 3.4. Since the equilibrium model does not explicitly solve the dissolved water transport in the catalyst layer, all previous equilibrium models have assumed that the water production is either in the liquid or in the vapor phase. Therefore, to make the comparison more meaningful the water production of the non-equilibrium model is also assumed to be in the liquid phase in this subsection. Moreover, constant sorption/desorption rates that are commonly used in the literature are used in this subsection.

Figure 5.6 demonstrates the variation of membrane water content on a line that crosses the CCL-membrane-ACL. The difference in water content between the actual value (λ) and the equilibrium value (λ_e) in the CCL and ACL represents the driving force for membrane water desorption and absorption, respectively. For the equilibrium model, these values coincide. However, absorption and desorption still occurs, only it is instantaneously balanced. For zero sorption rate coefficients, however, absorption and desorption no longer takes place and the water dynamics decouple. In Figure 5.6(a), the absorption and desorption rate are assumed to be equal. It shows that the difference between λ_e and λ decreases with increasing water absorption/desorption rate. Finally, as the system reaches equilibrium at around $\gamma_{ad} = 100$ 1/s the water content distribution of the non-equilibrium model almost coincides with that of the equilibrium model. In Figure 5.6(b), two cases (line 2 & 4) with their absorption rate reduced to 1/10 of their desorption rate are investigated to simulate the second stage of the two-step dynamics of membrane sorption [101], as mentioned in Section 3.3.3. It is seen that for both cases (line 2 & 4) the water content difference between the actual and the equilibrium value decreases in the CCL but increases in the ACL compared to the cases corresponding to an equal rate for the sorption and desorption processes (line 1 & 3). This means that the water desorption in the CCL is accelerated but the water absorption in the ACL is slowed down in the second sorption stage, which agrees well with the experimental observations in [101].

As shown in Figure 5.6, the water content in the catalyst layer differs between the equilibrium and non-equilibrium approaches at the final equilibrium state. This is probably due to the mathematical conversion approximation of the equilibrium

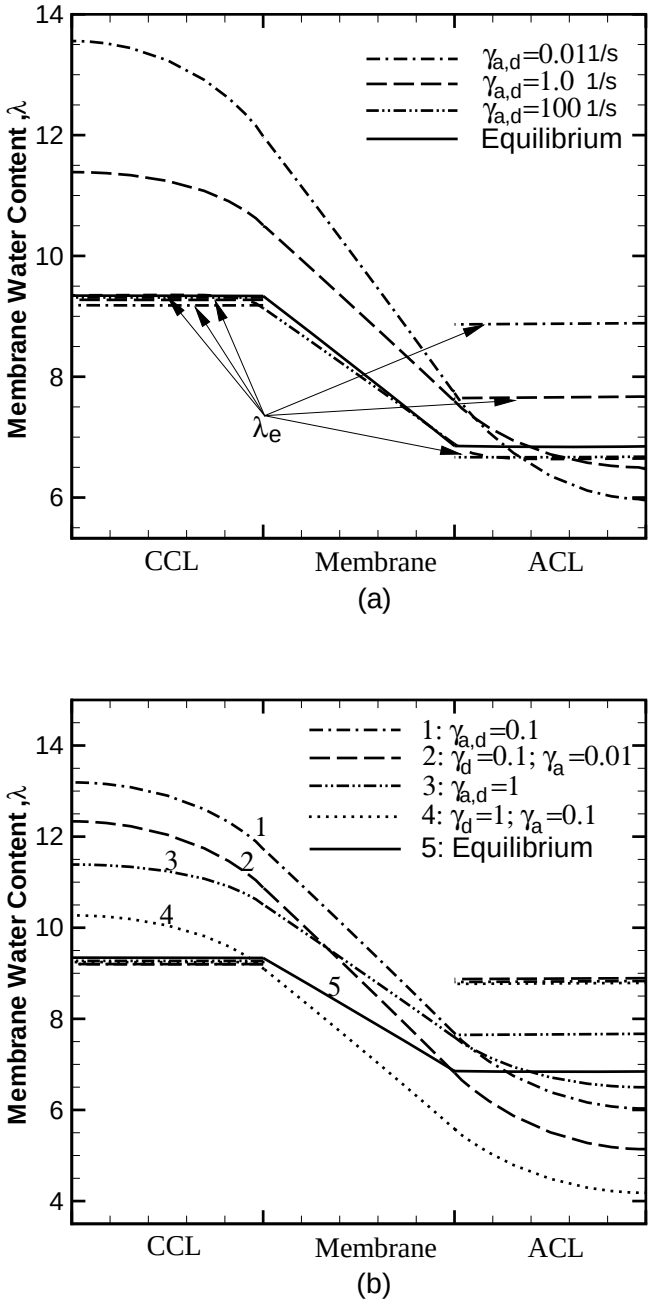

Figure 5.6: Distribution of the actual and the equilibrium membrane water content on a line across the anode catalyst layer (ACL)-membrane-cathode catalyst layer (CCL) (at $x = 3.75 \times 10^{-4}$ m and $z = 0.025$ m) for the membrane water sorption and desorption rate coefficient of γ_a and γ_d: (a) $\gamma_a = \gamma_d$; (b) $\gamma_a = 0.1\gamma_d$.

model, as discussed in Section 3.3.3. To better demonstrate the water content evolution with increasing sorption rate and to show the differences between the two approaches, 2D contour plots along the x-z cross section of the ACL are shown in Figure 5.7. It is seen that the actual water content (λ) increases along the flow direction at low sorption rates because the sorption resistance is relatively high at this stage and water tends more to back-diffuse from the cathode side. At high sorption rates or in the equilibrium model, however, the water content presents a parabolic-type distribution. It decreases first, owing to the electro-osmotic drag effect, then increases towards the outlet due to back diffusion. Comparing Figures 5.7(c) and (d), it clearly shows that once the sorption equilibrium is approached, the water content distribution in both models are quantitatively and qualitatively similar. Therefore, Figures 5.6 and 5.7 can be regarded as good numerical validations for both equilibrium and non-equilibrium models.

Figure 5.8 shows the transient variation of the cell current output during a step change in relative humidity from $RH = 1$ to $RH = 0.5$. The response time for the cell to reach 99% of its steady state value is about 20.9, 23.8, 25.4, and 42.2 seconds for the equilibrium model and for the non-equilibrium model with sorption rates of $\gamma_{ad} = 100, 10$, and 1 s^{-1}, respectively. Not surprisingly, the equilibrium model has the fastest response because one of the slowest transient processes, the membrane water sorption, is simply neglected when the equilibrium assumption is adopted. Therefore, Figure 5.8 underlines another large advantage of the non-equilibrium water sorption model, namely, the transient process of water sorption is accounted for explicitly.

5.3.3 Comparison of Water Production Mechanisms

As elucidated in Section 3.3.1, water is produced in the dissolved phase during the electrochemical reaction and, in principle, a small amount of water can be produced in the liquid phase. Nevertheless, water production can not be in the vapor phase for PEM fuel cells during normal operation. Regardless, we are going to compare three different water production mechanisms, namely, vapor, liquid and dissolved water production, and examine what potential error the vapor and liquid production assumptions may induce.

Basically, there are four main factors that have been considered in the current model to differentiate between different water production mechanisms. The first and most important factor comes from the water source terms as shown in Table 3.4. Secondly, since the entropy changes for vapor and liquid water production are different (refer to Table 3.3), the heat generation from the reversible electrochemical reaction, $\frac{T\triangle S}{4\mathscr{F}}$ (the first energy source term in the cathode catalyst layer as shown in Table 3.4), should be revised accordingly. The third difference among these assumptions has been implicitly accounted for by the latent heat generation or absorption during phase change, as shown in the energy source terms in Table 3.4. The last important factor comes from the determination of the reversible cell

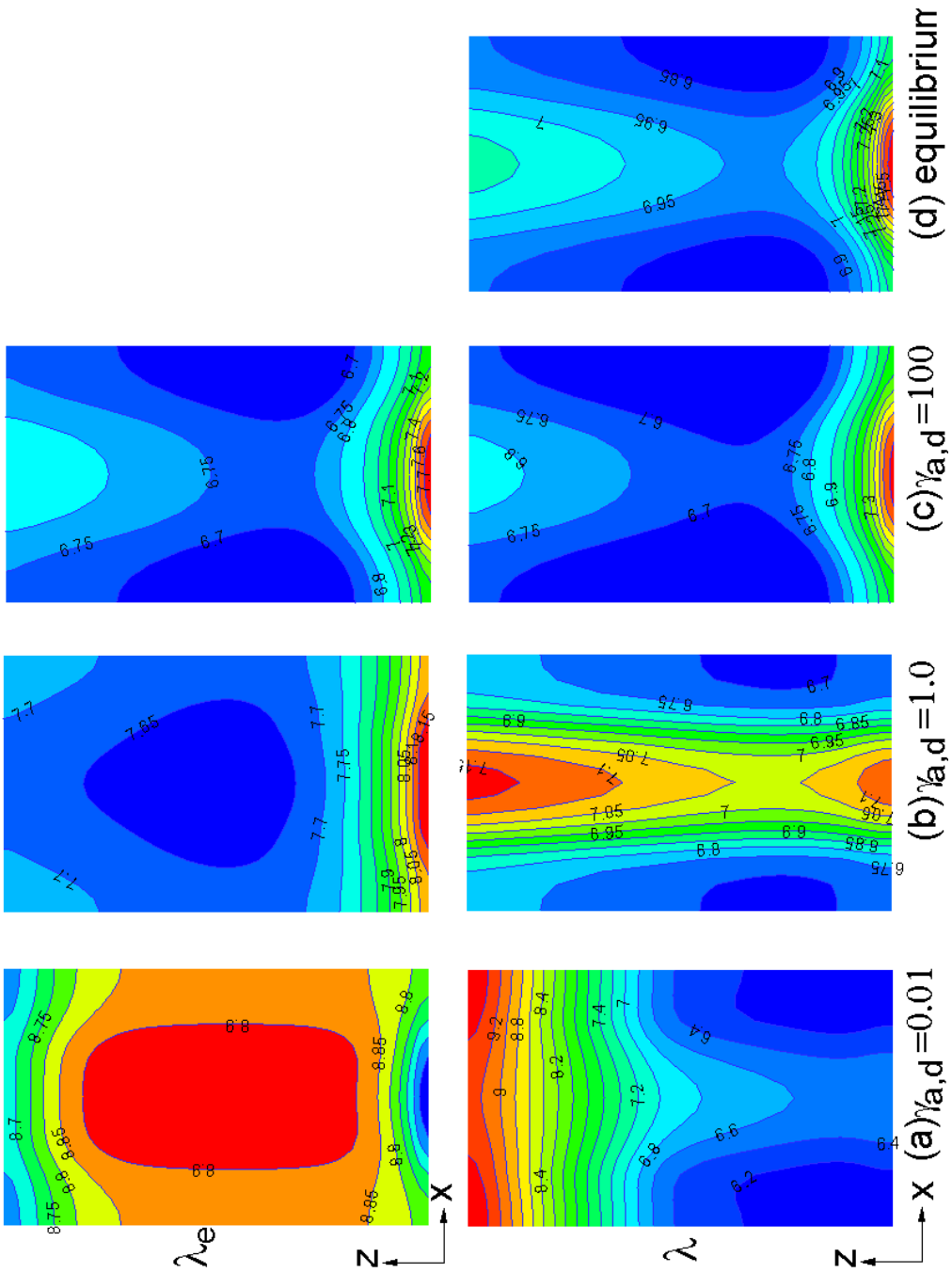

Figure 5.7: Distribution of the actual and the equilibrium membrane water content along the middle x-z cross section of the anode catalyst layer (ACL): (a) $\gamma_{a,d} = 0.01$ 1/s; (b) $\gamma_{a,d} = 1.0$ 1/s; (c) $\gamma_{a,d} = 100$ 1/s; (d) equilibrium model.

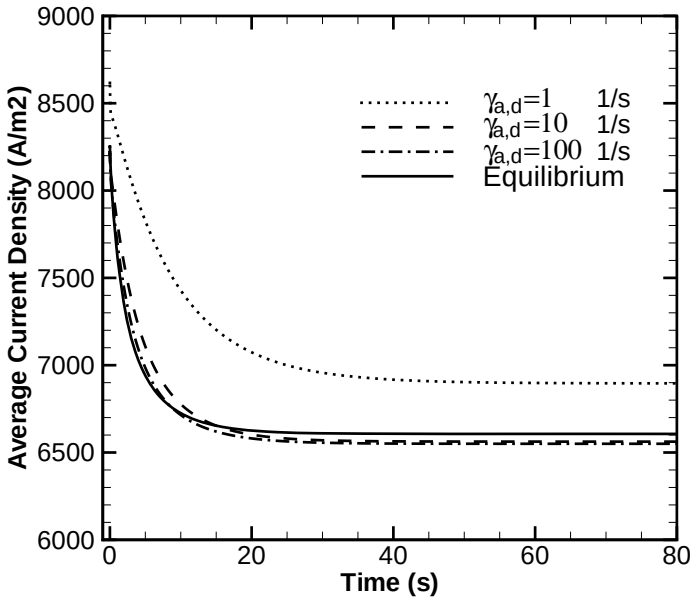

Figure 5.8: Cell dynamic response corresponding to different water sorption rates and with respect to a step change in relative humidity from $RH_{a,c} = 1.0$ to $RH_{a,c} = 0.5$.

potential, Equation (5.1). As shown in Table 3.3, the value of $\triangle G^{\text{ref}}$ and $\triangle S^{\text{ref}}$ are different for different water products [3]. $\triangle G^{\text{ref}}$ and $\triangle S^{\text{ref}}$ for dissolved water production are not available in the open literature, the values for liquid production are thus used temporarily in this study.

The vapor and liquid water production mechanisms are related and differentiated by condensation/evaporation processes, which are determined by the phase transfer rate coefficient, Sh_{ce}. The dissolved and liquid water production models are related and differentiated by water absorption/desorption processes, and thus the absorption/desorption rate coefficient, γ_{ad}, is of significance. Therefore, the comparison among three water production assumptions is best conducted for two separate phase transfer mechanisms, which are characterized by Sh_{ce} and γ_{ad}, respectively.

Liquid Water Production vs. Water Vapor Production

Figure 5.9 demonstrates the variation of average cell current density versus the phase transfer rate coefficient, Sh_{ce}, for the liquid and vapor production assumptions. It shows that the liquid production model is almost independent of the phase transfer rate coefficient throughout the whole range. This is sensible since the system is already fully saturated and evaporation is not likely to occur even at high phase transfer rates. The slight fluctuation of the current density with increasing

rate coefficient might be caused by local under-saturation due to thermal effects. The vapor production model, on the other hand, is significantly affected by the phase transfer rate coefficient. It shows that the current density increases as the rate coefficient Sh_{ce} is reduced because more and more vapor product tends to remain in its original gas phase, thus alleviating the flooding level. Finally, as Sh_{ce} reaches zero no condensation occurs and the model returns to a single-phase model. In contrast, if the rate coefficients are increased towards infinity, water vapor will condense to liquid water. When the system reaches equilibrium, it is found that the current density of the vapor production model reaches its minimum value which is almost identical to the liquid production model. This is expected since both models should converge towards identical solutions in the limit of infinite evaporation/condensation rate coefficients. The range of the estimated phase transfer rate from this study is also marked in Figure 5.9. It shows that the estimated range is very close to the equilibrium state but more likely corresponding to a quasi-equilibrium region. Therefore, the assumption of phase equilibrium used in the mixture model [52] should work reasonably well. From this point of view, although the liquid and vapor production assumptions are not physically correct, they can serve as a tool to identify the phase equilibrium state and help understand the phase transfer processes.

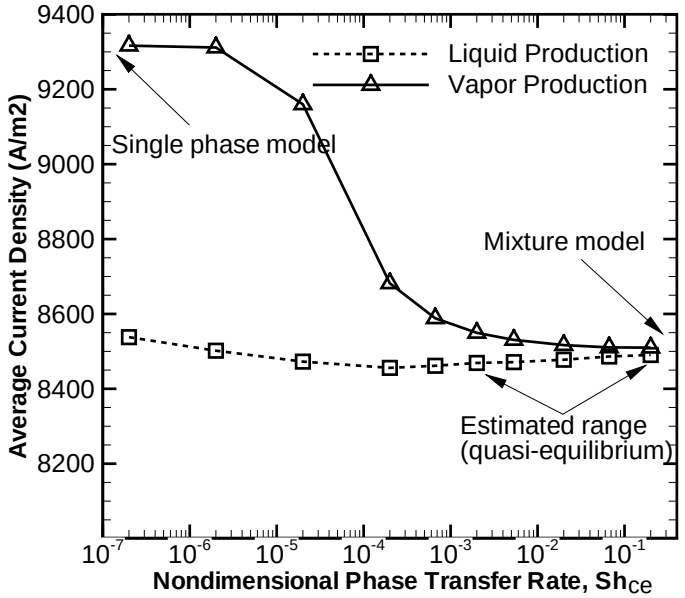

Figure 5.9: Variation of average current density with phase transfer rates, Sh_{ce}, corresponding to vapor and liquid water production assumptions.

Dissolved Water Production vs. Liquid Water Production

Figure 5.10 demonstrates the variation of the average cell current density versus the water absorption/desorption rate coefficient, γ_{ad}, for the dissolved and liquid production assumptions. It is seen that the general trends are similar for both assumptions, the cell current density increases with decreasing sorption rate because the membrane tends to be better hydrated when the sorption rate is low and, thus, the absorption/desorption resistance is high. For the same reason, the dissolved water production model exhibits better cell performance than the liquid production model throughout the whole range because more water is present in the membrane when water is produced in the dissolved phase. On the other hand, as the absorption/desorption rate increases towards equilibrium, the difference between the liquid and dissolved water production models gradually diminishes and the current density approaches the value at the sorption equilibrium state. At $\gamma_{ad} = 100$ s $^{-1}$ which is deemed to be very close to the sorption equilibrium, the current density of the liquid and dissolved production models are 8063.2 and 8164.14 A/m^2, respectively, and it seems that the difference between the two models does not vary further with increasing sorption rate. This final distinction between the liquid and dissolved production models may arise from the estimate of the changes in standard entropy and Gibbs free energy, as well as the reaction heat $\frac{T\triangle S}{4\mathscr{F}}$ for the dissolved production model, where the values of liquid production have been used as an approximation. Moreover, the current density predicted from the equilibrium model is 8104.85 A/m^2 and it is also identified in the figure. Again, the difference between the equilibrium model and non-equilibrium liquid production model is probably due to the mathematical conversion approximation (refer to Equation (3.45)) of the equilibrium model. In addition, Figure 5.10 indicates that using the traditional equilibrium model slightly overestimates the current density at the equilibrium state but significantly underestimates the actual current density if the real scenario takes place at non-equilibrium.

Sample Results

In Figure 5.11, the pressure and velocity distribution of the gas phase have been displayed on a $x-y$ cross section of the cathode GDL and CCL close to the channel outlet. In the vapor production model (Figure 5.11(a)), the amount of water vapor production surmounts the oxygen consumption; and it turns out that the gas pressure increases from the gas channel towards the catalyst layer. Consequently, the convective flow is from the catalyst layer to the gas channel, which means the oxygen can only arrive at the reaction site by diffusion processes. Similar flow behavior has also been presented in many previous single-phase studies, since produced water can only be assumed in a vapor phase in single-phase models.

In the liquid and dissolved water production model, however, since only oxygen is consumed in the gas phase, it shows that the gas phase pressure decreases from the channel towards the catalyst layer and it reaches its minimum at the corner

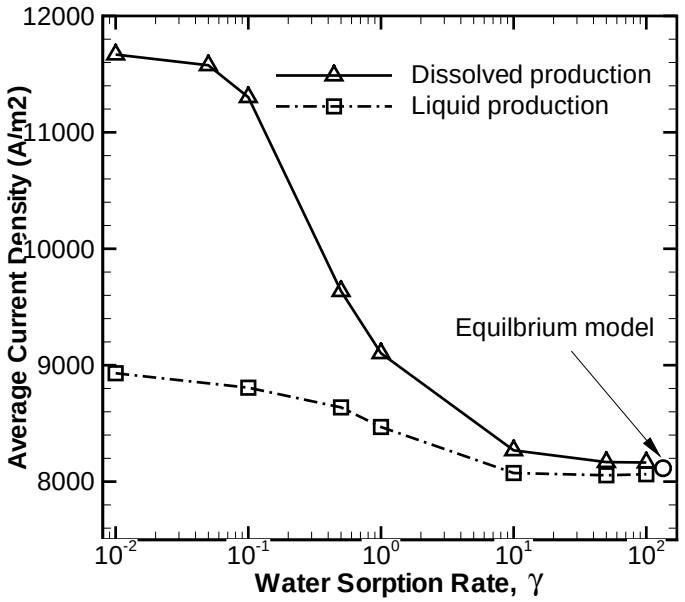

Figure 5.10: Variation of average current density with absorption/desorption rates, γ, corresponding to liquid and dissolved water production assumptions.

of the land region, as shown in Figure 5.11(b)&(c). Accordingly, the convective flow is from the gas channel towards CCL which tends to enhance the oxygen diffusion process. This figure indicates that the flow fields predicted by the liquid water production model are reasonably close to the real mechanism (dissolved water production), while the results from the water vapor production model are rather unrealistic.

Figures 5.9-5.11 demonstrate the significance of an appropriate (dissolved) water production assumption because non-negligible differences exist among three water production assumptions under non-equilibrium phase transfer situations. Starting from the next section till the end of this thesis, the dissolved water production model will be adopted exclusively.

5.3.4 Empirical Expressions for Capillary Pressure

In most of the previous modeling studies, the Leverett J-function is usually used to evaluate the capillary pressure in PEM fuel cells. The Leverett function was originally derived for geological materials with homogeneous wettability and hence, it may not be applicable to PEM fuel cells which are considered highly heterogenous. In this study, therefore, two of the newly developed capillary pressure correlations that are specific to PEM fuel cells are examined and the resulting saturation characteristics are compared with the standard Leverett function approach. Two

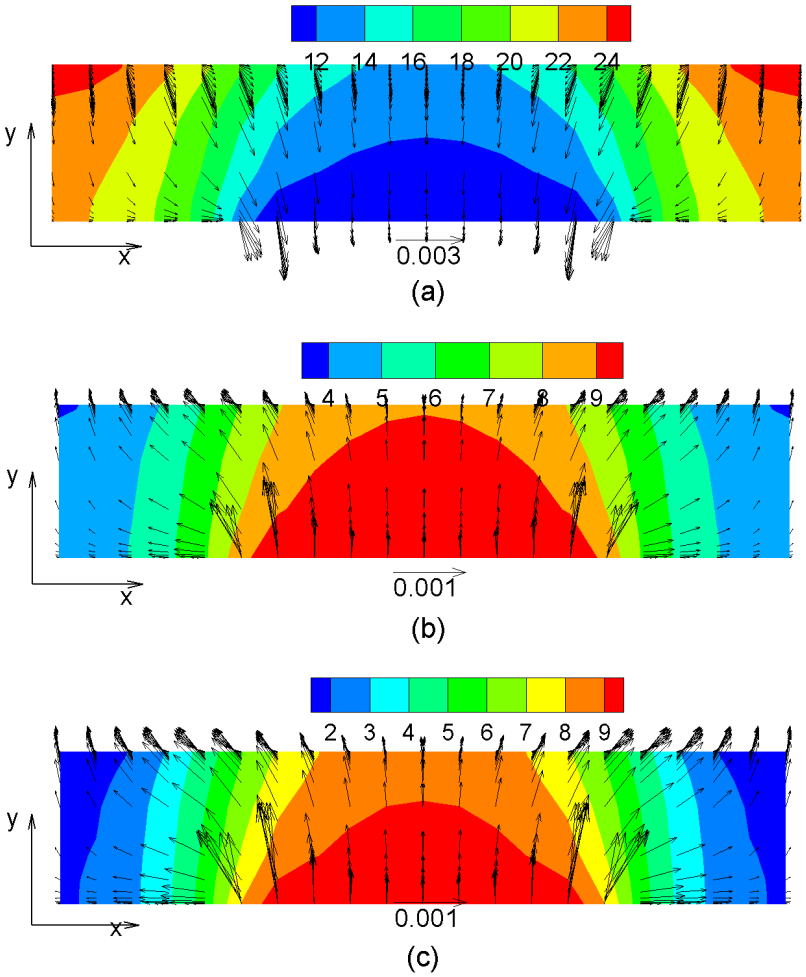

Figure 5.11: Contour plot of gas pressure and vector plot of gas velocity on a $x-y$ cross section of the CCL and cathode GDL close to the channel outlet: (a) water vapor production; (b) liquid water production; (c) dissolved water production.

correlations chosen here were developed by Kumbur *et al.* [63, 64, 65] and Ye *at al.* [114], respectively. More details have been given previously in Section 3.3.4.

The saturation distribution resulting from Kumbur's and Ye's capillary correlations are compared with the standard Leverett function and the results are shown in Figure 5.12. The standard Leverett function and Kumbur's expression are applied in both GDL and catalyst layer. Consequently, the figures exhibit a smooth saturation decrease from the catalyst layer to the gas flow channel (Figure 5.12(a)&(b)). In contrast, the GDL and catalyst layer are differentiated by two separate capillary expressions in Ye's approach and two plots are presented for the catalyst layer (Figure 5.12(c)-1) and GDL (Figure 5.12(c)-2). It is found that Ye's approach results in a very high level of liquid flooding in the catalyst layer but the saturation decreases steeply towards the GDL. For the main part of the GDL domain, the saturation from Ye's approach is even smaller than Kumbur's and the standard Leverett function approach. Comparing Figure 5.12(b)&(c) to Figure 5.12(a), it is seen that the saturation distribution predicted by the Leverett function is more uniform. This can be observed more easily in the vicinity of the gas flow channel. This uniformity may be looked at as counter-evidence of the applicability of the Leverett function in PEM fuel cells, since it implicitly treats the backing layer as homogenous materials (soil or sand) with uniform wetting properties.

5.3.5 Empirical Expressions for Relative Permeability

Similar to the capillary pressure, various forms of relative permeability correlations (as functions of saturation) have been employed in previous PEM fuel cell modeling efforts due to a lack of experimental support. Among them, the power law function (Equation (3.84)) with an exponential factor of 3, the so-called Wyllie's cubic power law [125], is commonly adopted in the literature and it is used as the base case in the current study. The saturation distribution with this cubic power law has been used for the results shown in Figure 5.12. On the other hand, based on the analysis of [61, 90], several recent studies [90, 99, 114] have used an exponent of $n = 4.5$ for the GDL while keeping the exponent at 3.0 in the catalyst layer. As a comparison to the cubic power law, this approach is implemented in this study to investigate the effect of relative permeability on the distribution of the liquid saturation.

Three different capillary pressure correlations are investigated again for comparison purposes and the results are presented in Figure 5.13. A significant increase of the liquid saturation is observed for all three capillary pressure correlations when compared to Figure 5.12. This is because the saturation is always smaller than 1, hence an increase in the exponent in Equation (3.84) tends to reduce the relative permeability exponentially, which in turn results in a much reduced water removal ability for the porous backing layer.

Figure 5.13 clearly demonstrates the importance of the determination of relative permeability. It indicates that the relative permeability has an even more significant impact on the modeling results than the capillary pressure. Therefore, apart from

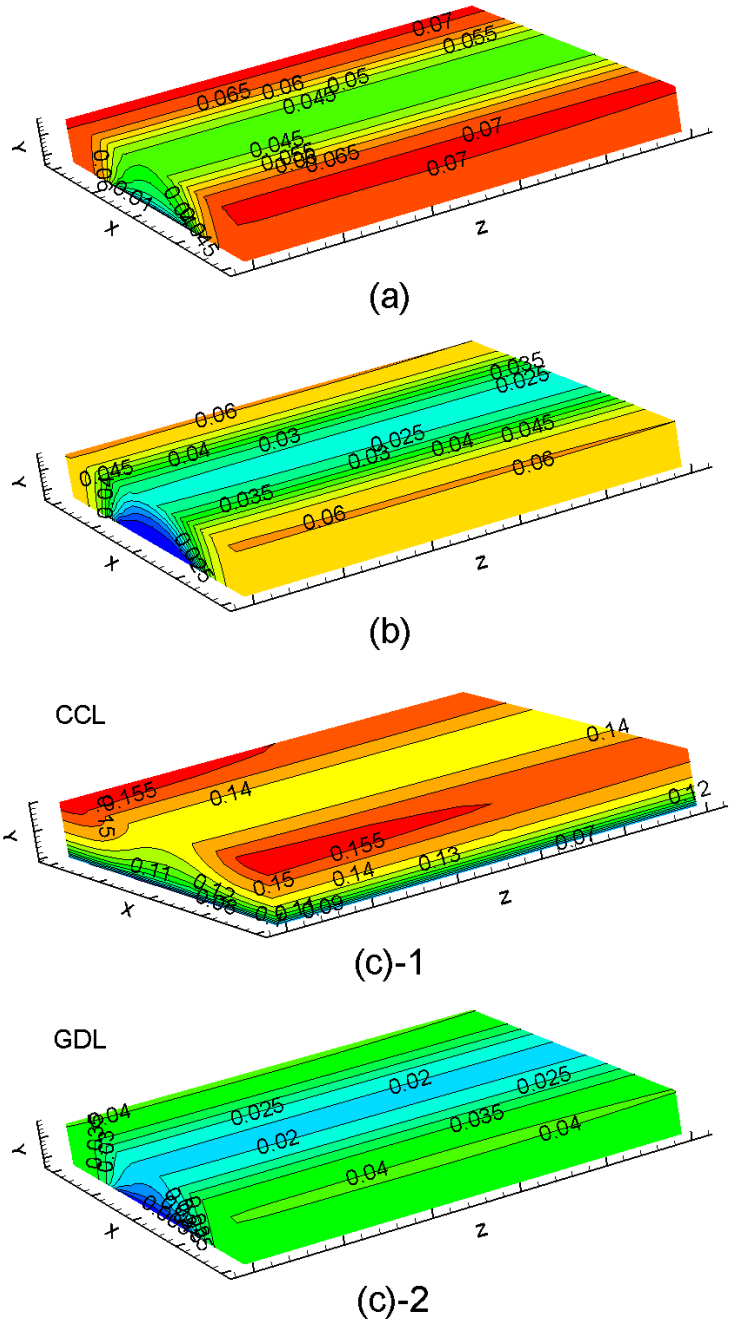

Figure 5.12: Saturation distribution in cathode catalyst layer (CCL) and cathode gas diffusion layer (GDL) with respect to the empirical function of capillary pressure used: (a) standard Leverett function; (b) Kumbur's expression; (c)-1 Ye's expression, CCL; (c)-2 Ye's expression, GDL.

the measurements of capillary pressure the relative permeability for PEM fuel cells should also be measured, which is a relatively rare focus of attention to-date.

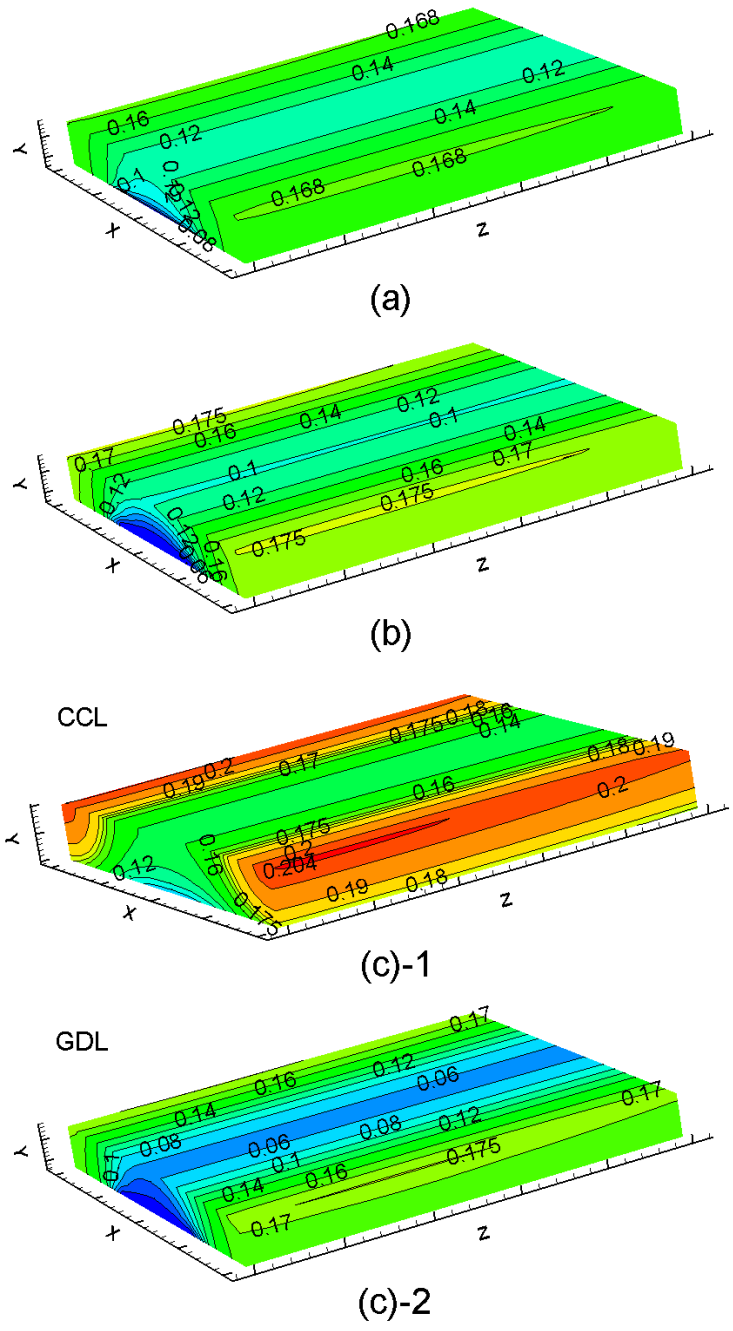

Figure 5.13: Saturation distribution in cathode catalyst layer (CCL) and cathode gas diffusion layer (GDL), with a power of 4.5 for the relative permeability in GDL with the capillary pressure given by: (a) standard Leverett function; (b) Kumbur's expression; (c)-1 Ye's expression, CCL; (c)-2 Ye's expression, GDL.

5.4 Dynamic Responses of PEM Fuel Cells with Respect to Operating Condition Changes

Dynamic performance is one of the most important considerations for the design of PEM fuel cells. This is particularly true for the applications of PEM fuel cells in mobile environments such as automobiles. In this section, the dynamic responses of PEM fuel cells with respect to some typical operating condition changes will be presented. Based on the analysis in the previous section, the dynamic response case studies were accomplished with the following model implementations: (i) the non-equilibrium sorption/desorption submodel with the sorption/desorption rates determined by Equation (3.51)&(3.52); (ii) the dissolved water production submodel; (iii) Kumbur's expression for the capillary pressure; and, (iv) Wyllie's cubic power law for the same expression of relative permeability in both GDL and CL. Furthermore, the condensation/evaporation rates are assumed to be $Sh_{ce} = 2.0 \times 10^{-3}$, unless otherwise specified.

5.4.1 Hysteresis Effects During Voltage Sweep Test

As mentioned earlier in the section of model validation, a hysteresis phenomenon exists on the polarization curves. The polarization curves from the current model at partially humidified conditions ($RH_{a,c} = 0.5$) are shown in Figure 5.14 for three dynamic voltammetry sweep cycles with sweep rates of 10 mV/s, 25 mV/s, and 50 mV/s, respectively. Note that, since the liquid saturation increases quickly in the mass transport limitation region as indicated in [138], the present model becomes extremely sensitive to the voltage change and subtle under-relaxation schemes and much prolonged computation time are required to obtain a fully converged solution in this region. To ensure a rapidly converged solution at each voltage step, this mass transport limitation region has been excluded from the present study. Consequently, it is seen that the hysteresis effect is not very strong in these low to moderate current regions. Further, it is found that the hysteresis of polarization curves decreases when voltage sweep rate is increased.

The polarization hysteresis can be interpreted by examining the variation of membrane water content during these sweep cycles. Figure 5.15 demonstrates the average water content at the middle $x - z$ cross section of the ACL and the bulk membrane (Plane 1&2, refer to Figure 5.1). Strong hysteresis variation of the water content is found for all three sweep cycles on both planes, indicating that the hysteresis phenomenon can be much more pronounced in certain domains than the polarization curve might suggest. This is because a large amount of dissolved water is produced as the cell reaches its maximum current density at the end of the forward sweep, but the accumulated water cannot be timely transferred to other regions at the beginning of the backward sweep since both membrane desorption and hydration are rate limiting processes. Furthermore, Figure 5.15 shows that the hysteresis effects are attenuated as the sweep rate increases, explaining the

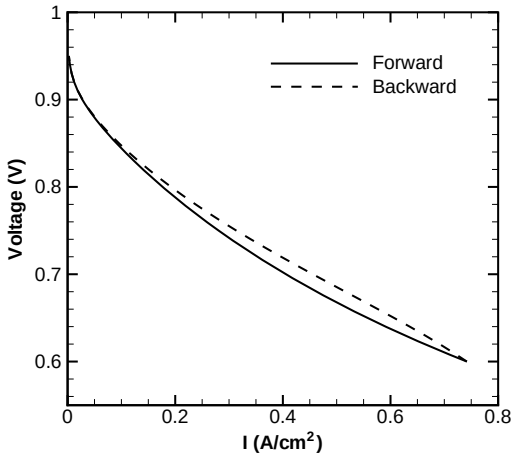

(a) 10 mV/s

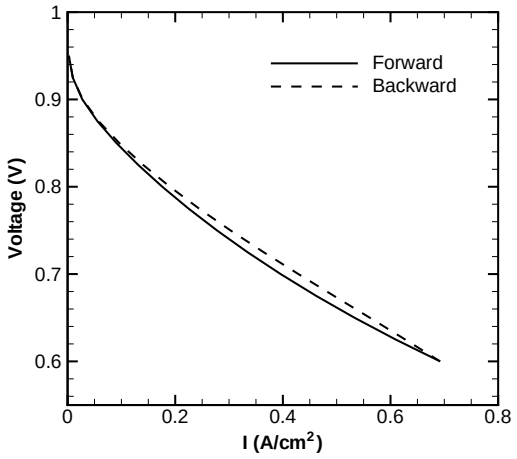

(b) 25 mV/s

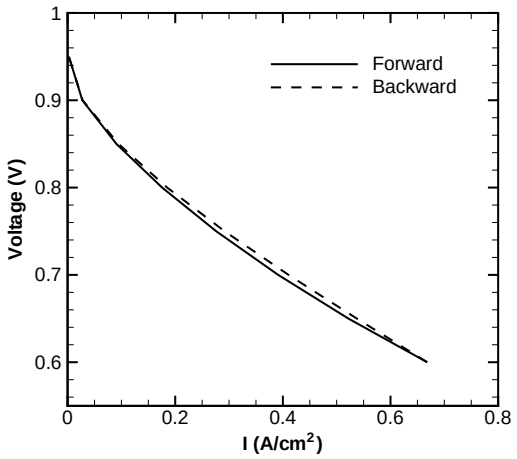

(c) 50 mV/s

Figure 5.14: Polarization curve under partially humidified conditions ($RH_{a,c} = 0.5$) and with the voltage sweep rate of: (a) 10 mV/s; (b) 25 mV/s; (c) 50 mV/s.

corresponding trends in the polarization curves in Figure 5.14. This is because the membrane has plenty of time to absorb accumulated water when the sweep rate is low, but its water retention ability is greatly weakened if the sweep rate is high. In addition, Figure 5.15 also discloses some interesting transport phenomena related to the membrane hydration/dehydration process. During the forward sweep, it shows that the water content at the center of the membrane (Plane 2) always increases for all three sweep rates because the water produced at the CCL can easily reach this plane and elevate the local water content. Along the middle plane of the ACL (Plane 1), however, it is found that the effect of electro-osmotic drag outweighs that of back diffusion because the electro-osmotic drag increases instantaneously with the current density but it takes some time for the produced water to diffuse through the membrane and hydrate the ACL. Consequently, the water content in the ACL gradually decreases as the current density is increased. This phenomena has been verified by many experimental studies and is usually referred to as "anode drying out". The results from this study suggest that the anode dry out can be alleviated if a low sweep rate is used or if the membrane thickness is reduced. In both cases, the anode will benefit from an enhanced back diffusion effect.

Figure 5.16 demonstrates the variation of liquid saturation in the CCL at Point 1 (refer to Figure 5.1) during three sweep cycles. Similar to the water transport within the membrane phase, the liquid water transport in the porous backing layer also exhibits a strong hysteresis behavior. There is no liquid water present at the beginning of the forward sweep process since the cell is operated with partially humidified conditions. As more water is released from the dissolved phase at higher current densities, liquid water starts to appear and increases almost linearly with the current density with its slope depending on the voltage sweep rate. During the backward sweep, liquid water is removed in a wholly nonlinear manner in all three sweep cycles. The nonlinearity of the liquid saturation looks very similar to that of the water content (Figure 5.15), whereas the underlying transport mechanisms are entirely different. In fact, the accumulated dissolved water that is produced at higher current densities will be removed via two separate paths during the downward change of the current density. The first path is through the back diffusion which directs water molecules from the cathode side towards to the anode; the other way is through the membrane desorption process during which the dissolved water is transferred into the liquid phase and removed from the porous backing layer in terms of capillary diffusion. Therefore, the hysteresis behavior shown in Figure 5.16 is really including two transient mechanisms: the membrane desorption, and the liquid flow in the backing layer.

5.4.2 Dynamic Response Corresponding to Nonlinear Impedance Load Change

The experimental work of Ziegler *et al.* [138] shows that different dynamic transport processes in a testing cell can be separated by the use of a low-frequency

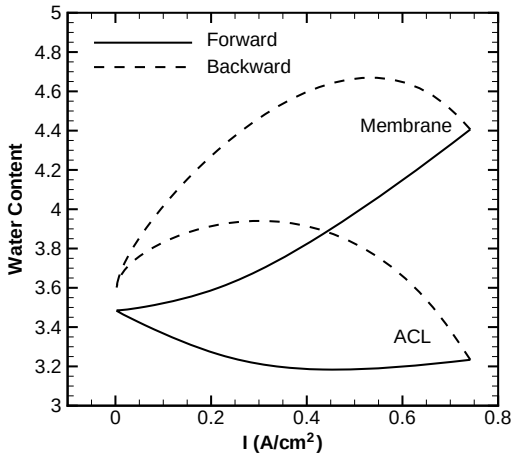

(a) 10 mv/s

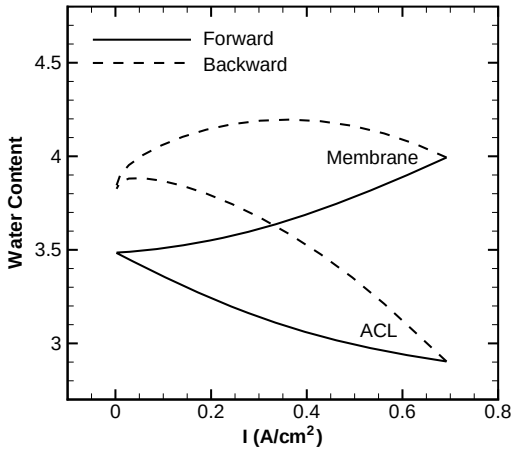

(b) 25 mv/s

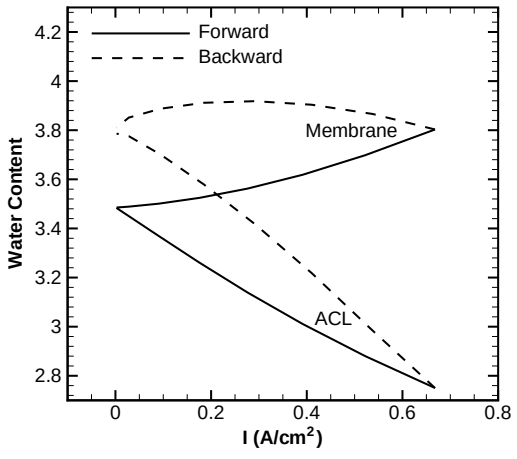

(c) 50 mv/s

Figure 5.15: Hysteresis response of the average membrane water content at the middle $x-z$ cross section of the anode catalyst layer (ACL) and membrane (Plane 1&2, refer to Figure 5.1), with a voltage sweep rate of: (a) 10 mV/s; (b) 25 mV/s; (c) 50 mV/s.

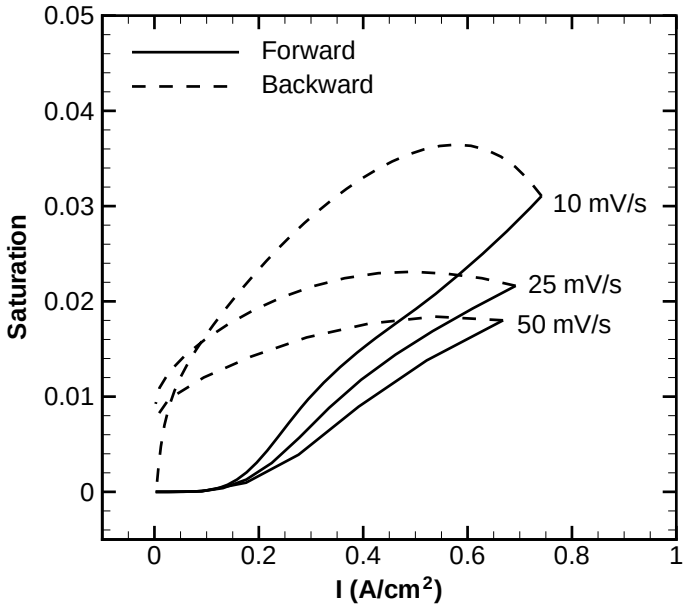

Figure 5.16: Hysteresis response of the liquid saturation at Point 1 (refer to Figure 5.1) during the voltage sweep cycles.

impedance approach. A similar impedance study is performed in this numerical study with fully humidified conditions, utilizing a sinusoidal functional change of the cell operating voltage which serves as a boundary condition for the solid phase potential (refer to Figure 5.4)

$$\phi_{cell} = 0.7 + 0.1\sin(2\pi ft), \tag{5.2}$$

where 0.7 is the base voltage, 0.1 is the amplitude of the voltage perturbation, f is the frequency of the sine wave, and t is the operating time. Figure 5.17 demonstrates the dynamic responses of the cell average current density, temperature (at Point 1, refer to Figure 5.1) and liquid saturation (at Point 1) during one sinusoidal cycle under four different frequencies. As can be seen, there are obvious phase shifts among the three variables at the frequency of 10 Hz (Figure 5.17(a)), indicating their corresponding transports have different characteristic time scales. These phase shifts are then reduced when the impedance frequency decreases since local equilibrium can be reached more easily when the rate of change in the system slows down. Finally, the characteristic time scales of heat transfer and liquid water transport are identified to be 10 s and 100 s, respectively, as their phase shifts vanish at about 0.1 Hz (Figure 5.17(c)) and 0.01 Hz (Figure 5.17(d)), respectively. Applying classical diffusion theory, Ziegler *et al.* [138] estimated the time scale for capillary diffusion of liquid water in the GDL to be only about 1 s which is far less than 100 s. This means that the liquid water transport is dominated by the membrane desorption process rather than by the capillary diffusion in the GDL.

Consequently, it is deduced that the time scale for membrane desorption is on the order of 100 s, which agrees with the experimental results shown in [100, 101].

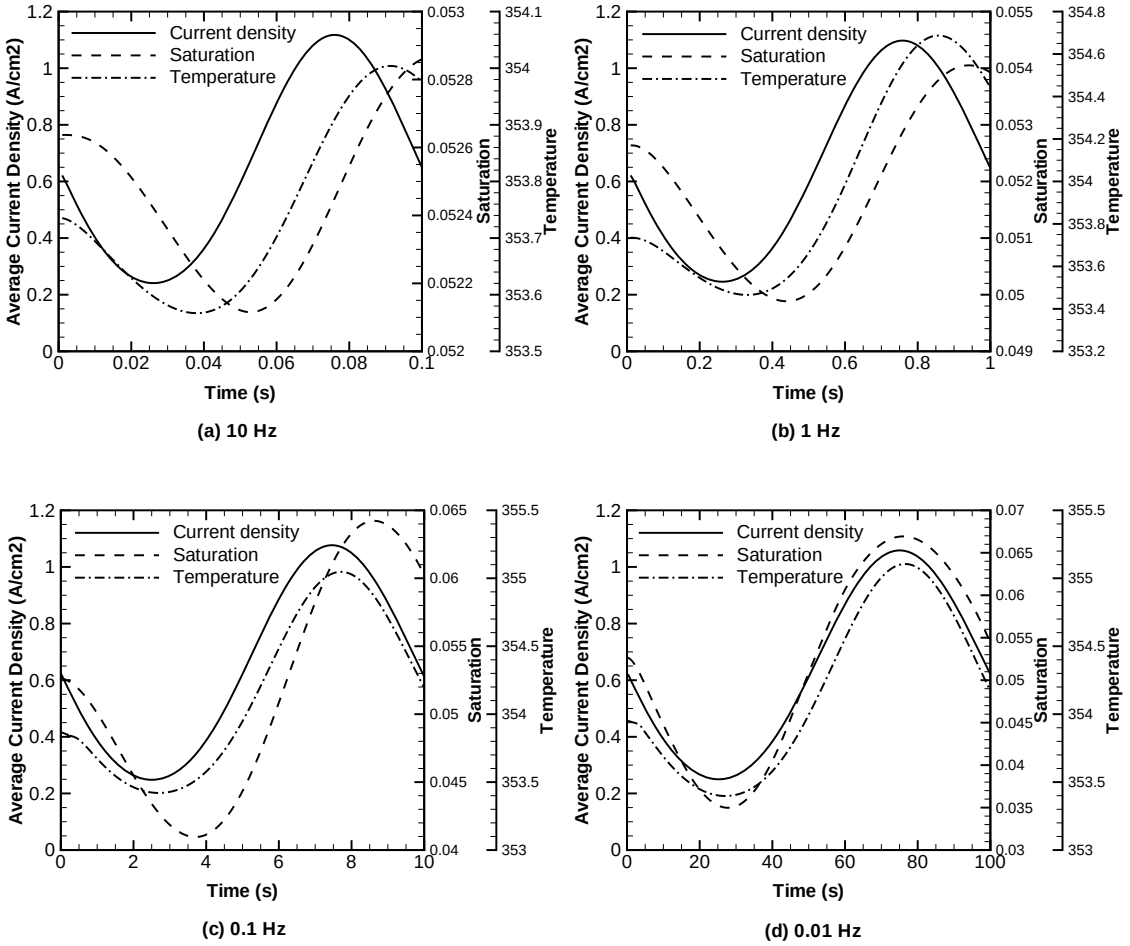

Figure 5.17: Dynamic responses of average current density, liquid saturation and temperature, corresponding to different impedance frequencies under fully humidified conditions.

The same impedance simulation is extended for 20 seconds at a frequency of 1 Hz and the results are shown in Figure 5.18. Since the membrane is well hydrated under fully humidified conditions and the GDL is only slightly flooded in this simulation (refer to Figure 5.18), it is found that the cell current density responds to the voltage change very fast and there is no obvious phase shift between the voltage and current density. On the other hand, the responses of the liquid saturation and temperature are much slower and it is seen that there is a transition period before the liquid saturation and temperature finally reach their dynamic equilibrium. The oscillation amplitude of the liquid saturation quickly increases in the first 5 seconds, then it gradually declines throughout the remaining time interval. The transition

of temperature is relatively gentle and well within 10 seconds. Generally, Figure 5.18 reveals that the most important transient transport phenomena occur within the first 5 seconds under fully humidified conditions.

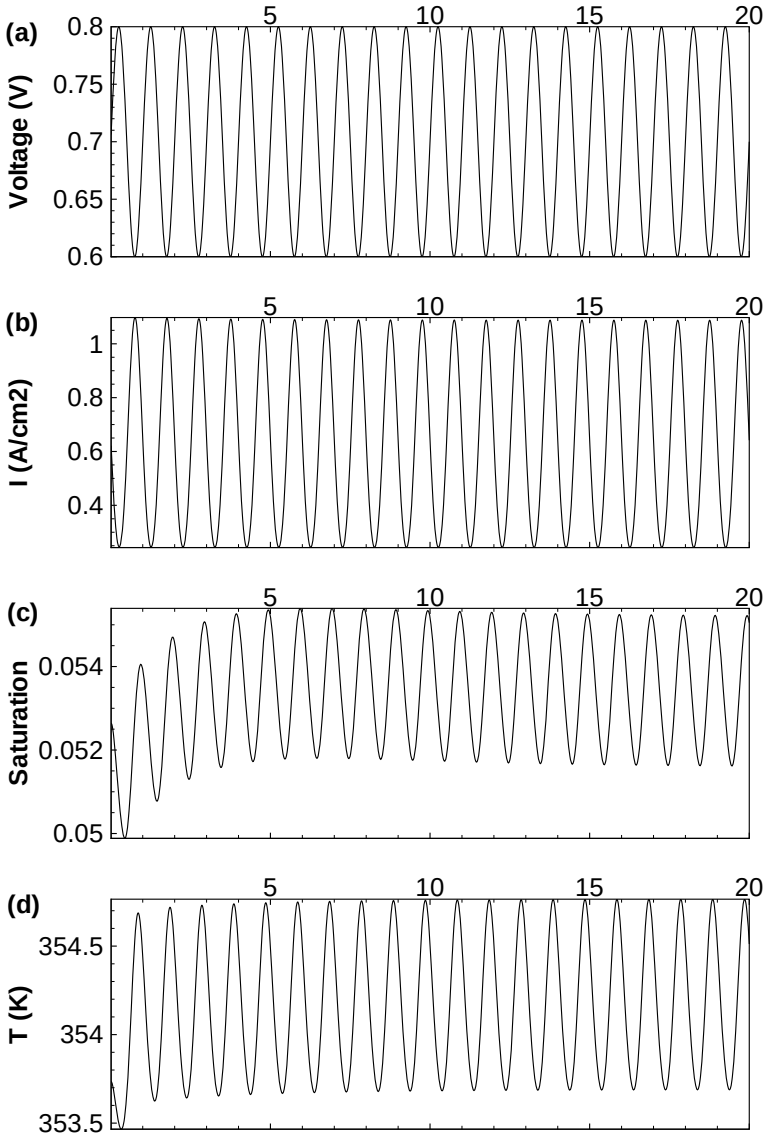

Figure 5.18: Time extended dynamic responses of average current density, liquid saturation and temperature, corresponding to an impedance frequency of 1 Hz under fully humidified conditions.

A similar impedance simulation has been conducted for partially humidified conditions ($RH_{a,c} = 0.5$) as well and the results are demonstrated in Figure 5.19. It shows that the transition period of liquid saturation and membrane water content is greatly extended to about 50 seconds. Similar to the voltage sweep study, this prolonged transition time is mainly due to the combined effect of various wa-

ter transport processes, including the liquid evaporation in the porous backing layer, membrane hydration/dehydration in the bulk membrane, and membrane sorption/desorption in the catalyst layer.

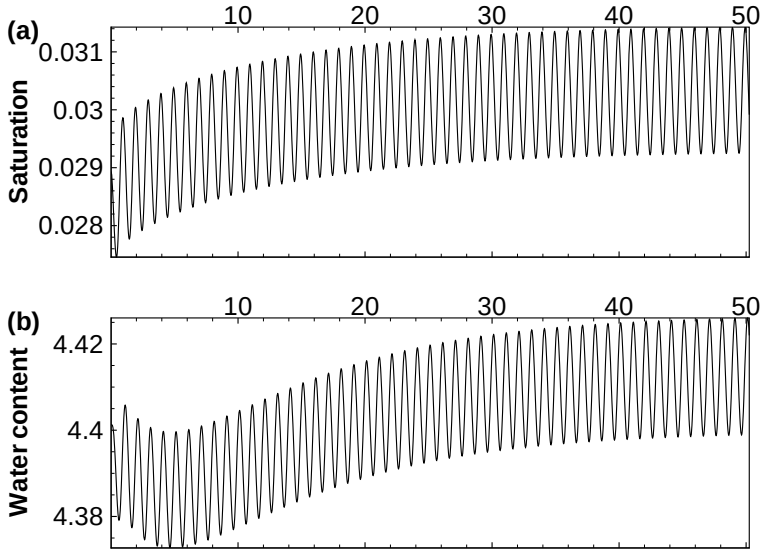

Figure 5.19: Time extended dynamic responses of liquid saturation and water content, corresponding to an impedance frequency of 1 Hz under partially humidified conditions ($RH_{a,c} = 0.5$).

5.4.3 Effect of Step Change in Relative Humidity

Figure 5.20 demonstrates the transient variation of the cell current during two step changes in relative humidity ($RH_{a,c} : 1 \rightarrow 0.5 \rightarrow 1$). It shows that the dynamic cell response is not symmetric under symmetric changes in relative humidity. It takes about 60 seconds for the cell to reach steady state during the step decrease, which is much slower than the response during the step increase which is less than 30 seconds. This phenomenon is mainly due to the nonlinear multi-water phase transport behavior. A similar trend has also been found in [44].

5.4.4 Effect of Step Change in Cell Voltage

In Figure 5.21, the transient variation of the cell current output during a serial step change in cell voltage is demonstrated. An undershoot in current density is observed during a voltage step increase from 0.65 V to 0.7. This is because the oxygen concentration remains low as in the previous high current state; as the oxygen consumption rate becomes smaller under lower operating current, the oxygen concentration recovers gradually and the current reaches steady state. For

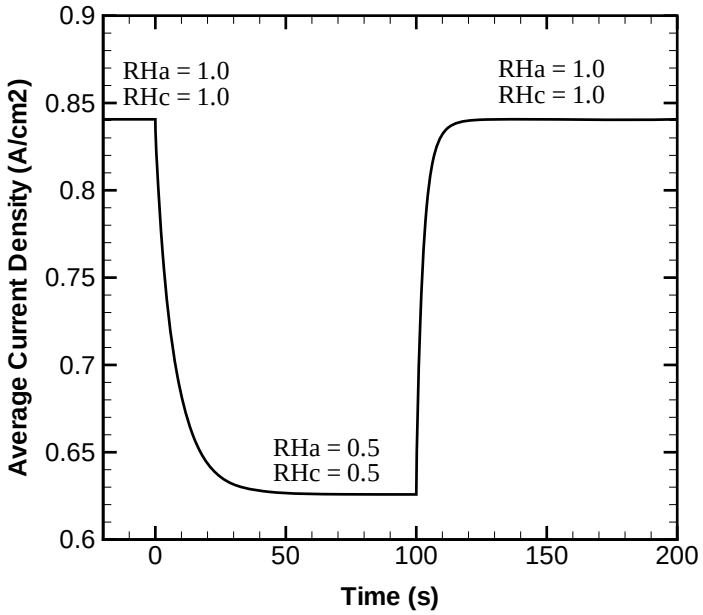

Figure 5.20: Current response corresponding to step changes in relative humidity.

similar reasons, overshoots in current density are observed when the cell experiences voltage step decreases (from 0.7 V to 0.65 V, and from 0.65 V to 0.6V). As exhibited earlier, the most important transport phenomena occur in the first 5 seconds under fully humidified conditions (refer to Figure 5.18). Correspondingly, it is seen that the cell current reaches steady state within 5 to 10 seconds during all step changes. In addition, the figure demonstrates that the overshoot is slightly larger when the step change is performed at high current densities. A similar prediction is also seen in [98].

The cell dynamic performance under low relative humidity ($RH_{a,c} = 0.5$) working conditions is also studied and the results are demonstrated in Figure 5.22. It clearly shows that the cell dynamic characteristics at lower relative humidity are totally different from that at fully humidified operation (Figure 5.21). This is mainly because the membrane can take up more water under lower relative humidity conditions than at fully humidified conditions. When the cell voltage is switched from 0.65 to 0.7 V during the first step change, an undershoot occurs (refer to the enlarged figure) at the initial stage due to the low species concentrations from the previous high current state. With the recovery of reactant species and due to the relatively higher temperature and, hence, better electrochemical performance at the initial stage, the cell current density increases and an overshoot appears. On the other hand, a large amount of water is accumulated in the membrane at the initial high current density state. Therefore, the membrane dehydrates gradually due to the reduced water production at lower current density. Accordingly, the cell

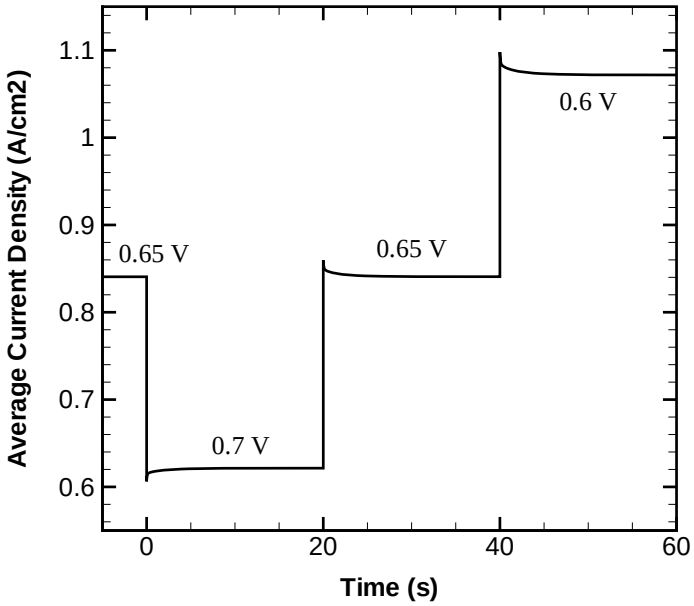

Figure 5.21: Current response corresponding to step changes in cell voltage.

current density decreases gradually till it reaches an equilibrium state at around 50 seconds. For similar reasons, a reverse transient curve is exhibited when the cell voltage decreases from 0.7 to 0.65 V. An undershoot follows an overshoot due to the species transient, then the current density gradually increases during the membrane hydration process and reaches steady state around 40 seconds.

5.4.5 Effect of Step Change in Operating Pressure

In Figure 5.23, the transient variation of the cell current output during a serial step change in gas feed pressure is demonstrated. As with Figure 5.21, overshoots and undershoots are clearly seen during all step changes which are also caused by the transient species transport. Furthermore, the figure shows that the cell performance has a substantial improvement (42.9%) when the gas feed pressure is switched from 1 to 2 atm. However, the performance change is only about 8.7% when the gas flow pressure is raised from 3 atm to 4 atm. Meanwhile, the figure also exhibits that the cell response time is reduced and the current overshoot is weakened when the step change is made at higher pressure conditions.

In summary, the study of the pressure step changes underlines that the pressure effects are more significant at low pressure conditions. Such behaviors have been verified by experimental findings of Yan *et al.* [139].

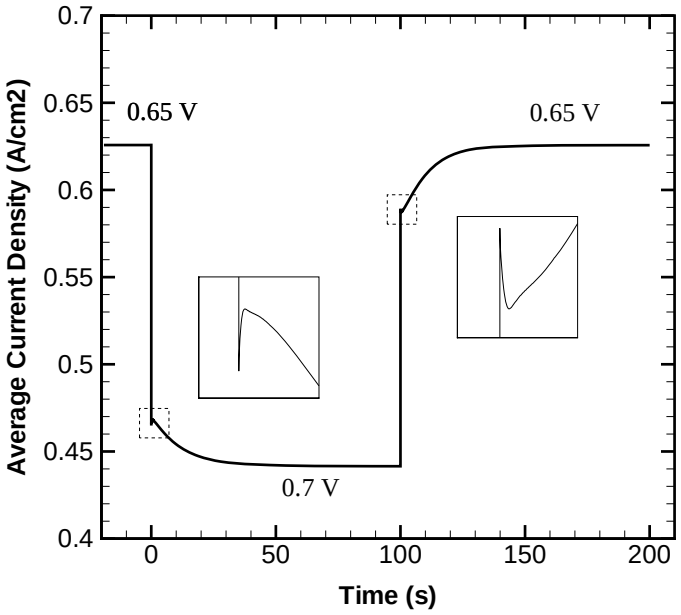

Figure 5.22: Current response corresponding to step changes in cell voltage at partial humidified conditions ($RH_{a,c} = 0.5$).

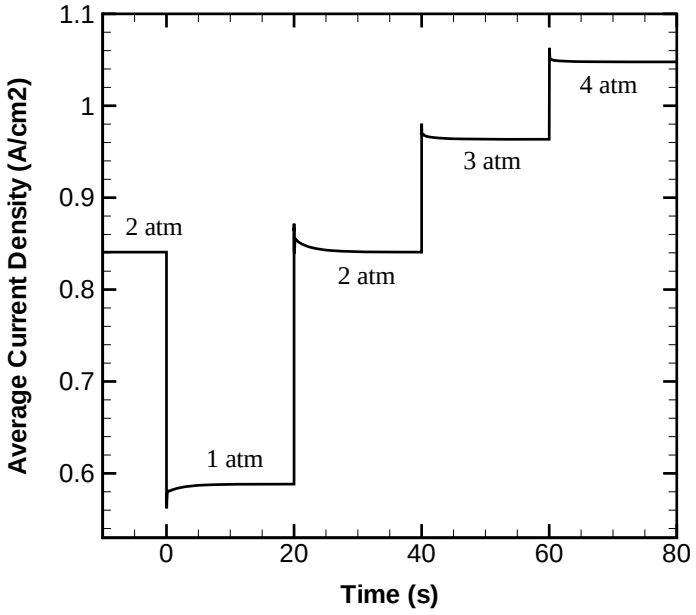

Figure 5.23: Current response corresponding to step changes in operating pressure.

5.4.6 Effect of Step Change in Gas Flow Stoichiometric Ratio

Finally, the transient variation of the cell current output during a serial step change in flow stoichiometric ratio is shown in Figure 5.24. Compared to other operating condition changes, it is found that an increase of the gas flow rate does not necessarily influence the cell current in a significant way (less than 1%). Again, this agrees well with the experimental study of Yan *et al.* [139]. The authors found that the stoichiometric ratio is of significance only in the mass transport limitation region.

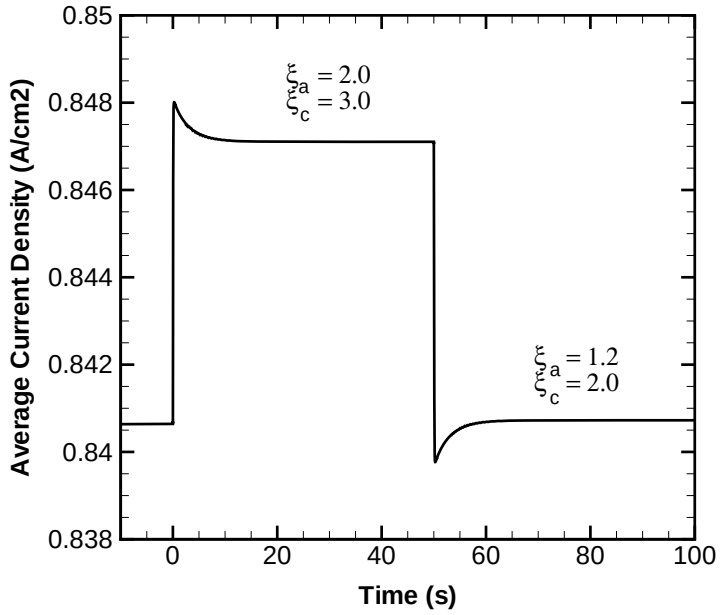

Figure 5.24: Current response corresponding to step changes in stoichiometric ratio.

5.5 Transient Transport Phenomena Within PEM Fuel Cells

The length scales of a PEM fuel cell's main components are ranging from the micro over the meso to the macro level, and the time scales of various transport processes range from milliseconds up to a few hours. This combination of various spatial and temporal scales makes it extremely challenging to conduct in-situ measurements or other observations through experimental means. Thereby, numerical simulation sometimes becomes the unique tool to help understand the underlying electrochemical reaction kinetics and transient transport phenomena inside the cell.

The underlying transport phenomena predicted by the current model are presented in this section. All of the transient simulations presented below are achieved with a step change in relative humidity, $RH_{a,c} : 1 \rightarrow 0.5$ (refer to the first step change in Figure 5.20); while all the steady-state results presented in this section are based on conditions shown in Table 5.1.

5.5.1 Transport of Gas Species

Transport of the reactant gas species is probably the most important transport characteristic of PEM fuel cells, since it directly determines the electrochemical reaction rates and the ensuing cell performance. In addition, most of the other transport processes, such as the liquid and dissolved water transport and heat transfer processes, are closely coupled to the gas flow behavior. Therefore, the gas phase transport needs to be understood before going into any details of other transport processes.

Bulk Gas Flow Field

Firstly, the bulk gas flow field at the steady state of the base case conditions is examined. In Figure 5.25, the distribution of the gas phase gauge pressure and the flow streamlines are demonstrated. Clearly, the gas flow is directed from the gas flow channel towards to the catalyst layer at both the anode and the cathode side. This trend corresponds to the pressure distribution which drops from the flow channel towards catalyst layer due to the reactants consumption at the reaction site (catalyst layer). As mentioned previously, this flow behavior contradicts the single-phase model which predicts that the convective gas flow is from the catalyst layer towards the gas flow channel at the cathode side and, thus, oxygen reaches the reaction site by a diffusion process only.

Both hydrogen and water vapor are consumed in the ACL, whereas only oxygen is consumed at the CCL. Consequently, the pressure drop through the porous GDL and catalyst layer is more significant at the anode side, as shown in Figure 5.25(a). On the other hand, the pressure drop along the flow channel (refer to Figure 5.25(b)) is mainly caused by friction loss which can be estimated by the Darcy-Weisbachs correlation [140]

$$\triangle P = C_f \frac{\rho V L}{2 d_h}. \tag{5.3}$$

Here, C_f is the friction coefficient; ρ and V are the average density and velocity of the gas flow, respectively; L and d_h are the length and hydraulic diameter of the flow channel, respectively. For laminar flow in a straight square flow channel which is the case in the present study, the friction coefficient is formulated as [140]

$$C_f = \frac{56.9}{Re}. \tag{5.4}$$

The Reynolds number, Re, is defined based on the hydraulic diameter of the flow path

$$Re = \frac{\rho V d_h}{\mu}, \tag{5.5}$$

where μ represents the average dynamic viscosity of the flow.

Substituting Equations (5.4) and (5.5) into Equation (5.3), the pressure drop along the gas flow channel can finally be calculated as

$$\triangle P = 56.9 \frac{\mu L}{2 d_h^2} V. \tag{5.6}$$

The oxygen concentration at the cathode side is much lower than the hydrogen concentration at the anode side since pure hydrogen and air are fed as reactants. To match the reaction rate at the anode side, the cathode mass flow rate (and thus the flow velocity) has to be several times that of the anode gas flow. Furthermore, the dynamic viscosity of the air-vapor mixture is almost double that of the hydrogen-vapor mixture. From Equation (5.6), the pressure drop in the cathode flow channel should be much higher than in the anode flow channel, and this is verified in Figure 5.25(b).

The gas phase does not exist in the membrane layer; hence, no streamlines are present in that region.

Transport of Hydrogen

The transport of hydrogen is interconnected with the transport of water vapor at the anode side. In theory, there are two moles of protons produced for each mole of hydrogen molecules being split. The protons are then transferred from the ACL towards the CCL through the ion-selective membrane. The movement of protons tends to move along some water molecules with them by means of the electro-osmotic drag. On the other hand, the transfer of the water molecules is counteracted by the back diffusion process and the rate-limited membrane sorption process. The net water transfer between the anode and cathode side really depends on the specific local conditions.

Figure 5.26 illustrates the transient variation of the hydrogen concentration during a step change in relative humidity ($RH_{a,c} : 1 \rightarrow 0.5$). At $t = 0.001$ s, it is found that the hydrogen concentration slightly increases along the flow channel which violates intuition since hydrogen is consumed during the electrochemical reaction. However, inspecting the water vapor transport can easily disclose the reason. It is found that the cell is still fully humidified at this time instance resulting in water vapor being consumed faster than hydrogen. Consequently, some of space that was previously occupied by water vapor is taken over by hydrogen molecules. Similar hydrogen transport characteristics are also reported by [109] in a steady-state study.

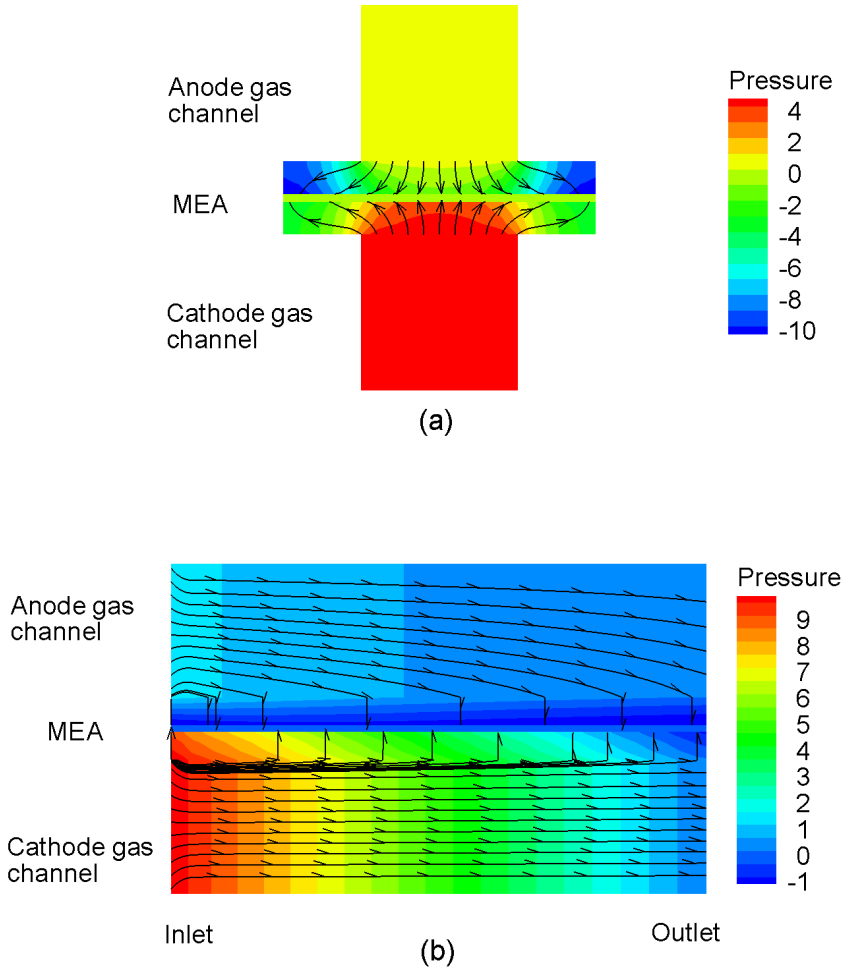

Figure 5.25: Flow streamline (vector plot) and pressure (P, Pa) distribution (contour plot) at steady state: (a) plane 4, and (b) plane 5 (refer to Figure 5.1).

At $t = 1$ s, the anode flow field is significantly disturbed by the relatively dry incoming flow stream. It shows that the hydrogen concentration decreases from the channel inlet all the way down to the outlet. The reasons for the decline are two-fold. Firstly, the hydrogen concentration jumps from about 53 to 60 mol/m^3 at the channel inlet because more hydrogen is supplied when the relative humidity is reduced by half; secondly, more water tends to be transferred from the CCL towards the ACL by means of back diffusion and, thus, less water vapor is consumed at the ACL during the vapor sorption process. As will be shown shortly in Section 5.5.2, the water vapor concentration actually increases along the anode gas flow channel due to back diffusion. The latter is the main reason causing the hydrogen concentration to decline.

In the remaining transient period, the hydrogen concentration varies in a similar manner as at $t = 1$ s. It finally reaches steady state at around 50 seconds.

Transport of Oxygen

The transient variation of the oxygen concentration during the step change in relative humidity is illustrated in Figure 5.27. Only oxygen is consumed at the cathode side, hence, its concentration decreases all the way from the channel inlet to outlet during the whole period. In addition, it is seen that the oxygen concentration gradually moves to a higher level since more air is available as the incoming flow becomes dry. This is similar to the transient variation of the hydrogen concentration.

5.5.2 Transport of Multi-Water Phases

Transport of Water Vapor

The transient variation of the water vapor concentration within the anode flow channel, GDL and catalyst layer is demonstrated in Figure 5.28. As explained earlier, the cell is still fully humidified initially ($t = 0.001$ s) which results in the water vapor absorption being faster than the hydrogen consumption. Consequently, the hydrogen concentration slightly increases and the water vapor concentration decreases along the channel, as shown in Figure 5.28(a). At other time instances ($t = 1, 10, 50$ s), the partially humidified gas stream prevails the flow field. It is seen that the water vapor concentration increases along the channel due to the enhanced effect of back diffusion. Moreover, it should be noted that the maximum water vapor concentration at the final steady state ($t = 50$ s) is about 14 mol/m^3 which is less than that at the beginning ($t = 0.001$ s), indicating that the anode side flow field is partially humidified throughout

The transient variation of the water vapor concentration within the cathode side flow channel, GDL and catalyst layer is demonstrated in Figure 5.29. Unlike the anode side, there is no water vapor being absorbed or produced at the cathode side under fully humidified conditions. Hence, the water vapor concentration

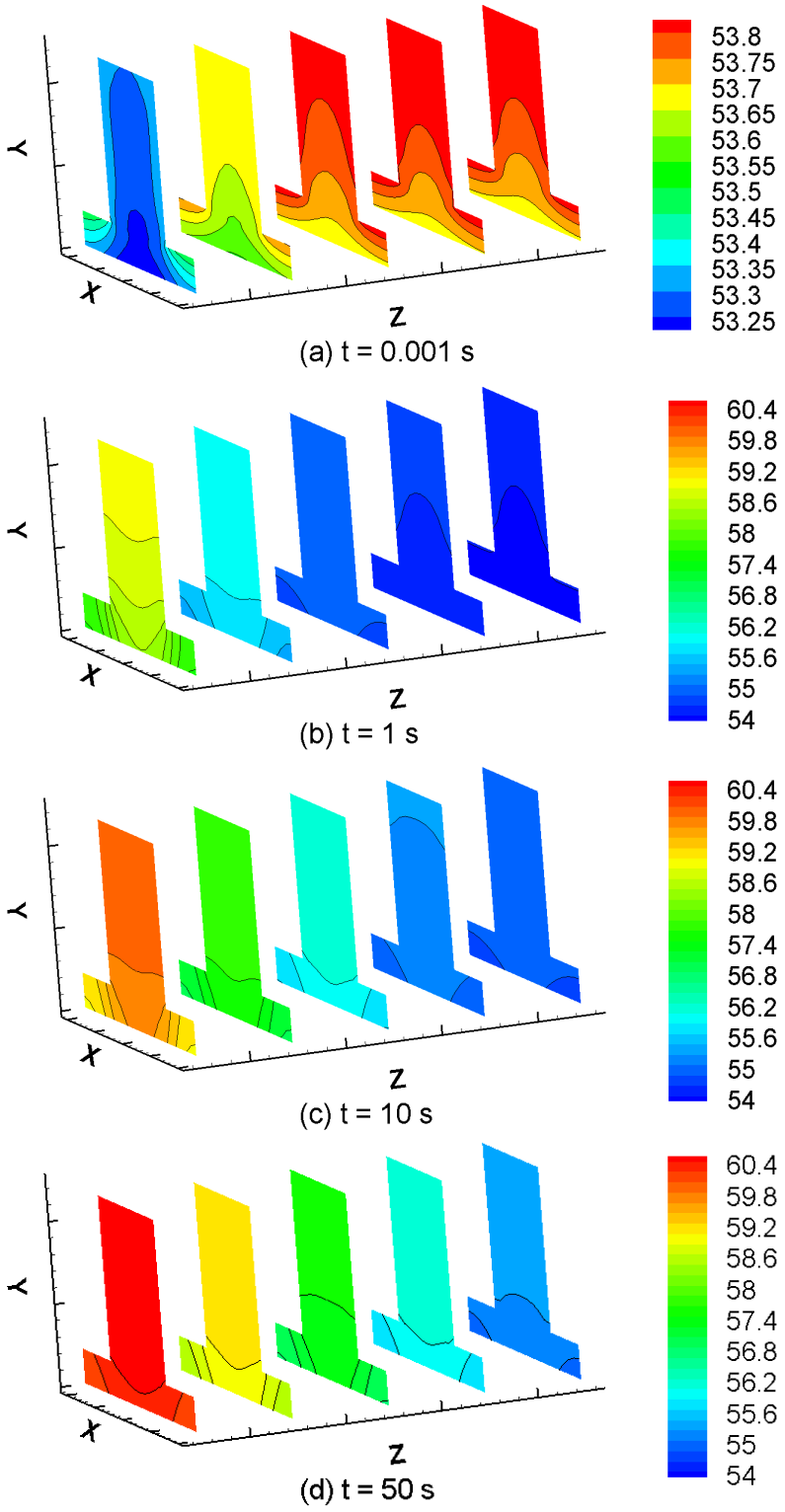

Figure 5.26: Transient variation of the hydrogen concentration, C_{h_2} (mol/m^3), within the anode side gas flow channel, GDL and catalyst layer (from top to bottom): (a) $t = 0.001$ s, (b) $t = 1.0$ s, (c) $t = 10.0$ s, and (d) $t = 50.0$ s.

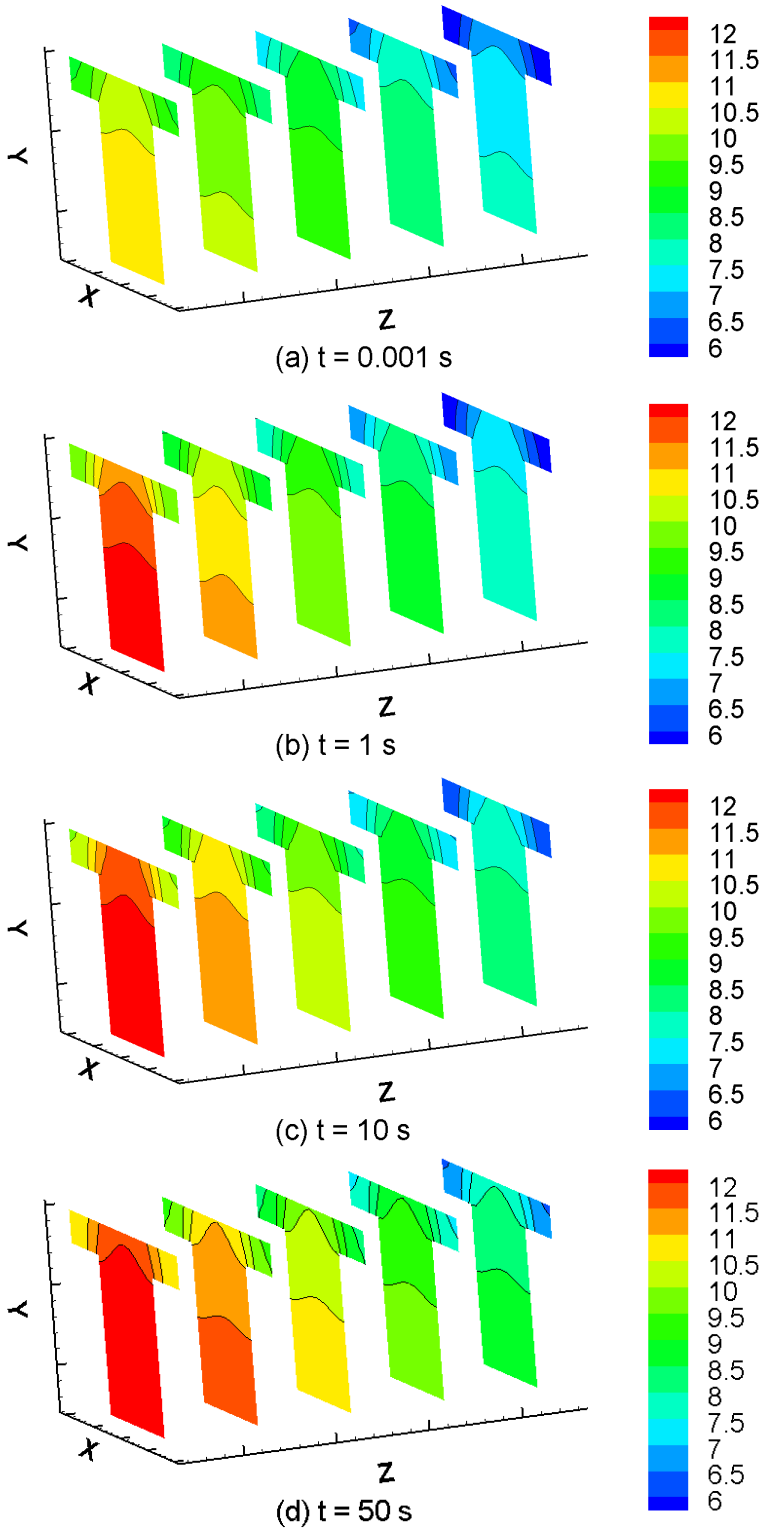

Figure 5.27: Transient variation of the oxygen concentration, C_{o_2} (mol/m^3), within the cathode side gas flow channel, GDL and catalyst layer (from bottom to top): (a) $t = 0.001$ s, (b) $t = 1.0$ s, (c) $t = 10.0$ s, and (d) $t = 50.0$ s.

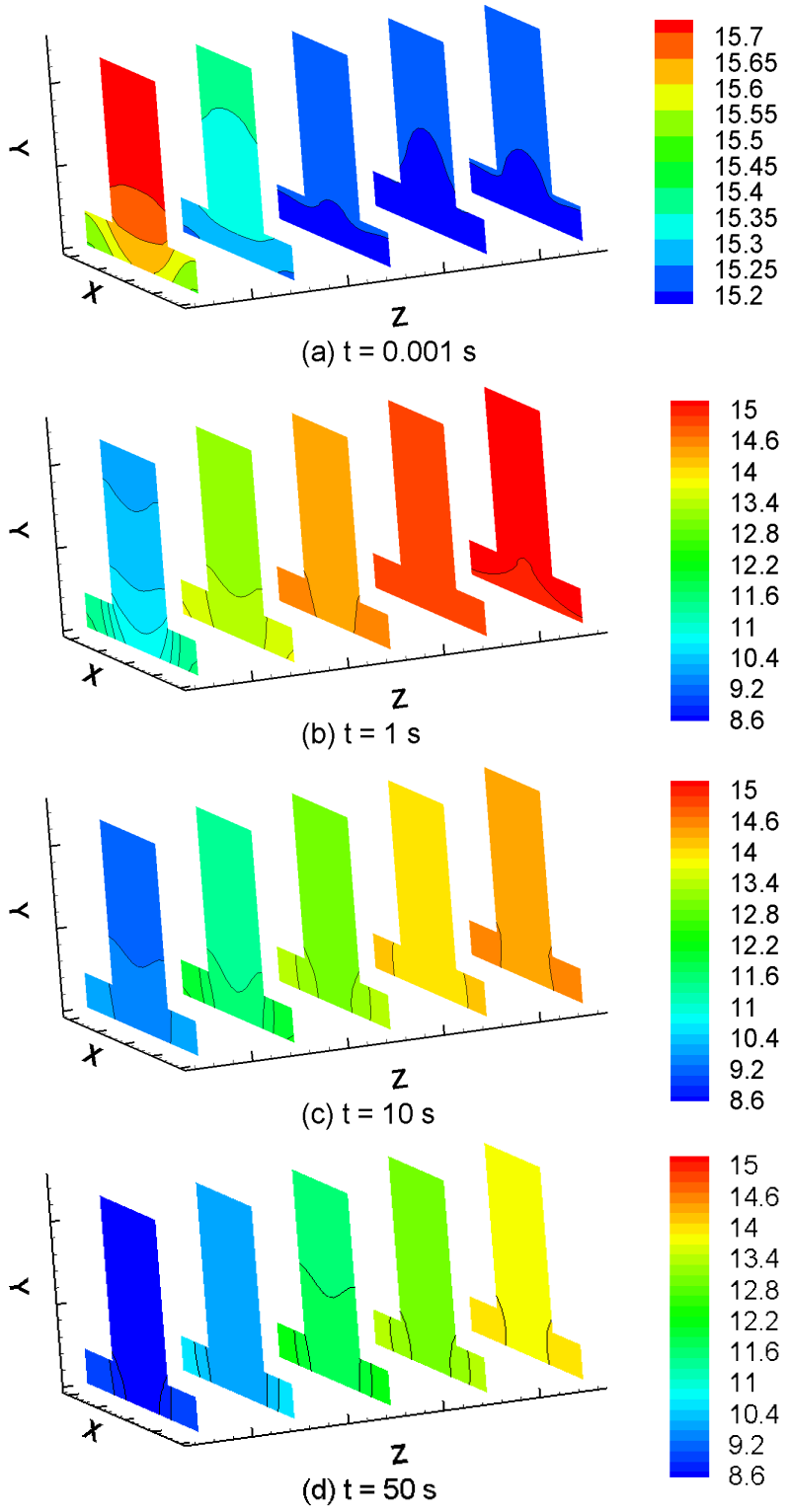

Figure 5.28: Transient variation of the water vapor concentration, C_{h_2o} (mol/m^3), within the anode flow channel, GDL and catalyst layer (from top to bottom): (a) $t = 0.001$ s, (b) $t = 1.0$ s, (c) $t = 10.0$ s, and (d) $t = 50.0$ s.

should remain constant. However, with the thermal effect being considered as in the current study, some of the liquid water will evaporate to water vapor as the local temperature increases due to various heat generation mechanisms. Therefore, the water vapor concentration indeed slightly increases along the channel at fully humidified conditions, as shown in Figure 5.29(a). As time elapses, more liquid water starts to evaporate and it gradually reaches equilibrium with water vapor through the finite rate evaporation/condensation process. Ultimately, Figure 5.29(d) shows that the water vapor concentration drops significantly at the channel inlet region but it increases along the channel as more evaporated vapor joins the flow stream. Approaching the channel outlet, the air is almost kept fully humidified in the GDL and catalyst layer region.

Transport of Dissolved Water

The dissolved water can only exist in the polymer electrolyte, hence, the transport of dissolved water is confined to the ACL, membrane and CCL regions. In practice, the dissolved water concentration is usually converted into a scaled membrane water content, using Equation (3.35), so as to describe the coupling with the equilibrium membrane water content which is determined by the water activity in the vapor phase.

Figure 5.30 demonstrates the dynamic variation of the actual membrane water content in the ACL, membrane and CCL during the relative humidity step decrease. Corresponding to the water vapor transport at both the anode and cathode sides, it is seen that the membrane water content decreases drastically with time, especially at the inlet region where the membrane is more severely dehydrated by the incoming dry gas streams.

In addition, Figure 5.30 also reveals that the anode side membrane dries out more easily during relative humidity decreases. Therefore, a relative higher humidity level for the anode side gas stream should be maintained in practical PEM fuel cell operations so as to prevent the anode from drying out.

Transport of Liquid Water

As shown for the water vapor distribution, the anode side is always under-saturated and, hence, no liquid water is found at the anode side in the current study. On the other hand, water is produced at the CCL in the form of dissolved water. Then, part of the produced water is transferred to the anode side by means of back diffusion; and part of it is converted into liquid or vapor phases during the membrane desorption process. The liquid water then passes through the porous backing layer and is removed by the gas flow in the flow channel.

In Figure 5.31, the dynamic variation of the liquid saturation during the relative humidity step change is displayed. First of all, it shows that the region under the land is always more severely flooded than the region under the channel because

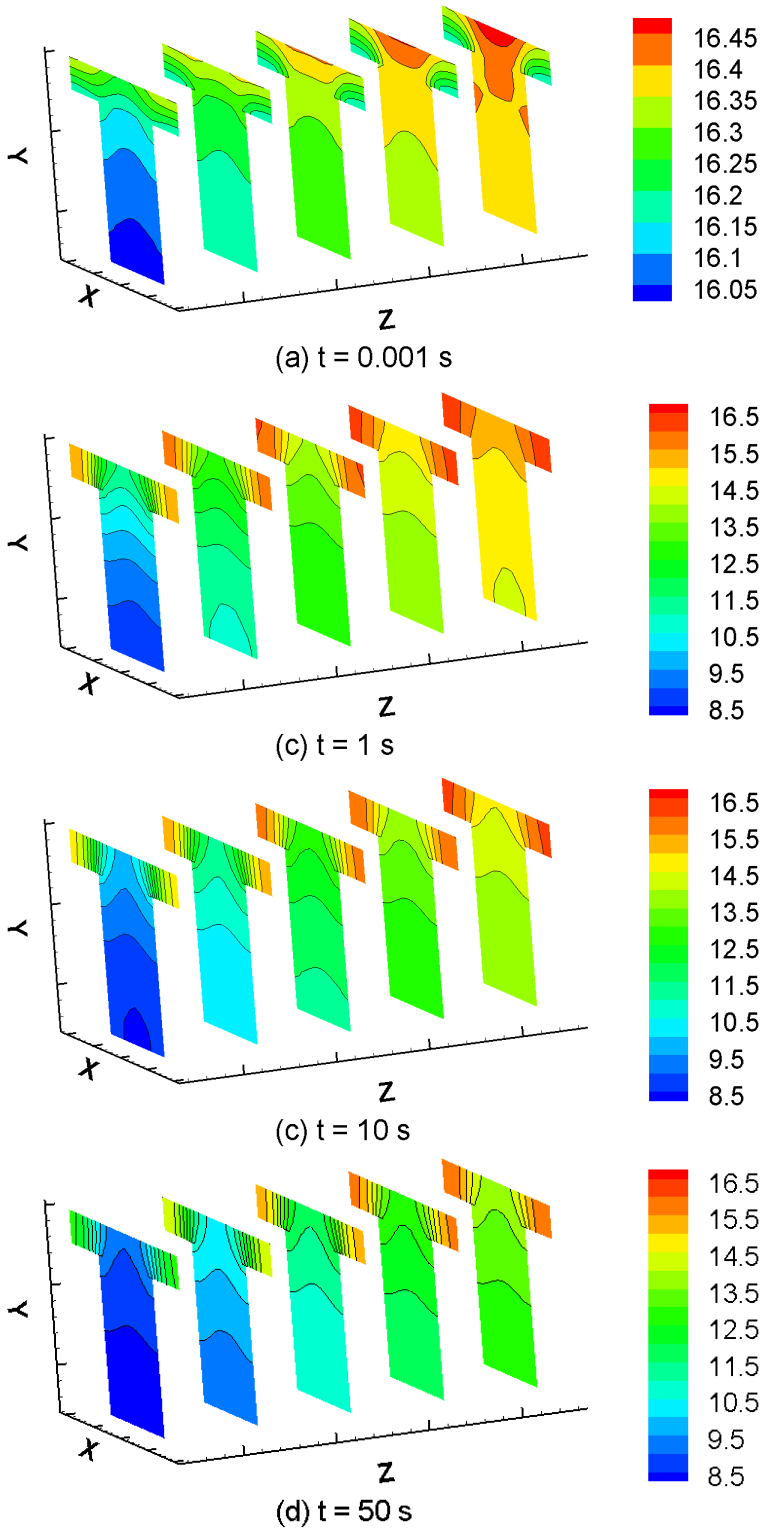

Figure 5.29: Transient variation of the water vapor concentration, C_{h_2o} (mol/m^3), within the cathode flow channel, GDL and catalyst layer (from bottom to top): (a) $t = 0.001$ s, (b) $t = 1.0$ s, (c) $t = 10.0$ s, and (d) $t = 50.0$ s.

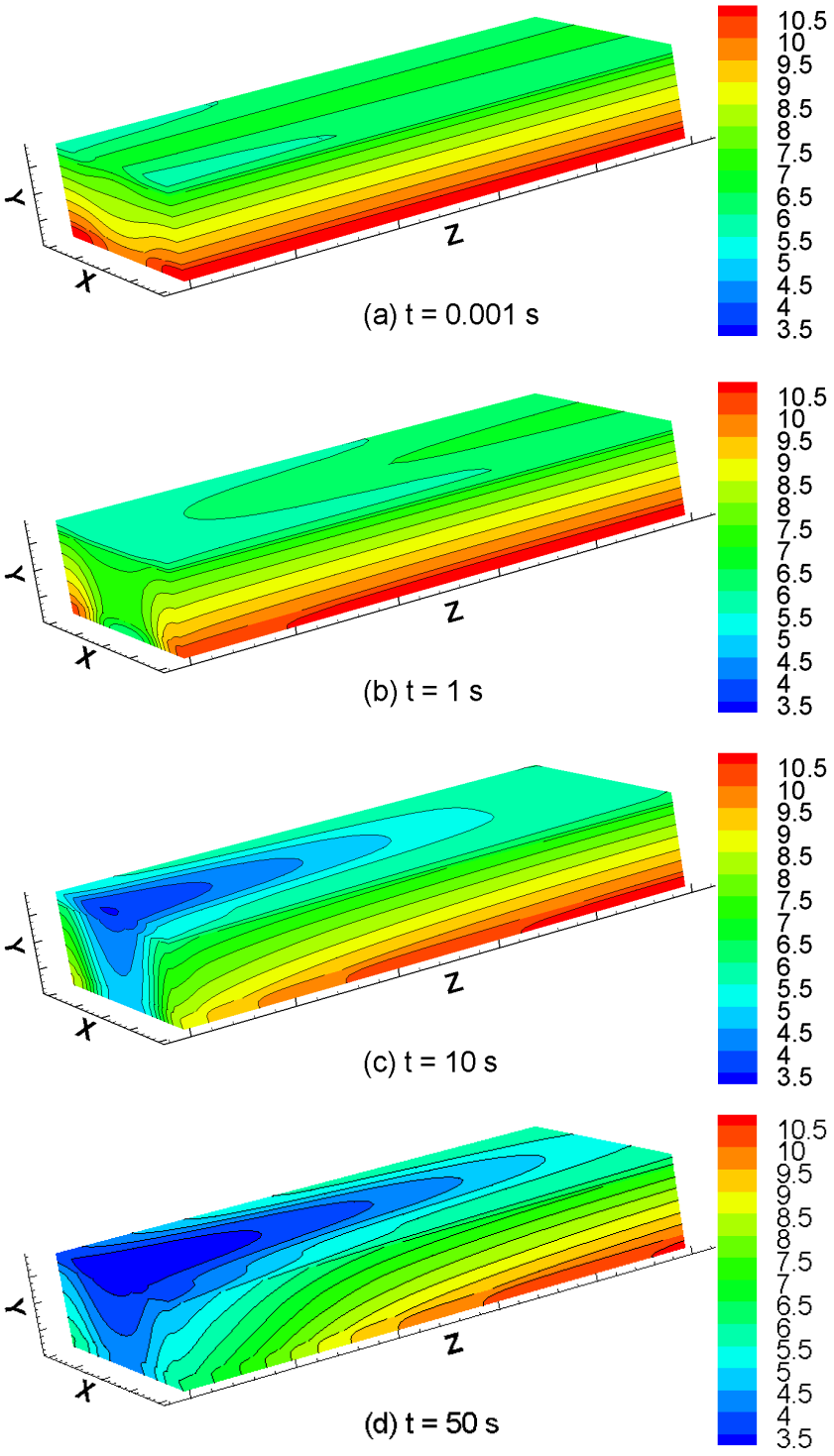

Figure 5.30: Transient variation of the dissolved water (actual membrane water content, λ) within the anode catalyst layer, membrane, and cathode catalyst layer (from top to bottom): (a) $t = 0.001$ s, (b) $t = 1.0$ s, (c) $t = 10.0$ s, and (d) $t = 50.0$ s.

liquid water can be more easily removed by the convective gas flow under the channel. Therefore, certain kinds of channel designs are required in order to enhance the convective flow and thus the liquid water removal under the land region. This will be the main focus in the next chapter. Moreover, Figure 5.31 vividly demonstrates how the liquid water flooding is alleviated during the relative humidity step decrease. As the relatively dry gas flows through the cell, liquid water evaporates to water vapor at the liquid/gas front and the front gradually moves downward till the phase equilibrium is reached at around 50 seconds. This figure may provide some insights into future water management designs.

It should be noted that the cell temperature always fluctuates in the practical operation of PEM fuel cells. If the cell temperature is lower than the gas feed temperature, the fully humidified water vapor may condense at the relative cooler surface of the gas channel and GDL. This could happen on both the cathode and anode side. Therefore, it is also very common to see liquid water flooding at the anode side in real operation. In this study, the inlet gas temperature is always lower than the inside cell temperature. Hence, the above process is of no concern and there is no liquid water present at the anode side.

5.5.3 Transport of Electric Charge

Transport of electric charge occurs almost instantaneously and the transient transport behavior has been usually neglected in the literature, and in this study. The results shown in this subsection are from the steady state simulation running at the base case conditions.

Distribution of Electronic Potential

In Figure 5.32, the distribution of the electronic potential at the middle $x-y$ cross section (Plane 4) of the anode and cathode side GDL and catalyst layer is depicted. As explained in Section 5.3.1, by using Method 2 for the solid potential boundary condition, what the figure really shows here is the ohmic potential losses rather than the real electronic potential within each components of the cell. A macroscopic approach is used in this study and the electronic conductivity of the porous backing layer is assumed to be isotropic. Therefore, the ohmic losses in the backing layer are mainly determined by the electronic current that flows through the solid material. The current density is higher under the land than under the channel (more details will be presented shortly). Consequently, it is seen that the potential varies more significantly under the land than under the channel.

Distribution of Protonic Potential

In Figure 5.33, the distribution of the protonic potential loss at the middle $x-y$ cross section (Plane 4) of the ACL, membrane and CCL is shown. The conductivity

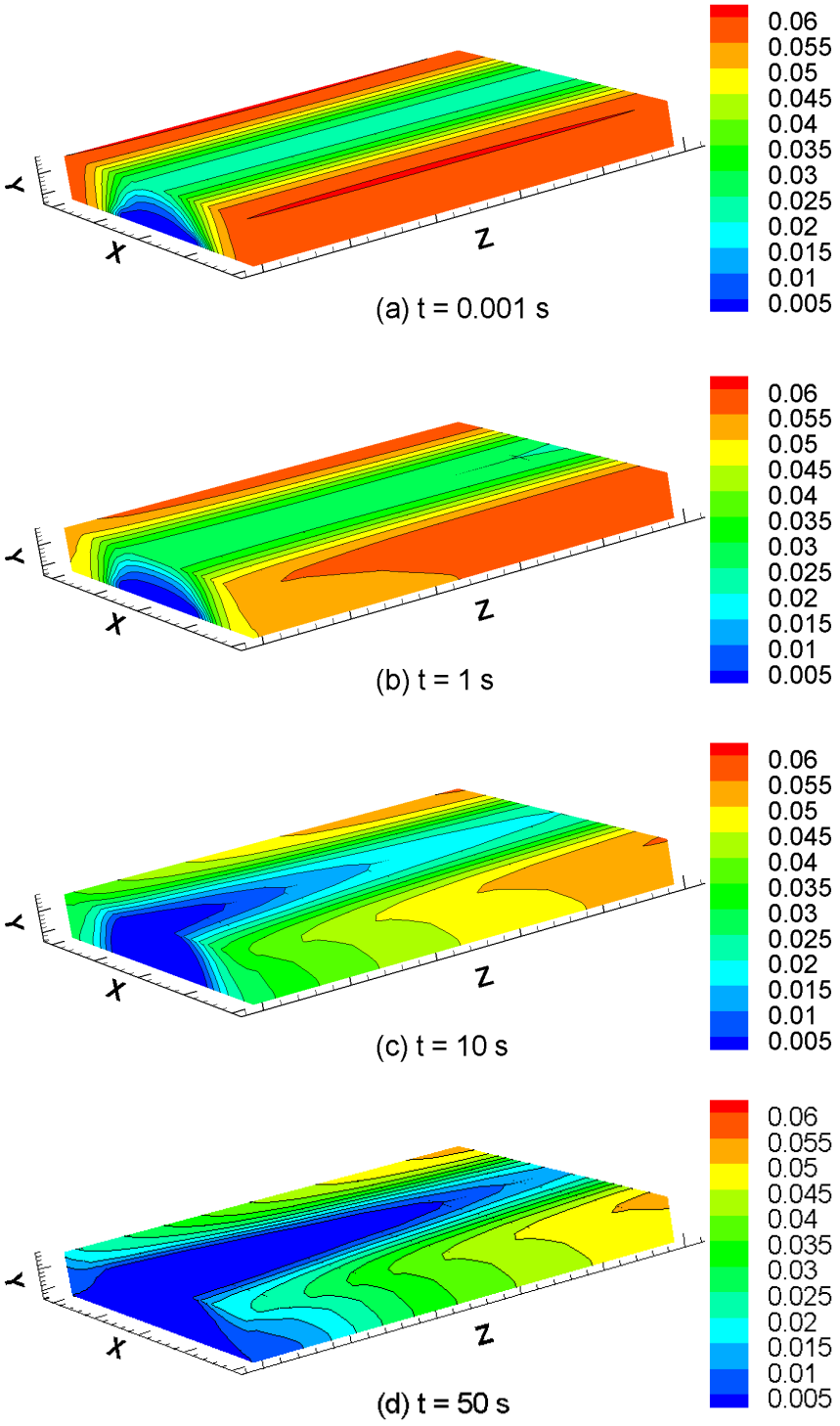

Figure 5.31: Transient variation of the liquid saturation, s, within the cathode side GDL and catalyst layer (from bottom to top): (a) $t = 0.001$ s, (b) $t = 1.0$ s, (c) $t = 10.0$ s, and (d) $t = 50.0$ s.

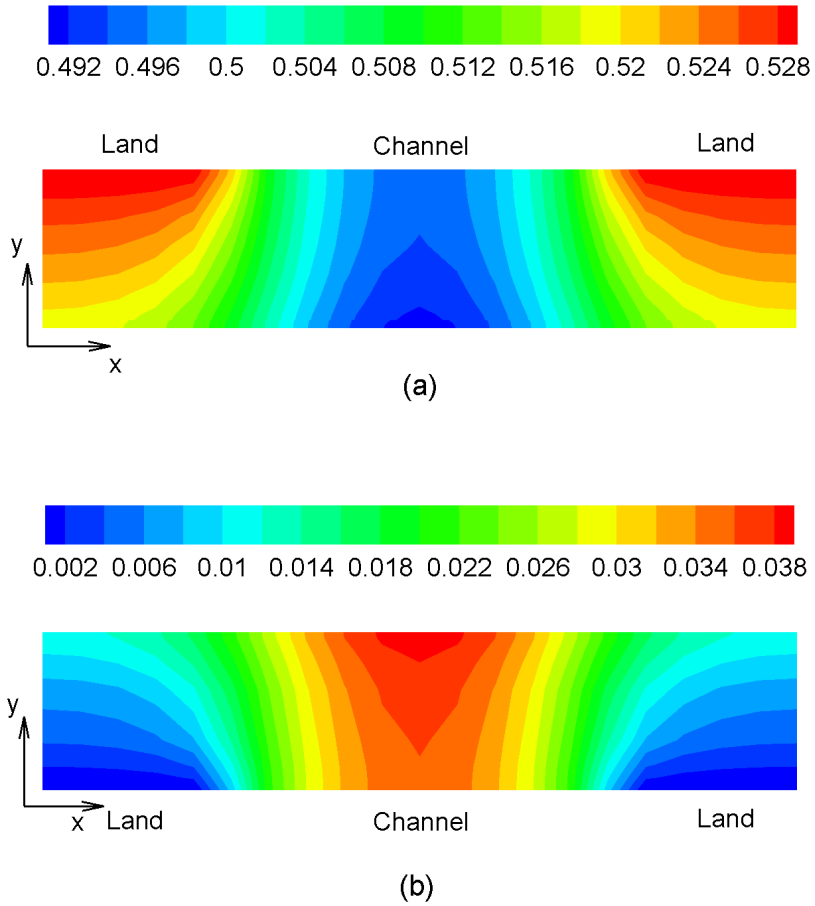

Figure 5.32: Distribution of the electronic potential loss, ϕ_s (V), at the middle $x-y$ cross section (Plane 4) of the GDL and catalyst layer: (a) anode side, (b) cathode side.

of the polymer membrane is much smaller than that of the backing layer. Therefore, it is seen that the maximum potential loss within the polymer membrane (around 0.1 V) is more than double that of the GDL&CL (less than 0.04 V), even though the membrane is much thinner than the backing layer. This figure discloses that the main ohmic loss of a PEM fuel cell is due to the proton transport in the electrolyte polymer.

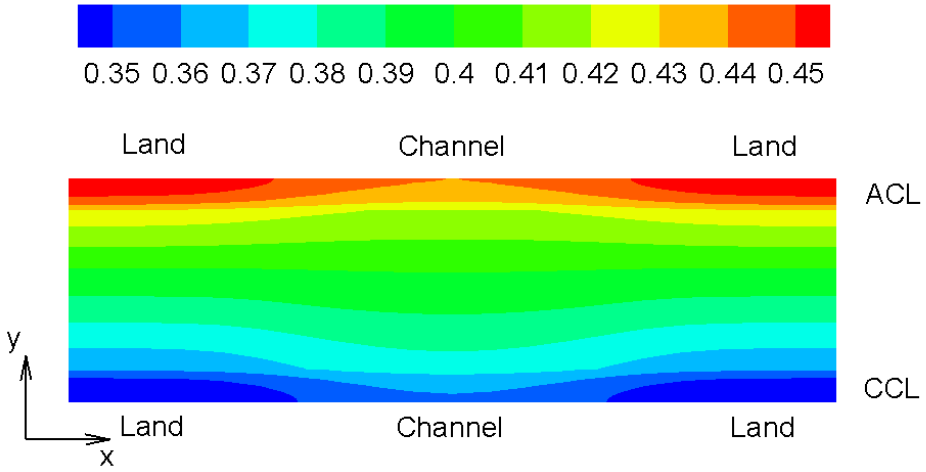

Figure 5.33: Distribution of the protonic potential, ϕ_m (V), at the middle $x-y$ cross section (Plane 4) of the ACL, membrane, and CCL.

Distribution of Current Density

The transport of electrons leads to electronic current in the solid matrix of the backing layer. Similarly, the transport of protons causes protonic current in the polymer electrolyte. In the catalyst layer, both the electronic and protonic currents coexist.

The distribution of the electronic and protonic current density at the middle $x-y$ cross section (Plane 4) of the CCL is shown in Figure 5.34. Current density is a vector quantity and only the transverse component (y-direction) contributes to the power output. Hence, only the y-component is shown here. For the electronic current density (Figure 5.34(a)), it decreases from the GDL towards the membrane and it finally drops to zero at the membrane/CL interface because the electron is not allowed to enter the membrane. In contrast, the distribution of the protonic current density (Figure 5.34(b)) is just opposite to that of the electronic current density. It decreases from the membrane towards the GDL and diminishes at the GDL/CL interface because the proton can not penetrate the backing layer.

The total current density within the catalyst layer is simply the summation of the electronic and protonic current density and it is shown in Figure 5.34(c). This

figure clearly demonstrates the effect of bipolar plates on the electric charge transfer: electrons under the land can be readily removed or supplied by the bipolar plate while the electrons under the channel have to travel a longer path. Accordingly, the current density under the land is higher than that under the channel.

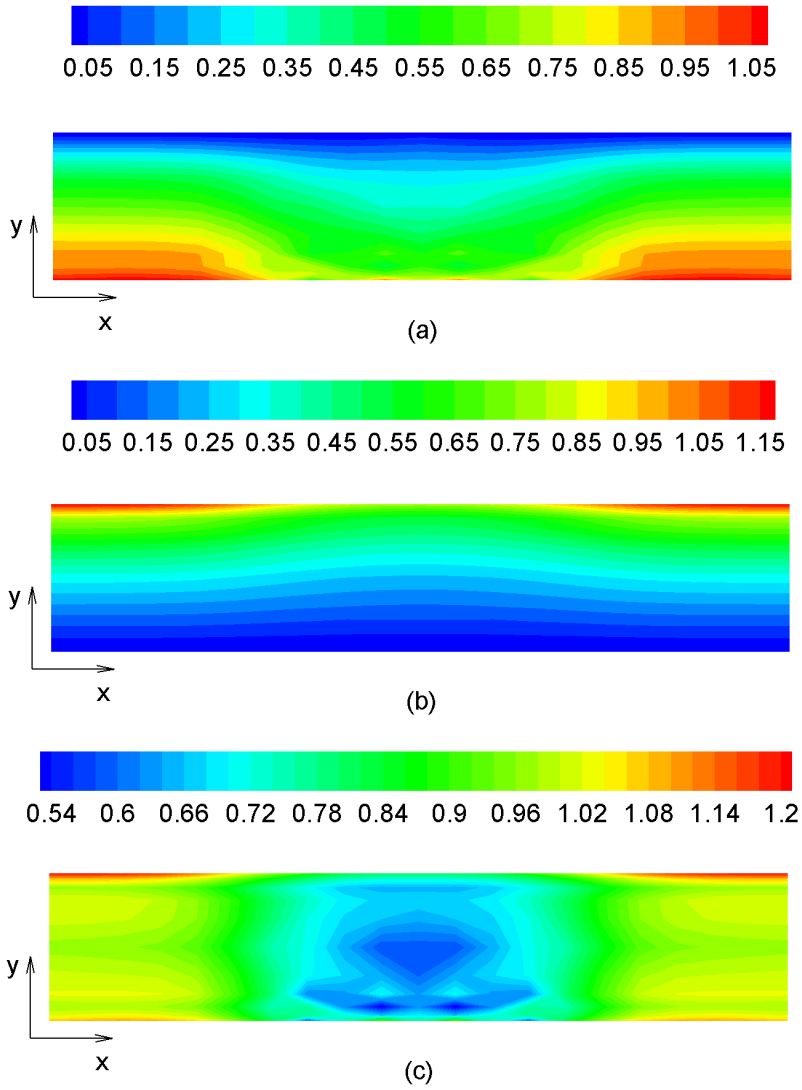

Figure 5.34: Distribution of the transverse current density, J^y, at the middle $x-y$ cross section (Plane 4) of the cathode catalyst layer: (a) electronic current density, J_s^y, (b) protonic current density, J_m^y, and (c) total current density, $J^y = J_s^y + J_m^y$.

The overall current output is also determined by the current density distribution along the flow channel direction. In Figure 5.35, the distribution of the transverse (y-direction) current density on Plane 2 (refer to Figure 5.1) is shown. Under fully humidified conditions (Figure 5.35(a)), the membrane is well hydrated and the current density is mainly dominated by the oxygen availability. The oxygen concentration decreases from the channel inlet towards the outlet. Hence, the cur-

rent density also varies in a similar pattern. Under partially humidified conditions, however, the cell performance is more dominated by the membrane water content, which increases from inlet to outlet. Consequently, it is seen that the current density increases along the channel. In both figures, the current density is higher under the land region than that under the channel, which is the same as Figure 5.34.

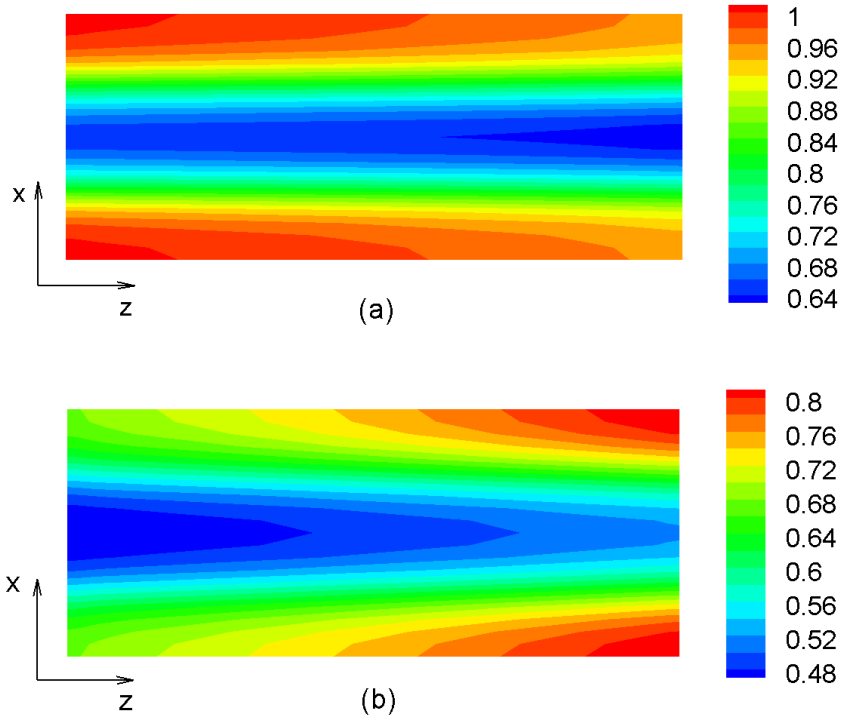

Figure 5.35: Distribution of the transverse current density, J^y (A/cm^2), at the middle $x-z$ cross section (Plane 2) of the membrane: (a) $RH_{a,c} = 1.0$, (b) $RH_{a,c} = 0.5$.

In Figure 5.36, the current distribution across the cell (x-y plane) gained from an experimental work [141] is demonstrated. The current distribution at various load conditions were investigated and it shows that the current distribution is indeed load dependant. At low loads, the measured distribution is very similar to the predicted trends of the present model, which is higher under the rib (land) than under the channel. Therefore, the current distribution is resistance-dominated at low loads operating conditions. As the load reaches extremely high, oxygen transport under the land is greatly impaired due to the increased oxygen consumption rate and liquid water flooding level. Consequently, the current distribution is mass transport dominated and it is seen that the current peak appears under the channel. The load usually resides in the low to middle range in the practical operation of PEM fuel cells. Thus, the present model could predict the current distribution reasonably well.

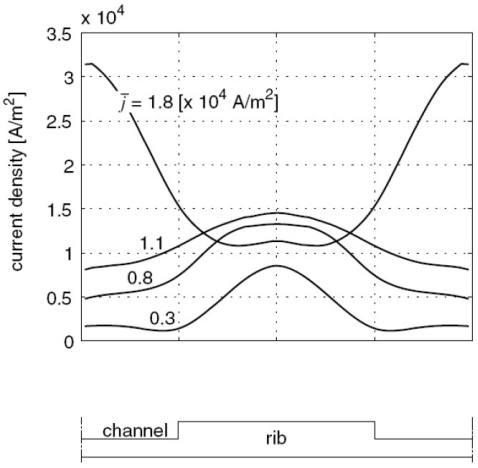

Figure 5.36: Current density distribution from experimental measurement [141].

Reaction Kinetics

Figure 5.37 illustrates the distribution of the activation overpotential within the anode and cathode side catalyst layers. Obviously, the activation overpotential in the CCL is much larger than that in the ACL. This is because the HOR can occur easily in the ACL, and a very small overpotential is sufficient to drive the reaction. However, this is not true at the CCL, where the ORR is more obstinate and a much larger overpotential is required to drive the reaction.

The distribution of the volumetric reaction rates corresponding to the HOR and ORR, is shown in Figure 5.38. It is surprising that the reaction rate is increasing from the GDL to the membrane, although the reactants (hydrogen & oxygen) concentration is decreasing as shown in Figure 5.26 & 5.27. This might be explained by the Butler-Volmer equation, Equation (3.22), where the activation overpotential appears in the exponential term and might therefore have a more significant impact than the concentration term. Consequently, the reaction rate depends on the distribution of the activation overpotential which increases from the GDL to the membrane, and from the region next to the channel to the region adjacent the land.

5.5.4 Transport of Energy

The transient variation of the cell temperature during the step change in relative humidity is demonstrated in Figure 5.39. As elucidated in Section 3.5, various heat generation mechanisms, ranging from the reaction heat, ohmic heat, to the latent heat during various phase transfer processes, are considered in the current model. Among those, the heat generated from the ORR is the most dominant one. Hence, it is seen that the temperature in the CCL is usually higher than in other regions most of the time. However, this situation is changed after about 1 second into

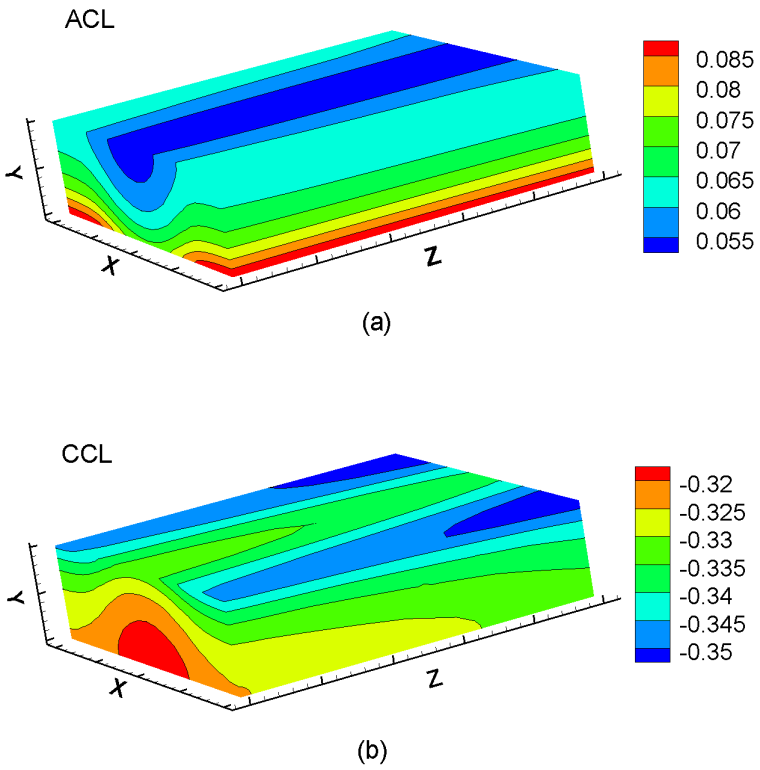

Figure 5.37: Distribution of the activation overpotential, η (V), within the: (a) anode catalyst layer, (b) cathode catalyst layer.

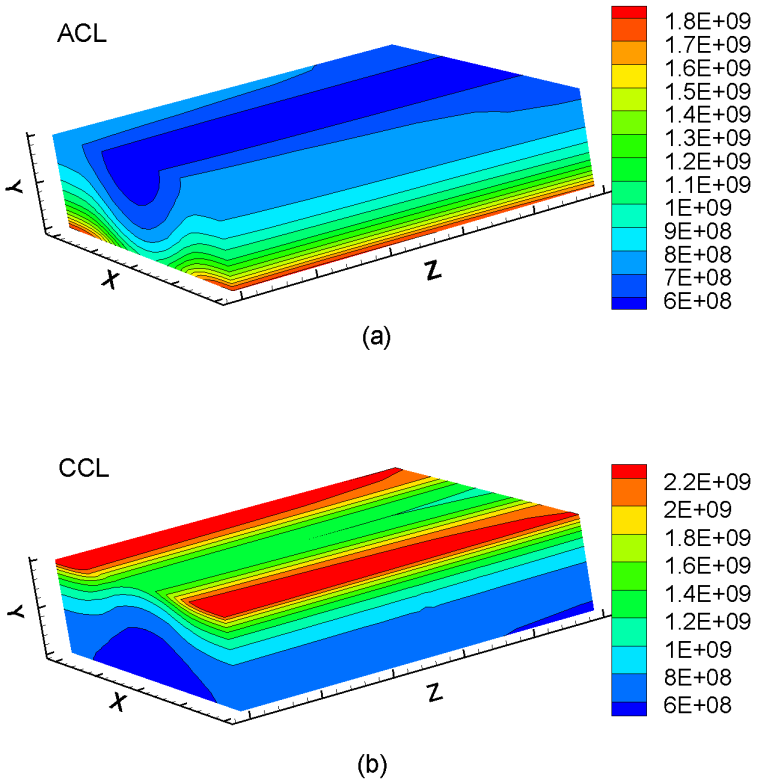

Figure 5.38: Distribution of the volumetric reaction rate, $\mathcal{R}_i$ (mol/m^{3}s), at: (a) anode catalyst layer, (b) cathode catalyst layer.

the step change at which a "cold" spot appears at the CCL and GDL close to the cell inlet. The local temperature drops drastically from about 354.2 to 352.4 K, as shown in Figure 5.39(b). In fact, the liquid water will start to evaporate once it met the incoming dry gas and the evaporation will continue unless all liquid water is evaporated or, locally, a fully humidified condition is reached. Accompanying the evaporation process, a significant amount of heat is absorbed, thereby cooling down the cell. The temperature at the "cold" spot recovers once all the liquid is evaporated, as can be seen in Figure 5.39(c).

Furthermore, it can be seen that the temperature increases along the channel before the step change (Figure 5.39(a)), but it decreases along the channel once the new steady state is reached after the step change (Figure 5.39(d)). This trend resembles the variation of the current density shown in Figure 5.35(a) & (b), indicating that the temperature distribution along the cell (z-direction) is dominated by the current density distribution in terms of the ohmic heating effect. On the other hand, the temperature distribution across the cell ($x-y$ plane) is more dominated by the reaction heat effect, thus the temperature decreases from the CCL towards both the anode and cathode flow channels.

5.6 Summary

In this chapter, the results from the single-channel model are presented. Firstly, several approaches traditionally used in modeling studies have been examined. It is found that the most widely used methods for the specification of the boundary condition for the solid phase potential is numerically not the most efficient and most stable. Moreover, the equilibrium model for the membrane sorption/desorption processes tends to underestimate the cell current output, even under steady conditions, and the cell response time if transient phenomena are of concern for which a non-equilibrium model with finite sorption/desorption rates should be used. The effect of the water production mechanism during the half cell reaction (ORR) on the cell performance has also been investigated; the assumption of vapor or liquid water production mechanisms may cause non-negligible discrepancies in the cell performance. Water produced in the membrane should be considered as the proper mechanism of water formation in practical PEM fuel cells. Capillary pressure and relative permeability have a significant effect on water transport, and relative permeability has an even greater impact on the liquid water transport than the capillary pressure.

The model is measured against experimental results by means of a voltage sweeping study and qualitative agreement is achieved. It shows that the hysteresis effects are caused by the sluggish membrane hydration/dehydration and sorption/desorption processes. A sinusoidal impedance approach is employed to identify the time scales for different dynamic transport processes and it is found that the time scale for heat transfer is about 10 seconds, while the time scale for various water transport processes are closely correlated and the slowest is on the

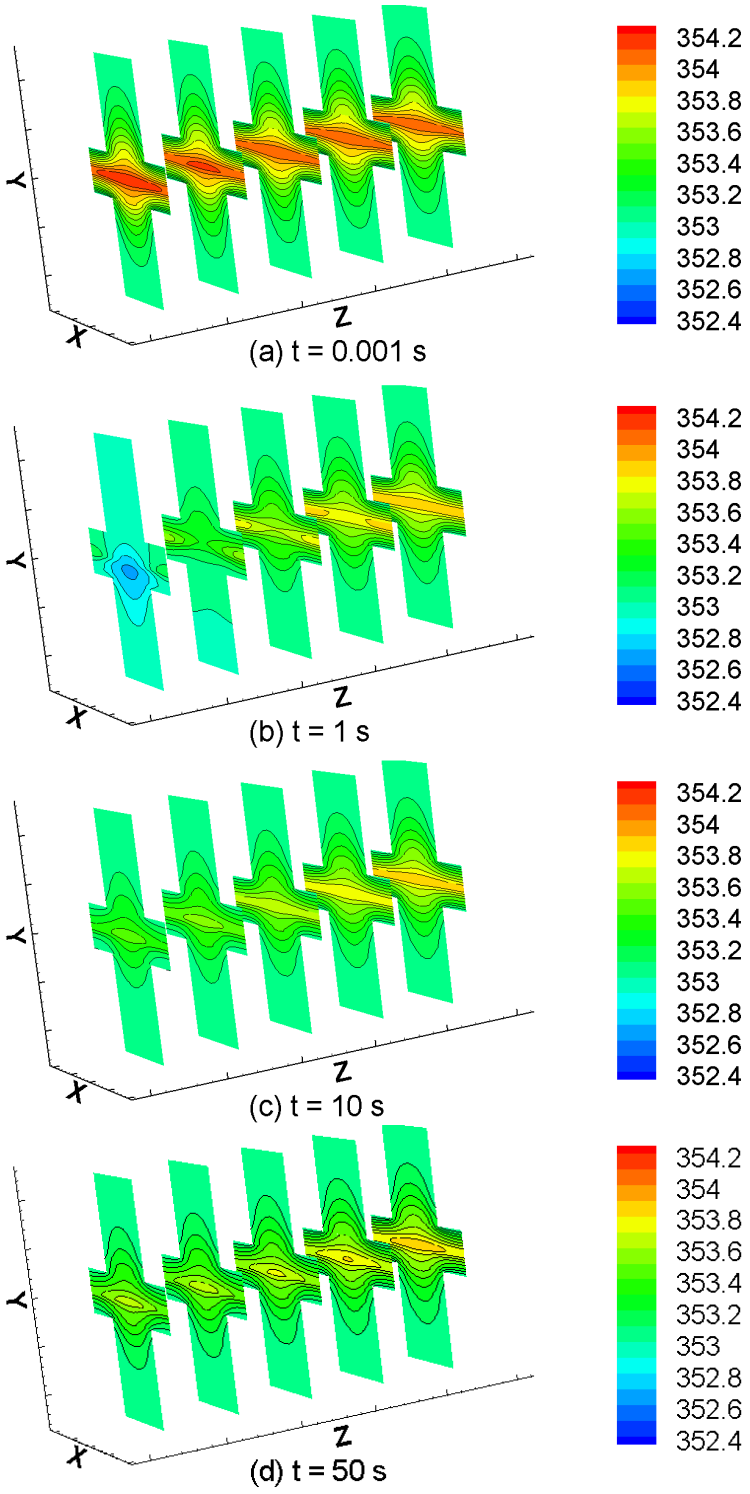

Figure 5.39: Transient variation of the cell temperature, T (K): (a) $t = 0.001$ s, (b) $t = 1.0$ s, (c) $t = 10.0$ s, and (d) $t = 50.0$ s.

order of 100 seconds. The study of step changes in operating conditions demonstrates that the current overshoot is slightly larger when a voltage step change is performed at high current densities; the pressure effects are more significant at low pressure conditions; the current overshoot decreases with the increasing of gas flow pressure; and the increase of the gas flow rate does not influence the cell current significantly, except in the mass transport limitation region.

Finally, using the step change in relative humidity as an example, various transient transport phenomena within the PEM fuel cells, specifically, the transport of gas species, multi-water phases, electric charge, and energy are disclosed and analyzed. It is found that the distribution of hydrogen and oxygen greatly depends on the water vapor transport which, in turn, is coupled with the transport of liquid and dissolved water. The electric charge transfer behavior is mainly determined by the electrochemical reactions which is more drastic under the land than under the channel. The temperature distribution is a compromise of various heat generation/absorption mechanisms. In general, the temperature across the cell is dominated by the reaction heat, while the temperature along the channel is more dominated by the ohmic heat effect.

Chapter 6

Results and Discussion – Part II: Multi-Channel Model

The performance of PEM fuel cells greatly relies on the gas transport processes. Therefore, an optimum flow channel layout which is capable of feeding the reactants more uniformly to the reaction site is highly desirable. Furthermore, the bipolar plates, into which the gas flow channels are grooved, make up for about 80% of the total weight of PEM fuel cells. Hence, a careful design of the flow-field may reduce the cell weight and the overall cost significantly. A variety of flow channel configurations and layouts have been proposed in different designs, including pins, straight parallel channels, interdigitated channels, serpentine channels, integrated channels and channels formed from sheet metals. These different flow field designs have pros and cons associated with them which in turn make them suitable for different applications. A comprehensive review of up-to-date flow-field designs can be found in [142].

In this Chapter, the three most common channel layouts, namely, the straight parallel channel, interdigitated channel, and serpentine channel, are investigated to show the effects of flow field layout on cell performance. Due to the significantly increased computational expense compared to the single-channel model, only four representative channel branches are considered in the current multi-channel models and the simulations are confined to steady-state only. Nonetheless, the dynamic behavior and the underlying transient transport phenomena of the multi-channel model can be deduced from the single-channel modeling results presented in the previous chapter.

6.1 Computational Domain

Figure 6.1 shows the channel layouts of the three kinds of flow-field design. The straight parallel channel layout simply has four separate parallel channels that share the same inlet and exhaust headers. The interdigitated channel layout is configured

with two incoming and two outgoing flow channels, and each of them has a dead end. Therefore, the incoming gas has to flow through the porous backing layer to reach the outgoing channels, resulting in an enhanced convective mass transport in the porous backing layer. The serpentine channel layout essentially has only one continuous flow channel that has an inlet at one end and an outlet at the other. Since the channel is relatively long, a substantial pressure drop and a significant concentration gradient from inlet to outlet are expected with this layout.

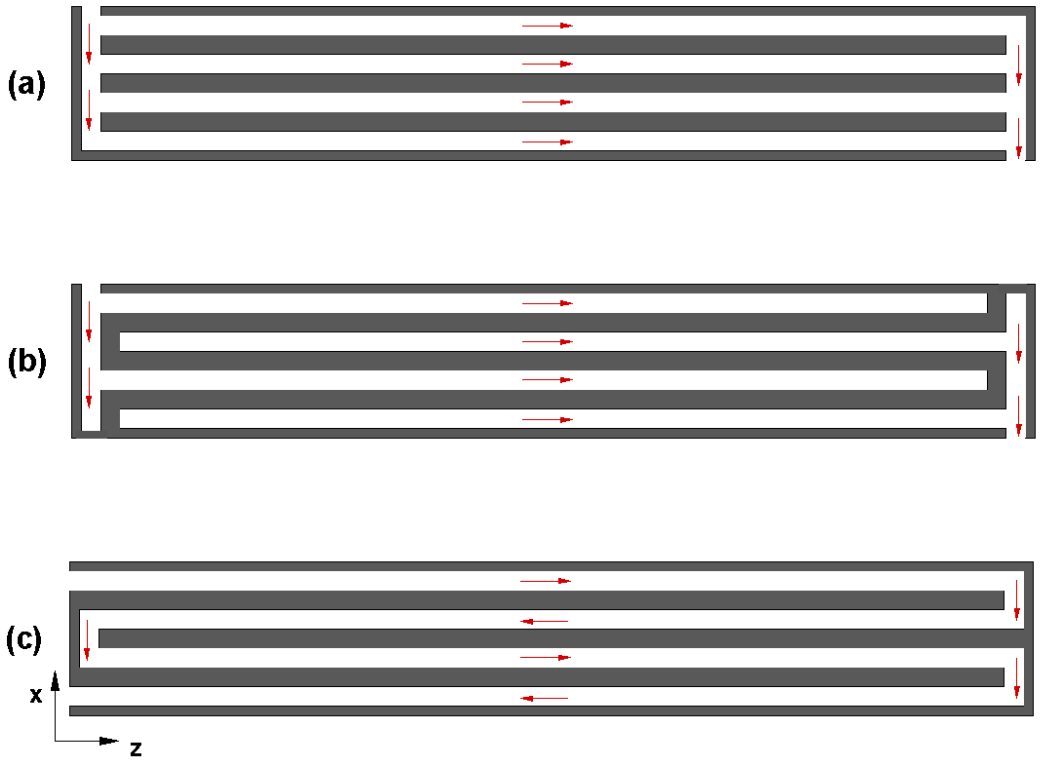

Figure 6.1: Gas flow channel layouts: (a) straight parallel channel, (b) interdigitated channel, (c) serpentine channel.

The PEM fuel cell is simply a membrane electrode assembly (MEA) sandwiched with a certain channel layout at its two sides. In theory and reality, there are many possible combinations of the channel layout for the anode and cathode flow-field. The situation can be more complex if the orientation of the channel inlets and outlets is considered since the location of the inlets and outlets can differ (co-flow, intersect-flow and counter-flow, etc.) between the two sides, even if the same pair of channel layout is chosen. In this study, only the simplest case, i.e. same pair of channel layout and co-flow, is investigated. The mesh of the current multi-channel computational domain has been shown in Figure 4.7 and are not repeated here.

The same set of parameters, as used in the single-channel model (Table 3.1-3.3), are maintained in the multi-channel model, except for the stoichiometric ratio for which the serpentine channel layout has experienced convergence difficulties with

stoichiometric ratios of 1.2 for the fuel and 2 for the air stream, implying that the serpentine channel design is more likely to cause mass concentration limitations compared to the other two designs. Finally, two increased stoichiometric ratios (2 at the anode side and 4 at the cathode side) are used for all three channel layouts.

A detailed description of various transport phenomena and electrochemical kinetics have been made in the previous chapter. Hence, to avoid unnecessary details the results and discussion presented below will mainly focus on the mass transport effects caused by the flow-field configurations.

6.2 Flow Field

In Figure 6.2, the gauge pressure distribution at the cathode side flow channel, GDL and catalyst layer is demonstrated. The plots at the top of each figure show the pressure distribution at the middle $x - z$ cross-section of the gas flow channel. The plots at the bottom of each figure show the pressure distribution at 5 slices located at z/L_{ch} =1/10, 3/10, 5/10, 7/10 and 9/10, respectively. The pressure difference between the channel inlet and outlet represents the pressure drop through the cell. For the straight parallel channel, each channel is short and connects directly to the flow manifolds. Therefore, the pressure drop is very small, only about 63 Pa. In contrary, there are no direct flow paths in the interdigitated channel layout and the gas flow has to pass through the gas diffusion layer to reach the adjacent outgoing flow channels. Therefore, the flow resistance is quite large in the interdigitated channel layout, resulting in a substantial pressure drop between adjacent flow channels. The pressure drop in the serpentine channel layout is also very large. This is because the length of the serpentine channel is more than four times that of the straight parallel channel, thus the friction loss along the channel is significantly increased. Moreover, minor pressure losses arise from the channel bend and the secondary flows around the channel U-turn region.

Figure 6.3 demonstrates the velocity profiles on the same slices as in the previous figure for three flow channel layouts. Corresponding to the pressure distributions, the velocity profile in the flow channel and porous backing layers are totally different among three layouts. In Figure 6.3(a), the maximum channel flow appears in the bottom (4^{th}) channel next to the manifold outlet, and the velocity in the channel decreases as closer to the manifold inlet. In Figure 6.3(b), the optimum flow field appears in the two center (2^{nd} and 3^{rd}) channels. At the dead end of each channel, the flow is almost stagnant and the gas is thus forced to pass through the porous gas diffusion layer underneath. For the serpentine channel layout (Figure 6.3(c)), the maximum flow velocity resides in the first and last straight branch of the channel. The velocity in the two center channels is weakened by the cross flow between adjacent channels due to the pressure drop. Furthermore, checking the local Reynolds number shows that the maximum Reynolds number is less than 200 for the current four-channel modeling domains, justifying the laminar flow assumption made in Chapter 3.

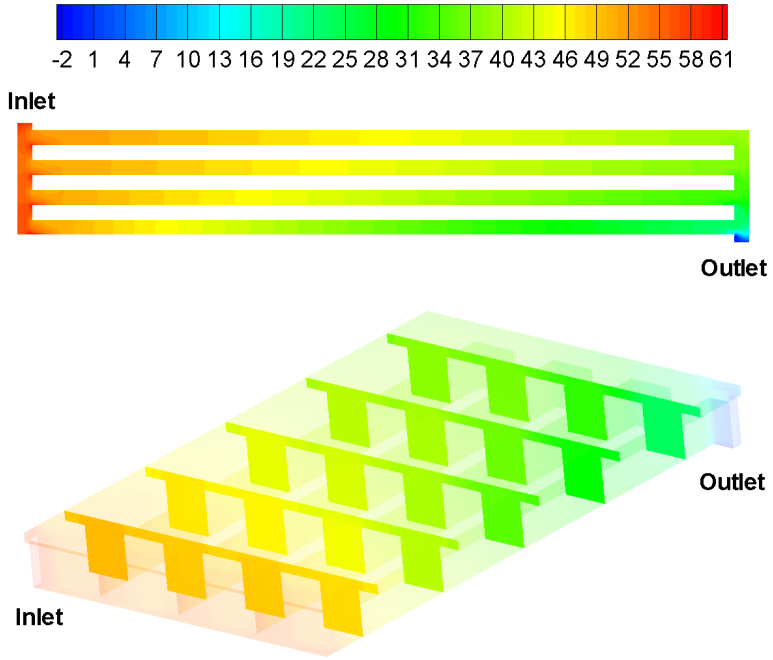
-2 1 4 7 10 13 16 19 22 25 28 31 34 37 40 43 46 49 52 55 58 61
Inlet
Outlet
Outlet
Inlet

(a)

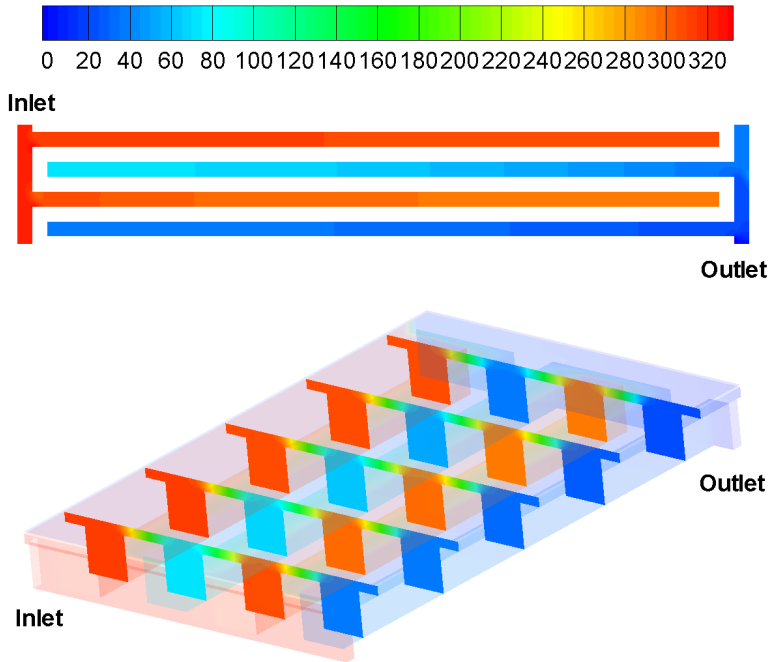
0 20 40 60 80 100 120 140 160 180 200 220 240 260 280 300 320
Inlet
Outlet
Outlet
Inlet

(b)

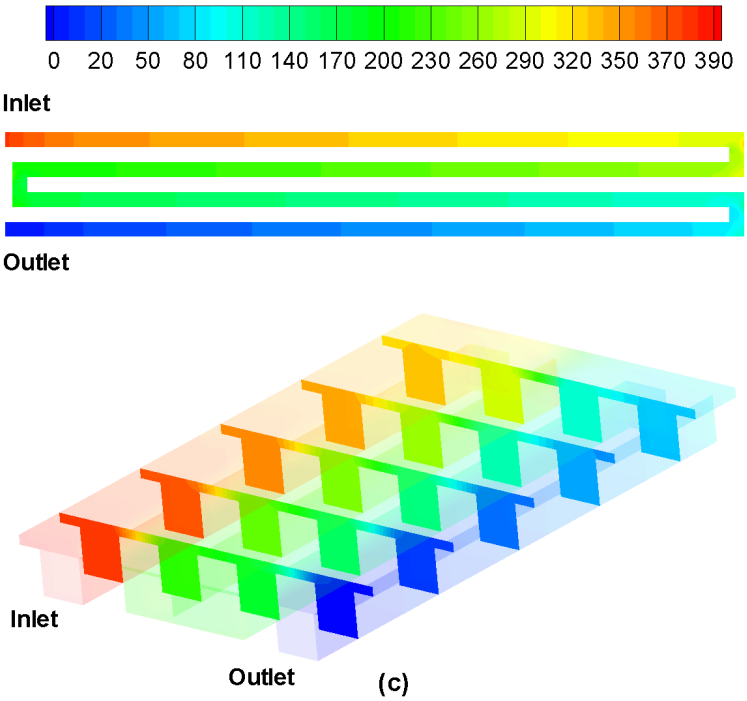

Figure 6.2: Distribution of the gas pressure: (a) straight parallel channel, (b) interdigitated channel, (c) serpentine channel.

In addition, due to the centrifugal effect of the flow stream, a secondary flow forms around the sharp corner of the channel. Figure 6.4 shows the enlarged view of the secondary flow at the channel joint of the interdigitated layout and at the U-turn region of the serpentine layout. These vortices result in enhanced mixing and lead to flow unsteadiness and pressure drops.

The pressure and velocity distribution at the anode side flow channel, GDL and catalyst layer are very similar to the cathode side but with much lower numerical values. The details are not given here. Generally speaking, Figure 6.2-6.4 exhibited the advantage and disadvantage of the three channel designs. Design and fabrication of the straight parallel channel is simple. However, the pressure drop within each flow channel is low. Hence the liquid droplets, once they form in the channel, are difficult to be removed from the cell. Eventually, some of the flow channels may be entirely clogged with liquid water and stagnant areas tend to form at various locations, resulting in poor gas flow distributions. The interdigitated and serpentine flow-field designs are more effective in terms of liquid water removal. However, significant pressure losses arise from such designs, prohibiting their application in large scale cell stacks.

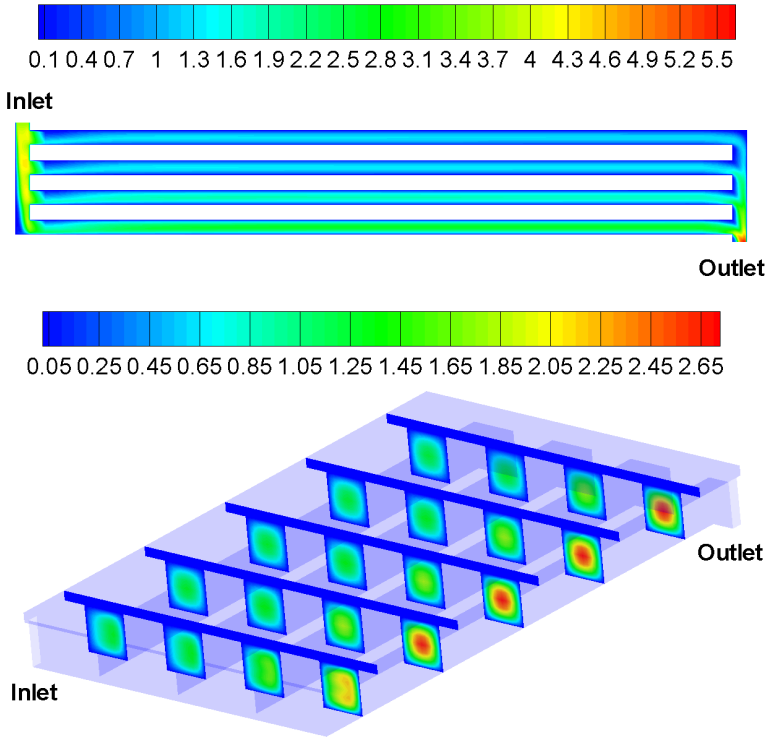
0.1 0.4 0.7 1 1.3 1.6 1.9 2.2 2.5 2.8 3.1 3.4 3.7 4 4.3 4.6 4.9 5.2 5.5
Inlet
Outlet
0.05 0.25 0.45 0.65 0.85 1.05 1.25 1.45 1.65 1.85 2.05 2.25 2.45 2.65
Outlet
Inlet

(a)

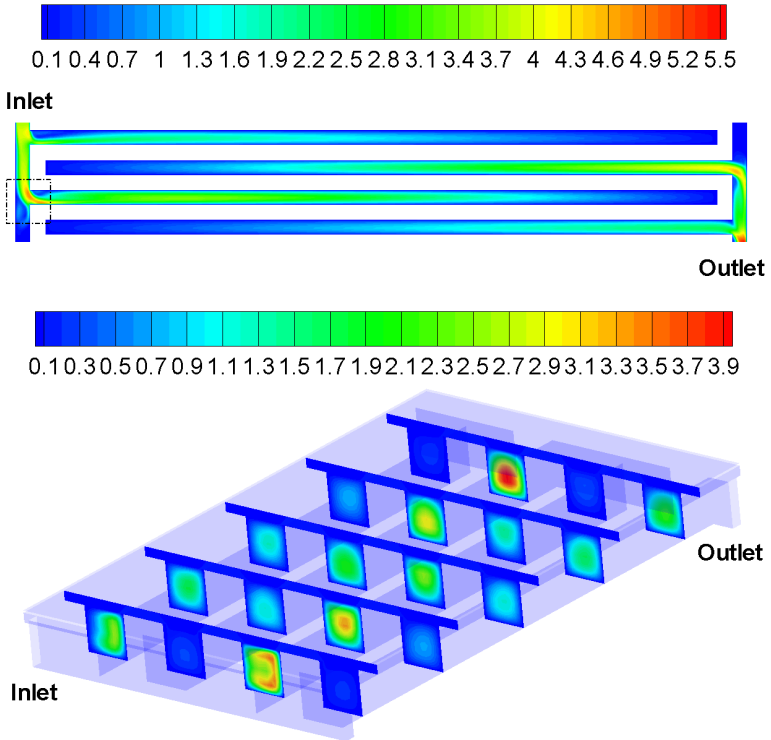
0.1 0.4 0.7 1 1.3 1.6 1.9 2.2 2.5 2.8 3.1 3.4 3.7 4 4.3 4.6 4.9 5.2 5.5
Inlet
Outlet
0.1 0.3 0.5 0.7 0.9 1.1 1.3 1.5 1.7 1.9 2.1 2.3 2.5 2.7 2.9 3.1 3.3 3.5 3.7 3.9
Outlet
Inlet

(b)

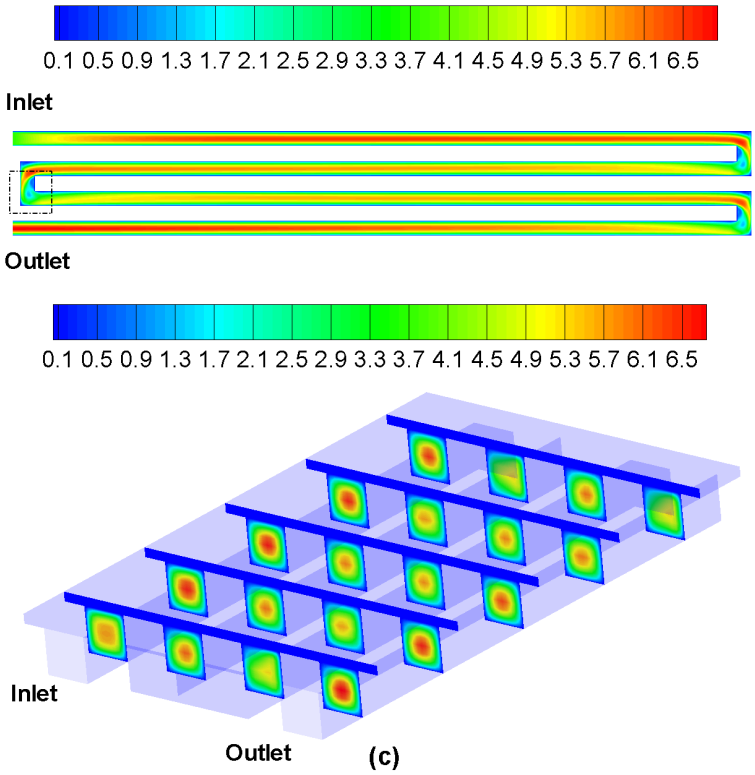

Figure 6.3: Velocity profiles: (a) straight parallel channel, (b) interdigitated channel, (c) serpentine channel.

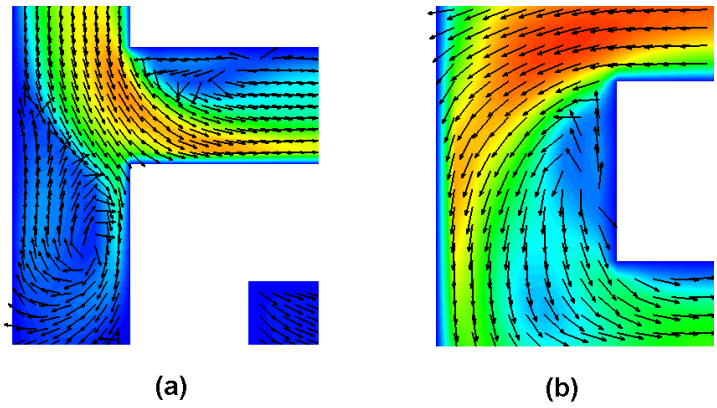

Figure 6.4: Vortex around the sharp corner: (a) interdigitated channel, (b) serpentine channel.

6.3 Oxygen Distribution

The distribution of the oxygen molar concentration in the cathode flow channel, GDL, and catalyst layer is illustrated in Figure 6.5. It can be seen that the oxygen concentration decreases along the flow path from the channel inlet towards the outlet in all three channel layouts. Especially in the interdigitated and serpentine channel layouts, the oxygen concentration at the downstream land region is very low. For the former, this is because the convective mass transfer is weak close to the interdigitated cell boundary where the oxygen is mainly supplied by a diffusion process; for the latter, it is mainly due to the oxygen consumption along the long serpentine flow path. Comparatively speaking, the straight parallel channel layout provides the most uniform oxygen supply. To take advantage of the water removal ability of the serpentine channel and the uniform gas supply of the straight parallel channel, a hybrid design that combines the straight and serpentine channel layouts by using multiple parallel serpentine channels is usually adopted. As such, the length of each serpentine channel is shortened and the pressure drop through each channel is also reduced. Such a patented design is schematically shown in Figure 6.6.

6.4 Liquid Water Distribution

Water management as a whole, and liquid water removal in particular, is probably the most challenging issue that PEM fuel cell technology is facing. At certain operating conditions such as high current densities or low operating temperature (e.g. cold start), electrode pores are prone to be filled with liquid water, impeding reactant transport to catalyst sites. This phenomenon, known as "flooding", is an important limiting factor of PEM fuel cell performance. To avoid liquid flooding, various liquid water removal approaches have been explored in the literature and they are generally categorized into three main groups. The first is through the modification of materials. By coating the GDL and gas flow channel surface with certain hydrophobic materials, or by introducing a micro-porous layer between the GDL and the catalyst layer, liquid water can be more timely removed from the catalyst layer, thus allowing the catalyst for effective reactions. Secondly, liquid water removal can be achieved by adjusting the operating conditions, such as the cell temperature, gas flow temperature, mass flow rate, or operating pressure, etc. Finally, the liquid flooding can also be alleviated by optimum flow-field designs. This is the main objective of the multi-channel model presented in this chapter.

It should be noted that due to the extremely complex two-phase flow behavior in the gas channel, the current model assumes that the liquid water can be instantaneously removed once the liquid droplet emerges at the GDL/channel interface, thus entailing a zero liquid saturation boundary condition at the GDL/channel interface. This is a reasonable assumption for cells with a single straight parallel channel operating with high gas flow rate conditions. In an industrial-sized PEM

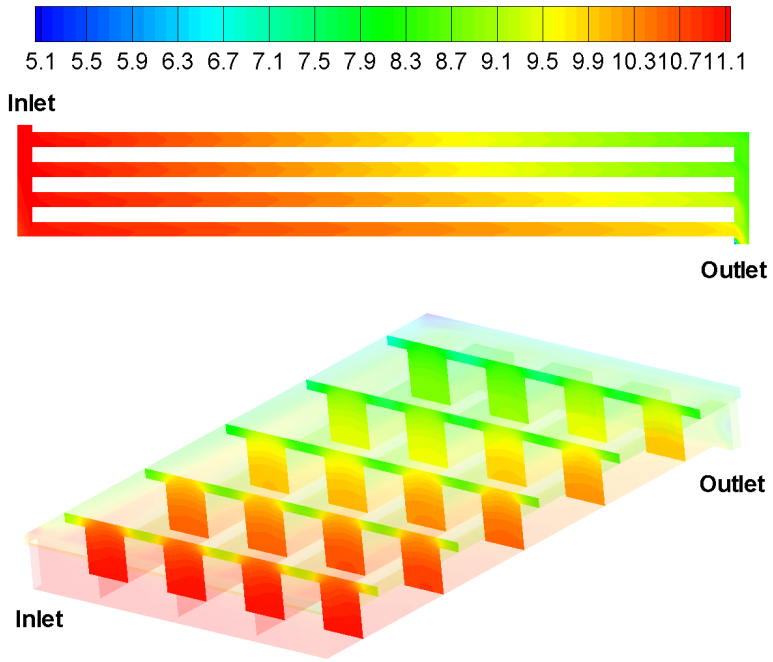
5.1 5.5 5.9 6.3 6.7 7.1 7.5 7.9 8.3 8.7 9.1 9.5 9.9 10.310.711.1
Inlet
Outlet
Outlet
Inlet

(a)

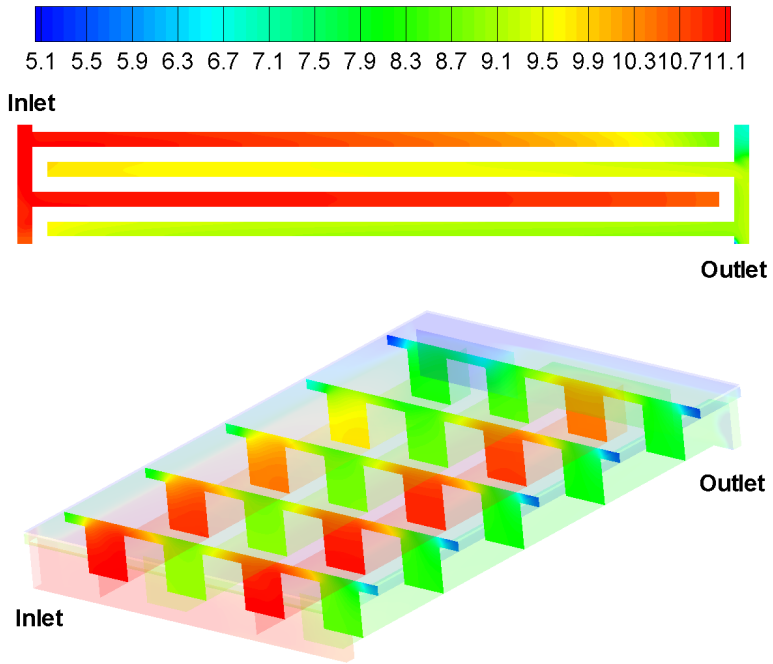
5.1 5.5 5.9 6.3 6.7 7.1 7.5 7.9 8.3 8.7 9.1 9.5 9.9 10.310.711.1
Inlet
Outlet
Outlet
Inlet

(b)

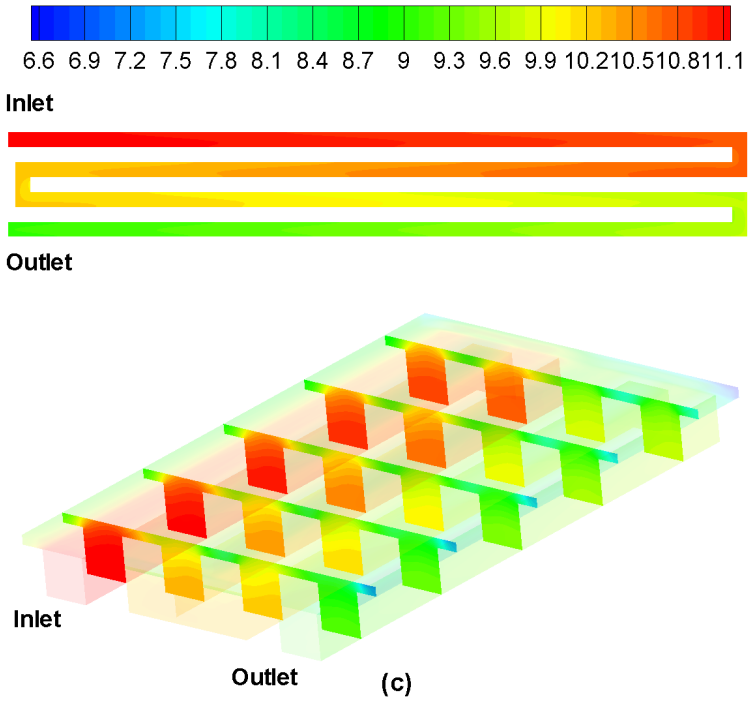

Figure 6.5: Distribution of oxygen concentration (mol/m^3): (a) straight parallel channel, (b) interdigitated channel, (c) serpentine channel.

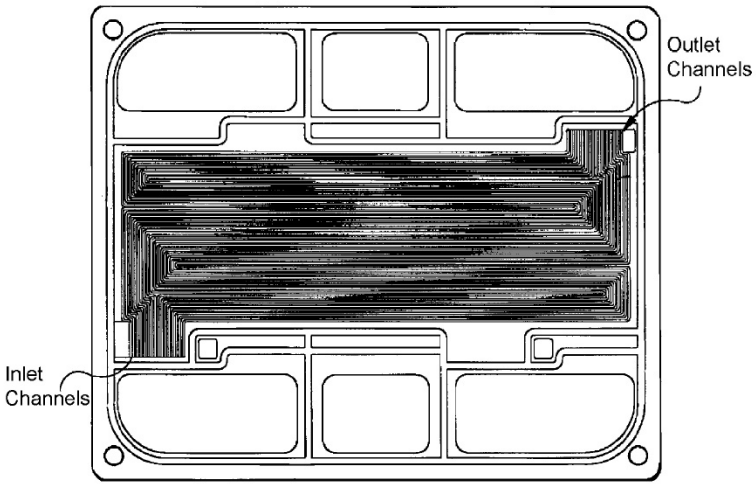

Figure 6.6: Multiple serpentine flow channels [143].

fuel cell that possesses multiple flow channels, however, it is common to see a large amount of water droplets accumulated inside the flow channel, particularly around the channel bend region. Such liquid water transport characteristics would require a real two-phase channel flow model, which is beyond the scope of this study. Instead, the current multi-channel model is only trying to provide some insights into how the flow-field design may affect the liquid saturation distribution in the porous backing layer.

Figure 6.7 compares the liquid saturation distribution at the middle $x-z$ cross-section of the CCL for three different channel designs. For all these designs, the maximum saturation lies under the land region close to the channel corners or cell boundaries, where the convective flow is relatively weak and liquid water is mostly removed by capillary diffusion. In the middle of the cell, the three channel layouts exhibit different saturation distributions. This is mainly because of the cross-flow effects. In fact, due to the pressure difference between adjacent flow channels in the interdigitated and serpentine flow channels, some of the flow will pass through the porous backing layer instead of through the channel. The resulting flow field is not simply a superposition of laminar flow in the channel and Darcy flow in the GDL but that of a non-linear coupling of the flow in the channel and GDL. Therefore, with increasing distance from the bend or dead end, the liquid saturation presents a non-uniform distribution. In contrast, the liquid saturation is rather uniform along the land in the straight parallel channel layout, because the pressure difference between adjacent parallel channels is small and, thus, no obvious cross flows exist between them.

The cross flows within the interdigitated and serpentine flow channels can be more easily observed from the cross-section plots shown in Figure 6.8 and Figure 6.9. The $1^{st}, 3^{rd}$ and 5^{th} slices present in the velocity profiles (refer to Figure 6.3) are shown here again along with the velocity vector plot. These slices correspond to the upstream, middle and downstream of the flow channel, respectively.

In Figure 6.8, intense cross flow appears between adjacent interdigitated flow channels in all three slices. Hence, the land region between two channels is less flooded compared to the land next to the cell boundary. Meanwhile, it is seen that the cross flow results in a distinct shift of the saturation distribution from the incoming channel towards the exhaust channel.

The cross flow within the serpentine flow-field presents a different behavior. In Figure 6.9(a), the cross flow is significant between the 1^{st} & 2^{nd} channel as well as between the 3^{rd} & 4^{th} channel, but it is weak between the 2^{nd} & 3^{rd} channel. This is simply because the plot-slices of the second and third channel are just taken before and after a channel bend. Therefore, the pressure drop between two channels is still relatively small at this location. Corresponding to the cross flows, the liquid saturation is smaller between the 1^{st} & 2^{nd} and 3^{rd} & 4^{th} channels and it shifts towards the downstream channel, but it is larger and more uniform between the 2^{nd} & 3^{rd} channel. The situation in slice 5 is just opposite to that of slice 1. The cross flow between the 1^{st} & 2^{nd} and 3^{rd} & 4^{th} channels is insignificant

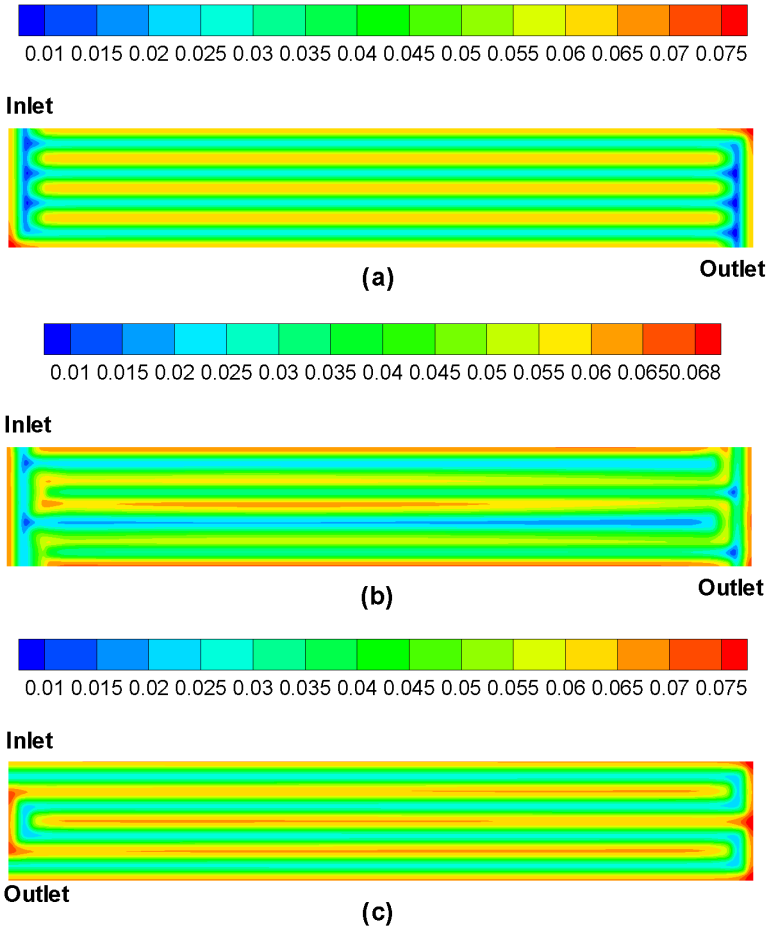

Figure 6.7: Distribution of liquid saturation at the middle $x-z$ cross-section of the cathode catalyst layer: (a) straight parallel channel, (b) interdigitated channel, (c) serpentine channel.

but it is stronger between the 2^{nd} & 3^{rd} channel. Consequently, liquid flooding is alleviated only between the two center channels, as shown in Figure 6.9(c). Slice 3 lies in the middle of the flow channels, hence, the pressure drop and cross flow between adjacent channels is moderate and similar. Therefore, the magnitude and distribution of the liquid saturation between any two adjacent channels is quite similar, as shown in Figure 6.9(b).

More effective liquid water removal can be achieved through enhanced cross flow effects. This can be done by increasing the gas flow rate, the porosity and permeability of the backing layer, or by reducing the land width and the GDL thickness, etc. As an illustration, the intrinsic permeability of the porous backing layer is arbitrarily increased by an order of magnitude (from about 8.0×10^{-12} to 8.0×10^{-11} m^2, refer to Equation (3.61)). The corresponding liquid saturation distribution is shown in Figure 6.10. Clearly, the saturation is almost unchanged in the straight parallel channel layout but it moderated in the interdigitated and serpentine channels as compared to Figure 6.7, manifesting the effectiveness of the cross flow on liquid water removal.

6.5 Current Density Distribution

Figure 6.11 shows the transverse current density (J^y) distribution at the middle $x - z$ plane of the membrane layer. As with the single-channel modeling results shown in Figure 5.35, it is seen that the current density under the land is much higher than under the channel in all three multi-channel layouts. In the straight parallel channel model, the distribution of current density is very similar to that of the oxygen concentration. The current density is higher where the oxygen supply is more sufficient. In the interdigitated and serpentine models however, the current density distribution is affected by both the oxygen distribution and the cross flow effects. It is found that the current density is locally boosted where the cross flow is strong.

One should note that the average cell current densities generated from three multi-channel models differ from each other and are different from the single-channel model. At the base case, the average current density of the single, straight, interdigitated, and the serpentine channel models are 8407.3, 8398.4, 8502.4, and 8711.4 A/m^2, respectively. The discrepancies between these models can be even larger if the liquid flow in the channel is accounted for. This raises a big difficulty regarding the validation of the numerical model of PEM fuel cells. In most of the previous modeling studies, the validation is usually made by comparing 1D, 2D, or 3D single-channel modeling results to experimental data retrieved from testing an industrial-sized fuel cell with intricate flow-field design in terms of the polarization curve. However, the results from the current study indicate that such comparisons may not be accurate or appropriate. In order to make the validation more meaningful, the numerical models at least should have the same geometric layouts as the testing cells.

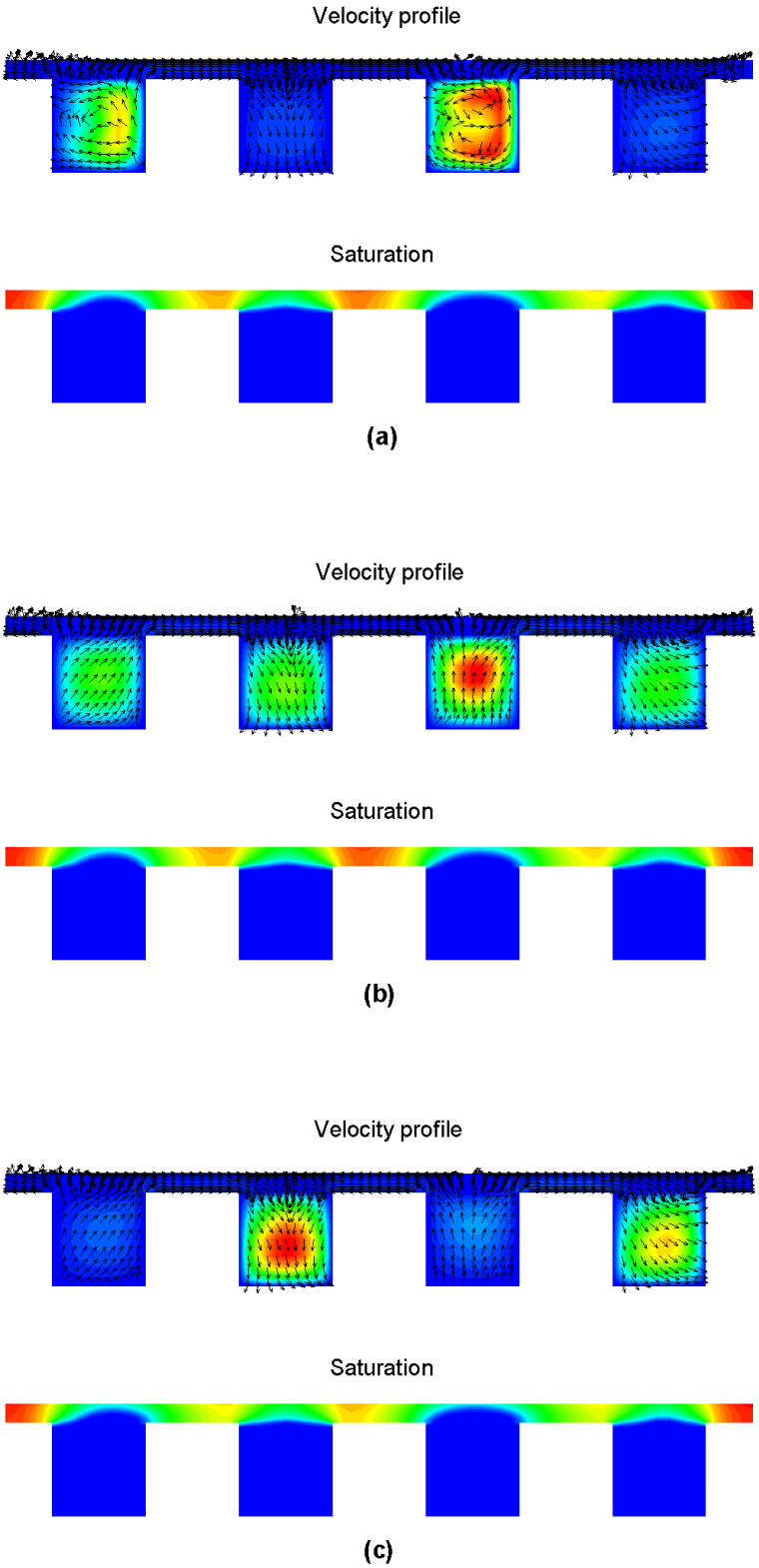

Figure 6.8: Effect of cross flow between interdigitated channels on the distribution of liquid saturation: (a) slice 1 ($z/L_{ch} = 1/10$), (b) slice 3 ($z/L_{ch} = 5/10$), (c) slice 5 ($z/L_{ch} = 9/10$).

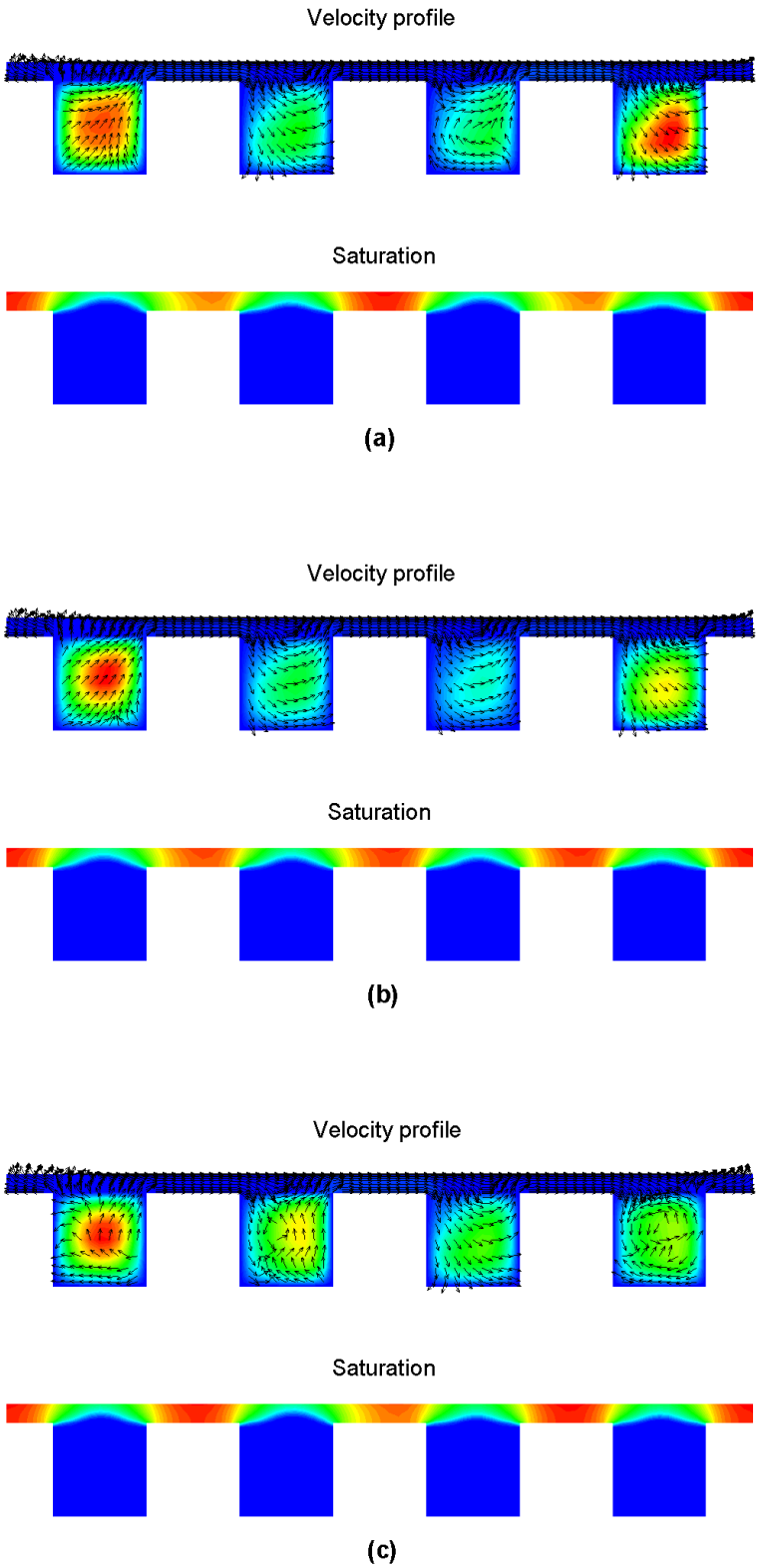

Figure 6.9: Effect of cross flow between serpentine channels on the distribution of liquid saturation: (a) slice 1 ($z/L_{ch} = 1/10$), (b) slice 3 ($z/L_{ch} = 5/10$), (c) slice 5 ($z/L_{ch} = 9/10$).

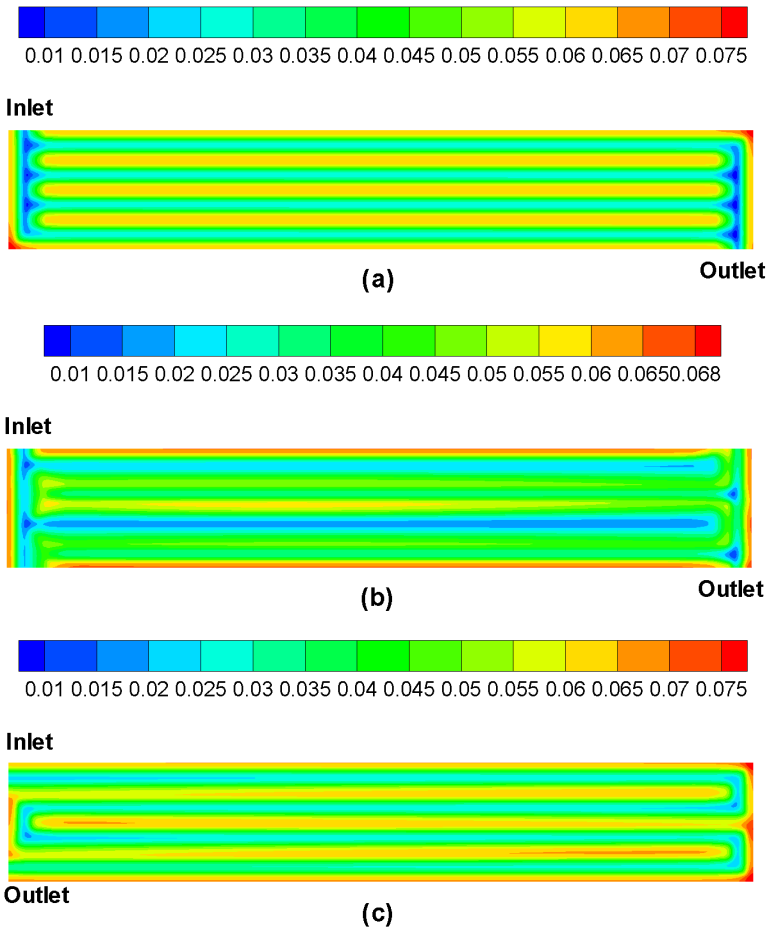

Figure 6.10: Effect of intrinsic permeability on the distribution of liquid saturation: (a) straight parallel channel, (b) interdigitated channel, (c) serpentine channel.

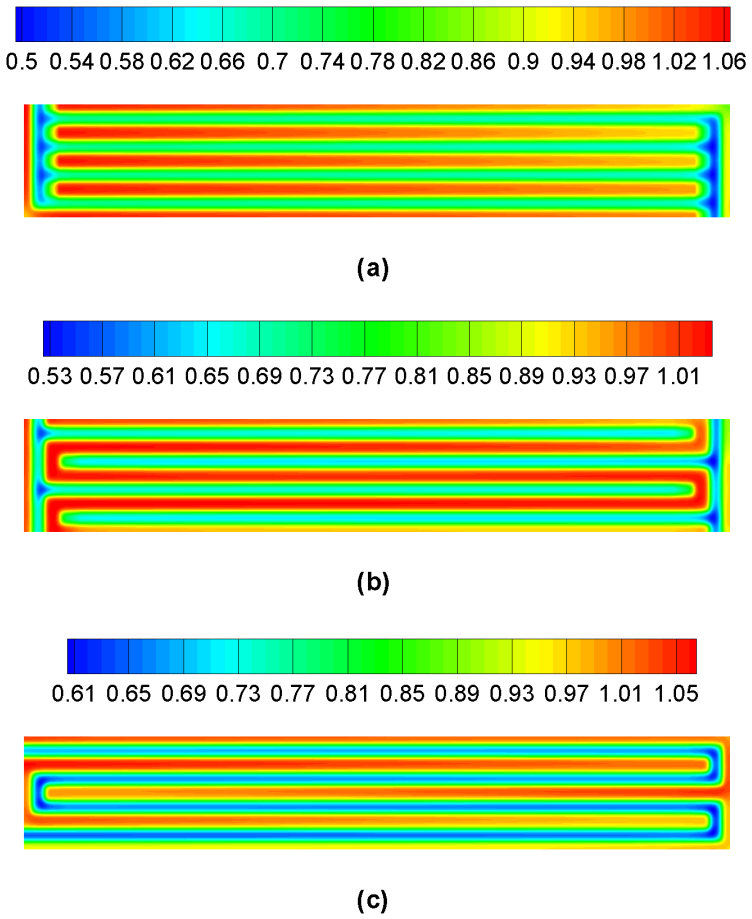

Figure 6.11: Distribution of the transverse current density, J^y, at the middle $x-z$ cross-section of the membrane layer: (a) straight parallel channel, (b) interdigitated channel, (c) serpentine channel.

6.6 Summary

Flow field design is one of the most important considerations in the development of PEM fuel cells. A good flow field design cannot only provide optimum reactant gas supply but also reduce the overall cell weight and cost. In this chapter, the three most common flow field designs (straight, interdigitated and serpentine) are investigated, using the multi-channel model developed in this study. The results show that owing to the pressure difference between adjacent flow channels, some of the gas may bypass the flow channel and move through the porous backing layer to the next channel directly, forming a cross flow between two neighboring channels. This cross flow facilitates the reactant transport and liquid water removal within the backing layer, leading to enhanced cell performance.

Chapter 7

Summary and Future Work

A rigorous three dimensional transient mathematical model for PEM fuel cells has been developed in this thesis research. The complete set of governing equations consists of the conservation of mass, momentum, and species for the gas phase, the conservation of dissolved water and liquid water, the conservation of electric charge, and the conservation of energy for all phases and species. A comprehensive inclusion of various transient transport phenomena and phase transfer processes is achieved in this model, including the non-equilibrium phase transfer between the liquid water and water vapor (condensation/evaporation); the non-equilibrium membrane water sorption/desorption; water transport within the bulk membrane (membrane hydration/dehydration); liquid water transport in the porous backing layer; heat transfer; gas diffusion towards the reaction sites; and the convective gas flow in the gas channels. Furthermore, some of the conventionally used modeling assumptions and approaches have been incorporated into the current model. Depending on the modeling purposes, the resulting model can be readily switched between steady and unsteady, isothermal and non-isothermal, single- and multi-phase, equilibrium and non-equilibrium membrane sorption/desorption, and three water production assumptions.

The final equation set is discretized and solved with finite volume based commercial software, Fluent, with user provided subroutines that describe various model parameters, empirical correlations, material properties, boundary conditions, and source terms. In addition, some control strategies and numerical under-relaxation schemes were developed and implemented into this model, to handle the stiffness inherent of a PEM fuel cell system. Superior convergence performance is achieved with these schemes, even for multi-channel models with increased cell size. Stringent numerical tests were performed to ensure that the solutions were independent of grid size and time step. It is found that the number of grid points in the through plane direction (y-direction) has a dominant effect on the solution precision and model stability. Moreover, it is found that coarsening or refining of the mesh may both lead to divergence. The former is mainly due to the increased discretization error while the latter is due to the increased grid aspect ratio.

Using a single-channel model, some of the commonly used assumptions and modeling approaches were examined and analyzed. For the first time, the water production mechanism is clarified and it is argued that the water production during the ORR is in the dissolved phase. Two widely used water production assumptions (liquid water production and water vapor production) were also investigated and compared to the dissolved water production mechanism. It exhibits that all three assumptions have identical results as the equilibrium state is finally reached. However, for more realistic non-equilibrium states, non-negligible discrepancies exist among these three assumptions. Moreover, by varying the condensation/evaporation rate coefficients that are developed as part of this thesis research, the relationship between the present model, the single-phase model and the mixture model is demonstrated. The results indicate that although the liquid and vapor production assumptions are not physically correct, they can serve as a tool to identify the phase equilibrium state and help understand the phase transfer processes.

The membrane sorption/desorption process has been widely treated as an instantaneous process in the literature. In this study, a novel finite-rate membrane sorption/desorption submodel is developed by adopting two new correlations for the sorption/desorption rate coefficients that are derived based on the experimental work of Ge *et al.* The non-equilibrium and equilibrium submodels agree with each other very well as the sorption/desorption rate coefficients increase towards their upper limits. This can be regarded as a good numerical validation for the current models. Under non-equilibrium conditions, the results manifest that the equilibrium approach tends to underestimate the cell current output for steady state modeling, and the cell response time if transient phenomena are of concern.

The effects of capillary pressure and relative permeability on the liquid saturation distribution were inspected with several empirical expressions that are commonly adopted in the literature. The standard Leverett J-function for the capillary pressure is compared with two newly developed expressions that pertain to PEM fuel cell materials. The results demonstrate that the liquid saturation distribution predicted by the standard Leverett function is more uniform than for the other two expressions, indicating that the non-uniform wetting properties of the PEM fuel cell materials cannot be correctly accounted for by the most widely used Leverett function approach. A similar comparison is made for the relative permeability with two empirical power law expressions. This part of the study shows that the relative permeability has an even more significant impact on the modeling results than the capillary pressure, highlighting a research area that still lacks experimental attention.

Furthermore, two methods for the specification of the boundary conditions for the solid phase potential were examined. It is found that the solutions from two different methods are exactly the same. However, the computational expense and the model stability are slightly different. The comparison from this study suggests that a rarely used method is indeed more efficient and stable.

With the optimal choices for the above mentioned assumptions and modeling

approaches, extensive transient simulations were carried out to explore the dynamic responses of a PEM fuel cell and the transient transport phenomena within it. Firstly, the cell responses with respect to various changes in operating conditions were simulated. The voltage sweep study discloses a hysteresis effect for the polarization curve, where the curve in the forward sweep does not coincide with the backward sweep. A similar hysteresis effect has been confirmed by experimental observations. Examination of the membrane water content variation indicates that this hysteresis behavior is mainly caused by the sluggish membrane hydration/dehydration and sorption/desorption processes. A sinusoidal impedance approach is employed to identify the time scales for different dynamic transport processes and it is found that the time scale for heat transfer is about 10 seconds, while the time scale for various water transport processes are closely correlated and are on the order of 100 seconds. Further, the study of step changes in operating conditions demonstrates that the current overshoot is slightly larger when a voltage step change is performed at high current densities; the pressure effects are more significant at low pressure conditions; the current overshoot decreases with the increasing of gas flow pressure; and the increase of the gas flow rate does not influence the cell current significantly, except in the mass transport limitation region.

Various transient transport phenomena exist in PEM fuel cells which, because of in-situ measurement difficulties, can only be probed through numerical simulations. However, most of the previous transient studies have only focused on the cell dynamic responses, using models with reduced dimensions (1D/2D) or neglected transient processes. A comprehensive 3D analysis of the main transient transport processes in PEM fuel cells is still rarely seen in the literature. This gap is now filled by the current study which forms one of the major contributions of this thesis research.

The transient transport processes, including the transport of gas species (hydrogen, oxygen), multi-water phases (vapor, dissolved and liquid), electric charges (electrons and protons), and energy, during a step change in relative humidity were demonstrated. It is found that since both water vapor and hydrogen are consumed at the anode side catalyst layer, the hydrogen concentration increases along the flow channel at the initial fully humidified conditions. As the incoming gas becomes dry, consumption of the hydrogen surmounts that of the water vapor and the hydrogen concentration starts to decrease along the channel after about 1 second and this trend remains for the rest of the time period. On the other hand, only oxygen is consumed at the cathode side. It is seen that the oxygen concentration decreases along the channel during the whole transition period.

The transient variations of three water phases are interrelated and very similar. Significant variations in the water vapor concentration, membrane water content and liquid saturation were observed, especially around the cell inlet. Moreover, it shows that the anode side membrane is more easily drying out during the step change process, suggesting that higher relative humidity conditions should be maintained for the anode side gas stream. A liquid/gas front and its evolution during the relative humidity change is successfully captured. This part of the results may

provide some insight into how the liquid water flooding can be alleviated through appropriate variations of operating conditions.

The transport of electrons forms an electronic current in the solid backbone of the porous backing layer. Similarly, the transport of protons creates a protonic current in the polymer electrolyte membrane. These two currents are interconnected through the electrochemical reactions at the ACL and CCL. It is found that the electrochemical reaction rates increase from the GDL/CL boundary towards the membrane/CL boundary for both the ORR and HOR reactions, indicating that the reaction rate is more dominated by the electric overpotential rather than by the reactants' concentration. Furthermore, it is seen that the electrochemical reactions are more pronounced under the land than under the channel because under the land electrons can be supplied more easily to the electrochemical reaction sites.

The temperature distribution is a compromise of various heat generation/absorption mechanisms. A temporal local temperature drop is observed at the cell inlet, where significant liquid evaporation occurs and a fair amount of heat is absorbed. Further, it is found that the temperature distribution across the cell is dominated by reaction heat while the temperature along the channel is more dominated by ohmic heating.

Finally, using the multi-channel model, the three most common flow field designs (straight, interdigitated and serpentine) were investigated. The distributions of the bulk flow field, reactant concentration, liquid saturation and current density were demonstrated for all three designs. The results indicate that the cross flows, which form between adjacent flow channel branches due to a pressure difference, tend to facilitate the reactant transport and liquid water removal within the backing layer, and can lead to enhanced cell performance.

In summary, several key conclusions can be drawn from this thesis research:

- the dissolved water production mechanism should be exclusively adopted in future studies;
- the non-equilibrium phase transfer processes, particularly the non-equilibrium membrane sorption/desorption process, are necessary for both steady-state and transient simulations;
- prediction of the liquid saturation distribution is sensitive to the empirical correlations for the capillary pressure and relative permeability. Therefore, correlations that pertain to PEM fuel cell materials should be derived;
- the initial abrupt overshoot/undershoot of the cell dynamic response is mainly caused by the limitation of gas reactant transport, whereas the remaining slow response of the cell is more dominated by the sluggish water transport and heat transfer processes;
- liquid flooding can be alleviated and the cell performance can be improved through appropriate flow-field designs.

Furthermore, the results of this thesis research also highlight a few areas for future studies, as summarized below:

- the mechanism of proton transport in the polymer electrolyte is still not well understood and requires more fundamental research efforts;
- simulation of the liquid flow in the porous backing layer could be done with more realistic heterogenous pore structures;
- determination of the empirical correlations that pertain to PEM fuel cells would demand more experimental work;
- for practical-size fuel cells, the liquid water transport in the gas flow channel can be a dominating factor that limits the cell performance. Therefore, a sophisticated two-phase channel flow model is highly desirable;
- industrial-size fuel cells and cell stacks should be modeled with more powerful computing facilities in terms of parallel processing.

APPENDICES

Appendix A

List of User Defined Functions

A.1 User Subroutines

double Get_sat (double T)

Calculate the saturation pressure based on the local temperature, T.

double Mass_Frac_Anode (int i)

Return the mass fraction of species i at the anode side.

double Mass_Frac_Cathode (int i)

Return the mass fraction of species i at the cathode side.

double Water_Activity (double T, cell_t c, Thread *t)

Calculate the water activity based on the local temperature; equilibrium approach.

double Water_content_cl (cell_t c, Thread *t, double act)

Calculate the equilibrium membrane water content in the catalyst layer based on the local water activity.

double Water_content (cell_t c, Thread *t)

Calculate the membrane water content; non-equilibrium approach.

double Osmotic_Drag_Coefficient (double lambda)

Calculate the osmotic drag coefficient based on the local membrane water content.

double Membrane_Conductivity (double lambda, double T)

Calculate the membrane conductivity based on the local membrane water content and temperature.

double Water_Membrane_Diffusivity (double lambda)

Calculate the dissolved water diffusivity in the membrane.

double Eta_total ()

Calculate the total potential loss based on the reversible and the output cell potential.

double RR_a (cell_t c, Thread *t)

Calculate the Butler-Volmer reaction rate at the anode side (HOR).

double RR_c (cell_t c, Thread *t)

Calculate the Butler-Volmer reaction rate at the cathode side (ORR).

double D_Cwm_Cw (double T, cell_t c, Thread *t)

Conversion from the membrane water to water vapor; equilibrium approach.

double Get_K_GDL (cell_t c, Thread *t)

Calculate the permeability of the porous backing layer.

double Get_mu_g (double T)

Calculate the temperature dependent gas phase viscosity.

double Get_mu_w (double T)

Calculate the temperature dependent water viscosity.

double Get_Krl (cell_t c, Thread *t)

Return the relative permeability of the liquid phase.

double Get_Krg (cell_t c, Thread *t)

Return the relative permeability of the gas phase.

double Get_lambda_l (cell_t c, Thread *t)

Return the relative mobility of the liquid phase.

double Get_lambda_g (cell_t c, Thread *t)

Return the relative mobility of the gas phase.

double Get_niu (cell_t c, Thread *t)

Calculate the kinetic viscosity.

double Get_J_s (cell_t c, Thread *t)

The Leverett J-function.

double Get_dJ_ds (cell_t c, Thread *t)

Return the derivative of the J-function with respect to liquid saturation, s.

double Get_Pc (cell_t c, Thread *t)

Return the local capillary pressure.

double Get_Sw_vl (cell_t c, Thread *t)

Source of phase change between the vapor and liquid phase.

double Gamma_a (cell_t c, Thread *t)

Return the membrane sorption-desorption rate coefficient, anode side;

double Gamma_c (cell_t c, Thread *t)

Return the membrane sorption-desorption rate coefficient, cathode side;

double Get_Sw_vd (cell_t c, Thread *t)

Source of phase change between the vapor and dissolved phase.

A.2 Fluent Standard UDFs

DEFINE_PROFILE(char name, Thread *t, int i)

```
{
        face_t f;

        begin_f_loop(f,t)
        {
                F_PROFILE(f,t,i) = ......;
        }
        end_f_loop(f,t)
}
```

Usage: call user defined subroutines to specify various boundary conditions, e.g., overpotential, mass flux, mass fraction, pressure, temperature, and membrane water content if equilibrium approach is used, etc.

DEFINE_ADJUST (char name, Domain *d)

```
{
        Thread *t;
        cell_t c;


        thread_loop_c(t,d)
        {
                Zone_ID = THREAD_ID(t);

                begin_c_loop_all(c,t)
                {
                        if (Zone_ID == Channel_a)       ......;
                        if (Zone_ID == Anode)   ......;
                        if (Zone_ID == CL_a)    ......;
                        if (Zone_ID == Membrane)        ......;
                        if (Zone_ID == CL_a)    ......;
                        if (Zone_ID == Cathode)         ......;
                        if (Zone_ID == Channel_c)       ......;
                }
                end_c_loop_all(c,t)
        }

}
```

Usage: (i). update all physical properties and the source terms in each layer of the fuel cell. (ii). implement the equilibrium membrane water transport approach here. Convert the water flux at the membrane-CL boundary to source terms on the first layer of the grid as explained in Section 3.3.3. (iii). apply inner and outer under relaxations as illustrated in Section 4.1.3.

DEFINE_EXECUTE_AT_END(char name)

```
{
        Domain *d;
        Thread *t;
        cell_t c;

        d = Get_Domain(1);

        thread_loop_c(t,d)
        {
                Zone_ID = THREAD_ID(t);

                begin_c_loop_all(c,t)
                {
                        if (Zone_ID == Channel_a)        ......;
                        ......
                }
                end_c_loop_all(c,t)
        }

}
```

Usage: calculate the phase current density vector, J_s, J_m.

DEFINE_INIT(char name, Domain *d)

```
{
        Thread *t;
        cell_t c;

        thread_loop_c(t,d)
        {
                Zone_ID = THREAD_ID(t);

                begin_c_loop_all(c,t)
                {
                        if (Zone_ID == Channel_a)       ......;
                        ......
                }
                end_c_loop_all(c,t)
        }

}
```

Usage: initialize the flow-field.

DEFINE_UDS_UNSTEADY (char name, cell_t c, Thread *t, int i, double *apu, double *su)

```
{
        int Zone_ID = THREAD_ID(t);

        if (i == Dissolved)
        {
                if (Zone_ID == CL_a || Zone_ID == CL_c)
                {
                        *apu = ......;
                        *su = ......;
                }
                else
                {
                        *apu = ......;
                        *su = ......;
                }
        }
        if (i == Liquid)
        {
                *apu = ......;
                *su = ......;
        }
}
```

Usage: customize unsteady terms in the user-defined scalar (UDS) transport equations.

DEFINE_UDS_FLUX (char name, face_t f, Thread *t, int i)

```
{
                if (BOUNDARY_FACE_THREAD_P(t))
                {
                        ......;
                        flux = ......;
                }
                else
                {
                        ......;
                        flux = ......;
                }
        return flux;
}
```

Usage: customize convective terms in the user-defined scalar (UDS) transport equations.

DEFINE_DIFFUSIVITY (char name, cell_t c, Thread *t, int i)

```
{
        int Zone_ID = THREAD_ID(t);

        if (i == Hydrogen)
        {
                diff = ......;
        }
        ......;

        return diff;
}
```

Usage: define diffusivity for gas species and UDS equations.

DEFINE_SOURCE (char name, cell_t c, Thread *t, double dS, int eqn)

```
{
        double Var;
        Var = ......;
        dS[eqn] = ......;

        return Var;
}
```

Usage: specify custom source terms for the different types of solved transport equations, e.g, mass equation, multi-species equations, liquid and dissolved water transport equations, electric charge equations, and energy equations.

References

[1] Technical plan - Fuel Cell: Cost analysis of Fuel Cell systems for transportation, *Department of Energy*, United States, 2008. 1

[2] G. Hoogers, *Fuel Cells Technology Handbook*, CRC Press, 2003. 3

[3] X. Li, *Principles of Fuel Cells*, Taylor & Francis, 2005. 3, 25, 26, 54, 82

[4] N. Sammes, *Fuel Cells Technology: Reaching Towards Commercialization*, Springer, 2005. 3, 9

[5] J. Larminie and A. Dicks, *Fuel Cell Systems Explained*, Wiley, West Sussex England, 2000.

[6] E.A. Ticianelli, C.R. Derouin, A. Redondo, and S. Srinivasan, Methods to advance technology of proton exchange membrane fuel cells, *Journal of the Electrochemical Society*, 135(9):2209-2214, 1988. 10

[7] S. Srinivasan, E.A. Ticianelli, C.R. Derouin, and A. Redondo, Recent advances in solid polymer electrolyte fuel cell technology with low platinum loading electrodes, *Journal of Power Sources*, 22(3-4):359-375, 1988. 10

[8] V. A. Paganin, E. A. Ticianelli, and E. R. Gonzalez, Development and electrochemical studies of gas diffusion electrodes for polymer electrolyte fuel cells, *Journal of Applied Electrochemistry*, 26(3):297-304, 1996. 10

[9] J. Kim, S.M. Lee, S. Srinivasan, and C. Chamberlin, Modeling of proton exchange membrane fuel cell performance with an empirical equation, *Journal of the Electrochemical Society*, 142(8):2670-2674, 1995. 10

[10] P.D. Beattie, V.I. Basura, and S. Holdcroft, Temperature and pressure dependence of O_2 reduction at Pt—Nafion® 117 and Pt—BAM® 407 interfaces, *Journal of Electroanalytical Chemistry*, 468(2):180-192, 1999. 10

[11] G. Squadrito, G. Maggio, E. Passalacqua, F. Lufrano, and A. Patti, An empirical equation for polymer electrolyte fuel cell (PEFC) behavior, *Journal of Applied Electrochemistry*, 29(12):1449-1455, 1999. 10

[12] J.C. Amphlett, R.M. Baumert, R.F. Mann, B.A. Peppley, and P.R. Roberge, Performance modeling of the Ballard Mark IV solid polymer electrolyte fuel cell, *Journal of the Electrochemical Society*, 142(1):1-15, 1995. 10

[13] L. Pisani, G. Murgia, M. Valentini, and B.D. Aguanno, A new semi-empirical approach to performance curves of polymer electrolyte fuel cells, *Journal of Power Sources*, 108(1-2):192-203, 2002. 10

[14] A.A. Kulikovsky, The voltage-current curve of a polymer electrolyte fuel cell: "exact" and fitting equations, *Electrochemistry Communications*, 4(11):845-852, 2002. 10

[15] M. Ceraolo, C. Miulli, and A. Pozio, Modeling static and dynamic behaviour of proton exchange membrane fuel cells on the basis of electro-chemical description, *Journal of Power Sources*, 113(1):131-144, 2003. 10

[16] J.J. Baschuk and X. Li, Modelling of polymer electrolyte membrane fuel cell stacks based on a hydraulic network approach, *International Journal of Energy Resources*, 28(8):697-724, 2004. 10

[17] F. Standaert, K. Hemmes, and N. Woudstra, Analytical fuel cell modeling. *Journal of Power Sources*, 63(2):221-234, 1996. 10

[18] F. Standaert, K. Hemmes, and N. Woudstra, Analytical fuel cell modeling; non-isothermal fuel cells, *Journal of Power Sources*, 70(2):181-199, 1998; 10

[19] V. Gurau, F. Barbir, and H. Liu, An analytical solution of a half-cell model for PEM fuel cells, *Journal of the Electrochemical Society*, 147(7):2468-2477, 2000. 10

[20] M. De Francesco and E. Arato, Start-up analysis for automotive PEM fuel cell systems, *Journal of Power Sources*, 108(1-2):41-52, 2002. 10

[21] W. Gao, Q. Yan, J. Wu, and B.S.Y. Choe, Transient model-based PEM fuel cell system control, *The Electrochemical Society Proceedings*, 24:233-239, 2003. 10

[22] F. Grasser and A. Rufer, A fully analytical PEM fuel cell system model for control applications *IEEE Industry Applications Conference - 41th IAS Annual Meeting*, Tampa, Florida, USA, 2006. 10

[23] D.M. Bernadi and M.W. Verbrugge, A mathematical model of the solid polymer electrolyte fuel cell, *Journal of the Electrochemical Society*, 139(9):2477-2491, 1992. ix, 12, 52, 53

[24] D.M. Bernadi and M.W. Verbrugge, Mathematical model of a gas diffusion electrode bonded to a polymer electrolyte, *AIChE Journal*, 37(8):1151-1162, 1991. 12

[25] T.F. Fuller and J. Newmann, Water and thermal management in solid polymer electrolyte fuel cells, *Journal of the Electrochemical Society*, 140(5):1218-1225, 1993. 12

[26] T.V. Nguyen and R.E. White, A water and heat management model for proton exchange membrane fuel cells, *Journal of the Electrochemical Society*, 140(8):2178-2186, 1993. 12, 17

[27] M. Eikerling, Y.I. Kharkats, A.A. Kornyshev, and Y.M. Volkovich, Phenomenological theory of electro-osmotic effect and water management in polymer electrolyte proton-conducting membranes, *Journal of the Electrochemical Society*, 145(8):2684-2699, 1998. 12

[28] T. Berning, D.M. Lu, and N. Djilali, Three-dimensional computational analysis of transport phenomena in a PEM fuel cell, *Journal of Power Sources*, 106(2):284-292, 2002. 12, 54

[50] G.J.M. Janssen and M.L.J. Overvelde, Water transport in the proton exchange membrane fuel cell: measurements of the effective drag coefficient, *Journal of Power Sources*, 101(1):117-125, 2001. 12, 13

[30] T.E. Springer, T.A. Zawodzinski, and S. Gottesfeld, Polymer electrolyte fuel cell model, *Journal of the Electrochemical Society*, 138(8):2334-2342, 1991. ix, 12, 31, 32, 34, 46, 52, 53

[31] T.E. Springer, M.S. Wilson, and S. Gottesfeld, Modeling and experimental diagnostics in polymer electrolyte fuel cells, *Journal of the Electrochemical Society*, 140(12):3513-3526, 1992. 12

[32] V. Gurau, H. Liu, and S. Kakac, Two-dimensional model for proton exchange membrane fuel cells, *AIChE Journal*, 44(11):2410-2422, 1998. 13

[33] S. Um, C.Y. Wang, and K.S. Chen, Computational fluid dynamics modeling of proton exchange membrane fuel cells, *Journal of the Electrochemical Society*, 147(12):4485-4493, 2000. 13, 33, 35

[34] S. Um and C.Y. Wang, Three-dimensional analysis of transport and electrochemical reactions in polymer electrolyte fuel cells, *Journal of Power Sources*, 125(1):40-51, 2004. 13, 33

[35] S. Dutta, S. Shimpalee, and J.W. Van Zee, Three-dimensional numerical simulation of straight channel PEM fuel cells, *Journal of Applied Electrochemistry*, 30(2):135-146, 2000. 13

[36] S. Dutta, S. Shimpalee, and J.W. Van Zee, Numerical prediction of mass exchange between anode and cathode channels in a PEM fuel cell, *International Journal of Heat Mass Transfer*, 44(11):29-40, 2001. 13

[37] T. Zhou and H. Liu, A general three-dimensional model for proton exchange membrane fuel cells, *International Journal of Transport Phenomena*, 3(3):177-198, 2001. 13, 17

[38] S. Mazumder and J.V. Cole, Rigorous three dimensional mathematical modeling of proton exchange membrane fuel cells. part 1: model predictions without liquid water transport, *Journal of the Electrochemical Society*, 150(11):A1503-A1509, 2003. 13

[39] W.K. Lee, S. Shimpalee, and J.W. Van Zee, Verifying predictions of water and current distributions in a serpentine flow field PEMFC, *Journal of the Electrochemical Society*, 150(3):A341-A348, 2003. 13

[40] A.A. Kulikovsky, Quasi-3D modeling of water transport in polymer electrolyte fuel cells, *Journal of the Electrochemical Society*, 150(11):A1432-A1439, 2003. 13, 31, 32, 33, 34

[41] T. Hinatsu, M. Mizuhata, and H. Takenaka, Water uptake of perfluorosulfonic acid membranes from liquid water and water vapor, *Journal of the Electrochemical Society*, 141(6):1493-1498, 1994. 13, 32

[42] S. Um and C.Y. Wang, Computational study of water transport in proton exchange membrane fuel cells, *Journal of Power Sources*, 156(2):211-223, 2006.

[43] H. Meng, A three-dimensional PEM fuel cell model with consistent treatment of water transport in MEA, *Journal of Power Sources*, 162(1):426-435, 2006. 13

[44] **H. Wu**, P. Berg, and X. Li, Non-isothermal transient modeling of water transport in PEM fuel cells, *Journal of Power Sources*, 165(1):232-243, 2007. 13, 19, 33, 35, 54, 97

[45] P.C. Sui, S. Kumar, and N. Djilali, Advanced computational tools for PEM fuel cell design: Part 1. Development and base case simulations, *Journal of Power Sources*, 180(1):410-422, 2008. 13

[46] T. Thampan, S. Malhotra, H. Tang, and R. Datta, Modeling of conductive transport in proton-exchange membranes for fuel cells, *Journal of the Electrochemical Society*, 147(9):3242-3250, 2000. 13

[47] P. Berg, K. Promislow, J.S. Pierre, J. Stumper, and B. Wetton, Water management in PEM fuel cells, *Journal of the Electrochemical Society*, 151(3):A341-A353, 2004. 13, 37, 54

[48] J.J. Baschuk and X. Li, A general formulation for a mathematical PEM fuel cell model, *Journal of Power Sources*, 142(1-2):134-153, 2005. 13, 22

[49] J. Fimrite, H. Struchtrup, and N. Djilali, Transport phenomena in polymer electrolyte membranes *Journal of the Electrochemical Society*, 152(9):A1804-A1814, 2005. 13

[50] G.J.M. Janssen, A phenomenological model of water transport in a proton exchange membrane fuel cell, *Journal of the Electrochemical Society*, 148(12):A1313-A1323, 2001. 12, 13

[51] A.Z. Weber and J. Newman, Transport in polymer-electrolyte membranes *Journal of the Electrochemical Society*, 150(7):A1008-A1015, 2003. 13, 33

[52] C.Y. Wang and P. Cheng, A multiphase mixture model for multiphase, multicomponent transport in capillary porous media—i. Model development, *International Journal of Heat and Mass Transfer*, 39(17):3607-3618, 1996. 14, 83

[53] U. Pasaogullari and C.Y. Wang, Two-phase transport and the role of microporous layer in polymer electrolyte fuel cells, *Electrochimica Acta*, 49(25):4359-4369, 2004. 14

[54] L. You and H. Liu, A two-phase flow and transport model for the cathode of PEM fuel cells, *International Journal of Heat Mass Transfer*, 45(11):2277-2287, 2002. 14

[55] L. You and H. Liu, A two-phase flow and transport model for PEM fuel cells, *Journal of Power Sources*, 155(11):219-230, 2006. 14

[56] S. Mazumder and J.V. Cole, Rigorous three dimensional mathematical modeling of proton exchange membrane fuel cells. Part 2: Model predictions with liquid water transport, *Journal of the Electrochemical Society*, 150(11):A1510-A1517, 2003. 14

[57] W. He, J.S. Yi, and T.V. Nguyen, Two-phase flow model of the cathode of PEM fuel cells using interdigitated flow fields, *AIChE Journal*, 46(10):2053-2064, 2000. 14, 41, 53, 54

[95] D. Natarajan and T.V. Nguyen, Three-dimensional effects of liquid water flooding in the cathode of PEM fuel cell using conventional gas distributors, *Journal of Power Sources*, 115(1):66-80, 2003. 14, 19, 41

[59] Z.H. Wang, C.Y. Wang, and K.S. Chen, Two-phase flow and transport in the air cathode of proton exchange membrane fuel cells, *Journal of Power Sources*, 94(1):40-50, 2001. 14

[60] T.V. Nguyen, G. Lin, H. Ohn, and X. Wang, Measurements of two-phase flow properties of the porous media used in PEM fuel cells, *ECS Transactions*, 3(1):415-423, 2006. 15, 17, 42, 43

[61] J.T. Gostick, M.W. Fowler, M.A. Ioannidis, M.D. Pritzker, Y.M. Volfkovich, and A. Sakars, Capillary pressure and hydrophilic porosity in gas diffusion layers for polymer electrolyte fuel cells, *Journal of Power Sources*, 156(2):375-387, 2006. 15, 42, 44, 87

[62] J.D. Fairweather, P. Cheung, J. St-Pierre, and D.T. Schwartz, A microfluidic approach for measuring capillary pressure in PEMFC gas diffusion layers, *Electrochemistry Communications*, 9(9):2340-2345, 2007. 15, 42, 44

[63] E.C. Kumbur, K.V. Sharp, and M.M. Mench, Validated Leverett approach for multiphase flow in PEFC diffusion media I. Hydrophobicity effect, *Journal of the Electrochemical Society*, 154(12):B1295-B1305, 2007. 15, 41, 42, 43, 44, 53, 87

[64] E.C. Kumbur, K.V. Sharp, and M.M. Mench, Validated Leverett approach for multiphase flow in PEFC diffusion media II. Compression effect, *Journal of the Electrochemical Society*, 154(12):B1305-B1315, 2007. 15, 42, 43, 44, 87

[65] E.C. Kumbur, K.V. Sharp, and M.M. Mench, Validated Leverett approach for multiphase flow in PEFC diffusion media III. Temperature effect, *Journal of the Electrochemical Society*, 154(12):B1315-B1325, 2007. 15, 42, 43, 44, 87

[66] J.H. Nam and M. Kaviany, Effective diffusivity and water-saturation distribution in single- and two-layer PEMFC diffusion medium, *International Journal of Heat Mass Transfer*, 46(24):4595-4611, 2003. 15, 41, 53

[67] U. Pasaogullari and C.Y. Wang, Liquid water transport in gas diffusion layer of polymer electrolyte fuel cells, *Journal of the Electrochemical Society*, 151(3):A399-A406, 2004. 15

[68] P. Quan, B. Zhou, A. Sobiesiak, and Z. Liu, Water behavior in serpentine micro-channel for proton exchange membrane fuel cell cathode, *Journal of Power Sources*, 152(1):131-145, 2005. 15

[69] K. Jiao, B. Zhou, and P. Quan, Liquid water transport in parallel serpentine channels with manifolds on cathode side of a PEM fuel cell stack, *Journal of Power Sources*, 154(1):124-137, 2006. 15

[70] K. Jiao, B. Zhou, and P. Quan, Liquid water transport in straight micro-parallel-channels with manifolds for PEM fuel cell cathode, *Journal of Power Sources*, 157(1):226-243, 2006. 15

[71] A. Theodorakakos, T. Ous, M. Gavaises, J.M. Nouri, N. Nikolopoulos, and H. Yanagihara, Dynamics of water droplets detached from porous surfaces of relevance to PEM fuel cells, *Journal of Colloid Interface Science*, 300(2):673-687, 2006. 15

[72] X. Zhu, P.C. Sui, and N. Djilali, Dynamic behaviour of liquid water emerging from a GDL pore into a PEMFC gas flow channel, *Journal of Power Sources*, 172(1):287-295, 2007. 15

[73] A. Bazylak, D. Sinton, and N. Djilali, Dynamic water transport and droplet emergence in PEMFC gas diffusion layers, *Journal of Power Source*, 176(1):240-246, 2008. 15

[74] A. Vishnyakov and A.V. Neimark, Inside the hysteresis loop: Multiplicity of internal states in confined fluids, *Journal of Physical Chemistry B*, 104(3):4471-4476, 2000. 16

[75] P.G. Khalatur, S.K. Talitskikh, and A.R. Khokhlov, Structural organization of water-containing Nafion: The integral equation theory, *Macromolecular Theory and Simulation*, 11(5):566-586, 2002. 16

[76] S.S. Jang, V. Molinero, T. Cagin, and W.A. Goddard III, Nanophase-segregation and transport in Nafion 117 from molecular dynamics simulations: effect of monomeric sequence, *Journal of Physical Chemistry B*, 108(10):3149-3157, 2004. 16

[77] J. T. Wescott, Y. Qi, L. Subramanian, and T. W. Capehart, Mesoscale simulation of morphology in hydrated perfluorosulfonic acid membranes, *The Journal of Chemical Physics*, 124(13):134702/1-14, 2006. 16

[78] X.D. Niu, T. Munekata, S. Hyodo, and K. Suga, An investigation of water-gas transport processes in the gas-diffusion-layer of a PEM fuel cell by a multiphase multiple-relaxation-time lattice Boltzmann model, *Journal of Power Source*, 172(2):542-552, 2007. 16

[79] T. Koido, T. Furusawa, and K. Moriyama, An approach to modeling two-phase transport in the gas diffusion layer of a proton exchange membrane fuel cell, *Journal of Power Source*, 175(1):127-136, 2008. 16

[80] L. Hao and P. Cheng, Lattice-Boltzmann simulations of anisotropic permeabilities in carbon paper gas diffusion layers, *Journal of Power Source*, 186(1):104-114, 2009. 16

[81] M. Wöhr, K. Bolwin, W. Schnurnberger, M. Fischer, and W. Neubrand, Dynamic modelling and simulation of a polymer membrane fuel cell including mass transport limitation, *International Journal of Hydrogen Energy*, 23(3):213-218, 1998. 17

[82] A. Rowe and X. Li, Mathematical modeling of proton exchange membrane fuel cells, *Journal of Power Sources*, 102(1-2):82-96, 2001. 17

[83] G. Maggio, V. Recupero, and C. Mantegazza, Modelling of temperature distribution in a solid polymer electrolyte fuel cell stack, *Journal of Power Sources*, 62(2):167-174, 1996. 17

[84] S. Shimpalee and S. Dutta, Numerical prediction of temperature distribution in pem fuel cells, *Numerical Heat Transfer, Part A*, 38(2):111-128, 2000. 17

[85] H. Ju, H. Meng, and C.Y. Wang, A single-phase non-isothermal model for PEM fuel cells, *International Journal of Heat and Mass Transfer*, 48(7):1303-1315, 2005. 17

[86] T. Berning, D.M. Lu, and N. Djilali, A 3D, multi-phase, multicomponent model of the cathode and anode of a PEM fuel cell, *Journal of the Electrochemical Society*, 150(12):A1598-A1598, 2003. 17

[87] H. Meng and C.Y. Wang, Large-scale simulation of polymer electrolyte fuel cells by parallel computing, *Chemical Engineering Science*, 59(16):3331-3343, 2004. 17

[88] Y. Wang and C.Y. Wang, Ultra large-scale simulation of polymer electrolyte fuel cells, *Journal of Power Sources*, 153(1):130-135, 2006. 18

[89] S. Shimpalee, S. Greenway, and J.W. Van Zee, The impact of channel path length on PEMFC flow-field design, *Journal of Power Sources*, 160(1):398-406, 2006. 18

[90] Y. Wang and C.Y. Wang, Transient analysis of polymer electrolyte fuel cells, *Electrochimica Acta*, 50(6):1307-1315, 2005. 18, 33, 87

[91] S. Shimpalee, W.K. Lee, J.W. Van Zee, and H.N. Neshat, Predicting the transient response of a serpentine flow-field PEMFC i: Excess to normal fuel and air, *Journal of Power Sources*, 156(1):355-368, 2006. 19

[92] S. Shimpalee, W.K. Lee, J.W. Van Zee, and H.N. Neshat, Predicting the transient response of a serpentine flow-field PEMFC ii: Normal to minimal fuel and air, *Journal of Power Sources*, 156(1):369-374, 2006. 19

[93] W. Yan, C. Soong, F. Chen, and H. Chu, Transient analysis of reactant gas transport and performance of PEM fuel cells, *Journal of Power Sources*, 143(1-2):48-56, 2005. 19

[94] **H. Wu**, X. Li, and P. Berg, Numerical analysis of dynamic processes in fully humidified PEM fuel cells, *International Journal of Hydrogen Energy*, 32(12):2022-2031, 2007. 19, 67

[95] D. Natarajan and T.V. Nguyen, A two-dimensional, two-phase, multicomponent, transient model for the cathode of a proton exchange membrane fuel cell using conventional gas distributors, *Journal of the Electrochemical Society*, 148(12):A1324-A1335, 2001. 14, 19, 41

[96] P. Berg, K. Promislow, J. Stumper, and B. Wetton, Discharge of a segmented polymer electrolyte membrane fuel cell, *Journal of Fuel Cell Science and Technology*, 2(2):111-120, 2005. 19

[97] J. Stumper, H. Haas, and A. Granados, *In-Situ* Determination of MEA resistance and electrode diffusivity of a fuel cell, *Journal of the Electrochemical Society*, 152(4):A837-A844, 2005. 19, 25

[98] H. Meng, Numerical investigation of transient responses of a PEM fuel cell using a two-phase non-isothermal mixed-domain model, *Journal of Power Sources*, 171(2):738-746, 2007. 19, 98

[99] Y. Wang and C.Y. Wang, Two-phase transients of polymer electrolyte fuel cells, *Journal of the Electrochemical Society*, 154(7):B636-B643, 2007. 19, 87

[100] F. Opekar and D. Svozil, Electric resistance in a Nafion membrane exposed to air after a step change in the relative humidity, *Journal of Electroanalytical Chemistry*, 385(2):269-271, 1995. 19, 37, 95

[101] M.B. Satterfield and J.B. Benziger, Non-Fickian water vapor sorption dynamics by Nafion membranes, *Journal of Physical Chemistry B*, 112(12):3693-3704, 2008. 19, 37, 49, 78, 95

[102] A. Vorobev, O. Zikanov, and T. Shamim, A computational model of a PEM fuel cell with finite vapor absorption rate, *Journal of Power Sources*, 166(1):92-103, 2007. 20, 37

[103] A.A. Shah, G.S. Kimb, P.C. Sui, and D. Harvey, Transient non-isothermal model of a polymer electrolyte fuel cell, *Journal of Power Sources*, 163(2):793-806, 2007. 20, 37

[104] V. Gurau, T.A. Zawodzinski, and J. Adin Mann, Two-phase transport in PEM fuel cell cathodes, *Journal of Fuel Cell Science and Technology*, 5:021009/1-12, 2008. 20

[105] D. Gerteisen, T. Heilmann, and C. Ziegler, Modeling the phenomena of dehydration and flooding of a polymer electrolyte membrane fuel cell, *Journal of Power Sources*, 187(1):165-181, 2009. 20

[106] **H. Wu**, P. Berg, and X. Li, Steady and unsteady 3D non-isothermal modeling of PEM fuel cells with the effect of non-equilibrium phase transfer, *Applied Energy*, in press, doi:10.1016/j.apenergy.2009.06.024. 20

[107] **H. Wu**, X. Li, and P. Berg, On the modeling of water transport in PEM fuel cells, *Electrochimica Acta*, 54(27):6913-6927, 2009. 20

[108] **H. Wu**, P. Berg, and X. Li, Modeling of PEM fuel cell transients with finite-rate phase transfer processes, *Journal of the Electrochemical Society*, accepted, 2009. 20

[109] J.J. Baschuk, Comprehensive, consistent and systematic approach to the mathematical modeling of PEM fuel cells, *PhD thesis*, University of Waterloo, 2006. 22, 74, 103

[110] *Fluent User Manual 6.3*. 23, 46, 60, 67

[111] P. Berg, A. Novruzi, and K. Promislow, Analysis of a cathode catalyst layer model for a polymer electrolyte fuel cell, *Chemistry Engineering Science*, 61(13):4316-4331, 2006. x, 29, 38

[112] Q.P. Wang, M. Eikerling, D.T. Song, and Z.S. Liu, Structure and performance of different types of agglomerates in cathode catalyst layers of PEM fuel cells, *Journal of Electroanalytical Chemistry*, 573(1):61-69, 2004. 29

[113] L.M. Onishi, J.M. Prausnitz, and J. Newman, Water diffusion equilibria. Absence of Schroeder's paradox *Journal of Physical Chemistry B*, 111(34):10166-10173, 2007. 37

[114] Q. Ye and T.V. Nguyen, Three-dimensional simulation of liquid water distribution in a PEMFC with experimentally measured capillary functions, *Journal of the Electrochemical Society*, 154(12):B1242-B1251, 2007. 37, 43, 44, 87

[115] S. Ge, X. Li, B. Yi, and I.M. Hsing, Absorption, desorption, and transport of water in polymer electrolyte membranes for fuel cells *Journal of the Electrochemical Society*, 152(6):A1149-A1157, 2005. 37, 38

[116] R. Bird, W. Stewart, and E. Lightfoot, *Transport Phenomena (2nd Edition)*, Wiley, New York, 2002. 39

[117] H.K. Cammenga, Evaporation mechanisms of liquids, *Current Topics in Materials Science (Editor: E. Kaldis)*, Chapter 4, North-Holland, 1980. 40

[118] J.G. Collier and J.R. Thome, *Convective Boiling and Condensation*, 3rd ed., Clarendon Press, Oxford, 1994. 40

[119] H. Kim, P.S.C. Rao, and M.D. Annable, Determination of effective air-water interfacial area in partially saturated porous media using surfactant adsorption, *Water Resource Research*, 33(12):2705-711, 1997. 41

[120] M.C. Leverett, Capillary behavior in porous solids, *Transaction of AIME*, 142:151-169, 1941. 42

[121] M. Kaviany, *Principles of Heat Transfer in Porous Media*, 2nd ed., Wiley, New York, 1995. 44

[122] J. Chen, J. Hopmans, and M. Grismer, Parameter estimation of two-fluid capillary pressure saturation and permeability functions, *Advances in Water Resources*, 22(5):479-493, 1999. 44

[123] J.B. Kool, J.C. Parker, and M.T. Van Genuchten, Parameter estimation for unsaturated flow and transport models - A review, *Journal of hydrology*, 91(3-4):255-293, 1987. 44

[124] P. Ustohal, F. Stauffer, and T. Dracos, Measurement and modeling of hydraulic characteristics of unsaturated porous media with mixed wettability, *Journal of Contaminant Hydrology*, 33(1-2):5-37, 1998. 44

[125] T.A. Corey, *Mechanics of Immiscible Fluids in Porous Media*, 1st ed., Colorado, 1994. 44, 87

[126] Y. Wang, S. Basu, and C.Y. Wang, Modeling two-phase flow in PEM fuel cell channels, *Journal of Power Sources*, 179(2):603-617, 2008. 44

[127] C.Y. Wang, Fundamental models for fuel cell engineering, *Chemical Reviews*, 104(12):4727-4766, 2004. 46

[128] V.E. Ostrovskii and B.V. Gostev, Heat effects and rates and molecular mechanisms of water sorption by perfluorinated polymer materials bearing functional groups, *Journal of Thermal Analysis and Calorimetry*, 46(2):397-416, 1996. 48

[129] **H. Wu**, X. Li, and P. Berg, Transient Analysis of Fully Humidied PEM Fuel Cells, Editors: I. Dincer and X. Li, ISBN: 0-9781236-0-3, *Proceedings of the* 2^{nd} *Int. Green Energy Conference*, Oshawa, ON, 2006. 49, 76

[130] Z. Qi and A. Kaufman, Low Pt loading high performance cathodes for PEM fuel cells, *Journal of Power Sources*, 113(1):37-43, 2003. 53

[131] K. Ito, K. Ashikaga, H. Masuda, T. Oshima, Y. Kakimoto, and K. Sasaki, Estimation of flooding in PEMFC gas diffusion layer by differential pressure measurement, *Journal of Power Sources*, 175(2):732-738, 2008. 53

[132] F.P. Incropera and D.P. Dewitt, *Fundamentals of Heat and Mass Transfer*, John Wiley & Sons, 5^{th} Edition, 2002. 54

[133] E.I. du Pont de Nemours and Company, http://www.dupont.com. 54

[134] S.V. Patankar, *Numerical Heat Transfer and Fluid Flow*, McGraw-Hill, New York, 1980. 61

[135] J. Hamelin, K. Agbossou, A. Laperriere, F. Laurencelle, and T.K. Bose, Dynamic behavior of a PEM fuel cell stack for stationary applications, *International Journal of Hydrogen Energy*, 26(6):625-629, 2001. 72

[136] H. Yu and C. Ziegler, Transient behavior of a proton exchange membrane fuel cell under dry operation, *Journal of the Electrochemical Society*, 153(3):A570-A575, 2006. 72, 74

[137] C. Marr and X. Li, An engineering model of proton exchange membrane fuel cell performance, *ARI* 50(4):190-200, 1998. 75

[138] C. Ziegler, T. Heilmann, and D. Gerteisen, Experimental study of two-phase transients in PEMFCs *Journal of the Electrochemical Society*, 155(4):B349-B355, 2008. 90, 92, 94

[139] Q. Yan, H. Toghiani, and H. Causey, Steady state and dynamic performance of proton exchange membrane fuel cells (PEMFCs) under various operating conditions and load changes, *Journal of Power Sources*, 161(1):492-502, 2006. 99, 101

[140] F.M. White *Fluid Mechanics*, 5th edition, McGraw Hill, 2003. 102

[141] S.A. Freunberger, M. Reum, A. Wokaun, and F. N. Büchi, Expanding current distribution measurement in PEFCs to sub-millimeter resolution, *Electrochemistry Communications*, 8(9):1435-1438, 2006. xiii, 117, 118

[142] X. Li and I. Sabir, Review of bipolar plates in PEM fuel cells: flow-field designs, *International Journal of Hydrogen Energy*, 30(4):359-371, 2003. 124

[143] H.M. Russel and C.M. Carlstrom, US patent No. 6,500,580, 2008. xiii, 133